Self Calibrating Interferometric Sensor

Sørensen, Henrik Schiøtt

Publication date:
2006

Document Version
Publisher's PDF, also known as Version of record

Risø-PhD-19(EN)

Self Calibrating Interferometric Sensor

Henrik Schiøtt Sørensen

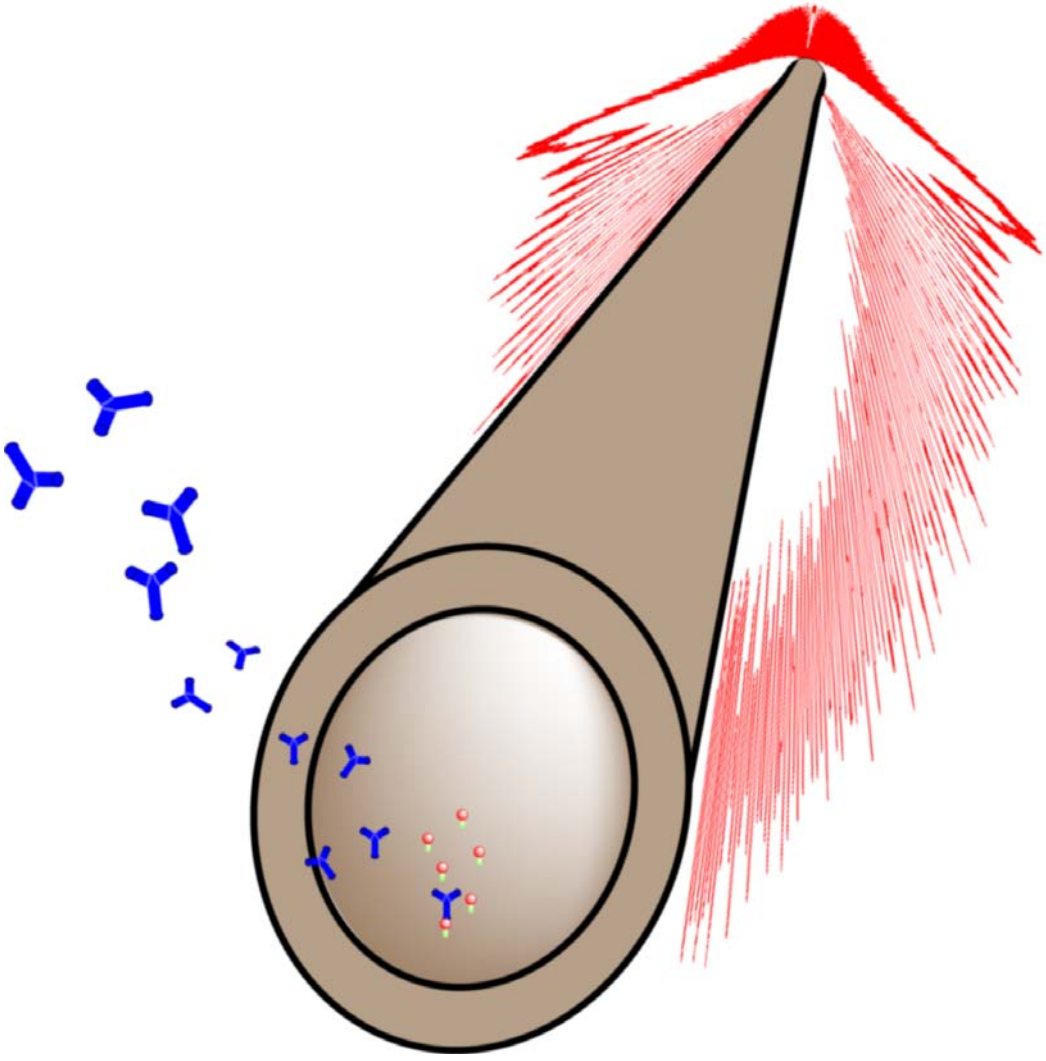

Risø National Laboratory
Roskilde
Denmark
January 2006

Risø-PhD Thesis

Author: Henrik Schiøtt Sørensen
Title: Self Calibrating Interferometric Sensor
Department: Optics and Plasma Research Department

This thesis is submitted in partial fulfilment of the requirements for the Ph.D. degree at the Technical University of Denmark

Abstract (max. 2000 char.):
This thesis deals with the development of an optical sensor based on micro interferometric backscatter detection (MIBD). A price effective, highly sensitive and ready for mass production platform is the goal of this project. The thesis covers three areas. The first part of the thesis deals with theoretical models for describing the optical phenomena utilized in this technique. A model based on ray–tracing has been developed and shown to be a valuable tool for describing certain features in the fringe pattern. The MIBD measurement technique has been expanded to do absolute determination of the refractive index, with an experimental precision of $2.5 \cdot 10^{-4}$, using this newly discovered feature. As the MIBD has been used as a biosensor for detecting molecular scaled species, a model valid for changes in system sizes below the geometrical optics regime has been developed. Modeling based on solutions to Maxwell's equations has with high accuracy described the optical effects when binding events occurs on the inside of a capillary. It is of paramount importance to find a practical stop criteria for the else infinite summation used to find the scattering constants, which is the basis for the model. Different geometries have been modeled, including semicircular, circular and rectangular flowchannels. Theoretical work has shown that the sensitivity of the rectangular geometry is caused by diffraction off the corners. The second part of the thesis deals with the fabrication of injection molded polymer microflow chips. The MIBD technology has been transferred to a chip based platform with a close–to–capillary like geometry. These assembled chips has in the MIBD setup shown detection limits of $\Delta n = 4 \cdot 10^{-6}$. The fabrication has been done by isotropic etching in silicon through a silicon nitride sacrificial mask. The fabricated micro structures have been electroplated for later injection molding, showing the potential of the MIBD sensor to be mass produced with high reproducibility and sensitivity. In part three MIBD experiments on vital biological systems are described. Label–free binding studies of bio molecules have been performed in easy to fabricate micro flow channels in elastomer material (PDMS), both surface bound and in free solution. Thermodynamic binding constants for protein–protein interactions has been found and validated by other techniques. The detection limit obtained from these experiments were 9 attomole Human IgG in a 495 pL measurement volume. The free solution protein binding experiments and results places MIBD in a unique position with comparable thermodynamic capabilities with the golden standard ITC, but orders of magnitude faster and less analyte sample consuming. The completion of a Lab–on–a–chip device making a complete blood analysis will be a paradigm shift moving the analysis from the laboratories closer to the bedside.

Risø-PhD-19(EN)
January 2006

ISBN 87-550-3495-0

Contract no.:

Group's own reg. no.:
1705079

Sponsorship:
The BIOP Graduate School
Grant 643-01-0092
The National Science Foundation
Grant DBI-0355435
National Institutes of Health
R01 EB003537-01A2

Cover :
Drawing of IgG molecules binding to the affinity layer inside the capillary. The scattered light pattern is simulated with models developed in the project describing the binding events occurring.

Pages:176
Tables:20
References:178

Risø National Laboratory
Information Service Department
P.O.Box 49
DK-4000 Roskilde
Denmark
Telephone +45 46774004
bibl@risoe.dk
Fax +45 46774013
www.risoe.dk

Self Calibrating Interferometric Sensor

Henrik Schiøtt Sørensen

PhD thesis

Abstract

This thesis deals with the development of an optical sensor based on micro interferometric backscatter detection (MIBD). A price effective, highly sensitive and ready for mass production platform is the goal of this project. The thesis covers three areas. The first part of the thesis deals with theoretical models for describing the optical phenomena utilized in this technique. A model based on ray–tracing has been developed and shown to be a valuable tool for describing certain features in the fringe pattern. The MIBD measurement technique has been expanded to do absolute determination of the refractive index, with an experimental precision of $2.5 \cdot 10^{-4}$, using this newly discovered feature. As the MIBD has been used as a biosensor for detecting molecular scaled species, a model valid for changes in system sizes below the geometrical optics regime has been developed. Modeling based on solutions to Maxwell's equations has with high accuracy described the optical effects when binding events occurs on the inside of a capillary. It is of paramount importance to find a practical stop criteria for the else infinite summation used to find the scattering constants, which is the basis for the model. Different geometries have been modeled, including semicircular, circular and rectangular flow channels. Theoretical work has shown that the sensitivity of the rectangular geometry is caused by diffraction off the corners. The second part of the thesis deals with the fabrication of injection molded polymer microflow chips. The MIBD technology has been transferred to a chip based platform with a close–to–capillary like geometry. These assembled chips has in the MIBD setup shown detection limits of $\Delta n = 4 \cdot 10^{-6}$. The fabrication has been done by isotropic etching in silicon through a silicon nitride sacrificial mask. The fabricated micro structures have been electroplated for later injection molding, showing the potential of the MIBD sensor to be mass produced with high reproducibility and sensitivity. In part three MIBD experiments on vital biological systems are described. Label–free binding studies of bio molecules have been performed in easy to fabricate micro flow channels in elastomer material (PDMS), both surface bound and in free solution. Thermodynamic binding constants for protein–protein interactions has been found and validated by other techniques. The detection limit obtained from these experiments were 9 attomole Human IgG in a 495 pL measurement volume. The free solution protein binding experiments and results places MIBD in a unique position with comparable thermodynamic capabilities with the golden standard ITC, but orders of magnitude faster and less analyte sample consuming. The completion of a Lab–on–a–chip device making a complete blood analysis will be a paradigm shift moving the analysis from the laboratories closer to the bedside.

Abstract – Dansk resume

Denne afhandling omhandler udviklingen af en optisk sensor baseret på Mikro Interferometrisk Tilbagespredt Detektion (MITD). Afhandlingen dækker tre områder. Den første del af afhandlingen omhandler teoretiske modeller, der beskriver fænomenerne bag den interferometri baserede sensor. En stråle baseret optisk model er blevet udviklet og har vist sig at være et værdifuldt værktøj, der beskriver strukturter i stribe mønstret, der muliggør bestemmelse af det absolutte brydningsindeks. Gennem eksperimenter har denne fundamentale nye måde at benytte MITD metoden på bestemt det absolutte brydningsindeks med en præcision på $2.5 \cdot 10^{-4}$. Da MITD er blevet benyttet som en biosensor til måling af molekylære størrelser, er en gyldig model blevet udviklet for størrelsesændringer mindre end beskrevet ved geometrisk optik. Den elektromagnetiske bølge model har med høj nøjagtighed beskrevet bindingsreaktioner, der foregår på indersiden af et kapilærrør. Det har kun været muligt ved at finde et brugbart stop kriterium til den ellers uendelige sum, der benyttes til at finde spredningskonstanterne, modellen bygger på. Teoretisk arbejde har vist at følsomheden fra den rektangulære geometri stammer fra diffraktion fra hjørnerne. Den anden del af afhandlingen omhandler fremstillingen af sprøjtestøbte polymer mikroflow chips. MITD teknologien er blevet overført til en chip baseret platform med en kapillærrør–lignende geometri. Disse samlede chip har i MITD opsætningen vist målegrænser på $\Delta n = 4 \cdot 10^{-6}$. Fremstillingen er udført ved at ætse isotropisk i silicium gennem en siliciumnitrid maske. De fremstillede mikrostrukturer er blevet galvaniseret for senere at blive sprøjtestøbt, derved er potentialet for MITD sensoren for at blive masseproduceret med høj reproducerbarhed og følsomhed vist. I tredje del er MITD eksperimenter beskrevet. Markørfri bindingsstudier af biomolekyler er blevet udført i mikroflow kanaler i et elastisk materiale (PDMS). Dette er udført hhv. med reaktatterne i fri opløsning eller bundet til en overflade. Termodynamiske bindings konstanter for protein–protein reaktioner er bestemt og eftervist med andre teknikker. Målegrænser opnået med disse eksperimenter var 9 attomol Human IgG i et 495 pL stort målevolume. Eksperimenterne med protein reaktioner i opløsning og de opnåede resultater placerer MITD i en unik position, hvor man hurtigere og med mindre prøve forbrug kan få termodynamiske data, der er sammenlignelige med den gyldne standard ITC. Færdiggørelsen af et Lab–on–a–chip, der kan udføre komplete analyser på blod vil være et paradigmeskift, der flytter analysen ud af laboratoriet og tættere på patienterne.

Contents

List of publications

Reviewed papers

- Sørensen, H.S.; Pranov, H.; Larsen, N.B.; Bornhop, D.J.; Andersen, P.E., Absolute refractive index determination by microinterferometric backscatter detection. Analytical Chemistry. (2003) 75 , 1946-1953
- Latham, J.C.; Markov, D.A.; Sørensen, H.S.; Bornhop, D.j.; Photobiotin Surface Chemistry Improves Label-Free Interferometric Sensing of Biochemical Interactions. Accepted in Angewandte Chemie Int. Ed. 23 Sep 2005, Published Online: 30 Dec 2005; http://dx.doi.org/10.1002/anie.200502418
- Sørensen, H.S.; Latham, J.C.;Markov, D.A.; Andersen, P.E.; Bornhop, D.j.; Larsen, N.B., Fabrication of polymer flow chips with capillary-like geometry for an interferometric sensor. Manuscript in preparation for submission to Lab-On-A-Chip.
- Sørensen, H.S.; Latham, J.C.; Bornhop, D.j.; Larsen, N.B.; Andersen, P.E., Modeling of intreferometric bio sensing in capillary tubes. Manuscript in preparation for submission to Applied Physics Letters.
- Latham, J.C.; Markov, D.A.; Kussrow, A.; Sørensen, H.S.; Bornhop, D.j., Label-free interferometric sensing in free solution. Manuscript in preparation for submission to Science.

Patents

- Bornhop D.J.; Andersen P.E.; Sorensen H.S.; Pranov H., Refractive index measurement method for small volume of liquid, involves conducting analysis of pattern to determine refractive index which is related to sample refractive index dependent variations in light intensity. Patent WO2004023115-A1.
- Sørensen, H.S.; Latham, J.C.;Markov, D.A.; Wikswo, J.; Bornhop, D.j.,Single step microfluidic titrator for molecular interaction analysis with near real–time optical detection. Patent application.

International conferences

- Sørensen, H.S.; Pranov, H.; Larsen, N.B.; Bornhop, D.j.; Andersen, P.E., Absolute refractive index determination by micro interferometric backscatter detection. BioMEMS and Biomedical Nanotech, Columbus, OH(US), 6–8 Sep 2002. Poster
- Sørensen, H.S.; Larsen, N.B.; Andersen, P.E.; Bornhop, D.J., Fabrication of a polymer based bio-sensing optical component. LabAutomation 2004, San Jose, CA (US), 3–5 Feb 2004. Poster.
- Latham, J.C.;Sørensen, H.S.; Forster, F.; Larsen, N.B.; Andersen, P.E.; Bornhop, D.J., Structural investigations of poly(dimethylsiloxane) channel geometry used for a chip scale interferometer. Nano Tech 2004, Montreux (CH), 16–18 Nov 2004. Oral presentation.
- Sørensen, H.S.; Latham, J.C.; Markov, D.; Larsen, N.B.; Bornhop, D.J.; Andersen, P.E., Microfluidic polymer chip for biosensing based on micro–interferometric backscatter detection. Photonics West 2005, San Jose, CA (US), 22–27 Jan 2005. Oral presentation.
- Sørensen, H.S.; Latham, J.C.; Larsen, N.B.; Bornhop, D.J.; Andersen, P.E., Analytical modeling of the micro–interferometric backscatter detection scheme based on an electromagnetic–wave–based description. Photonics West 2005, San Jose, CA (US), 22–27 Jan 2005. Oral presentation.
- Sørensen, H.S.; Latham, J.C.;Markov, D.A.; Bornhop, D.j.; Andersen, P.E.; Larsen, N.B.,Chip Scale Interferometry A micro fluidic platform for biochemical sensing. In: Book of abstracts. Bio Photonics '05, Ven, Sweden, 21 Jun 2005. Poster.

National meetings

- Sørensen, H.S.; Pranov, H.; Larsen, N.B.; Bornhop, D.j.; Andersen, P.E., Absolute refractive index determination by micro interferometric backscatter detection. Biomedical optics'02 (BIOP 2002), Lyngby (DK), 22 Oct 2002. Poster.
- Sørensen, H.S.; Pranov, H.; Larsen, N.B.; Bornhop, D.J.; Andersen, P.E., Absolute refractive index determination by micro-interferometric backscatter detection. In: Book of abstracts. DOPS annual meeting, Risø(DK), 21–22 Nov 2002. (Dansk Optisk Selskab; Forskningscenter Risø, Roskilde, 2002). Oral presentation.
- Sørensen, H.S., Microstructure fabrication for an optical polymer based bio–chip sensor. Biomedical optics '03 (BIOP 2003), Lyngby (DK), 28 Oct 2003. Poster.
- Sørensen, H.S., Label-free interferometric sensing of biochemical interactions. Biomedical optics '04 (BIOP 2004), Lyngby (DK), 2 Nov 2004. Oral presentation.
- Sørensen, H.S.; Latham, J.C.;Markov, D.A.; Bornhop, D.j.; Andersen, P.E.; Larsen, N.B.,Chip Scale Interferometry A micro fluidic platform for biochemical sensing. In: Book of abstracts. DOPS Annual Meeting 2005, Risø,(DK), 17–18 Nov 2005. (Dansk Optisk Selskab; Forskningscenter Risø, Roskilde, 2005). Poster. "Winner of the Best Poster Award"

Preface

This thesis presents work carried out in the period October 2002 – January 2006 and is submitted in partial fulfilment of the requirements for the PhD (Philosophiae Doctor) degree at the Technical University of Denmark.

I have been enrolled at the Department of Manufacturing Engineering and Management at the Technical University of Denmark, under the supervision of Associate Professor Henrik K. Rasmussen.

The work has been carried out at the Optics and Plasma Research department at Risø National Laboratory supervised by Senior Scientist Peter E. Andersen from the Optics and Plasma Research department and Research Professor Niels B. Larsen from the Danish Polymer Centre also located at Risø. During the project I spend close to one year in the United States. Research were done at Texas Tech University, Lubbock, TX and at Vanderbilt University, Nashville, TN and both places supervised by Professor Darryl J. Bornhop.

The project has been funded by:

- The BIOP Graduate School Grant 643–01–0092
- The National Science Foundation Grant DBI–0355435
- National Institutes of Health Grant R01 EB003537–01A2

Henrik Schiøtt Sørensen
January 2006

Acknowledgements

There are many people, to whom I owe thanks for helping out in my project one way or the other.

I would like to thank my supervisor from DTU, Henrik Rasmussen for helping me get through the project.

Peter, Niels and Darryl! You have been an excellent combination of mentors. You have been a huge source of inspiration. I am thankful for always getting your full support. Your guidance has made me perform so much more than I thought possible. Darryl has always raised the expectations into the sky, while Niels has kept my feet on the ground. Mentally I am prepared by Peter to go to the final frontier where no one has gone before.

I have really enjoyed the company of many new friends at Vandy. Especially the BAD ASS group. I would like to thank Professor Wikswo and Professor Davidson for assistance and use of lab space during my visit.

Tim, you and the guys gave me a warm welcome in Texas. Thanks for letting me stay in your house and I am sorry for any inconvenience. Good luck with the goat farm.

From the first moment you have always tried ti teach me about science. Dima, I am glad that we over the years have agreed on most of the subjects.

I have been welcomed into the Latham family and Joey has become a very dearly friend of mine. We have had so many experiences during all the time we have been living together. The exchange has been a good experience. You are always welcomed at my place.

Back home at Risø I have had the pleasure of having many good colleagues, that always had a good advise. I thank Jørgen and Lene for making the long hours in the clean room more enjoyable.

I have always enjoyed going to the Polymer department. Most of the time not finding Niels but kept running into Susan. It has been many good hours talking, not just science.

For nearly ten years I have been working together with Henrik Pranov. During this project you have been a good friend and colleague helping with practical stuff and putting things in another perspective.

I have had the pleasure of spending three years in the same office with Nina. Your always positive attitude and humor has made the corner office one of the best working places at Risø.

I would like to thank my family for your support and strange questions, that made me rethink about the science. Hannah, I feel sorry for your losses caused by this project, but it could not have been realized without your carrying support and immence patience. Hannah and Nicklas, you are the reason I wake up in the morning.

1 Introduction

1.1 Background

The monitoring of the environment [1, 2] and fast scanning of biomedical samples [3, 4] are booming markets. The establishment of "Medicon Valley" in the region around Copenhagen and the 40% year–on–year growth in proteomics [5] are indicators of the potential of this field. The major demand is ultra high sensitivity in terms of detecting very small amounts of chemicals [6]. The use of electrochemical sensors are widely used for detection in electrophoresis [7]–[9] although this method only works for analytes that are chemically active. In electrochromatography, low detection limits may be reached by laser induced fluorescence [10]–[14]. Not all analytes fluoresce at available laser wavelengths and therefore complex and time–consuming chemical tagging steps are often used [15]. Recently measuring the refractive index as sensing principle has shown potential and the phenomena used are often based on the evanescent wave behavior of light confined in a guiding material. The reverse symmetry waveguide [16] has with its high penetration depth monitored living cells in minute samples. Photonic crystals in waveguides are well suited for detecting DNA molecules close to the material surface [17], but most attention has in the past decade been given to the surface plasmon resonance (SPR) sensor first described by Otto [18]. The principle was first used for bio–sensing more than 20 years ago by Liedberg [19] but is still being optimized for better sensitivity. The SPR sensor is fundamentally limited by its complexity and expensive sample containers, which requires a thin metal layer in order to function.

The field of microanalysis is growing rapidly [20] for several reasons. A major advantage of the micro–total–analysis-systems (μ–TAS) [21] or Lab–on–a–chip is their dramatic decrease in precious analyte and analysis reagents volumes, typically 3–4 orders of magnitude. Another novel ability of μ–TAS devices is their multi–functionality that may comprise a complete measurement system in one unit [22]. They may be designed for a single purpose or to analyze for multiple chemicals. A μ–TAS has the advantage of no outside intervention, when making a multi-step procedure. The implementation of traditional measurement methods in a μ–TAS will often affect their detection limit. The decrease in detection limits is due to the smaller detection volume providing much less analyte to detect. The micro interferometer backscatter detection (MIBD) scheme is a method using change in refractive index of fluids in micro flow channels.

1.2 Motivation

In this work is presented theoretical and experimental work done on the Micro interferometric backscatter detection scheme. This is a competitive alternative to the methods mentioned above. There are a number of desirable features of a sensor before deployment as a tool in these analyte detections [23]:

- short response times for fast measurements,
- possibility of continuous flow devices,
- miniaturization,
- targeted specificity,
- versatile in multiple materials as polymers and glasses,
- cost effective, suitable for mass production.
- universal high sensitivity.

Micro interferometer backscatter detection (MIBD) is one detection scheme that may be miniaturized [24, 25]. The detection limit does not decrease when using smaller volumes in the measurement. The method detects concentration, i.e. mass per volume. The MIBD system is a detection method at the same level of detection as the methods mentioned above. Even though commercial lab–on–chip devices are available, these devices are still somewhat limited by detection methodologies. Some of their limits may be overcome by the MIBD scheme since it is not dependent on e.g. fluorescence or absorbance. The MIBD scheme is deployed in situ without changing the fluid hence making fast analysis possible. The response times are reduced to a minimum using this method, since the optical response to a change in refractive index occurs immediately when the contents of the fluid changes. However, since the MIBD scheme is a universal detection method it has no specificity. The challenge is to improve the MIBD method to perform a measurement on the desired analyte only.

Simple micro interferometric systems have been able to detect small changes in refractive index in fluids. The term micro interferometry arise from the flow channel involved in the measurement. The flow is guided to the detection point by structures on the micrometer scale. The microstructure acts as the interferometer, hence the term micro interferometry. The experimental laboratory system, which has been set up to demonstrate the method, consists of a laser, micro flow channel and a detector [26]. A photograph of a set–up is shown in Figure 1.

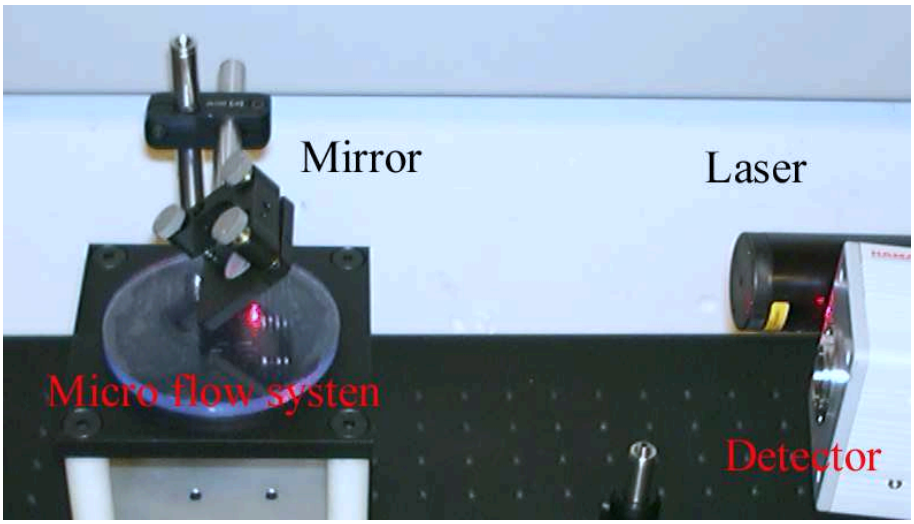

Figure 1. Images of the laboratory setup. A laser beam is reflected of the mirror impinging the micro flow system below. An interference pattern arises and is reflected back towards the detector, in this case a CCD–camera.

When illuminating the flow channel perpendicular to the flow by a laser, a 360° fan of scattered light is produced normal to the flow. The backscattered beam contains several sets of high contrast interference fringes, see Figure 2. The detector is placed to detect the light scattered back in the direction from where the laser source is impinging. The fringes are viewed on a flat plane in the backscattered configuration. When the refractive index of the fluid inside the capillary changes it results in a shift in fringe position on the detector. Thus, the fringe shift is the phenomenon that is detected. It has been shown that this simple system is capable of detecting Δn at the 10^{-6} level [24], just recently lowered 3 orders of magnitude [27]. Since the refractive index depends upon a wide range of parameters the method is universal. Thereby one is able to detect changes in temperature [28] or concentration [29, 30].

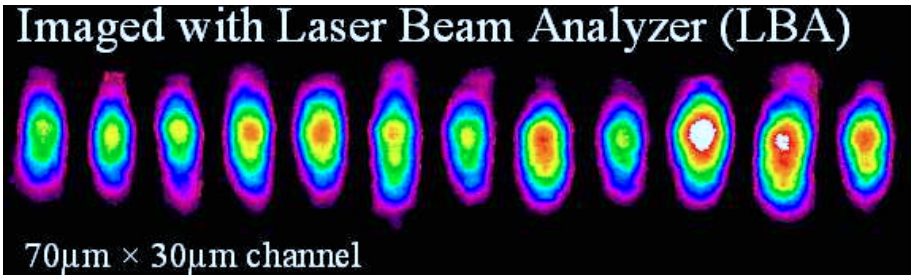

Figure 2. A laser beam analyzer has recorded the backscattered interference pattern. The pattern arises from a PDMS flow chip, with 30 µm wide and 70 µm deep channels. The liquid inside the channel is water.

1.3 Scope

- Theoretical models is developed and used to further give a fundamental understanding of the optical phenomenon behind this highly sensitive detection method.
- To mature the sensing technique further the capillary based technology is transferred to polymer flow chips. A goal of this work is to fabricate an inexpensive, highly refractive index sensitive, chip based system, to form a platform, which may be applied to a wide range of novel analytical applications.
- The biological and physical applications includes protein detection and thermodynamic analysis of bio–molecular interactions. All detected label–free with this refractive index sensor.

To achieve this, key issues of reproducibility, specificity and fundamental understanding of the optical phenomenon on chip–based systems are to be thoroughly investigated and discussed.

A more detailed theoretical and practical understanding of the fundamental physical behavior of this system is necessary. Development of a model containing micro flow channels is a major milestone in reaching the necessary stage of understanding to produce the desired platform. This includes optical numerical models which can be validated by or explain the experiments performed in all the relevant regimes involved in this work both geometry and dimension wise.

Implementation of the system requires meticulous material considerations. Most μ–TAS are fabricated by fast prototyping in polydimethylsilane (PDMS) [31, 32] or etched in glass. The MIBD scheme is not limited to those materials only. It may be fabricated in thermoplastic polymers, thus making a device more mechanically stable than PDMS and reducing the cost of a single chip compared to glass micro flow systems [33]. For making such highly advanced micro flow channel photolithography is used for making a master. The master is then used for fabrication in injection molding. This is a well-known technique that ensures that demands on sealing, mechanical stability and replication are met.

As the pharmaceutical industry develops and tests an ever increasing number of drug candidates, there is an increasing demand for high–throughput screening capabilities. Advanced future personalized medicine still needs an affordable platform in order to be realized. As Human Immunoglobulin G (IgG) plays a major role in the body's defensive system, this protein is a relevant choice for biological investigations.

1.4 Organization

The thesis is covering three major areas including optical modeling, micro fabrication and interferometry experiments.

In chapter 1: The background, motivation and scope are presented.

In chapter 2: The theoretical models are presented. A 6–beam ray–tracing based model of a capillary is described. By electro–magnetic wave theory models has been developed for a flow system with circular geometry. The model has been expanded to describe capillaries with affinity layers as well. Different geometry systems has been modeled by the commercial available software ASAP from Breault research.

In chapter 3: Several fabrication techniques are presented. Isotropical etching in fused silica and in silicon procedures for making circular structures has been developed and are presented.

In chapter 4: A fundamental new way of using MIBD for determining the absolute refractive index is presented.

In chapter 5: Experiments of surface bound protein–protein interactions in capillaries is presented. Modeled results are compared to the experiments.

In chapter 6: The polymer chip fabrication is described. Assembled chips has been used for temperature and concentration experiments.

In chapter 7: Bio–molecular interactions are described as they occur in micro flow chips and are being monitored label–free by MIBD, both surface bound and in free–solution.

In chapter 8: Discussions concerning the improvement and future applications for MIBD sensors are presented. The sensor is compared to state–of–the–art competitive techniques.

In chapter 9: The concluding remarks on the work done with MIBD sensor is presented.

References are marked by square brackets, [ ], and are found at the end of the thesis. In Appendix, the published papers are enclosed.

2 Optical modeling of micro interferometric backscatter detection

Previously systems of similar geometry as the MIBD scheme has been modeled by obtaining solutions to Maxwell's equations governing light propagation[34] or by optical ray tracing. Kerker and Matijevic[35] made the first complete model based on solutions to Maxwell's equations describing two concentric cylinders. Watkins confirmed these results experimentally[36]. However Watkins consider optical glass fibers with thick claddings and do therefore obtain results significantly different to those observed in MIBD, as the interference pattern is claimed not to be dependent of the refractive index of the core in the backscatter angle regime. Marcuse and Presby[37] extended this model to also take into account the case of a thin cladding of the fibers. From their results, an abrupt change in the backscattered light intensity pattern is observed. However, it was not realized that this abrupt change could be utilized to obtain the absolute refractive index with high precision, since they were attempting to determine the outer radius of the glass fiber, and they were not concerned with the core index. Note that the position of the abrupt change depends on the core index, see below. Here is presented a ray–tracing based model. Horton and Williamson[38] made a ray tracing model of an optical fiber obtaining information about the ratio between inner and outer radii of the fiber. The approach they used is a back calculation assuming a planar wave front of the output. The rays considered in their model are not the same as in our model, as they consider fibers with a thick cladding, and make use of multiple reflections inside the cladding. This is due to the fact that they use significantly different refractive indices of the core than those considered in MIBD. As the MIBD method has been applied to bio–sensing, with affinity layers a electromagnetic wave based model has been developed. The wave based model is using exact solutions to Maxwell's equations, hence valid in this regime well outside the range for geometric optics used for the ray–tracing model. Commercial available software has been used to compare different geometries used in MIBD. The theoretical work presented here has revealed the phenomena behind the high sensitivity of the MIBD scheme, e.g. the fringe shift in rectangular channels arise from diffraction off the corners.

2.1 Ray tracing-based modeling

The MIBD system has been modeled using a ray-tracing model by H. Tarigan et al.[39]. However, their model is limited by considering only small angle backscattered light $(0 - 3^\circ)$.

We have extended the model to include backscattering angles up to 90° (side scattered). This is done in the geometric optics regime by using Snell's law,

$$n_i sin(\Theta_i) = n_j sin(\Theta_j) \tag{1}$$

where n_i and n_j are the refractive indices of the media and Θ_i and Θ_j are the angles of light propagation in the respective media. Furthermore the law of reflection, $|\Theta_{in}| = |\Theta_{out}|$, is used. For angles beyond a few degrees it is not possible to use the assumption $(sin\Theta \approx \Theta)$ done by Tarigan et al. This implies that a simple analytical equation cannot be obtained. Our model traces six beams, see figure 3, through the system and calculates their interference in a detection plane placed in the far field region. For each type of beam a number of rays (typically 1000) are traced. The information carried along with each ray is its position, angle, intensity and phase. The intensity is calculated for each media interface incidents. An extension to pure ray tracing is the usage of *Fresnel equations* for determining

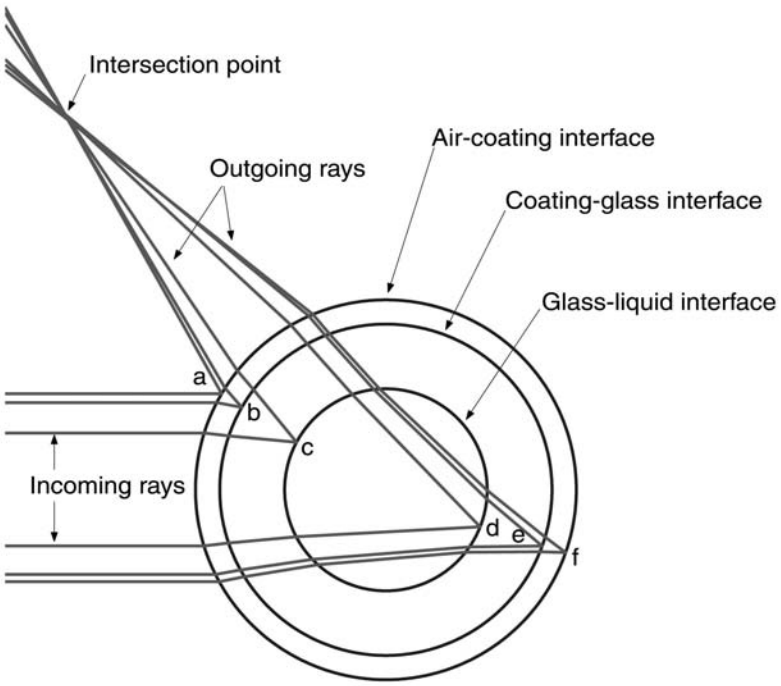

Figure 3. View of the cross-section of the capillary showing the ray paths through the capillary system. Six types of parallel incoming beams are considered corresponding to their interface of reflection (a - f). For each type of beam a number of rays (typically 1000) are traced yielding information about phase and intensity as function of position in a given detection plane for each type of beam. The interference between these six different types of beams is then calculated for multiple intersection points in the detection plane.

the reflection and transmission:

$$R = r^2 = \left(\frac{E_r}{E}\right)^2 = \left(\frac{\cos\Theta - \sqrt{n^2 - sin^2\Theta}}{\cos\Theta + \sqrt{n^2 - sin^2\Theta}}\right)^2 \tag{2}$$

$$T = 1 - R \tag{3}$$

$$n = \frac{n_j}{n_i} \tag{4}$$

The phase ρ changes 180° in case of external reflection and internal reflection is governed by:

$$\rho = 0^\circ \qquad \text{if } \Theta < \Theta_c$$

$$\rho = 2\arctan\left(\frac{\sqrt{\sin^2\Theta - n^2}}{\cos\Theta}\right) \qquad \text{if } \Theta > \Theta_c$$

$$\Theta_c = \arcsin n \tag{5}$$

Θ_c is the critical angle and angles above will lead to a complex phase and the light cannot escape the media, this is known as *total internal reflection*. At the

detection plane the interference is calculated based on the information packages of all rays. The six beams considered in the model interfere by

$$I_{ij} = 2\sqrt{I_i I_j} cos(\rho_i - \rho_j) \tag{6}$$

where I is the intensity and ρ is the phase of each individual ray, and i and j are indices for each ray, respectively. The model is developed to also take into account the polymer coating on the capillary, thus requiring six beams. The model assumes circular geometry of the capillary and that the laser can be described by plane waves.

Justification of assumptions.

The model assumption of capillary circular geometry is justified by the observation that no significant change in the pattern was observed during rotation of the capillary (TSP100170, Polymicro Technologies) around the capillary central axis. The tilt of the wave front from the laser (05-LHR-HeNe, Melles Griot) was analyzed using a beam analyzer (CLAS-2D, Wave Front Sciences) and was observed to be less than 0.01 μrad, thus justifying the assumption of a planar wave front. The smallest spacing of refractive index changes is the thickness of the coating of 12 μm . The assumption of geometrical optics being adequate is justified since the wavelength used (632.8 nm) is much smaller than the distances otherwise present in the system.

The ray tracing model has been constructed using the *Fresnel equations* for the TE–mode, transverse electric. This means that the E–field is perpendicular to the plane of incidence. If instead the magnetic field is transverse to the incidence plane, it is called TM–mode- Any arbitrary polarization direction can be represented by linear combinations of the TE– and the TM–modes. The reflection occurring in TM–mode is slightly different than in TE–mode, equation (2).

$$R = \left(\frac{n^2 \cos\Theta - \sqrt{n^2 - sin^2\Theta}}{n^2 \cos\Theta + \sqrt{n^2 - sin^2\Theta}} \right)^2 \tag{7}$$

The large difference is the change in phase upon reflection. with external reflection ($n_1 < n_2$), there is no phase changes until the angle of incidence reaches the *Brewster angle*,$\Theta_p = \arctan \frac{n_2}{n_1}$, also known as the polarization angle. From this angle on the phase shift is 180°, meaning that only one polarization is allowed, the TE–mode. Concerning internal reflection the phase shift is 180° until the *Brewster angle*. By only using TE–mode the model is still in good agreement with experiments as shown below.

6–beam model used on the fused silica capillary

In the micro interferometric backscatter detection scheme a capillary of 100 μm inner diameter (ID) is often used. The capillary has an outer diameter (OD) of 165 μm with a polyimid coating with a thickness of 12 μm. This capillary has been modeled with the 6–beam ray tracing based model. If the capillary is filled with water the backscattered fringe pattern is modeled to appear as shown in figure 4.

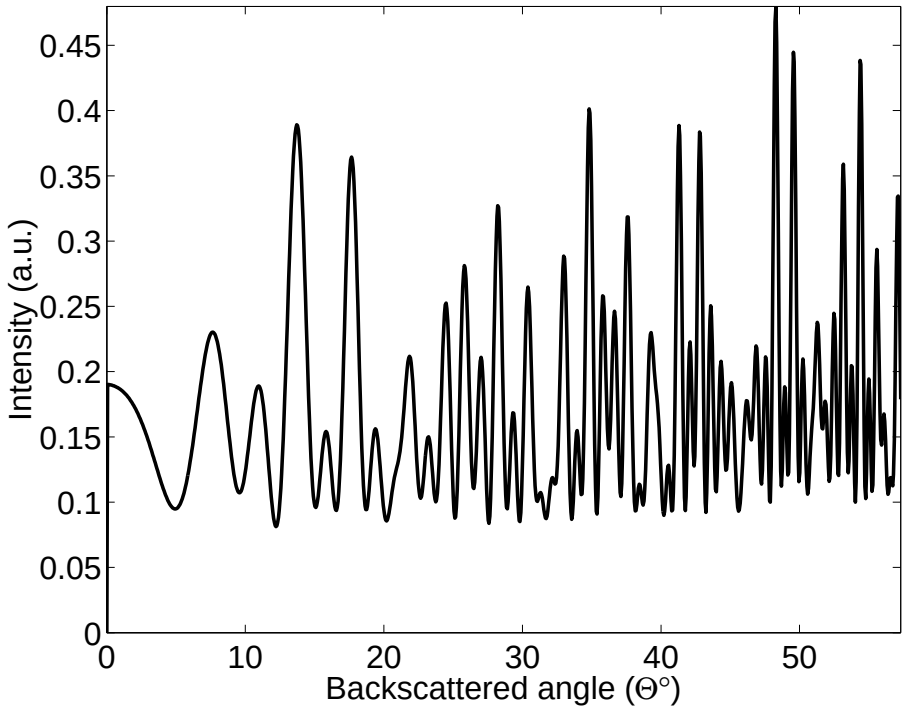

Figure 4. Calculated fringe pattern for a 100 μm *ID/*165 μm *OD/*12 μm *coating capillary. The refractive index of the liquid used is 1.333. The centroid is seen as the feature from 0 to* 5° *and the first fringe stops at* 9.5°.

The sensitivity of the first fringes is found, from the 6–beam model, to be:

$$S_{6-beam} = \frac{d\Theta}{dn} = \frac{12.9}{0,02} = 645^\circ \tag{8}$$

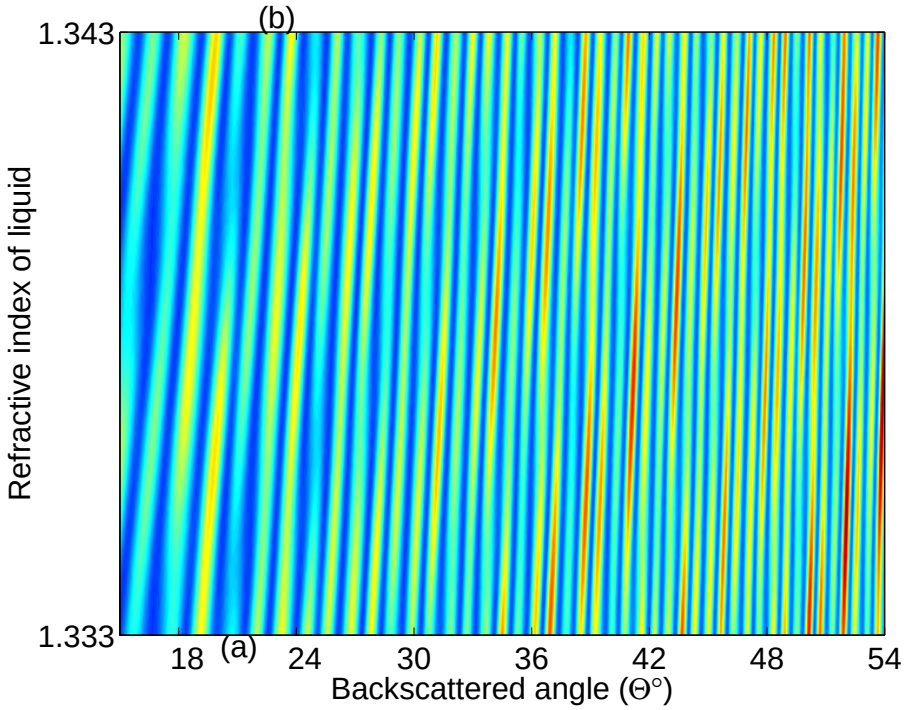

Figure 5. Calculated backscattering pattern for a refractive index index range from a 100 μm *ID/*165 μm *OD /*12 μm *coating capillary. The movement of the fringes at a backscattering angle of* 20° *is measured to be* 2.1° *per 0.01 refractive index change, measuring from (a) to (b).*

The results from the model are plotted in figure 5 as function of backscatter angle and refractive index of the liquid for a 100 μm ID/165 μm OD /12 μm coating capillary. The colorbar represents the intensity of the pattern in the given backscattered angle for the given refractive index of the liquid.

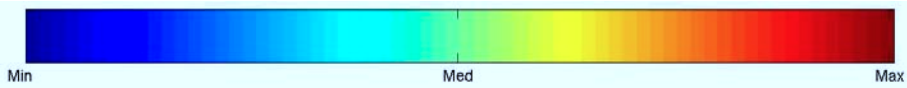

Experimentally obtained data are plotted the same way as the model and the results are shown in figure 6. At each refractive index a line profile of the intensity of the interference pattern has been made (figure 4). Each line profile has been extended vertically. The extended line profiles have been stacked into a single plot. These figures are used to directly compare the model and the experiment. In the MIBD experiments two sets of fringes are always present. The fringes moving outwards (medium frequency) with increasing refractive index are measured to move 4.0° when the refractive index is changed by 0.01 at a backscattering angle of 20° (a, b in figure 6). The model predicts a movement of 2.1° (a, b in figure 5). These are the fringes traditionally used for measuring refractive index using the MIBD technique.

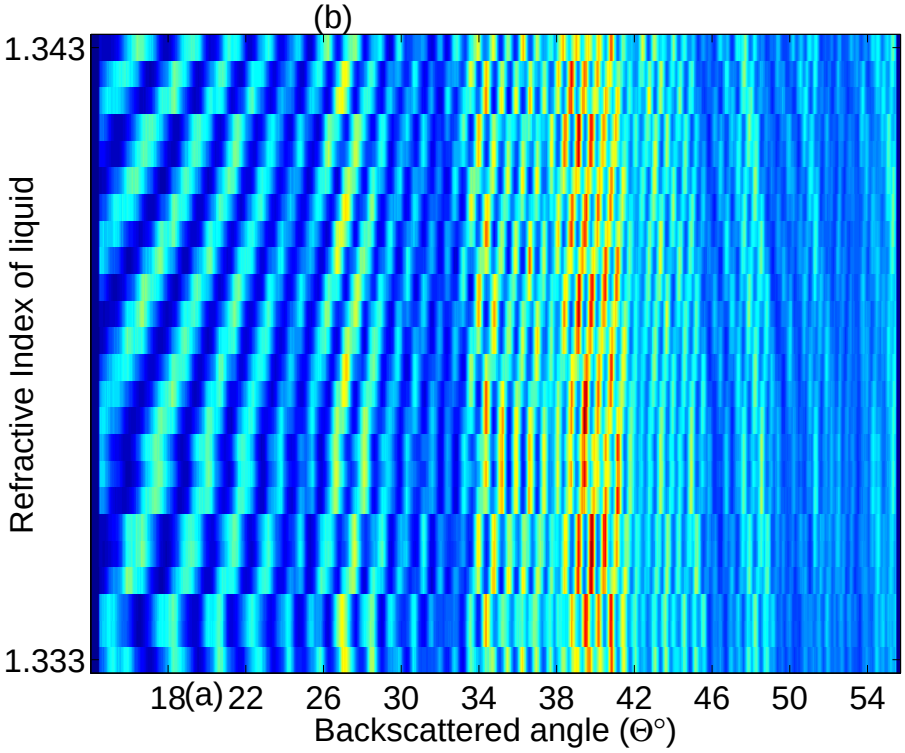

Figure 6. Experimentally obtained data for dilute sucrose solutions in a 100 μm *ID/*165 μm *OD /*12 μm *coating capillary. . The refractive index interval between measurements is less than the change required to move a fringe one fringe-width, thus allowing one to monitor the medium frequency fringes as continuous bands. The movement of these fringes varies with backscattering angle. For a backscattering angle of* 20° *this movement is measured to be* 4.0° *per 0.01 refractive index change, measuring from (a) to (b). Low frequency variations are seen as vertical light bands.*

This model predicts both low frequency and medium frequency variations of the pattern. These frequencies will be discussed below. The low frequency fringes are not moving significantly with changing refractive index. The model predicts no movement of these fringes. The number of these fringes in the model is 13 and in the experiment 10 fringes are observed within a range of backscattering angles from 14 to 54°.

2.2 Wave-based modeling

Description of model

A generic solution for describing the case of electromagnetic waves being scattered from concentric cylinders has been given by Kerker and Matijevic's paper from 1961 entitled "Scattering of Electromagnetic Waves from Concentric Infinite Cylinders" [35]. A numerical model describing scattering from an infinite cylinder is shown in the book by Bohren and Huffman, "Absorption and Scattering of Light by Small Particles" [40]. I have used the generic solution and applied it to the MIBD system. The solution uses a summation in order to describe the scattering constants from zero to infinity. A practical stop criteria has been found and the developed model is compare to the Bohren–Huffman model. In [35] a set of differential equations is used to describe the scattered electromagnetic field when it is interacting with two concentric cylinders. A system is depicted in Figure 7.

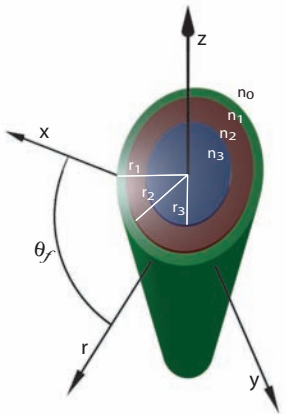

Figure 7. The electric field is imping along the x direction. Here is shown the geometry and coordinates for a $j = 3$ system which describes a capillary setup, with three interfaces. r_1 is the complete radius including glass tube with polyimid coating. n_3 is the refractive index of the liquid inside the capillary. The angle between the r– and the x–axis is the scattering angle Θ_f

The scattering angle Θ_f is defined as being 0 for the directly forward scattered direction. The backscattered angle Θ is $180-\Theta_f$, and is the one of interest for this work as detection is in this direction. The usual scattering amplitudes is found from b_m^0 and a_m^0:

$$T_1(\Theta_f) = b_0^0 + 2 \cdot \sum_{m=1}^{\infty} b_m^0 \cos(m \cdot \Theta_f) \tag{9}$$

$$T_2(\Theta_f) = a_0^0 + 2 \cdot \sum_{m=1}^{\infty} a_m^0 \cos(m \cdot \Theta_f) \tag{10}$$

An array of equations can be constructed by the following set of equations, from which the scattering coefficients, b_m^0 and a_m^0, is to be isolated, all depending on the number of interfaces, described by $j = 1, 2, \ldots k$:

$$b_m^{j-1} n_{j-1} H_m(n_{j-1}\alpha_j) - \bar{\delta_1} B_m^{j-1} n_{j-1} J_m(n_{j-1}\alpha_j)$$
$$-\bar{\delta_j} b_m^j n_j H_m(n_j\alpha_j) + B_m^j n_j J_m(n_j\alpha_j)$$

$$= \delta_1 n_{j-1} J_m(n_{j-1}\alpha_j) \tag{11}$$

$$b_m^{j-1} n_{j-1}^2 H_m^{'}(n_{j-1}\alpha_j) - \bar{\delta_1} B_m^{j-1} n_{j-1}^2 J_m^{'}(n_{j-1}\alpha_j) - \bar{\delta_j} b_m^j n_j^2 H_m^{'}(n_j\alpha_j) + B_m^j n_j^2 J_m^{'}(n_j\alpha_j) = \delta_1 n_{j-1}^2 J_m^{'}(n_{j-1}\alpha_j) \tag{12}$$

$$a_m^{j-1} n_{j-1}^2 H_m(n_{j-1}\alpha_j) - \bar{\delta_1} A_m^{j-1} n_{j-1}^2 J_m(n_{j-1}\alpha_j) - \bar{\delta_j} a_m^j n_j^2 H_m(n_j\alpha_j) + A_m^j n_j^2 J_m(n_j\alpha_j) = \delta_1 n_{j-1}^2 J_m^{'}(n_{j-1}\alpha_j) \tag{13}$$

$$a_m^{j-1} n_{j-1} H_m^{'}(n_{j-1}\alpha_j) - \bar{\delta_1} A_m^{j-1} n_{j-1} J_m^{'}(n_{j-1}\alpha_j) - \bar{\delta_j} a_m^j n_j H_m^{'}(n_j\alpha_j) + A_m^j n_j J_m^{'}(n_j\alpha_j) = \delta_1 n_{j-1} J_m^{'}(n_{j-1}\alpha_j) \tag{14}$$

, where $\alpha_j = \frac{2\pi r_j}{\lambda}$ is the size parameter. The r_j is found in Figure 7 as the radius of j'th media. n_j is the refractive index of the j'th material. H_m and J_m are the Hankel and Bessel functions of the first kind, respectively. The set of equations is governed by these δ-functions:

$$\delta_1 = 1 \text{ if } j = 1 \text{ and } \delta_1 = 0 \text{ if } j \neq 1 \tag{15}$$

$$\bar{\delta_1} = 0 \text{ if } j = 1 \text{ and } \bar{\delta_1} = 1 \text{ if } j \neq 1 \tag{16}$$

$$\bar{\delta_j} = 0 \text{ if } j = k \text{ and } \bar{\delta_j} = 1 \text{ if } j \neq k \tag{17}$$

From equations (11) to (17) any system of concentric cylinders can be described [35]. When T_1 is calculated for a given system the TE-wave mode of light can be computed from [40] :

$$E_{TE} = e^{i\frac{3}{4}\pi} \cdot \sqrt{\frac{2}{\pi kr}} \cdot e^{ikr} \cdot T_1(\Theta_f) \cdot E_0 \tag{18}$$

,where

$k = \frac{2\pi}{\lambda}$, is the wavenumber

r , is the distance to the observer in the far field

E_0 , is the incoming field

In a similar fashion the TM-wave mode is calculated and the the E-field is found:

$$E = \sqrt{|E_{TE}|^2 + |E_{TM}|^2} \tag{19}$$

The stop criteria

The modeling code is constructed by first determining the system variables such as sizes of the cylinders, refractive indices of the media and the wavelength. With these inputs the scattering field can be calculated. In equations (9) and(10) is used a summation from 1 to ∞, this is not possible in practice so a reasonable stop-criteria is needed. The code calls a function that outputs a such number. The input to the function is the size-parameter α_j and the refractive index n_j. The function calculates the value for $J_m(n_j\alpha_j)$, $J'_m(n_j\alpha_j)$, $H_m(n_j\alpha_j)$ and $H'_m(n_j\alpha_j)$ from $m = 1$ and towards infinity. When the Bessel function and its derivative reaches a value in the range from 10^{-16} to 10^{-19} the function outputs this value of m. For the Hankel function the range is 10^{16} to 10^{19}. These ranges are chosen as

a longer summation will not change the end results, plus will increase computing time even further. In [40] is given a different stop criteria based exclusively on empirical trials. That stop criteria is defines as:

$$m_{stop} = x + 4 \cdot x^{1/3} + 2 \quad \text{,where} \tag{20}$$

$$x = \frac{2 \cdot \pi}{\lambda \cdot n \cdot r} \tag{21}$$

There is a difference in the value of m_{stop} between the two methods, see figure 8(A) where the first method results in a higher value of this counter.

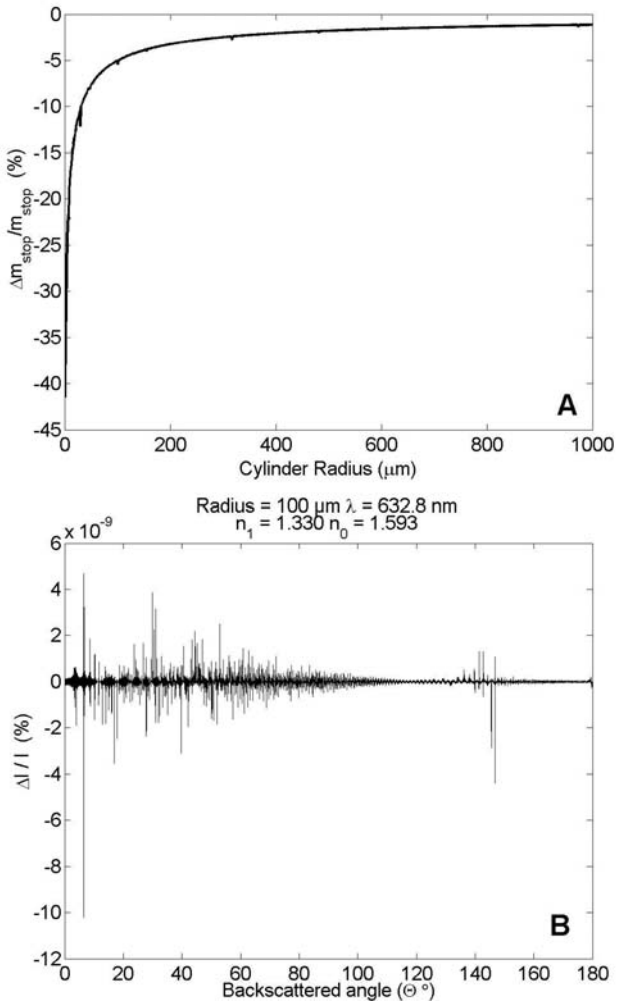

Figure 8. The value of m_{stop} is calculated with the two different approaches. The radius is changed from 1 μm to 1 mm which corresponds to the sizes used in this project. The difference is mostly present for small radii (A). For $r = 1$ μm the found m_{stop} is 41 and 27. In (B) the effect on the calculated E-field for $r = 100\mu m$ is shown as the difference in intensity. The intensity change is on the 10^{-9} % level.

As the radius increases a higher number of Bessel functions is needed to describe the scattering event. For $r = 1000\ \mu m$ the value of m_{stop} from equation (20) is 13302 and 13454 from own code. As seen in figure 8(B) the difference in m_{stop} in the resulting E-field is at a low level. For $r = 1\ \mu m$, the ratio $\frac{\Delta I}{I} = 10^{-8}$ so even a 34 % difference in m_{stop} has little influence on the calculated E-field. Since

larger radii demands a higher value of m_{stop} for a complete description, concentric cylinders cannot have the same m_{stop}. Each individual combination of size parameter and refractive index result in a given value for the four functions,$J_m(n_j\alpha_j)$, $J'_m(n_j\alpha_j)$, $H_m(n_j\alpha_j)$ and $H'_m(n_j\alpha_j)$, m^i_{stop}. The smallest value is stored for each combination to ensure a usable value. Afterwards all of the individual values are compared and the largest value is chosen to be used in the model m^{max}_{stop}. This ensures complete description of the largest feature, while the smaller features uses the values up until their individual value of m^i_{stop} is reached. To be able to complete the summation the last value of m^i_{stop} is used until m^{max}_{stop} is reached. Then T_1 and T_2 from equations (9) and (10) is calculated and the scattered E-field is constructed.

The wave based model has been constructed for systems from $j = 1$, the infinite cylinder, to $j = 4$, a capillary with an affinity layer. These systems will be discussed in the following sections.

The infinite cylinder, $j = 1$

This is the simplest system imaginable for calculating the scattered E-field. The system is an infinite long cylinder surrounded by a media, where the E-field impinges the the cylinder perpendicular to the long axis. The system of an infinite cylinder is not trivial, since it describes the MIBD system performed with at circular flow channel in a chip.

In order to validate the wave-based model developed in this work, the Fortran code provided by Bohren and Huffmann [40] is used for direct comparison for the infinite cylinder. The scattering constants are provided and are found from these equations:

$$b^0_m = \frac{\left[nD_m(nx) + \frac{m}{x}\right] \cdot J_m(x) - J_{m-1}(x)}{\left[nD_m(nx) + \frac{m}{x}\right] \cdot H_m(x) - H_{m-1}(x)} \tag{22}$$

$$a^0_m = \frac{\left[\frac{D_m(nx)}{n} + \frac{m}{x}\right] \cdot J_m(x) - J_{m-1}(x)}{\left[\frac{D_m(nx)}{n} + \frac{m}{x}\right] \cdot H_m(x) - H_{m-1}(x)} \tag{23}$$

$$D_m(\rho) = \frac{J'_m(\rho)}{J_m(\rho)} \tag{24}$$

Along with the code a set of calculated scattering coefficients are provided and will be the basis for the first comparison. The code was originally written to be compiled in Fortran and was transformed to be processed in Matlab instead. The results from their work was reproduced with all the digits provided. From equations (11) to (17) the equations concerning the scattering constants from [35] for this system, $j = 1$, is found:

$$b^0_m \cdot n_0 \cdot H_m(n_0\alpha_1) + B^1_m \cdot n_1 \cdot J_m(n_1\alpha_1) = n_0 \cdot J_m \cdot (n_0\alpha_1) \tag{25}$$

$$b^0_m \cdot n_0^2 \cdot H'_m(n_0\alpha_1) + B^1_m \cdot n_1^2 \cdot J'_m(n_1\alpha_1) = n_0^2 \cdot J'_m \cdot (n_0\alpha_1) \tag{26}$$

$$a^0_m \cdot n_0^2 \cdot H_m(n_0\alpha_1) + A^1_m \cdot n_1^2 \cdot J_m(n_1\alpha_1) = n_0^2 \cdot J_m \cdot (n_0\alpha_1) \tag{27}$$

$$a^0_m \cdot n_0 \cdot H'_m(n_0\alpha_1) + A^1_m \cdot n_1 \cdot J'_m(n_1\alpha_1) = n_0 \cdot J'_m \cdot (n_0\alpha_1) \tag{28}$$

The two constants are isolated:

$$b^0_m = \frac{n_0 \cdot J'_m(n_0\alpha_1) \cdot J_m(n_1\alpha_1) - J_m(n_0\alpha_1) \cdot n_1 \cdot J'_m(n_1\alpha_1)}{n_0 \cdot H'_m(n_0\alpha_1) \cdot J_m(n_1\alpha_1) - H_m(n_0\alpha_1) \cdot n_1 \cdot J'_m(n_1\alpha_1)} \tag{29}$$

$$a_m^0 = \frac{n_0 \cdot J_m(n_0\alpha_1) \cdot J'_m(n_1\alpha_1) - J'_m(n_0\alpha_1) \cdot n_1 \cdot J_m(n_1\alpha_1)}{n_0 \cdot H_m(n_0\alpha_1) \cdot J'_m(n_1\alpha_1) - H'_m(n_0\alpha_1) \cdot n_1 \cdot J_m(n_1\alpha_1)} \tag{30}$$

The two models are identical in their coding for calculating the scattered E-field. For identical inputs the models are compared in figure 9. Since the input

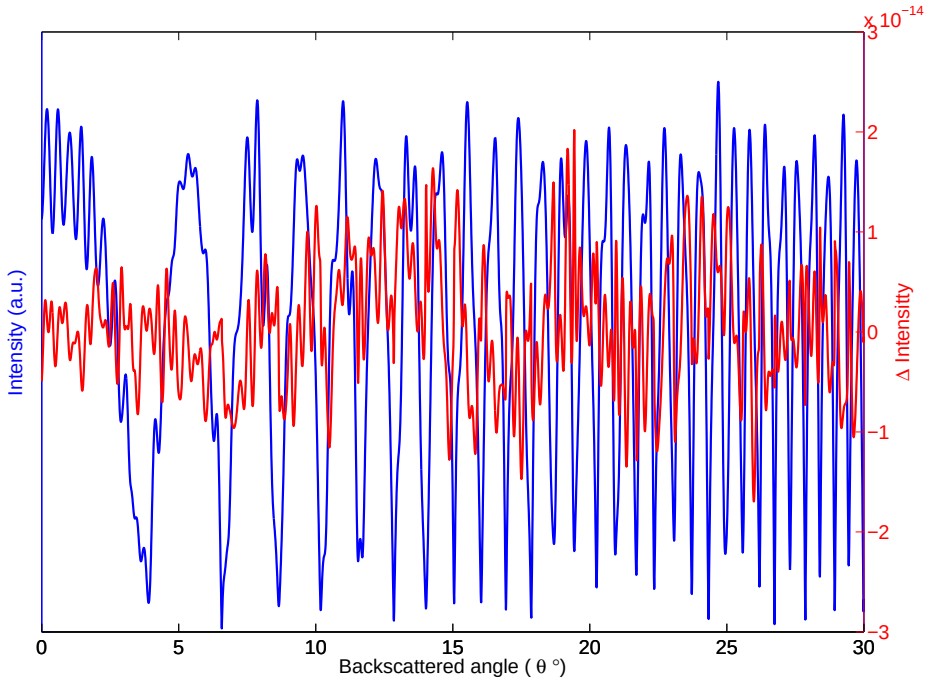

Figure 9. The interference pattern is calculated for $r = 100$ μm and shown on the left y–axis. On the right y–axis is shown the difference in intensity between the model from Bohren–Huffmann and own code. The intensity change is on the 10^{-14} level. It is the same stop criteria used in both approaches.

and stop criteria is kept the same the results in figure 9 arises from calculation of b_m^0 and a_m^0. The difference in the calculated E-field is in this case smaller than the contribution from different m_{stop}, hence the code is shown validated when compared to other published modeling results.

A system of a polymer chip with a cylindrical flow channel filled with water is modeled in figure 10 and the first part of the fringe pattern is shown. As the

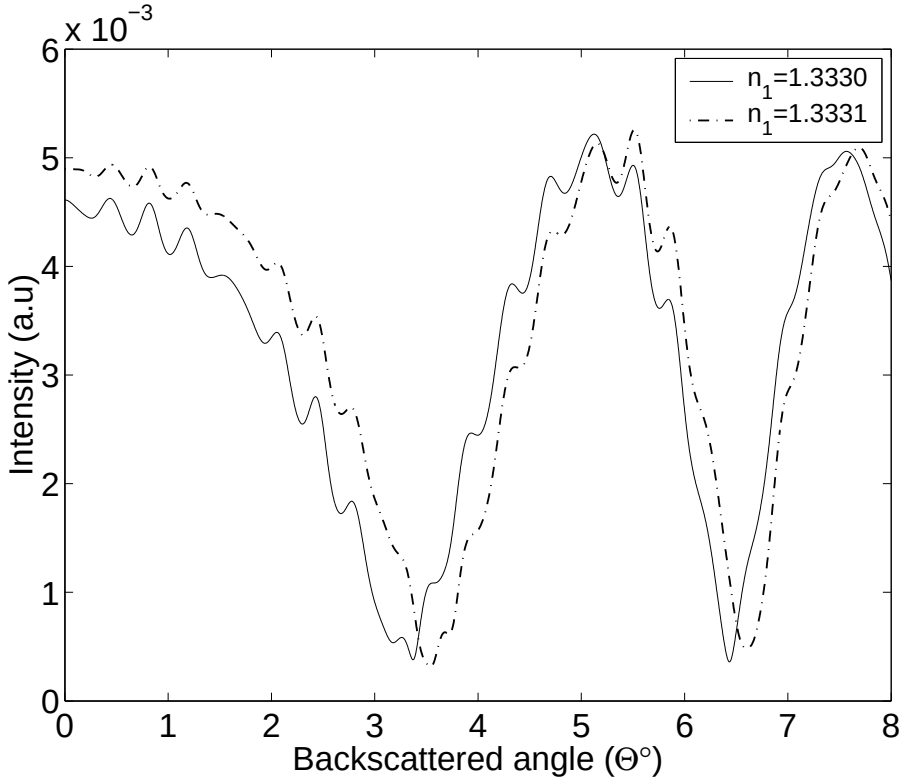

Figure 10. Calculated fringes in the backscattered range from 0 ° to 8 °. Radius of the cylinder is 100 μm*. The media has a refractive index of 1.53.* $\Delta n = 1 \cdot 10^{-4}$

refractive index of the liquid inside the flow channel is changed the fringes moves in angular space. The sensitivity of this system is seen as how much the first fringe moves as the refractive index changes. The first fringe is seen from 3.5° to 6.5°. The first fringe has in this case a sensitivity of,

$$S_{j=1} = \frac{d\Theta}{dn} = \frac{0.1692}{1 \cdot 10^{-4}} = 1692^{\circ} \tag{31}$$

The first fringe has been chosen in this work to be the measure of sensitivity. The centroid has the largest response to changes in refractive index but will be an intensity measurement and not a change in angular position. The sensitivity found in equation (31) corresponds to a relative movement in angular space of 5.53 % of the fringe width.

The fringe pattern changes if any of the path lengths in the system changes optical or actual. The system described by this model is a chip based system, where the fabrication tolerances is of interest. The radius of the flow channel has been changed to model how production tolerances will affect the fringe pattern, see figure 11.

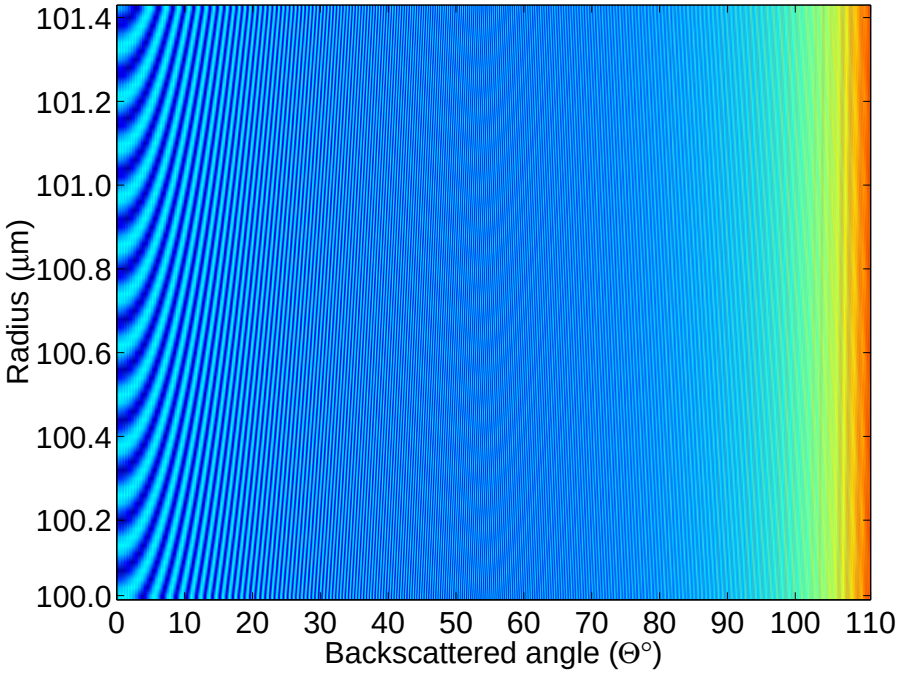

Figure 11. The change in radius is done over 71 steps. The angular space is compiled of 20001 points over 180 °. As the radius is increased the fringes move outwards. The change in radius of 1.4% moves the first fringe 16 °.

From a fabrication point of view the change in fringe pattern due to different radii of the liquid, shows that a perfect reconstruction of the fringe pattern from a fabricated chip is extremely difficult. The size dependents of this system can be compared to the refractive index dependents in the following way: The optical path length is found to be $1.333 \cdot 100 = 133.3$, after changes the path length is 135, this corresponds to a change in refractive index by .02, which again will give a sensitivity of

$$S = \frac{d\Theta}{dn} = \frac{16}{0.02} = 800^\circ \tag{32}$$

Compared to $S_{j=1}$ the dependents on the size is smaller than the dependents of the refractive index. The light has to pass through the liquid inside at least twice in the backscattering setup. The higher sensitivity must arise from the combination of optical pathlength dependent interferometry and the effects described by Snell's law of refraction, occurring at all angles as the geometry is circular. The pattern is repeated for every ∼100 nm step.

To evaluate the size dependents of the sensitivity different channel dimensions has been modeled on a larger scale. The radius has been change from 50μm to 100μm in 1μm steps. The result of the analysis is shown in Figure 12 and Figure 13.

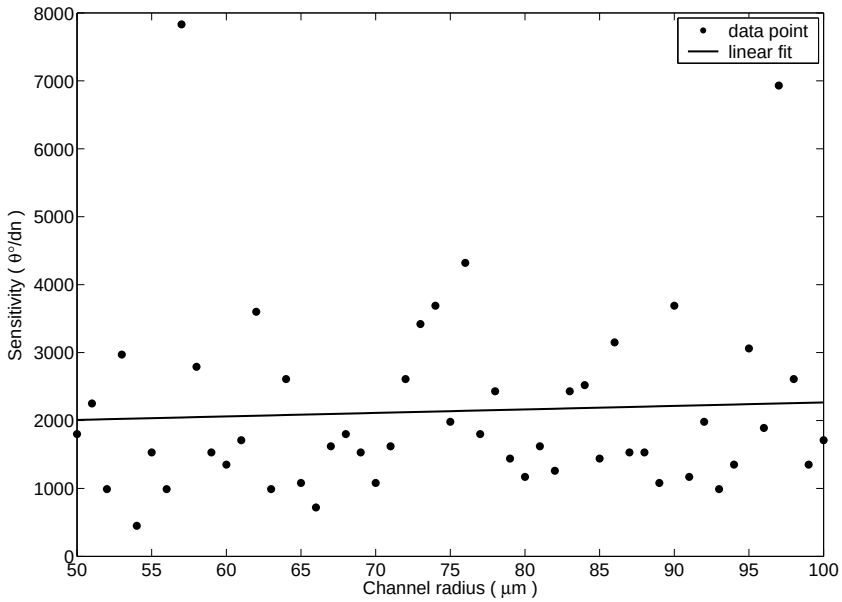

Figure 12. The fringe shift has been modeled. The shift of the first fringe is found as the radius of the channel is increased in 1 µm steps. The sensitivity points is fitted with a line and it shows a small increase in sensitivity towards the larger channels. The points are spread across many sensitivities ranging from 500 to almost 8000 °/dn.

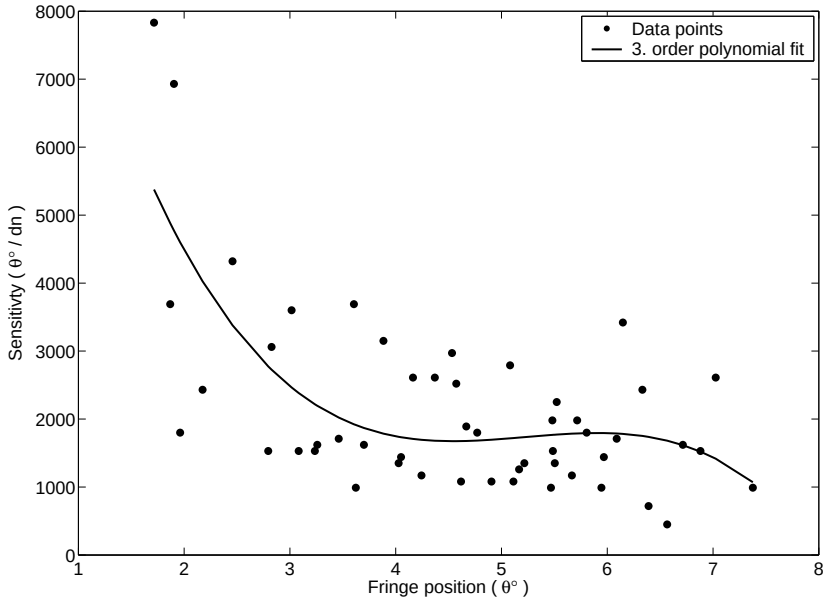

Figure 13. The fringe shift has been modeled. The shift of the first fringe is found. Here is plotted the sensitivity of the first fringe according to its angular position. As indicated by the polynomial fit the sensitivity goes up as the centroid is approached.

The sensitivity for a chip with 50μm to 100μm in diameter has approximately the same sensitivity of around 2000°/dn though increasing slightly with larger diameters. The big spread in data points is because the first fringe is positioned differently in angular space as the radius changes, and the refractive index is kept constant. The line fit indicates the average sensitivity. The sensitivity is mostly dependent on the first fringe position as is seen in Figure 13. Close to the centroid the sensitivity is at its maximum. This shows that the sensitivity of a fabricated chip will not be much dependent of the diameter, but rather the combination of refractive index and measuring position.

The Tube, $j = 2$

A glass tube is described by having two interfaces. It is not the tubes normally used in MIBD, but it is still possible to use. In [35] is given the solution for such a system and the scattering coefficients are found. An expansion of the model describing the $j = 1$ system is straight forward for this system, and the all important scattering coefficients can be found and validated in the paper by Kerker and Matijevic. The scattering constants for this system is to be isolated from these equations:

$$b_m^0 \cdot n_0 \cdot H_m(n_0\alpha_1) - b_m^1 \cdot n_1 \cdot H_m(n_1\alpha_1) + B_m^1 \cdot n_1 \cdot J_m(n_1\alpha_1) = n_0 \cdot J_m(n_0\alpha_1) \quad (33)$$

$$b_m^0 \cdot n_0^2 \cdot H'_m(n_0\alpha_1) - b_m^1 \cdot n_1^2 \cdot H'_m(n_1\alpha_1) + B_m^1 \cdot n_1^2 \cdot J'_m(n_1\alpha_1) = n_0^2 \cdot J'_m(n_0\alpha_1) \quad (34)$$

$$b_m^1 \cdot n_1 \cdot H_m(n_1\alpha_2) - B_m^1 \cdot n_1 \cdot J_m(n_1\alpha_2) + B_m^2 \cdot n_2 \cdot J_m(n_2\alpha_2) = 0 \quad (35)$$

$$b_m^1 \cdot n_1^2 \cdot H'_m(n_1\alpha_2) - B_m^1 \cdot n_1^2 \cdot J'_m(n_1\alpha_2) + B_m^2 \cdot n_2^2 \cdot J'_m(n_2\alpha_2) = 0 \quad (36)$$

$$a_m^0 \cdot n_0^2 \cdot H_m(n_0\alpha_1) - a_m^1 \cdot n_1^2 \cdot H_m(n_1\alpha_1) + A_m^1 \cdot n_1^2 \cdot J_m(n_1\alpha_1) = n_0^2 \cdot J_m(n_0\alpha_1) \quad (37)$$

$$a_m^0 \cdot n_0 \cdot H'_m(n_0\alpha_1) - a_m^1 \cdot n_1 \cdot H'_m(n_1\alpha_1) + A_m^1 \cdot n_1 \cdot J'_m(n_1\alpha_1) = n_0 \cdot J'_m(n_0\alpha_1) \quad (38)$$

$$a_m^1 \cdot n_1^2 \cdot H_m(n_1\alpha_2) - A_m^1 \cdot n_1^2 \cdot J_m(n_1\alpha_2) + A_m^2 \cdot n_2^2 \cdot J_m(n_2\alpha_2) = 0 \quad (39)$$

$$a_m^1 \cdot n_1 \cdot H'_m(n_1\alpha_2) - A_m^1 \cdot n_1 \cdot J'_m(n_1\alpha_2) + A_m^2 \cdot n_2 \cdot J'_m(n_2\alpha_2) = 0 \quad (40)$$

The two constants has been isolated by the symbolic equation solver in Matlab. This has also been done by hand for this $j = 2$ system, but is quit extensive work for the higher order systems as seen below. The scattering field can be found via these two constants:

$$b_m^0 = \frac{B_{top}}{B_{bottom}} \tag{41}$$

$$\begin{aligned}
B_{top} = n_0 \cdot (&H_m(n_1\alpha_1) \cdot J'_m(n_0\alpha_1) \cdot J_m(n_1\alpha_2) \cdot n_2 \cdot J'_m(n_2\alpha_2) - H_m(n_1\alpha_1) \cdot J'_m(n_0\alpha_1) \cdot J'_m(n_1\alpha_2) \cdot n_1 \cdot J_m(n_2\alpha_2) \\
&- J_m(n_1\alpha_1) \cdot J'_m(n_0\alpha_1) \cdot H_m(n_1\alpha_2) \cdot n_2 \cdot J'_m(n_2\alpha_2) + J_m(n_1\alpha_1) \cdot J'_m(n_0\alpha_1) \cdot H'_m(n_1\alpha_2) \cdot n_1 \cdot J_m(n_2\alpha_2)) \\
&- J_m(n_0\alpha_1) \cdot n_1 \cdot H'_m(n_1\alpha_1) \cdot J_m(n_1\alpha_2) \cdot n_2 \cdot J'_m(n_2\alpha_2) + J_m(n_0\alpha_1) \cdot n_1^2 \cdot H'_m(n_1\alpha_1) \cdot J'_m(n_1\alpha_2) \cdot J_m(n_2\alpha_2) \\
&+ J_m(n_0\alpha_1) \cdot n_1 \cdot J'_m(n_1\alpha_1) \cdot H_m(n_1\alpha_2) \cdot n_2 \cdot J'_m(n_2\alpha_2) - J_m(n_0\alpha_1) \cdot n_1^2 \cdot J'_m(n_1\alpha_1) \cdot H'_m(n_1\alpha_2) \cdot J_m(n_2\alpha_2)
\end{aligned} \tag{42}$$

$$\begin{aligned}
B_{bottom} = n_0 \cdot (&H_m(n_1\alpha_1) \cdot H'_m(n_0\alpha_1) \cdot J_m(n_1\alpha_2) \cdot n_2 \cdot J'_m(n_2\alpha_2) - H_m(n_1\alpha_1) \cdot H'_m(n_0\alpha_1) \cdot J'_m(n_1\alpha_2) \cdot n_1 \cdot J_m(n_2\alpha_2) \\
&- J_m(n_1\alpha_1) \cdot H'_m(n_0\alpha_1) \cdot H_m(n_1\alpha_2) \cdot n_2 \cdot J'_m(n_2\alpha_2) + J_m(n_1\alpha_1) \cdot H'_m(n_0\alpha_1) \cdot H'_m(n_1\alpha_2) \cdot n_1 \cdot J_m(n_2\alpha_2)) \\
&- H_m(n_0\alpha_1) \cdot n_1 \cdot H'_m(n_1\alpha_1) \cdot J_m(n_1\alpha_2) \cdot n_2 \cdot J'_m(n_2\alpha_2) + H_m(n_0\alpha_1) \cdot n_1^2 \cdot H'_m(n_1\alpha_1) \cdot J'_m(n_1\alpha_2) \cdot J_m(n_2\alpha_2) \\
&+ H_m(n_0\alpha_1) \cdot n_1 \cdot J'_m(n_1\alpha_1) \cdot H_m(n_1\alpha_2) \cdot n_2 \cdot J'_m(n_2\alpha_2) - H_m(n_0\alpha_1) \cdot n_1^2 \cdot J'_m(n_1\alpha_1) \cdot H'_m(n_1\alpha_2) \cdot J_m(n_2\alpha_2)
\end{aligned} \tag{43}$$

$$a_m^0 = \frac{A_{top}}{A_{bottom}} \tag{44}$$

$$\begin{aligned}
A_{top} = n_0 \cdot (&J_m(n_0\alpha_1) \cdot H'_m(n_1\alpha_1) \cdot n_1 \cdot J_m(n_1\alpha_2) \cdot J'_m(n_2\alpha_2) - J_m(n_0\alpha_1) \cdot H'_m(n_1\alpha_1) \cdot J'_m(n_1\alpha_2) \cdot n_2 \cdot J_m(n_2\alpha_2) \\
&- J_m(n_0\alpha_1) \cdot J'_m(n_1\alpha_1) \cdot n_1 \cdot H_m(n_1\alpha_2) \cdot J'_m(n_2\alpha_2) + J_m(n_0\alpha_1) \cdot J'_m(n_1\alpha_1) \cdot H'_m(n_1\alpha_2) \cdot n_2 \cdot J_m(n_2\alpha_2)) \\
&- J'_m(n_0\alpha_1) \cdot n_1^2 \cdot H_m(n_1\alpha_1) \cdot J_m(n_1\alpha_2) \cdot J'_m(n_2\alpha_2) + J'_m(n_0\alpha_1) \cdot n_1 \cdot H_m(n_1\alpha_1) \cdot J'_m(n_1\alpha_2) \cdot n_2 \cdot J_m(n_2\alpha_2) \\
&+ J'_m(n_0\alpha_1) \cdot n_1^2 \cdot J_m(n_1\alpha_1) \cdot H_m(n_1\alpha_2) \cdot J'_m(n_2\alpha_2) - J'_m(n_0\alpha_1) \cdot n_1 \cdot J_m(n_1\alpha_1) \cdot H'_m(n_1\alpha_2) \cdot n_2 \cdot J_m(n_2\alpha_2)
\end{aligned} \tag{45}$$

$$\begin{aligned}
A_{bottom} = n_0 \cdot (&H_m(n_0\alpha_1) \cdot H'_m(n_1\alpha_1) \cdot n_1 \cdot J_m(n_1\alpha_2) \cdot J'_m(n_2\alpha_2) - H_m(n_0\alpha_1) \cdot H'_m(n_1\alpha_1) \cdot J'_m(n_1\alpha_2) \cdot n_2 \cdot J_m(n_2\alpha_2) \\
&- H_m(n_0\alpha_1) \cdot J'_m(n_1\alpha_1) \cdot n_1 \cdot H_m(n_1\alpha_2) \cdot J'_m(n_2\alpha_2) + H_m(n_0\alpha_1) \cdot J'_m(n_1\alpha_1) \cdot H'_m(n_1\alpha_2) \cdot n_2 \cdot J_m(n_2\alpha_2)) \\
&- H'_m(n_0\alpha_1) \cdot n_1^2 \cdot H_m(n_1\alpha_1) \cdot J_m(n_1\alpha_2) \cdot J'_m(n_2\alpha_2) + H'_m(n_0\alpha_1) \cdot n_1 \cdot H_m(n_1\alpha_1) \cdot J'_m(n_1\alpha_2) \cdot n_2 \cdot J_m(n_2\alpha_2) \\
&+ H'_m(n_0\alpha_1) \cdot n_1^2 \cdot J_m(n_1\alpha_1) \cdot H_m(n_1\alpha_2) \cdot J'_m(n_2\alpha_2) - H'_m(n_0\alpha_1) \cdot n_1 \cdot J_m(n_1\alpha_1) \cdot H'_m(n_1\alpha_2) \cdot n_2 \cdot J_m(n_2\alpha_2)
\end{aligned} \tag{46}$$

The constants are also provided in [35] and it might not be obvious, but are identical. The capillaries is purchased from Polymicro Technologies (AZ,US) and they can provide capillaries with different dimensions, including the thickness of the fused silica tube walls. A sensitivity analysis has been done based on the $j = 2$ model, this means that the cladding protecting the capillary is not included, see Table 1. The relative change is based on the fringe width and its movement:

Table 1. Sensitivity of different capillaries with the same inner diameter (I.D.) but with changing outer diameter (O.D.). The refractive index is 1.33 and dn$= 5{\cdot}10^{-4}$.

Capillary	$\frac{d\theta}{dn}$	Relative change
100 μm I.D. 165 μm O.D.	3252°	2032
100 μm I.D. 193 μm O.D.	1668°	596
100 μm I.D. 238 μm O.D.	2652°	2027
100 μm I.D. 363 μm O.D.	1488°	2175

$$Relative\ change\ =\ \frac{fringe\ shift}{fringe\ size} \cdot \frac{1}{dn} \tag{47}$$

It is seen that the capillary with the thinnest wall shifts the most. But the relative change in position is comparable for the capillaries available, although the 100 μm I.D. 193 μm O.D. capillary is a bad choice for these measurements. The largest capillary has the smallest shift in fringe position, but as the fringes are thinner the relative change in position levels out. In Figure 14 is shown the modeled fringe pattern for the 100 μm I.D. 238 μm O.D. and the 100 μm I.D. 363 μm O.D. capillaries.

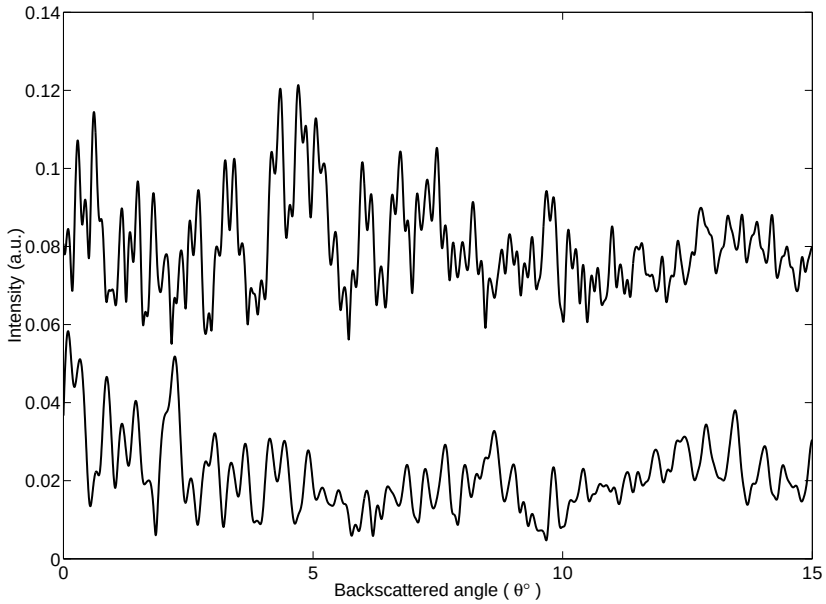

Figure 14. The modeled fringe patterns from a 100 μm I.D. 238 μm O.D. and a 100 μm I.D. 363 μm O.D. capillary is shown. The upper fringe pattern is the 100 μm I.D. 363 μm O.D. pattern offset for clarity. The fringes are thinner for the upper pattern, so even a smaller shift in position is relatively the same when the thickness of the fringe is considered.

The capillary, $j = 3$

In all capillary experiments with the MIBD scheme capillaries with a polyimid cladding is used. Hence the modeled system will be a $j = 3$ system. The polyimid protects the capillary from being scratched and isolates it from the atmosphere. The capillary has a tendency to become brittle when the cladding has been removed. Without the coating on the capillaries, dust becomes an issue, as it sticks to the surface interfering with the experiment. The refractive index of the cladding has been set to 1.6 in the models.

From equation 11 to 17 is found the equations that is later used for modeling the capillary case. The isolation of the scattering constants has been done in Matlab.

$$b_m^0 \cdot n_0 \cdot H_m(n_0\alpha_1) - b_m^1 \cdot n_1 \cdot H_m(n_1\alpha_1) + B_m^1 \cdot n_1 \cdot J_m(n_1\alpha_1) = n_0 \cdot J_m(n_0\alpha_1) \tag{48}$$

$$b_m^0 \cdot n_0^2 \cdot H'_m(n_0\alpha_1) - b_m^1 \cdot n_1^2 \cdot H'_m(n_1\alpha_1) + B_m^1 \cdot n_1^2 \cdot J'_m(n_1\alpha_1) = n_0^2 \cdot J'_m(n_0\alpha_1) \tag{49}$$

$$b_m^1 \cdot n_1 \cdot H_m(n_1\alpha_2) - B_m^1 \cdot n_1 \cdot J_m(n_1\alpha_2) - b_m^2 \cdot n_2 \cdot H_m(n_2\alpha_2) + B_m^2 \cdot n_2 \cdot J_m(n_2\alpha_2) = 0 \tag{50}$$

$$b_m^1 \cdot n_1^2 \cdot H'_m(n_1\alpha_2) - B_m^1 \cdot n_1^2 \cdot J'_m(n_1\alpha_2) - b_m^2 \cdot n_2^2 \cdot H'_m(n_2\alpha_2) + B_m^2 \cdot n_2^2 \cdot J'_m(n_2\alpha_2) = 0 \tag{51}$$

$$b_m^2 \cdot n_2 \cdot H_m(n_2\alpha_3) - B_m^2 \cdot n_2 \cdot J_m(n_2\alpha_3) + B_m^3 \cdot n_3 \cdot J_m(n_3\alpha_3) = 0 \tag{52}$$

$$b_m^2 \cdot n_2^2 \cdot H'_m(n_2\alpha_3) - B_m^2 \cdot n_2^2 \cdot J'_m(n_2\alpha_3) + B_m^3 \cdot n_3^2 \cdot J'_m(n_3\alpha_3) = 0 \tag{53}$$

$$a_m^0 \cdot n_0^2 \cdot H_m(n_0\alpha_1) - a_m^1 \cdot n_1^2 \cdot H_m(n_1\alpha_1) + A_m^1 \cdot n_1^2 \cdot J_m(n_1\alpha_1) = n_0^2 \cdot J_m(n_0\alpha_1) \tag{54}$$

$$a_m^0 \cdot n_0 \cdot H'_m(n_0\alpha_1) - a_m^1 \cdot n_1 \cdot H'_m(n_1\alpha_1) + A_m^1 \cdot n_1 \cdot J'_m(n_1\alpha_1) = n_0 \cdot J'_m(n_0\alpha_1) \tag{55}$$

$$a_m^1 \cdot n_1^2 \cdot H_m(n_1\alpha_2) - A_m^1 \cdot n_1^2 \cdot J_m(n_1\alpha_2) - a_m^2 \cdot n_2^2 \cdot H_m(n_2\alpha_2) + A_m^2 \cdot n_2^2 \cdot J_m(n_2\alpha_2) = 0 \tag{56}$$

$$a_m^1 \cdot n_1 \cdot H'_m(n_1\alpha_2) - A_m^1 \cdot n_1 \cdot J'_m(n_1\alpha_2) - a_m^2 \cdot n_2 \cdot H'_m(n_2\alpha_2) + A_m^2 \cdot n_2 \cdot J'_m(n_2\alpha_2) = 0 \tag{57}$$

$$a_m^2 \cdot n_2^2 \cdot H_m(n_2\alpha_3) - A_m^2 \cdot n_2^2 \cdot J_m(n_2\alpha_3) + A_m^3 \cdot n_3^2 \cdot J_m(n_3\alpha_3) = 0 \tag{58}$$

$$a_m^2 \cdot n_2 \cdot H'_m(n_2\alpha_3) - A_m^2 \cdot n_2 \cdot J'_m(n_2\alpha_3) + A_m^3 \cdot n_3 \cdot J'_m(n_3\alpha_3) = 0 \tag{59}$$

In the MIBD experiments different capillaries has been used. In Table 2 is calculated the sensitivity of three different sizes of capillaries. It is seen that the sensitivity decreases as the capillaries becomes larger. Even though the largest

Table 2. The sensitivity of three different capillaries has been calculated. For this comparison the refractive index of the liquid is 1.33 and has been changed by $5 \cdot 10^{-4}$.

Capillary	$\frac{d\theta}{dn}$	Relative change
100 μm I.D. 165 μm O.D. 12.5 μm cladding	5376°	2402%
250 μm I.D. 360 μm O.D. 18 μm cladding	2076°	2142%
542 μm I.D. 673 μm O.D. 24 μm cladding	1512°	1260%

capillary has the lowest sensitivity it still has been used, but the the dimensions has played a different role. In Chapter 4 the usage of the large capillary is discussed.

In Figure 15 is shown an experimentally obtained fringe pattern for the 100 μm I.D. 165 μm O.D. 12.5 μm cladding capillary and the modeled fringe pattern. The modeled fringe pattern has been low pass filtered and offset for clarity. The fringe position is in excellent agreement between the experiment and the model, see Table 3.

Table 3. The fringe positions has been found for both modeled and experimental obtained fringe pattern.

Minima	position
Experiment	Model
2.2 ±0.4°	2.2
4.8 ±0.4°	4.8
6.4 ±0.4°	6.2
7.5 ±0.4°	7.4
8.6 ±0.4°	8.4
9.7 ±0.4°	9.5

The simulation is accurate enough to describe the fringe pattern quantitatively.

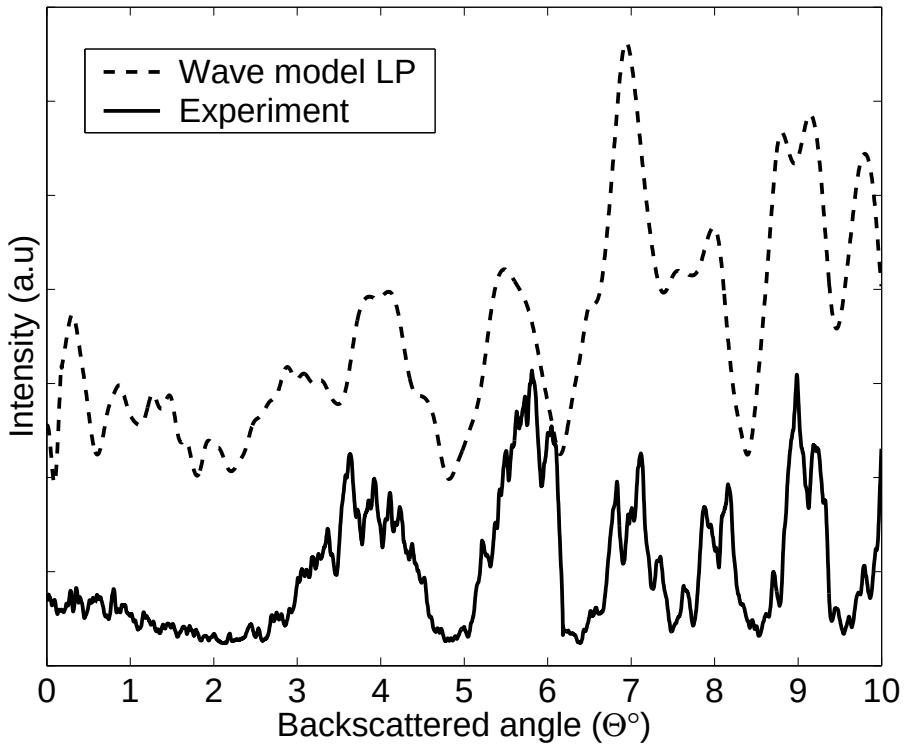

Figure 15. Experimental and modeled fringe patterns for a 100 μm I.D. 165 μm O.D. 12.5 μm cladding capillary. The refractive index of the liquid is 1.33. The wave model has been low pass filtered and offset for clarity. The filter is a moving average filter, and the window is 0.17°. There is excellent agreement between theory and experiments.

The affinity layer, $j = 4$

The MIBD scheme has shown to be a very sensitive refractive index measurement and its detection limits is relevant for many biological liquid samples. In order to make the capillary function as a bio–sensor, an affinity layer has to be deposited on the inside of the fused silica tubes. To model this affinity layer the $j = 4$ system has been developed. The actual binding event is a dynamic reaction and this model will only give a static result. In order to mimic the reaction taking place on the surface, the model variables are changed according to what is believed to happen. The affinity layer builds up as more molecules arrives to the surface. A target is immobilized on the surface, thereby the affinity layer has a thickness and a refractive index. If the sandwich structure of target and sample added to the height like building blocks, the system would appear with even more interfaces, thereby becoming a $j = 4+$ system. The system is seen as a combination of the above and is modeled as an average thickness change with an average change in refractive index of just one layer.

From equation 11 to 17 the equations used to describe this system is found. The scattering constants has been isolated in Matlab.

$$b_m^0 \cdot n_0 \cdot H_m(n_0\alpha_1) - b_m^1 \cdot n_1 \cdot H_m(n_1\alpha_1) + B_m^1 \cdot n_1 \cdot J_m(n_1\alpha_1) = n_0 \cdot J_m(n_0\alpha_1) \tag{60}$$

$$b_m^0 \cdot n_0^2 \cdot H'_m(n_0\alpha_1) - b_m^1 \cdot n_1^2 \cdot H'_m(n_1\alpha_1) + B_m^1 \cdot n_1^2 \cdot J'_m(n_1\alpha_1) = n_0^2 \cdot J'_m(n_0\alpha_1) \tag{61}$$

$$b_m^1 \cdot n_1 \cdot H_m(n_1\alpha_2) - B_m^1 \cdot n_1 \cdot J_m(n_1\alpha_2) - b_m^2 \cdot n_2 \cdot H_m(n_2\alpha_2) + B_m^2 \cdot n_2 \cdot J_m(n_2\alpha_2) = 0 \tag{62}$$

$$b_m^1 \cdot n_1^2 \cdot H'_m(n_1\alpha_2) - B_m^1 \cdot n_1^2 \cdot J'_m(n_1\alpha_2) - b_m^2 \cdot n_2^2 \cdot H'_m(n_2\alpha_2) + B_m^2 \cdot n_2^2 \cdot J'_m(n_2\alpha_2) = 0 \tag{63}$$

$$b_m^2 \cdot n_2 \cdot H_m(n_2\alpha_3) - B_m^2 \cdot n_2 \cdot J_m(n_2\alpha_3) - b_m^3 \cdot n_3 \cdot H_m(n_3\alpha_3) + B_m^3 \cdot n_3 \cdot J_m(n_3\alpha_3) = 0 \tag{64}$$

$$b_m^2 \cdot n_2^2 \cdot H'_m(n_2\alpha_3) - B_m^2 \cdot n_2^2 \cdot J'_m(n_2\alpha_3) - b_m^3 \cdot n_3^2 \cdot H'_m(n_3\alpha_3) + B_m^3 \cdot n_3^2 \cdot J'_m(n_3\alpha_3) = 0 \tag{65}$$

$$b_m^3 \cdot n_3 \cdot H_m(n_3\alpha_4) - B_m^3 \cdot n_3 \cdot J_m(n_3\alpha_4) + B_m^4 \cdot n_4 \cdot J_m(n_4\alpha_4) = 0 \tag{66}$$

$$b_m^3 \cdot n_3^2 \cdot H'_m(n_3\alpha_4) - B_m^3 \cdot n_3^2 \cdot J'_m(n_3\alpha_4) + B_m^4 \cdot n_4^2 \cdot J'_m(n_4\alpha_4) = 0 \tag{67}$$

$$a_m^0 \cdot n_0^2 \cdot H_m(n_0\alpha_1) - a_m^1 \cdot n_1^2 \cdot H_m(n_1\alpha_1) + A_m^1 \cdot n_1^2 \cdot J_m(n_1\alpha_1) = n_0^2 \cdot J_m(n_0\alpha_1) \tag{68}$$

$$a_m^0 \cdot n_0 \cdot H'_m(n_0\alpha_1) - a_m^1 \cdot n_1 \cdot H'_m(n_1\alpha_1) + A_m^1 \cdot n_1 \cdot J'_m(n_1\alpha_1) = n_0 \cdot J'_m(n_0\alpha_1) \tag{69}$$

$$a_m^1 \cdot n_1^2 \cdot H_m(n_1\alpha_2) - A_m^1 \cdot n_1^2 \cdot J_m(n_1\alpha_2) - a_m^2 \cdot n_2^2 \cdot H_m(n_2\alpha_2) + A_m^2 \cdot n_2^2 \cdot J_m(n_2\alpha_2) = 0 \tag{70}$$

$$a_m^1 \cdot n_1 \cdot H'_m(n_1\alpha_2) - A_m^1 \cdot n_1 \cdot J'_m(n_1\alpha_2) - a_m^2 \cdot n_2 \cdot H'_m(n_2\alpha_2) + A_m^2 \cdot n_2 \cdot J'_m(n_2\alpha_2) = 0 \tag{71}$$

$$a_m^2 \cdot n_2^2 \cdot H_m(n_2\alpha_3) - A_m^2 \cdot n_2^2 \cdot J_m(n_2\alpha_3) - a_m^3 \cdot n_3^2 \cdot H_m(n_3\alpha_3) + A_m^3 \cdot n_3^2 \cdot J_m(n_3\alpha_3) = 0 \tag{72}$$

$$a_m^2 \cdot n_2 \cdot H'_m(n_2\alpha_3) - A_m^2 \cdot n_2 \cdot J'_m(n_2\alpha_3) - a_m^3 \cdot n_3 \cdot H'_m(n_3\alpha_3) + A_m^3 \cdot n_3 \cdot J'_m(n_3\alpha_3) = 0 \tag{73}$$

$$a_m^3 \cdot n_3^2 \cdot H_m(n_3\alpha_4) - A_m^3 \cdot n_3^2 \cdot J_m(n_3\alpha_4) + A_m^4 \cdot n_4^2 \cdot J_m(n_4\alpha_4) = 0 \tag{74}$$

$$a_m^3 \cdot n_3 \cdot H'_m(n_3\alpha_4) - A_m^3 \cdot n_3 \cdot J'_m(n_3\alpha_4) + A_m^4 \cdot n_4 \cdot J'_m(n_4\alpha_4) = 0 \tag{75}$$

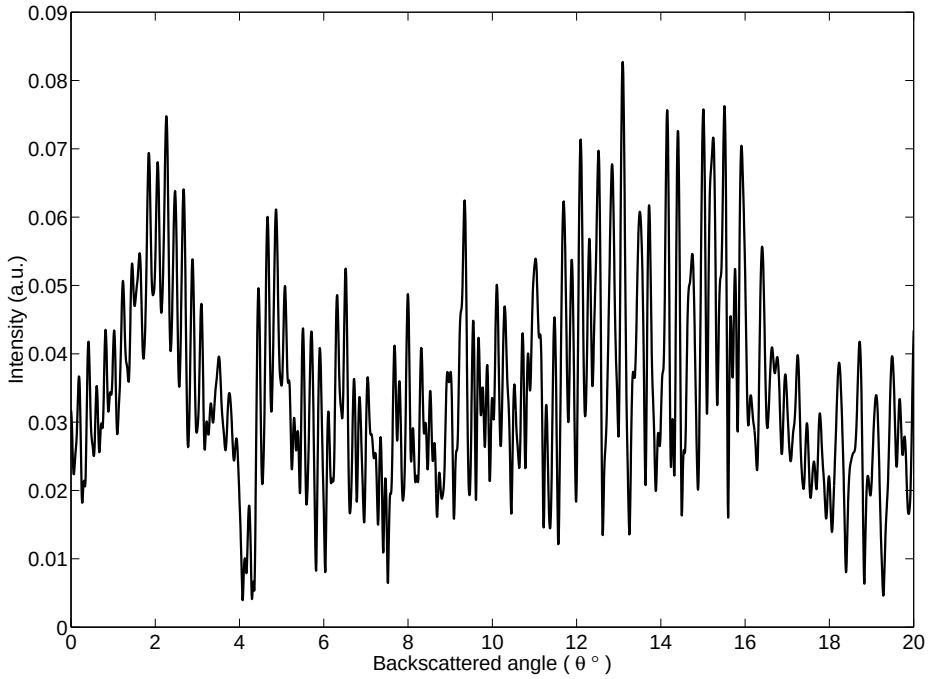

Figure 16. The interference pattern from a250 μm I.D. 360 μm O.D. 18 μm cladding capillary is plotted. The affinity layer modeled is 10 nm with a refractive index of 1.42. The liquid refractive index is set to be 1.33.

In Figure 16 is shown the interference pattern arising from a $j = 4$ system. The addition of the affinity layer does not change the overall appearance of the fringe pattern and only small changes will occur. The change of the fringe pattern is handled like the actual experiment. By a Fourier–transform the dominant frequency is found and the phase change of this frequency is then calculated and used for the change [41] in refractive index.

Table 4. The phase and the phase change have been found when changing the liquid refractive index, the affinity layer refractive index and the thickness of the layer.

System variables	Phase	Δ Phase
Thickness of affinity layer: 10nm Refractive index of liquid: 1.33 Refractive index of affinity layer: 1.42	0.409980	
Thickness of affinity layer: 10nm Refractive index of liquid: 1.3301 Refractive index of affinity layer: 1.42	0.363017	11.45%
Thickness of affinity layer: 10nm Refractive index of liquid: 1.33 Refractive index of affinity layer: 1.44	0.413572	-0.88%
Thickness of affinity layer: 11nm Refractive index of liquid: 1.33 Refractive index of affinity layer: 1.42	0.411772	-0.44%

In Table 4 it is seen results of calculations to see how the model behaves. Three variables have been changed to see their influence on the fringe pattern. It is seen that changes of the refractive index of the liquid has great influence on the pattern. $\Delta RI = 4 \cdot 10^{-6} \Rightarrow 0.45\% \Delta Phase$. This is understandable as the light travels much further in this material than the thin layer. This means that differences in the bulk liquid index has to be corrected for a direct comparison. Also it is seen that changing the layer thickness 1 nm corresponds to changing the layer refractive index by $1 \cdot 10^{-2}$. These two parameters is of equal importance to the model. The comparison with experiments is described in Chapter 4. Changing the refractive index of the affinity layer from 1.42 to 1.43 is a 0.7% change. Noticeable is that this change corresponds to a thickness change of 10% of the affinity layer, showing that the MIBD scheme is highly sensitive towards refractive index changes.

2.3 Modeling with software package ASAP

When moving from fused silica tubes and into micro fluidics the geometry of the channel will change. The geometries modeled in this section are rectangular, semicircular and full circle as shown in Figure 17. It is of great importance to identify

Figure 17. The three modeled geometries is drawn. The top part is modeled as being PDMS and the bottom part is modeled as glass. The cross–sectional area of the rectangular and the semicircular structure are also kept the same, thereby a direct comparision has been possible.

the performance of the three different geometries as their fabrication methods are different and the level of complexity in the procedures vary considerately. The semicircular and the circular channel geometry is a direct step from capillaries and into the flow chip regime. Again their individual fabrication processes are not on the same level of difficulties. The semicircular structure has much larger tolerances when aligned and assembled as it is more critical for the circular as it is assembled by two opposing parts with their structures facing each other. The rectangular shape is inspired by the PDMS chips often used in micro fluidics [31]. The modeling of these structures was performed with the commercial available software ASAP 8.0 from Breault Research, (AZ,US).

The modeling has been approached in 4 steps.

1. Simple ray–tracing.
2. Parabasal beams.
3. Beam propagation method (BPM)
4. Finite–Difference Time–Domain (FDTD)

In simple ray–tracing the light has no coherence and no polarization. This approach is poor for geometries with sharp edges as the rectangular structure. In ASAP the light source can emit so–called parabasal beams. They are used as rays, which carries phase and polarization information. But the main advantages is that the parabasal beam has a physical extension in space. So even if the central ray is missing an edge as it propagates, the beam is still bend according to how much of the surrounding beam touches the edge. These parabasal beams has been used for modeling the three geometries, resulting in moving fringe patterns.

The system is build in the ASAP Builder, where the channel geometry is described by either flat optical planes or cylindrical optical objects. The modeled laser is placed 28.3 cm (distance is close to the experimental setup) from chip surface and impinges on the channel perpendicular to the flow with a wavelength of 632.8 nm. The detector is placed 3500 μm above the chip surface and is 3000 μm

wide and is placed so that the center of the detector is directly at the 0° backscatter direction. The detector is placed at this distance to maximize the measured angle range at highest possible resolution as the software is limited by the number of pixels allowed on the detector. The pattern did not change when moving the detector backwards, so it appears that a miniaturized MIBD system can have the detector placed close to the micro flow system (< 4mm). The dimensions of the rectangular structure are 60 μm wide and 70 μm high channels, which has been fabricated in PDMS. In order to make a true comparison the semicircular channel had the same cross–sectional area.

$$Radius = \sqrt{\frac{2 \cdot Height \cdot Width}{\pi}} \tag{76}$$

All other system variables has been kept the same. In Figure 18 is shown the

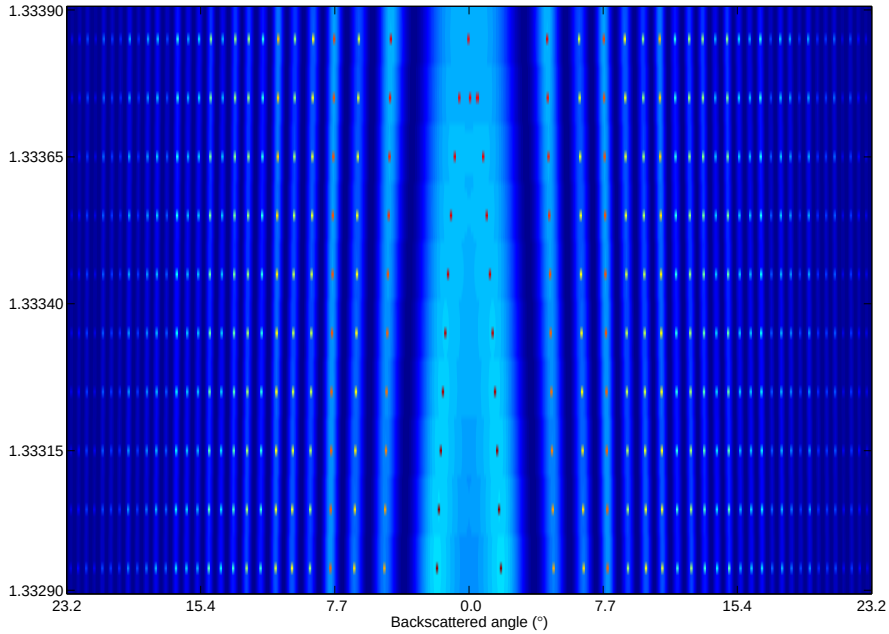

Figure 18. The refractive index of the liquid inside the rectangular channel has been changed from 1.33329 to 1.33339 and the fringe pattern modeled. In the center is the centroid. Indicated by rectangles is the fringe position, which is tracked for further pattern analysis.

calculated fringe pattern arising from a rectangular channel, where the liquid has changed refractive index. The refractive index has changed from 1.3329 to 1.3339. The data has been transferred to Matlab, where a routine has found and tracked the fringe position (indicated on the pattern in Figure 18), as the refractive index changed.

The procedure has also been completed for the two other geometries. The refractive index has also been changed in smaller and smaller steps until a change could not be seen from this modeling procedure. The modeling results are summarized to:

- For $\Delta RI = 1 \cdot 10^{-5}$
  - fringe pattern for rectangular channel moved 0.02°
  - fringe pattern for semicircular and circular channels moved 6°
- Interference pattern for rectangular channels could not be seen to shift for $\Delta RI = 1 \cdot 10^{-6}$
- Interference pattern for semicircular and circular channels could still be seen to shift for $\Delta RI = 1 \cdot 10^{-8}$

The beam propagation method (BPM) in ASAP is a function to solve Maxwell's equations as the light translates through the materials. This method has been tested on the MIBD setup. As the name says, the beam is propagating in the material, meaning that effects from forward propagating light interacting with backwards propagating light cannot be modeled by this method. As this sensing technique is based on the backscattered light it is obvious to the author, that this missing interaction would result in modeled fringe patterns far from the pattern in a real sensing situation.

In close collaboration with Florian Forster from Lund University, Lund, Sweden, the system has been modeled in his FDTD–based model. The model functions as the beam propagation method in ASAP, but both forward and backward propagating light interacts. As the calculation is done by tiny propagation steps through the system computation time is extensive. In ASAP the calculations are speeded up as the light is treated as rays until it reaches the interface where the E–field is then calculated and the light propagates through the interface and is decomposed on the other side again treated as rays. Only few results were obtained from the FDTD modeling, but an explanation for the phenomenon giving rise to the interference pattern from rectangular geometries were found. The pattern arises from light diffraction of the corners of the rectangle, in particular the two bottom corners where PDMS, glass and liquid interfaces.

A hypothesis was that the PDMS channels changed geometry when liquid was drawn through, so the walls of the channels would curve. This was tested by confocal microscopy. On the 3D–images it was seen that the shape stayed rectangular. A calibration curve has been made for a PDMS chip, with the modeled system variables, see Figure 19. An the detection limit reached experimentally is $\Delta n = 7 \cdot 10^{-5}$, leaving room for improvement according to the model.

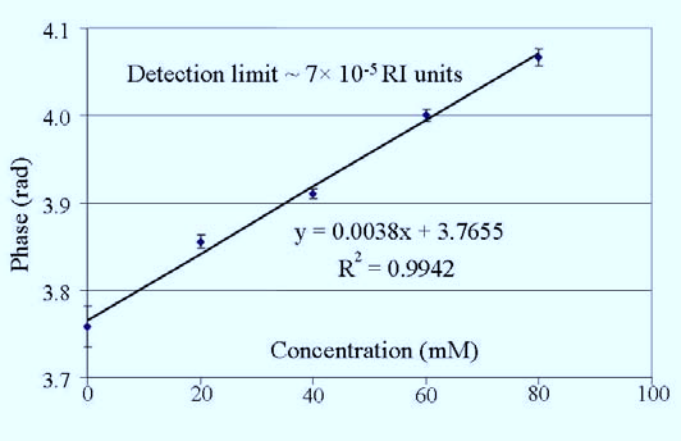

Figure 19. Concentration series of glycerol solutions has been used for producing a calibration curve. The slope of the best fitted line is 0.0038 and is a direct indication of the sensitivity. The noise,σ, is 0.0107 and with 3σ statistics the detection limit is found to be $\Delta n = 6.75 \cdot 10^{-5}$.

3 Master fabrication for micro injection molding

In this chapter is described procedures developed to fabricate a master tool for injection molding of micro flow chips. The desired flow channel design is fabricated on a substrate, which is electroplated into a nickel shim. This nickel shim is used to make replicas of the flow system on a mass production–like process. Several micro fabrication techniques have been used to achieve the desired geometry of the flow channel.

Much effort is done for developing different tool kits for the integrated Lab on a Chip. For liquid handling pumps [42], mixers [43, 44] and other unit operating parts [45] have been described for some time. The elegant designs delivers the liquid to perform an analysis, such as nanowire sensing [46], surface plasmon resonance [47] and interferometric sensing [48], in an efficient manor.

Micro Interferometric Backscatter Detection (MIBD) has been applied in several areas of analytical chemistry since the mid 90'ties [49]. The detection scheme is a way to monitor small changes in refractive indices of liquid samples and also determine the absolute refractive index [50]. The highest sensitivity has been achieved when capillaries has been used for sample containment where Δn by 10^{-9} has recently been detected [27]. The MIBD scheme has great potential for miniaturization when transferring the sampling handling from capillaries to micro fluidics and has been successful in PDMS chips with rectangular geometry of the flow channels [51].

In this work the micro fluidic system comprises completely in injection molded polymer with the by experience best geometry known from the circular capillaries. This has also been shown by optical modeling with ASAP software. Since this is a highly sensitive interferometric detection scheme there is high demands on the surface structure such as surface roughness and geometry uniformity. The strategy has been to fabricate the micro flow system shapes in materials most accurately engineered for this. These master shapes are transferred into an inverted metal relief structure by electroplating. The inverted metal structure may subsequently be used as a mold for polymer processes in a mass production-like process. There have in this work been tested two different substrates, fused silica and silicon wafers, with several different sacrificial masks for wet etching. The desired channel dimensions are from 50 to 100μm in radius, which has shown great promise when working with capillaries. The hole in the etching mask is in this case important to ensure the desired geometry [52]. The entry holes have been tested for sizes of 1.5, 2.5, 5 and 10μm. The desired feature is a groove with cross sectional geometry of a semicircle. The approach is to isotropically wet etch the feature in both fused silica glass and silicon. In the past many groups has achieved good isotropically etching to fabricate micro fluidic channels in glasses [53]–[55]. Few have shown concern with the cross–section geometry [56, 57] and surface roughness, as is the case for this work when using coherent light for this detection scheme, see Table 5.

Table 5. Summary of literature on how to make circular structures in glass. (1) Claimed in patent. (2) Considered semi circular by author in reference.

Substrate	Mask	Mask fabrication	Etchant	Temp	Stirring	Shape	Reference
Microscope slides	Photoresist	Spin coated	NH_4F/HF (BOE 5:1 and BOE 10:1)			8 μm deep flat channels with curved sidewalls	[58]
	Photoresist	Spin coated	Diluted NH_4F/HF		on	6.2 μm deep channels	[53] [54]
Fused quarts	30 nm Cr (100–400 nm) Au	Sputtered	Diluted NH_4F/HF	50 °C	on	7.6 μm trapezoidal with curved sidewalls	[59]
Fused silica	Cr/Au/Cr (25/100/25 nm)		Conc. HF/HNO_3			15 μm deep	[60]
Fused silica	Cr (400 Å)		NH_4F/HF	50 °C		28 μm deep, flat middle and curved sidewalls	[52]
Several, mostly Pyrex	200 Å Cr 1000 Å Au	Evaporated	Conc. $HF/HNO_3/H_2O$ (20:14:66)		slowly	Circular channels	[61]
Borofloat	Amorphous silicon	CVD	HF			35 μm, curved sidewalls	[55]
Borofloat	100–500 Å Cr w. thick Au	sputter	HF/HNO_3			100 μm diameter $\pm$2.5 μm (1)	[62]
Borofloat	30 nm Cr 500 nm Au	sputter	conc. HF			69 μm top to bottom 79 μm side to side. (2)	[56]

3.1 Isotropic etching in fused silica

From previous work it is known that the line width of the etching mask is important after isotropic etching with HF into fused silica through a tiny hole in the etching mask[56, 61]. The actual HF–etching in this section was done by Kaleido Technology A/S, Farum, Denmark, in a buffered oxide etch. The test pattern used was tiny crosses with different line thicknesses, see Figure 20. The smaller the lines the more uniform structure. As mentioned above the entry hole will affect the final feature.

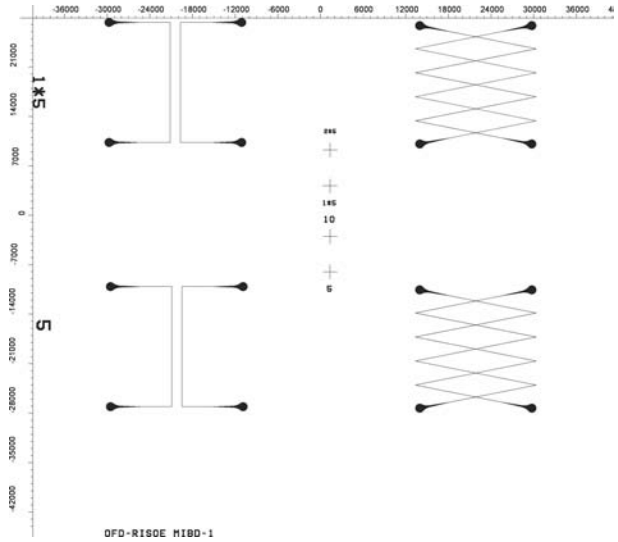

Figure 20. Photolithography Cr–mask used for isotropical etching experiments. In the center is the four crosses with different sizes from 1.5 to 10 μm. There are two designs on the mask of useable flow designs. One is two parallel lines and the other is two channels crossing. They are both in two line widths of 1.5 and 5 μm.

The sacrificial mask has been changed in each experiment hence a total of four different masks have been tested. The system investigated is fused silica with a metal mask. The entry holes are etched into the metal via a photoresist mask. This is done by standard photolithography procedures. All the substrates have been cleaned before use

1. 5 minutes in acetone.
2. 5 minutes in isopropanol.
3. 5 minutes in water.
4. 1 minute in chromium sulfuric acid.
5. rinsed in water.
6. 5 minutes in .1 M KOH.
7. rinsed in running water for 30 minutes.
8. dried in oven at 110 °C for 12 hours.

After depositing the metal masks the photoresist procedure is as follows:

1. Spin speed: 3000 RPM for 60 seconds with Microposit S1805 by Shipley.
2. Prebake: 30 min at 90 °C.
3. UV exposure. Several exposure times were tested to achieve the smallest features possible. The test lithography mask has four crosses with thicknesses of 1.5, 2.5, 5 and μm.
4. After exposure the photoresist is developed for 1:45 min in 15 % Microposit Developer.
5. rinsed in water and dried in filtered air.

The metal masks were opened by Cr–etch ($(NH_4)_2Ce(NO_3)_6$, CH_3COOH (glacial ethanoic acid) and water) and Au–etch (KI, I_2 and water). The mask was sputtered onto the fused silica. The sputter chamber was evacuated down to 10^{-6} atm and the sputtering process were at $2 \cdot 10^{-5}$ atm with argon as the carrier gas. A thick layer was sputtered onto the substrate. The layer was measured to 280 nm of chromium. A thin mask was fabricated as mentioned above except the deposited layer is 40 nm instead. Since the thick mask fell off during the first attempts of etching a surface adhesion promoter step was tested. Samples were exposed to hexa methyl disilazane (HMDS) prior to the sputtering and other samples were sputtered directly after cleaning. The HMDS reacts with the substrate surface, leaving it hydrophobic. By applying HMDS no water is present on the sample when entered into the vacuum chamber of the sputtering tool. The HMDS is burned in the plasma as the sputtering process begins. A combination of two metals was tested, Cr/Au. The chromium layer is 40 nm and will provide good adhesion to the fused silica. The gold layer is 2000 nm thick. The thickness will provide mechanical stability to the mask and reduce the number of pinholes. The pinhole number would decrease as defects in the Cr–layer are coated with thick gold. The gold is deposited directly onto the Cr without exposing the chromium to air, hence no oxidation of the first metal layer.

Thick Cr–mask results

During the etching process most of the metal mask was washed/flushed off, as seen in Figure 21(A). Even though much of the mask has disappeared few images were possible to obtain from these samples. In Figure 21(B) is an image of the groove etched in the fused silica sample. The bottom of the surface is actually nicely curved. But the sidewalls are straight. In the start of the etch the Cr–mask protects the surface from the aggressive etchant. When the mask fell off the entire surface is exposed, thereby the HF has free access to the surface. The microscope image is made from a polydimethylsiloxane (PDMS) cast. The cast is then cleaved and then viewed from the side.

PDMS replica procedure: The uncured PDMS is mixed with the curing agent in 10:1 ratio by weight. The curing agent is stirred into the PDMS for some minutes to ensure a homogeneous mixture. Afterwards the PDMS is degassed under vacuum for at least 30 minutes. Usually all bobbles have disappeared after this period of time. Meanwhile the old surface is prepared with HMDS. The HMDS will react

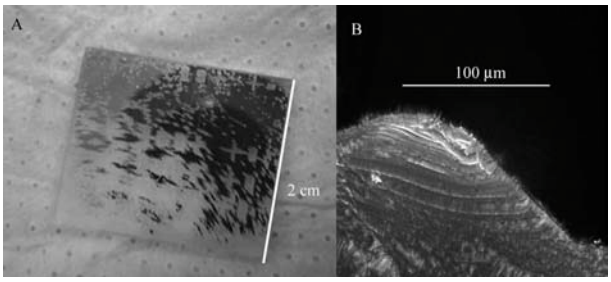

Figure 21. (A)Picture of sample after etch. The stirring has left its mark on the sample. Most of the Cr–mask has been removed. There has been exposed four patterns on the substrate and etched simultaneously. In (B) is seen the etched structure, seen as a cleaved PDMS replica. The bottom part of the structure has some curvature, but the major part is a flat surface.The sample was protected by thick Cr–metal mask.

with the mold surface creating a monolayer thick slip layer. After degassing the PDMS is poured slowly over the mold (sample which is to be replicated), trying to prevent any bobbles forming. If any bubbles is formed or to ensure better replication, the mould with PDMS on top is put into vacuum shortly. The PDMS is then cured in an oven for at least 2 hours at 90°C. A shorter baking time is achievable by increasing the temperature, but normally the sample is contained in plastic petridish. These will be damaged at higher temperature. The advantage of using these plastic dishes is that they are thrown away after the replication procedure.

When making side view microscope images of the micro structures fabricated PDMS replicas there are several advantages. It is, if done properly, a non destructive way of getting information about the fabricated structures in a fairly simple manor. PDMS has the ability to almost make a crystalline breakage. The surface is cut with a scalpel and then the replica is bend along the cut, the PDMS replica will then be sliced almost perfectly, resulting in a very flat cut, which makes it ideal for viewing through microscope objectives. Thereby the resolution of the microscope determines the smallest features detectable in microstructure.

Thin Cr–mask

The mask was fabricated as mentioned above except the deposited layer is 40 nm instead. Since the thick mask fell off during the first attempts of etching a surface preparation was tested. Two samples were exposed to HMDS prior to the sputtering and two samples were sputtered directly after cleaning. The HMDS reacts with the substrate surface leaving it hydrophobic. By applying the HMDS no water is present on the sample when entered into the vacuum chamber of the sputtering tool. This might improved the adhesion between the Cr and the glass surface. HMDS is used as adhesion promoter for other lithography applications, although this usually relates to adhesion of organic polymer coatings. The HMDS is burned in the plasma as the sputtering process begins. After sputtering the mask were tested for better strength, meant as the ability to stay on the glass. The mask could not be scratched by steel tweezers but only tiny scratches by a piece of silicon. Again the substrates were etched at Kaleido Technology.

The mask could resist the stirring during the etching process. There was no difference between samples with HMDS or without. But the mask quality was much improved by only depositing 40 nm of Cr. Again the surface at the bottom of the groove is curved, but again the sidewalls are not. Pinholes are becoming an issue on these samples. The pinholes are result of uneven distribution of the chromium on the surface or defects in the layer. Even the smallest defect or dust particle will become a hole, since the thickness of the mask is so small. The main cleaning problem is the sputtering process. The sputter target is sometimes exposed to air, that might introduce an oxide layer on the Cr–target. These molecules are the first to hit the glass surface. They could cause defects in the first nanometer. But the largest problem is that the sputter tool is not placed in clean room environment. Even though the samples are clean, they are exposed to dust, air and water when entered into the vacuum chamber.

Combined Chromium–Gold metal mask

A combination of two metals has been tested. The chromium layer is 40 nm and will provide good adhesion to the fused silica. The gold layer is 2000 nm thick. The thickness will provide mechanical stability to the mask and reduce the number of pinholes. The pinhole number would decrease as defects in the Cr–layer are coated with thick gold. The gold is deposited directly onto the Cr without exposing the chromium to air, hence no oxidation of the first metal layer. The entire process from the lithography step to final stage after etching has been verified by microscope images after each step.

First are the images after the lithography step. Next are the images from the Au and the Cr removal/etching. Then are images showing how the entry holes appear after the HF–etch. Then are images showing the entry holes and the etched structures taken from the backside of the substrates. Finally is a cross section of the groove. It is made by a PDMS casted on the substrate and then cut perpendicular to the groove. Below the images are graphs of the height of the PDMS cast made by a Dektak profilometer.

The shape of the etched grooves (via PDMS replica) is measured according to this drawing, the numbers 1 and 3 are the sidewall length, 2 is the length of the flat bottom and 4 is the structure depth:

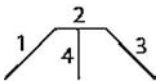

As an example is shown for one sample at one exposure time with each step and the lithography mask opening as rows and columns, respectively:

Table 6. Example of the verification steps. This is for sample 1 exposed for 6 seconds.

Step	2.5μm	1μm	10μm	5μm
Photoresist	 2.61μm	Not developed	 10.08μm	 4.77μm
Au opening			 10.96μm	 5.15μm
Au after HF	 3.15μm		 13.27μm	 6.75μm
PDMS	 Radius 64μm see Figure 24		 1:218μm 2:67μm 3:199μm 4:100μm	 1:μm 2:μm 3:μm 4:100μm
Dektak			94.5μm 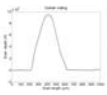	93.1μm 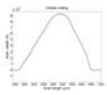

A typical etch result is shown in Figure 22:

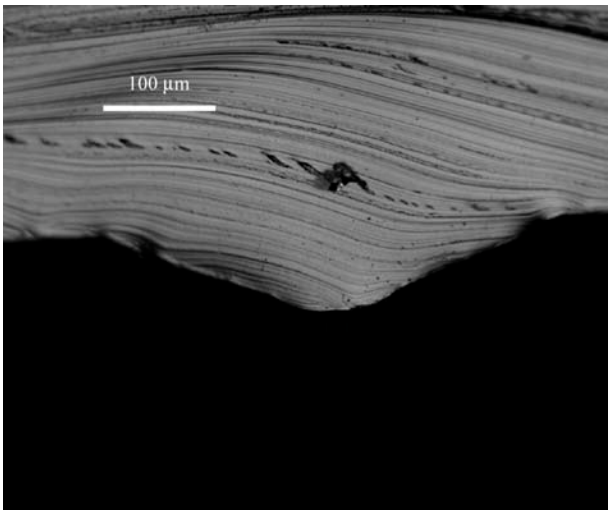

Figure 22. Typical etch result. Cast in PDMS of groove. This image is from sample 3 with exposure time of 21 seconds and the width of the lithography mask is 10 µm. The geometry numbers are 1: 202 µm 2: 50 µm 3: 200 µm 4: 75 µm The shape is typical trapezoidal.

The shape is trapezoidal with a flat bottom and two flat sidewalls. The fused silica surface has apparently been exposed to the HF–solution before the etch has removed the amorphous material in an isotropical fashion. The mask did not fell off during the etching process, as seen in Figure 23.

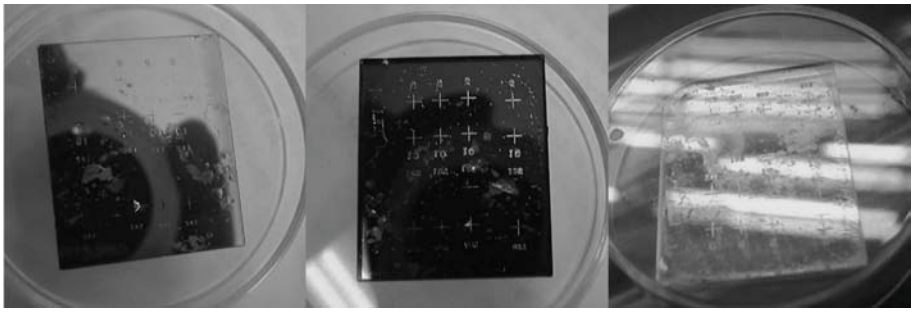

Figure 23. Pictures of a sample after HF etch. First is the front of sample. Then is the sample from the back. Finally is the sample with the mask removed. The presence of pinholes is almost nonexistent. Very few are observed. One is seen on sample 1 which appear at a cross that might not have been etched completely before the HF etching.

The addition of the Au-layer has reduced the number of pinholes. The pinholes has not been avoided completely.

In Figure 24 is shown a microscope image of a result of a pinhole. The size reveals

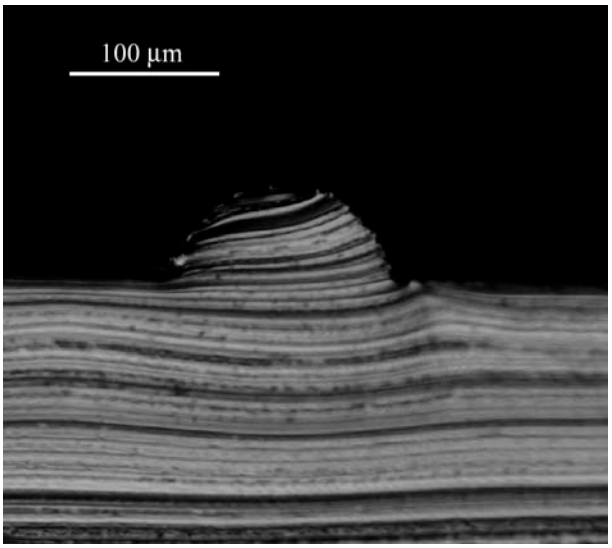

Figure 24. Pinhole from sample 1 at 6 seconds exposure. Radius is 64 μm. The pinhole etch actually ends up as a circular structure.

that the etching mask was not etched all the way through and the HF etch made a tiny hole during the glass etch. An interesting result, but it is not reproducible. But the image shows that it is possible to fabricate large semicircular structures by isotropic etching in fused silica. Normal entry holes results in trapezoidal shape.

Discussion of the etching in fused silica

The thick Cr–mask fell off during the HF etching. This is believed to be caused by internal stress in the metal layer as is also discussed in [55]. The resulting groove is nicely curved at the bottom, but the sidewalls are not curved. The glass was chemically cleaned, this is to introduce less surface stress in the glass. Both polishing and ultra sound cleaning increase the surface stress.

The thin Cr–mask had much better adhesion to the glass. The etching result was, when possible to compare, the same for samples with HMDS applied or not. The thickness is decisive of the mechanical strength since the thin layer was much more stable, but the number of pinholes is increasing as well as the thickness becomes smaller. The addition of gold on top of the Cr mask proved a large reduction of these pinholes. The one pinhole mentioned above, in Figure 24, is the result of a very tiny defect in the mask. The depth of the etch is approximately 30 μm smaller than the other etches on that sample. At Kalido, photoresist has previously been used for etching structures up until 30 μm. At that stage the photoresist is etched away by the HF. So the pinhole lags 30 μm because the mask defect was coated with photoresist.

The Au/Cr - mask could withstand the HF treatment, although it collapsed eventually. This collapse did not expose additional silica surface; it only made the entry holes a bit larger. This is not the reason for the shape of the groove. The

photolithography could be improved to produce lines down to 1.5 μm even though no effect is seen on the entire shape of the groove. In Figure 25 the statement from

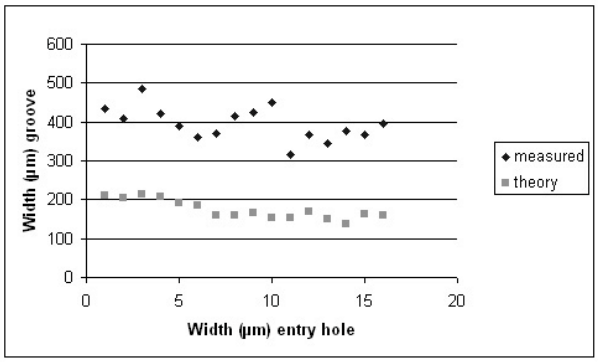

Figure 25. The grove width as function of the entry hole width. The width should be twice the etched depth plus the width of the entry hole. The measured widths are much larger than expected from the literature.

[61], which says that the resulting groove should be twice the depth plus the entry hole for isotropic etching, is tested. The grooves are much too wide, a factor of 2, in the case of the Cr/Au-mask. If the metal mask is underetched, then this underetch is the deciding etching rate, not isotropically etch into the fused silica.

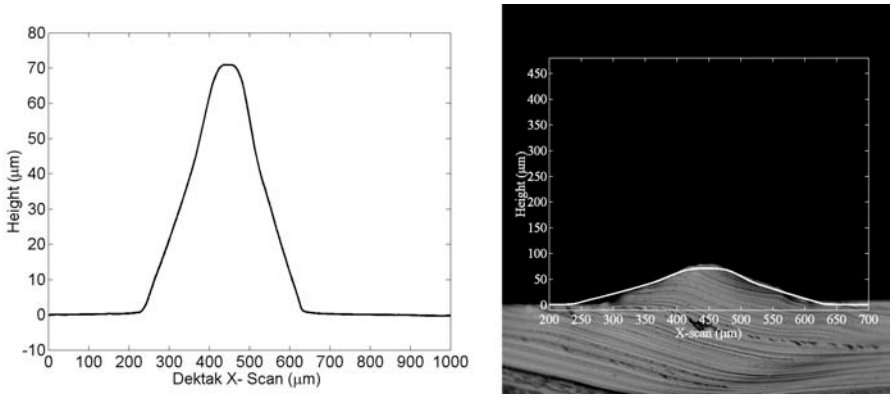

Figure 26. The fabricated structures have been investigated by two different measurement techniques. The microscope is touchless although the replication process demands contact. The Dektak profilometer is not contact less, but physically places a needle on the sample and mechanically measures the morphology. Here are the two techniques compared by overlaying the Dektak scan onto the micro scope image of the PDMS replica. This is for sample 3 exposed for 21 seconds with 10 μm mask opening. On the left is the Dektak profile alone to show that the height is 70.9μm.

The microscope and the Dektak profiler agree on the shape of the etched structures, see Figure 26. The depth is always some microns smaller for the Dektak measurement. This is caused by the fact that the profiler touches an elastomer (PDMS). This could influence the measurement as the soft material deforms to varying extend under the touching needle. Also on the microscope images it is a problem to find the edge, just a bit out of focus and the size is not completely correct.

The shape of the groove is not circular. The tip/bottom could be curved, but it is not satisfactory. The shape is in all experiments more trapezoidal. And the ratio of the shape is shown in Figure 27. One side in the trapeze is always longer

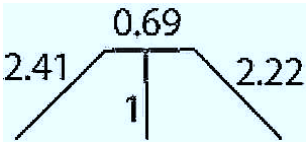

Figure 27. The average ratio of the samples investigated after HF etching.

or the same length as the other side. The sides would be expected to have the same length.

The shape has been discussed with Dr. Shaorong Liu from Texas Tech University. He has achieved circular channels before [62]. The resulting shape is caused by underetching of the Cr-layer. This layer is capable of withstanding the HF treatment if it is of excellent quality. The layers produced in these experiment were of too low a quality. The problem with surface tension of the glass as described in [61] is not the case here. That could explain why the Cr layer did not stay at the surface, but the difference between the expected shape and the actual shape is too large.

Table 7. The etch rate for the experiments with Cr/Au-mask.

Sample 1	Etching time	21h 28min
	Depth (microscope)	100 μm $\pm$1.0
	Depth (Dektak)	94.8 μm $\pm$0.6
	Etch rate (microscope)	77.6 nm/min
	Etch rate (Dektak)	73.0 nm/min
Sample 2	Etching time	18h 48min
	Depth (microscope)	89.7 μm $\pm$1.5
	Depth (Dektak)	83.6 μm $\pm$0.3
	Etch rate (microscope)	79.5 nm/min
	Etch rate (Dektak)	74.1 nm/min
Sample 3	Etching time	16h 59min
	Depth (microscope)	73.8 μm $\pm$3.9
	Depth (Dektak)	70.2 μm $\pm$0.9
	Etch rate (microscope)	72.4 nm/min
	Etch rate (Dektak)	68.9 nm/min

The depth increase linearly with time ($R^2 = 0.96$) ,see Table 7, so in the case of no underetch of the mask, a very uniform structure would be expected, more circular than trapezoidal in geometry.

Summary on isotropical etching in fused silica

Four different metal masks have been tested for isotropic etching in fused silica. The desired shape of a half circle was not achieved. The quality of the metal masks is found to be the main reason why the shape became trapezoidal instead of circular. The quality is affected by the cleanliness. The cleaning procedure used for sample preparation could not have introduced enough surface tension

to cause the etch results. The quality of the cleaning process may not be clean enough, since it is sometimes necessary to clean the sample twice or three times before they appear clean. Dirt and other residues may sometimes be seen after the cleaning process. To increase the quality of the mask all processes need to be in a controlled clean environment. Concentrated HF could be used instead of buffered HF, as this would reduce the etching time, thus not allowing enough time to underetch the mask. As mentioned in the literature a silicon nitride mask would provide a better mask as HF do not attack that mask and the mask may be formed in a very clean environment. The crystal structure is also more compatible with the surface ensuring good adhesion.

Photolithography mask fabrication

Photolithography has been chosen to be the obvious technique to use for transfer the design layout to the samples that is later to be etched. For this application the photolithography mask is a critical tool. Fabrication of such masks has been developed from early stages of the electronic industry starting with cutting in *rubylith* by hand that via down scale projection resulted in a useable feature size, going down 1000 times in size. Making smaller and smaller features has been the challenge as the minimum feature size in 2001 was around 100 nm using 248 nm DUV light and the feature size is expected to decrease to 20 nm in 2014 by using various forms of ultra short wave lengths and E-beam writing[63].

In a Scanning Electron Microscope (SEM) the sample is placed in vacuum and bombarded with high–energy electrons (0.5-40 keV), these electrons contains so much energy that they will continue into the sample surface. Inside the sample material the electrons are absorbed. By these events secondary electrons are created. These low–energy electrons (0-50 eV) are usually detected. The electron beam is scanned across the sample surface completing a surface image. A SEM has been used for writing in a resist material instead of using the SEM for imaging. The idea is to write a designed pattern with very small dimensions. This is to fabricate a photolithography mask, which is then used later on in the fabrication of circular micro flow channels. From Kaleido Technologies I was informed that 1.25 to 1.50 μm wide etching holes would result in cylindrical lenses (20 μm in diameter). In this work the resulting groove is to be 50 μm in diameter. The goal is to fabricate patterns with line widths around 1 μm to 3 μm.

It is the secondary electrons that is used to transfer the energy to the masking material. The charge density profile of such a low–energy electron can be seen in figure 28. The SEM is equipped with a shutter, that blocks the electron beam. By controlling the opening times of this shutter a known electron dose is directed to this small area or pixel. Pixel usually is known from bitmap–images, and such images where constructed such that the color information directly corresponds to the opening time. When two pixels are close to one another they will provide exposure to the neighboring pixel as well, the proximity effect [64, 65]. The effect can expose unwanted areas of the resist material leading to worse resolution. The effect can be reduced by changing the individual pixel value of the image you write, this is what is meant, when the pattern is proximity corrected. One could also distribute exactly the amount, that is needed for resist reaction. Making sure that the energy level is in the narrow region is possible but extremely difficult [66], alternative methods have been reported of applying a thin insulating layer between the resist material and the substrate [67]. Before each run the SEM had to be calibrated, so the correct opening times could be used. The dose has to be calculated before writing the image to the sample and can be found from equation (77).

$$Dose = \frac{n \cdot I \cdot t}{A} \tag{77}$$

n is the number of points in the image file. I is the current used, t is the opening times in ns and A is the area exposed. The area is the window size at a certain magnification. The calibration of the SEM determines which current values is available. As the tungsten filament ages the current changes. A resist material used was SAL 601 (Shipley, US) and the proper dose was between 0.12 $\mu C/cm^2$

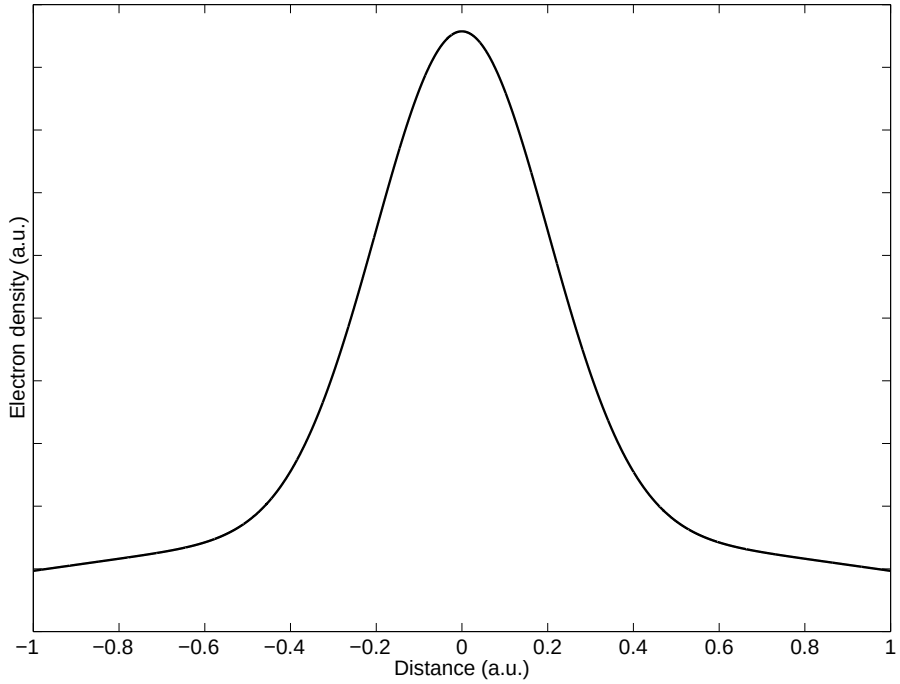

Figure 28. The profile of the energy distributed when electrons reach the resist material has two areas of interest (double Gaussian). The high–energy region centered around the middle region (-.4 to .4 arbitrary distance units) and the surrounding region where energy is dispersed over a large area. If two or more electrons has this low–energy region overlapping, it is called the proximity effect.

and 0.36 $\mu C/cm^2$ at 20 keV. A dose test image was constructed and can be seen in figure 29.

A dose test is run at different current levels. Afterwards the sample is developed and the proper dose is determined. Developed patterns is seen in figure 30.

After the best suitable dose has been determined the actual pattern is written on a new sample. The SAL–601 resist is a negative resist, meaning that the exposed material remains after development.

For the overall purpose of making a photolithography mask a dark–field mask is needed. With a dark–field mask most of the sample surface needed to be exposed, hence leading to longer writing times. The writing times became so long (2 to 8 hours) that the filament was not stable over time resulting in failure as the incorrect dosage was applied to the sample. Instead a different resist was tested, 4% PMMA in chlorobenzene with molecular weight of 495 kD. This is a positive resist, as the polymer chain is destroyed by the electrons, so only the pattern lines need exposure, resulting in much more practical writing times. Good results were achieved in a 5 X 5 mm area, completed in less than 30 seconds at low current settings. Faster writing times could be achieved with a higher current, but would result in lower resolution. The largest window of exposure usable was 2 X 2 mm (larger windows is less magnification, hence lines become larger that 1 μm) and a writing time of 15 minutes produced the smallest lines of 650 nm in width. The stepping motor on the translation stage on the SEM was then to be used for exposing neighboring windows to make the mask design into a full size mask having an area of at least 44 X 44 mm (limited by the nickel shim size and the

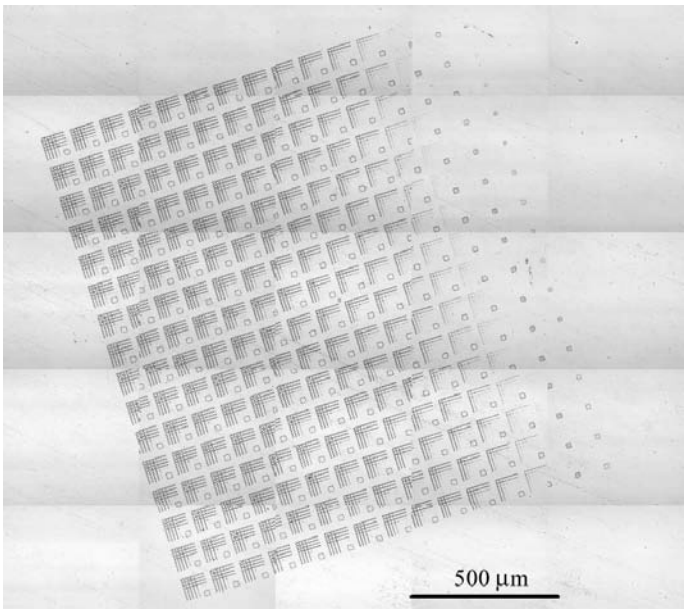

Figure 29. The dose test consists of 256 identical patterns one for each intensity level, from black to white. This image is made up from an 8196 by 8196 pixel bitmap. The written area is set to be 2 X 2 mm. So one pixel corresponds to 244 nm. From identifying the best pattern the dose can be set to give the best possible result for the given experiment.

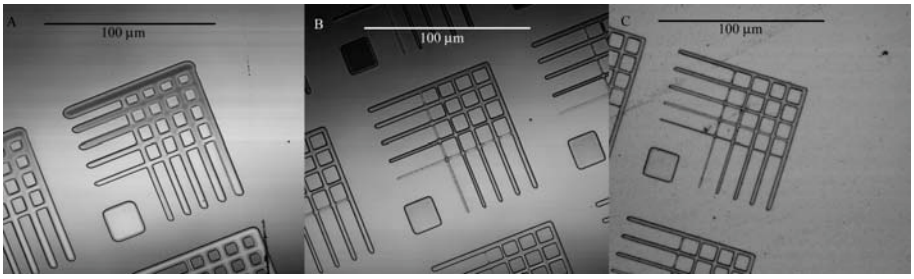

Figure 30. Microscope image of pattern number 255 in dose test, the highest dose (A). The smallest lines are 2.77 µm for the X-direction and 3.05 µm for the Y-direction. The smallest lines are made from 1 pixel wide lines. Pattern number 3 is shown in (B). Same sample as in (A), except the dose of electrons/energy are much lower. This is found to be the optimal dose, since the thinnest line is just present. The thinnest lines are now between 870 and 910 nm. When compared between the two images it is clear that the features are slimmer with the correct dose. In (C) the dose test has been proximity corrected. The factors used for that is 50% for nearest neighboring pixel and 15% from the pixel next to that. This has only effect for lines made up of more the than one pixel. Again the thinnest line is around 1 µm but each pixel is visible to be 650 to 780 nm.

injection molding tool). It was not possible to obtain any usable results by this stepping procedure.

To summaries it was achieved to make features of 650 nm in size accomplished by taking the proximity effect into consideration when designing and constructing the bitmap–image. It was found that the spot size has to be as small as possible, higher magnification leading to smaller exposed surface area per pixel. The fabrication of our own mask was abandoned as at the same time DeltaMask in Holland could deliver high quality masks with smallest feature size of the needed 1.5 μm. Their masks where made by direct–writing with a focused laser on a chrome–covered glass substrate with photoresist spun on top.

3.2 Isotropic etching in silicon

An alternative etching procedure has been developed. Instead of etching in fused silica the material used is silicon. Even though silicon is a crystalline material, it is still possible to isotropically etch into a silicon wafer. But the actual etching process is far more complicated than that of etching in glass with HF [68]. The etch used is HF–based, but also uses two other chemicals, nitric and acetic acid. The entire HNA–process is a multi step procedure as is seen in Figure 31.

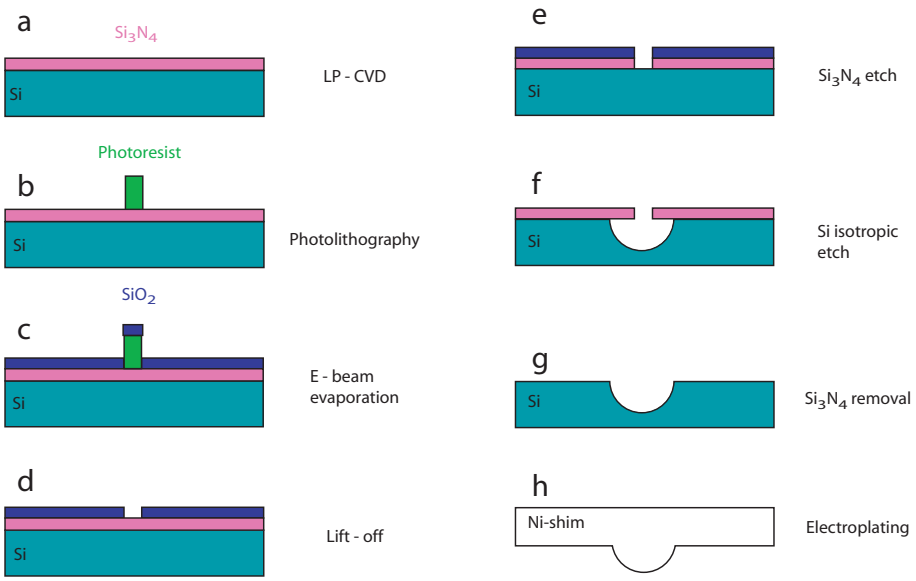

Figure 31. The HNA etching process. The following steps has been used in order to complete the process sketched in the diagram show. Cleaning of Si substrates – a) Deposition of Si_3N_4 layer – b) Photolithography – Plasma cleaning – c) Deposition of SiO_2 layer – d) Photo resist lift–off – e) Etching of Si_3N_4 through SiO_2 mask – f) HNA etching of Si through Ni_3N_4 mask – g) Removal of nitride mask in boiling phosphoric acid. h) The substrate is later electroplate to be used for making replicas.

The process begins with a bare silicon wafer and ends up with having the desired micro structures etched into the wafer, which is then electroplated for later polymer chip fabrication. The entire process had to be optimized for each step, since no standard procedure exist for this work.

The bare wafers are prepared in a RCA cleaning process, to ensure a perfectly clean surface before the sacrificial mask is deposited on the surface, process is shown in Table 8.

After the HF–step (B in Table 8) the wafer surface was tested for its hydrophillicity. If a droplet of water stayed on the surface, the wafer was then immersed into the HF–solution for another few seconds. The cleanliness of this step is very critical for the success of this entire process. As with the thin Cr–mask any defect in the mask material will result in pinholes creating uncontrollable features in the sample surface. As the surface is cleaned good adhesion and uniformity is ensured. The removal of the native SiO_2 layer is critical for this procedure as the etching bath contains HF, which would etch away that oxide layer underneath the protective mask, destabilizing the mask. The sacrificial mask is a layer of Si_3N_4 deposited

Table 8. Silicon wafer cleaning procedure, same as in [63], except the solvent removal step has not been used.

A Removes organic material and some metals ions.

1. Immerse in a (5:1:1) solution of $H_2O - NH_4OH - H_2O_2$. Heat solution to $75 - 80°C$ for 10 minutes.
2. Quench the solution under running DI water for 1 minute.
3. Wash in DI water for 5 minutes.

B Removes native SiO_2 layer.

1. Immerse in a (1:50) solution of $HF - H_2O$ for 15 seconds.
2. Wash in running DI water with agitation for 30 seconds.

C Removes heavy alkali metals.

1. Immerse in a (6:1:1) solution of $H_2O - HCl - H_2O_2$ for 10 minutes at $75 - 80°C$.
2. Quench the solution under running DI water for 1 minute.
3. Wash in DI water for 20 minutes.

onto the clean silicon wafer. The procedure used for depositing the nitride–mask is low pressure chemical vapor deposition (LP – CVD). The mask thickness was approximately 1900 Å. The nitride layer should not be affected by HF, hence protecting the wafer surface from being etched. The deposition of the mask was done via Prof. Davidson's lab at Vanderbilt University.

The test pattern used is four crosses with different line widths. All performed on 2X2.5 cm test samples (Si wafers diced). The test pattern is transferred to the samples by photolithography. The photoresist used was Futurex 1000 PY (negative resist) and developed in Futurex RD6. This resist is designed to underdevelop, so the footprint of the resist is smaller than that of the photolithography mask. This is intended to be used for a lift–off process as the undercut separates the deposited film so an excellent removal of the top layer is achieved, since it is not touching the bottom layer. In Table 9 is shown experimental runs to achieve reproducible and acceptable line features.

Table 9. Photolithography experiments. It is normal procedures as described by the resist supplier. The spin coating and the post exposure baking has been kept constant. Result describes the pattern created. E.g. –1.5 meaning all motives except the 1.5μ *pattern is transferred successfully. SR is sample reused, MOS is mask on substrate so the lithography mask is placed directly onto the sample. Maskaligner, means that the mask is fastened to the aligner allowing for multiple exposures.*

Spin speed: 3000 RPM for 40 seconds.

Acceleration: 664 RPM/s.

Post bake: 60 seconds at $100°C$.

Run	Prebake $150°C$	Exposure seconds	Development seconds	Result	Comments
1	60 s	220	12	–1.5	SR,MOS
2	60 s	220	15	–1.5 & 2.5	SR, MOS
3	60 s	220	20	only 10	SR, MOS
4	60 s	220	10	–1.5 & 2.5	SR, MOS
5	60 s	230	16	–1.5 & 2.5	SR, MOS
6	60 s	240	12+1	All	SR, MOS, removed 1.5 & 2.5 with extra developing
7	60 s	280	16.5+3 +30+20	All	SR, MOS, removed 1.5 & 2.5 after 33 s. development. Residue removed.
8	60 s	400	10+5	All	SR, MOS, removed 1.5 after +5 s., removed residue, Sample A
9	35 s	400	10+2	All	SR, MOS, Sample B
10	35 s	220	10	All	Maskaligner, Sample C
	35 s	400	10	All	Maskaligner, Sample C
11	35 s	220	13	All	Maskaligner, Sample D
	35 s	300	13	All	Maskaligner, Sample D
	35 s	400	13	All	Maskaligner, Sample D

As seen from Table 9 the resist pattern was still on the surface after 13 seconds. A longer development time and the resist was released from the surface. To remove the residue from the surface development time was more than 30 seconds. It was uncertain if the residue would cause problems further on the process, in particular the lift–off step. An alternative procedure to removing the residue by using the developer was needed. Removing the residue by exposing the surface to an oxygen plasma was tested. In Table 10 is seen the results from the plasma cleaning procedure and the resulting line widths. All of the residue was removed seen as the height of the structures changed more than the thickness of the residue layer was measured to be. Also the samples were visually inspected and the surface hydrophilicity was tested. All tests showed that the residue was removed.

Table 10. Plasma cleaning step. The low and high indicates the settings on the oxygen plasma device, an indication of the power put into the plasma champer. The extra label on the samples indicates the pattern exposure time.

Sample	Height	Plasma	Height	Δ
A	1.445 μm	1min low+30s+30s high	1.425 μm	20 nm
B	1.450 μm	1min low+2X30s+30s high	1.390 μm	60 nm
C	1.335 μm	1min low+30s+1min high	1.295 μm	40 nm
D	1.400 μm	1min low+2X30s+30s high	1.325 μm	75 nm
linewidth	1.5 μm	2.5 μm	5 μm	10 μm
A(400s)	0.84	2.33	4.69	9.03
B(400s)	1.49	2.15	4.95	9.24
C(220s)	2.15	2.64	5.28	9.57
C(400s)	1.49	2.48	5.28	9.57
D(220s)	1.82	2.64	5.28	9.57
D(300s)	2.15	3.30	5.61	10.09
D(400s)	3.80	2.31	5.61	10.40

A SiO_2 layer was deposited by E-beam evaporation in Prof. Wikswo's lab at Vanderbilt University. A quarts sample was used as the SiO_2 source. 200 nm of SiO_2 was deposited onto the sample surface. The oxide layer is to protect the nitride mask in future steps. After the addition of the oxide layer, lift–off procedures followed. Samples were placed in acetone for 60 hours. The acetone had no or little effect. Instead the samples were placed in photoresist stripper with sonication for 1 hour. All photoresist was removed opening the oxide mask. Again the features was measured, see Table 11, and the lines were much smaller than those found on the photolithography mask.

Table 11. Line dimensions after lift–off procedure. The lines are clearly much smaller than those used to fabricate them.

Linewidth Sample	1.5 μm	2.5 μm	5 μm	10 μm
A(400s)	0.52	0.84	1.33	2.33
B(400s)	0.66	0.66	1.32	2.48
C(220s)	0.66	0.66	1.16	2.31
C(400s)	0.33	0.66	1.16	2.31
D(220s)	0.37	0.89	1.20	2.36
D(300s)	0.50	0.84	1.33	2.32
D(400s)	1.16	1.49	1.65	2.97

To open the nitride mask the samples had to be placed in boiling concentrated phosphoric acid. A custom made piece of glass ware was designed and fabricated by the glass blower. A picture of the device is shown in Figure 32(left). The glass container was made to contain the sample holder shown in Figure 32(right). The wafer holder was made completely in Teflon, the only polymer material known to withstand the temperatures and etchants used. The etching in H_3PO_4 was done at 165–175°C for 50 minutes. The sample color was used as indicator for the process progress. The color had to change from deep purple – to golden – back into purple through the visual spectra again to golden ending with gray as the silicon surface is exposed. The boiling phosphoric acid also attacks the oxide layer, but 1000 times slower than for the nitride layer. The color change was viewed on the sample areas which has not been covered by the oxide layer, this could be the back of the wafer.

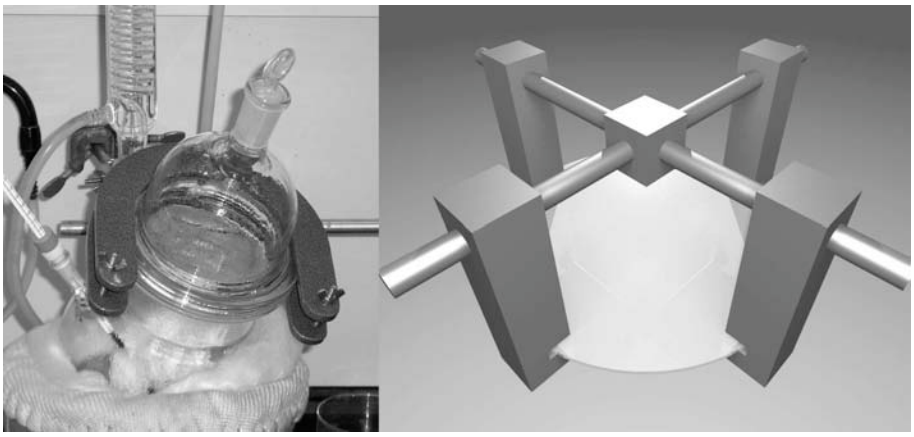

Figure 32. Left: The glass ware fabricated to contain the samples during the opening of the nitride mask in boiling phosphoric acid. The temperature is monitored via the thermometer and the acid is allowed to reflux to keep the temperature constant. Right: The sample holder used for both the boiling acid step and the actual HNA etching. It is made purely in Teflon. Other materials has been tested but failed. The holder can be adjusted to be used with 3" wafers (drawn) and the diced samples (2X2.5cm).

The entire sample holder with sample was immersed into the HNA etch for the isotropic etching of the silicon through the opened nitride mask. The HNA etch is a mixture of three acids, Hydrofluoric, Nitric and Acetic. The mixture used was (1:2:1) concentrated HF, Concentrated HNO_3 and concentrated acetic acid. The solution is mixed just before use and the liquid is kept in a polymer container large enough to contain the sample holder and still have space for the liquid to flow freely along the sidewalls. Agitation is influencing the etch rate, as fresh etchant has to replace the reaction products from the surface for continuous etching. The nitric acid oxidizes the silicon surface to silicon oxide. The SiO_2 is then etched by the HF in an isotropic fashion. The acetic acid is to reduce the surface tension and thereby reduce the number of bubbles attached to the surface. The oxidizing ability regime of the nitric acid is also enlarged by the acetic acid. Different agitation test has been performed. A sample was submerged into the HNA etch, while being sonicated during the etch. The reaction was too violent as the mask and sample was ruined very fast. The same result was found when degassing mode was used, even with less power introduced to the system. While stirring, the process was manageable and an etch rate of 10μm/minute was found. This was in good agreement with the literature and the mixture should place the resulting surface in the smooth area [68], as was desired for this to be used in an optical device. In Figure 33 is shown the result of 5 minutes etching. The structure is very close to being semicircular as the ratio between radius and diameter is .501.

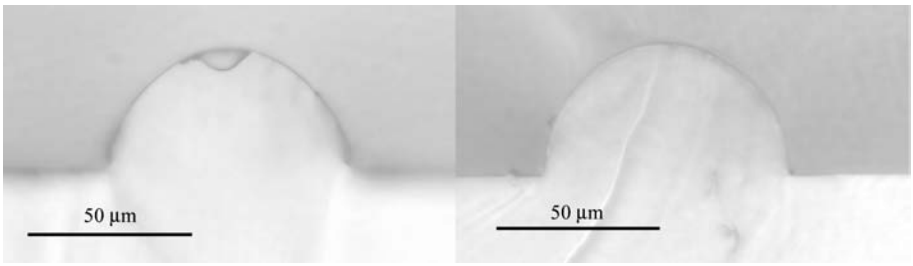

Figure 33. Microscope images show the result of a HNA etch in silicon through a nitride sacrificial mask with photolithography mask line widths of 5µm (left) and 10µm (right). The fabricated structure has a semicircular geometry and no visible flat spot transferred from the mask opening. When going to smaller openings (<2.5 µm) another agitation problem occurs when trying to exchange the fluids through very narrow openings. The best result obtained in this work is when the nitride sacrificial mask opening is between 2.5 and 5 µm. The ratio between top opening and depth has been measured on the PDMS replicas to be .505 and .501 with a profilometer, this is for the first time shown in this difficult length scale, how to fabricate semicircular structures in silicon.

The entire process was repeated for the two channel designs seen in Figure 20 using the 5 μm linewidth with the following process parameters used.

Photolithography: Pre–exposure bake is 35 seconds. Exposure is 400 seconds. Development is 13 seconds.

Plasma cleaning: 1 min low+2X30 seconds+30 seconds high.

Deposition of SiO_2 layer: 200 nm evaporated on by E-beam.

Lift–off: 1 hour in stripper and sonication.

Opening of Nitride mask: Two times through the color range.

HNA etch: (1:2:1) mixture for approx. 5 minutes.

All steps was repeated as the optimum setting from each step, except for the last etching step. The larger part of the wafer did not contain a patterned feature, so a polymer film [69], was attached to the surface and the desired pattern was cut into the polymer with a scalpel before attachment to the wafer. The pattern was cut by hand so the cut out pattern did not fit the lithography pattern perfectly, it was larger making sure none of the micro patterned features was sealed underneath the polymer film. The polymer film was clean room tape used to seal critical parts. The usage of the polymer film ensures that HNA etch did not come into contact with the wafer underneath, providing superb protection. The agitation had to be done differently since the use of entire 3" wafers changed the liquid flow completely. The stirring or exchange of liquid was instead done by hand, instead of a stirring magnetic stir bar, by pumping the liquid around by lifting and lowering the sample holder. The setup was tested with water as liquid before attempting with the acid mixture. Enough liquid was exchanged to remove bubbles from the surface. When etching the first wafer the reaction suddenly changed, the etch rate drastically increased and the nitride mask was removed in seconds. For the next samples it was decided to get as close to the intended 5 minutes of etching as possible, and when the reaction took off, stop the etching immediately. This would give the the largest features possible and keep the mask failure to a minimum. The failure of the mask can be seen as the broadening of the etched channel top. The silicon surface is exposed to the etching mixture too fast. With no mask failure the top corner of the channel is sharp as seen in Figure 33. The wafer was tested in a MIBD–setup and showed a clear fringe pattern although a speckle pattern was present also. To reduce the surface roughness of the obtained semicircular structures a chemical polishing step was done by using a mixture of NH_4F and H_2O_2 and removed approximately 1–2 μm. The sacrificial nitride mask was removed in boiling H_3PO_4.

To summarize, the semicircular structure set out to make has been created by isotropic etching in silicon. A multiple step procedure has been developed for making these structures. Most of these steps would lead to procedure failure if not done at optimum conditions. Since some of the masks failed and was dissolved in the HNA etch it has raised some questions on the different steps. The deposition of the nitride mask and the quality of this masking layer is unknown as the actual procedure were done at other labs with the aid of Prof. Davidson from Vanderbilt University. The evaporation step could only be verified be seing that the color of the wafer had changed uniformly. Uniformly is then an indication of a layer of SiO_2 covering the entire nitride surface. The lift–off process was done in sonication. Sonication has been known to further increase defects in surfaces and could introduce stress in the nitride mask or the oxide layer. Defects in the oxide layer would be transferred to the nitride layer in the boiling phosphoric acid step. Finally the HNA etch is complex and the sudden change in reaction rate can be explained by that the reaction is self catalyzed. So if the reaction is allowed to proceed without removing the catalyst the reaction rate is increased. The mixture of chemicals used must be kept the same as the reaction rate changes dramatically as seen in [68]. As the nitride mask breaks down the amount of silicon available for the reaction is largely increased again raising the etch rate. Underneath the polymer film no defects were seen. Defects away from the channel or next to it can be avoided in the sensor as you can focus the laser beam onto the channel thereby bypassing those unwanted features. The silicon wafers were tested in a MIBD setup and a clearly visible interference pattern was observed. The wafers were then shipped off to Dandisc, who electroplated the wafers to make nickel replicas.

3.3 Alternative procedures for making circular structures

Copper wire imprint

A copper wire was used to make imprints in poly(methyl methacrylate)(PMMA) also known as Plexiglas. Previously a glass wire has been used for making integrated wave guides, by Ulrich *et al.*[70]. The diameter of the copper wire was determined with a micrometer and optical microscope. The wire was straighten by pulling the wire making it possible to fabricate straight channels by the imprint. The diameter of the used wire was found to be 100 μm in diameter. In order not to press the wire completely into the PMMA sample, a wire holder was made. The wire should be pressed 50 microns into the sample so a holder having 50 μm deep channels were made in PDMS. The PMMA samples were 5 by 5 cm and 1 cm thick and the load was $\sim$ 1.5 kg. The wires were placed in the wire holder and then placed on top of the PMMA sample, as seen in figure 34. The entire sample was placed in a preheated oven for 10 minutes at 110 °C, with the preheated load (block of iron) on top. The embedded wires was removed from the sample by etching away the copper. The etch is a solution normally used for etching circuit boards, fine etch crystals (sodium persulfate), Lautronics (Lyngby, DK).

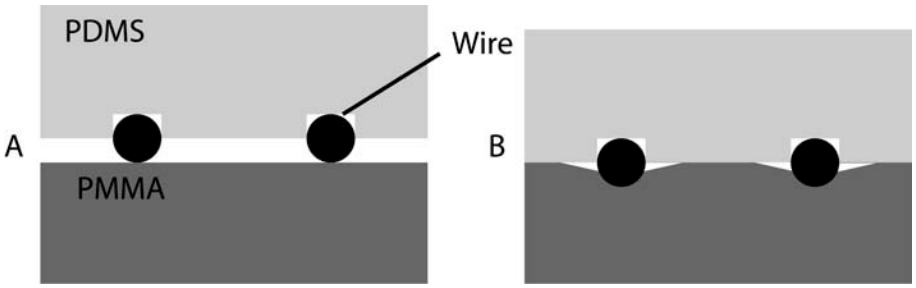

Figure 34. Diagram of the embossing process. A PDMS holder is loaded with the copper wires. The PDMS holder ensures that the wires are kept in the desired pattern (A) and keeping the wire from being pressed completely into the PMMA (B). A large area if the PMMA surface is effected by the imprint, also indicated in (B), as the surface surrounding the wire is pressed down as well. In a completed micro flow setup, this would lead to leaks, ruining the MIBD measurements.

The imprint was close to circular in the area around the wire, but the entire surface had been deformed as well. The material underneath the wire has to be removed and it is then pressing on the material next to the channel resulting in a down bending top surface making the imprint appear much larger than the width of the copper wire. This has also been reported in the literature, where a 25 μm wire resulted in a 168 μm wide impact area[71]. The replication of the copper wire was so good that the morphology of the metal crystals were copied into the PMMA, resulting in a noisy fringe pattern, where a speckle pattern was dominating the scattered light.

Laser ablation directly in plastic

A method of writing the desired micro flow system directly in plastic has been tested. The writing was done by Lennart Bitsch, MIC, Technical University of Denmark. It was done with their CO_2–laser writing system. A description of the system and the ablation process is found in [72]. A PDMS replica has been made of the fabricated channels. The shape of the grooves is seen in figure 35.

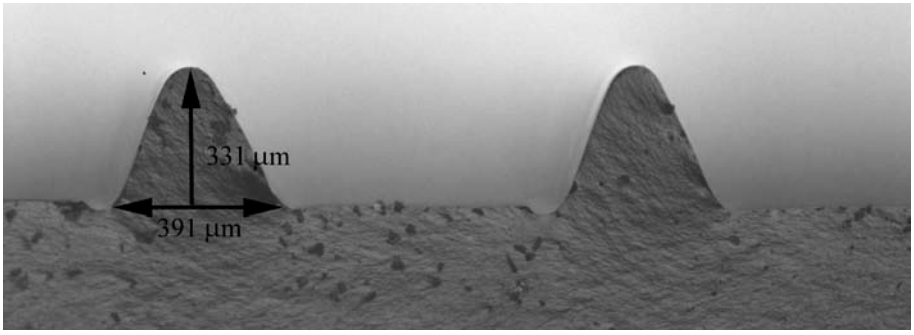

Figure 35. A V-shaped groove has been produced by laser ablation of a polymer sample. The opening width is 391 μm *and the depth is* 331 μm*. A PDMS replica has been made to produce a cross-sectional view of the produced structures. The size and the shape of the structure is not the desired semicircular structure with a* 100 μm *diameter.*

The shape and the size of the structures is not what was intended. The shape is a V-groove or Gaussian, and not semicircular. The samples was tested in a MIBD setup. When the laser impinged on the structures only speckle scatter was present. It was not possible to recognize a fringe pattern, that could be used for refractive index measurement. In [72] is also discussed the surface appearance after ablation. Some resolidified PMMA may be present at the top of the structure. These droplets have been reported as being $\sim$ 15 μm in diameter. Where the overall surface roughness is to be 1–2 μm, which is comparable with the wavelength used in the MIBD setup.

Laser ablation in silicon

This work was a collaborative method test between Risø National Laboratory and Danish Technological Institute (DTI), Christian B. Nielsen. DTI has performed the laser ablation and Risø has performed the chemical polishing and the analysis of the samples.

The hypothesis is to ablate a structure in the silicon, which is close to the desired shape, chemical polishing afterwards will lead to smooth surfaces of semi circular geometry of the grooves in the silicon.

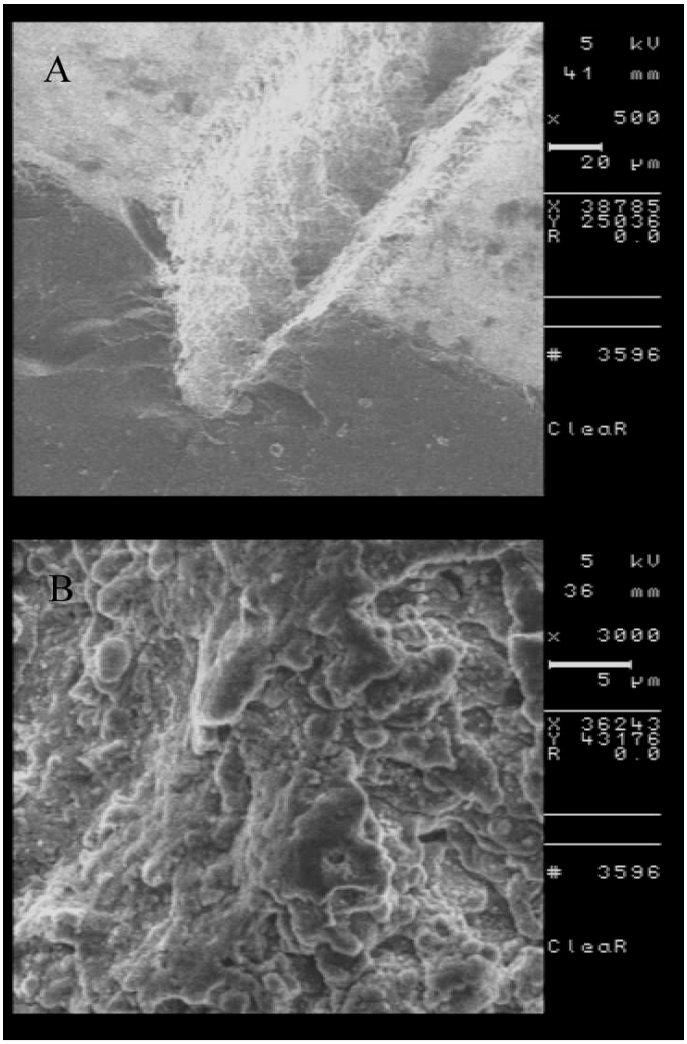

Figure 36. A V-shaped groove has been produced by laser ablation of the silicon surface. The opening width is ∼50 µm and the depth the same. The sample seen in (A) has been cleaved across the structure and tilted 45° in the SEM. In (B) is shown a close up of the surface and features range from some hundreds of nanometer to several microns.

A number of silicon samples were ablated with a femto second laser in a f–shaped design. This shape both has a curve, crossing and long straight lines. The width of the openings were approximately 50 μm and the samples were cut to different depths. Four depths on each sample ranging from 20, 50, 100 and 200 μm. At first the geometry was to be verified by making a PDMS replica. Even with HMDS as slip layer the surface was so rough, that the PDMS could not be

released from the grooves, hence only SEM pictures was obtained to obtain geometry and surface information. In figure 36 is seen an ablated groove(A) and the surface structure in (B). The initial shape was not as close to circular as expected as it is more in the shape of a V. On several positions the ablation has removed the silicon resulting in deep holes, resulting in an very nonuniform channel bottom.

The chemical polishing was performed with a mixture of hydrofluoric acid and nitric acid. The solution used was 15.5 mL HF (49.25%) and 26.4 ml HNO_3 (69.51%). Before polishing the solution was "initiated" by adding a tiny piece of silicon. The polishing procedure is a version of the HNA–etch[68], and is self catalytic, by adding the silicon the polishing will begin immediately when the sample is introduced to the solution. Samples were polished in the acid mix for 30, 60 and 90 seconds while the system was sonicated. After 30 seconds the surface

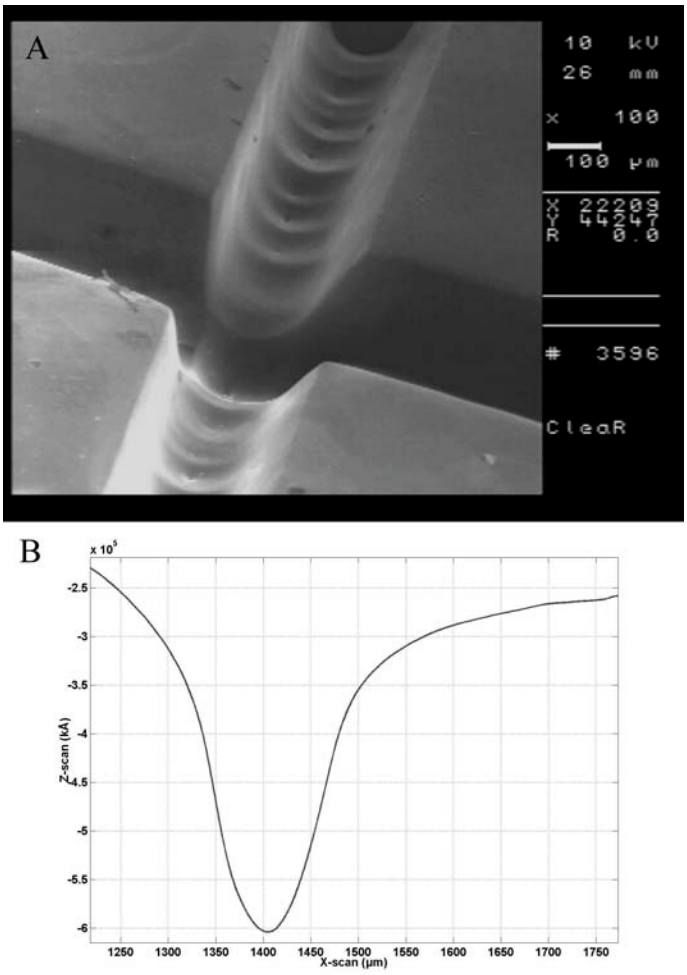

Figure 37. After polishing treatment almost all spikes have been removed. Those few ones left are small (∼1 µm). When investigating the larger area of the surface the roughness is less than 100 nm, limited by the SEM resolution. The ablated holes are visible in this crossing part of the structure. They are to big to be removed by this polishing procedure. The sample in (A) has been exposed to the acid mix for 30 seconds. The same sample is in (B) shown by its profile obtained by a Dektak profilometer. The top edges is rounded as well as the bottom.

is specular, and the surface roughness has been reduced significantly. In figure 37 (A) is seen the structure after the polishing treatment.

The deep holes ablated by the laser is clearly still visible and will be present at even longer polishing times than the tested 90 seconds. After 90 seconds the wafer is etched trough the backside. After the polishing treatment for 30 seconds the surface roughness is less than 100 nm with few defects roughly 1 micron in diameter. The bottom of the groove is curved in shape, but the sidewalls are not. The actual curvature is difficult to conclude by the SEM images. A PDMS replica was not possible since the samples after polishing were to thin and fragile. By polishing longer the effect of the ablated holes was reduced but could not be removed before the samples were etched all the way through.

The surface roughness is on an acceptable level after the polishing treatment ($\sim \frac{\lambda}{6}$) which is an improvement of approximately 50 compared to the ablation alone. It has not been possible to remove the effect of the ablation were the center of the beam results in deeper holes. The shape of the structure has been difficult to establish. But the shape is more curved after etching than the V-groove produced by the ablation. A mask less etch is not usable to fabricate the master tool because on the macroscopic level irregularities produced covering the entire surface. This results in a top surface that is not flat and eventually will be troublesome to seal in a chip. By performing the polishing treatment without a mask the top corners of the ablated structures are rounded also, as seen in figure 37 (B). It is fully expectable as it is attempted to remove roughnesses (very sharp edges) and at the same time have the top edges of the groove (less sharp edges). Applying a mask to the surface will improve the edges in the top of the channels.

Micro machining

An method of using a micro machining tool has been tested to fabricate circular structures. The machine used is an AutoGrav III, from AutoGrav (Fischbach, Germany). This method has the advantage of being relatively fast and user friendly. By user friendly is thought of as the entire processing can be done mainly on PC with very little human interference. The micro channel design is drawn directly in Corel Draw from where it is exported to the micro machining tool via floppy disk. For these tests polycarbonate has been used as the polymer platform. The structures where to be directly made into a polymer, which still has the possibility to be electroplated if necessary. CD-rom disks were used as source of polycarbonate. It is a cheap source of well defined flat plastic. The CD-rom is placed in the drilling bench and clamped into position. The tip of the drilling bit was aligned in all three dimensions, so that it just touched the polymer surface. All coordinates are stored in the PC controlling the machining tool. For these test a 2D-plot was used, more complex 3D plots are also possible. The movement in the x-y plane was set to a speed of .2 to 2 mm/s. The different speed was to move slowly enough, so that the cutting edge passed the surface several times in almost the same spot. Thereby the cutaway material could be removed. The z-direction resulted in the depth of the structure. Drilling bits with round heads were used to make the structure, with radius of 50 to 100 μm. To keep the polymer from melting or burning caused by the friction, the drilling head was air cooled. The best results was obtained with

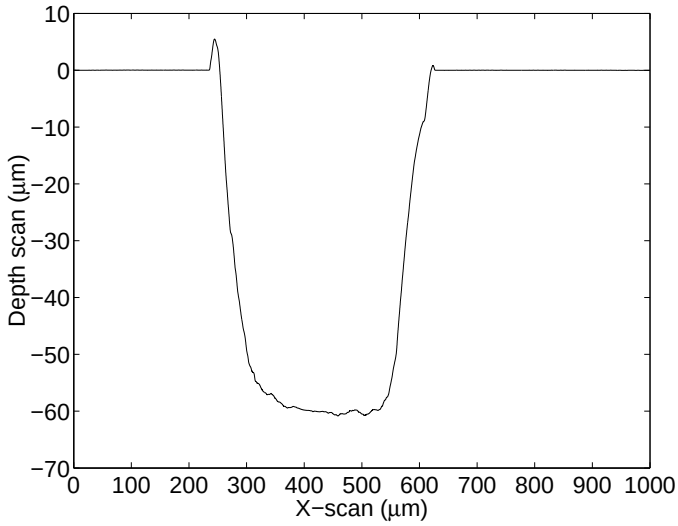

Figure 38. Profile of surface after micro machining. The drilling bit had a rounded head with a radius of 50 μm. *The x-y movement of the drilling head was set to .2 mm/s and the depth is 60* μm. *The machined structure is wider and has a flatten part in the center of the structure.*

highest cooling and the slowest x-y movement. In figure 38 is seen a cross sectional view of the micro machined structure. The width of the structure is larger than the desired 100 μm. The shape is mainly distorted by warbling in the drilling head. It has not been possible to overcome this issue. The drilling speed has been changed to look for different vibration frequencies in the system and the drilling bit has been shortened to get the head closer to the fixation point.

Micro grinding of capillary tubes

Objects are available with well–defined circular geometry and proper size. As has been mentioned before copper wiring is possible to find with a 100 μm diameter. From Polymicro Technologies (AZ, US) fused silica tubes with an inner diameter of 100 μm have been purchased. In order to utilize the smooth glass surface on the inside of the capillary, the idea is to grind/polish away half the tube to end up with a semicircular structure. This method has been tested with both copper wire and capillaries.

Copper wires were embedded in epoxy on a glass plate. The epoxy used was SU8 photoresist, which was spin coated on the glass to a thickness of 50 μm. When the wires had been placed by hand in the epoxy, more epoxy were added on top to give the sample a thickness of $\sim$ 200 μm. The sample was given time (24 hours) for the solvent in the photoresist to evaporate at room temperature. Then exposed to UV light and baked in an oven as described by the distributor. The sample was bonded to a sample holder via a bonding jig (Logitech Ltd., Scotland). The bonding was done by using hot melted wax and the sample was kept in the jig for 1 hour before usage. In the mean time the polishing machine, Logitech PM5 (Logitech Ltd. Scotland), was prepared. The iron polishing wheel was made flat with a parallelization jig for 30 minutes at 40 rpm with 9 μm Al_2O_3 particles in water as abrasive, which removes rust from the surfaces and at the same time smoothing it. This was done in lapping mode, where the jig moves across the polishing wheel continuously, while rotating, ensuring complete coverage of the iron surface. The bonded sample was attached to the automated polishing head. A data link is in connection with a digitized micrometer, so the grinding progress can be monitored and a fix height difference may be set. The grinding speed is controlled by rotation speed of the polishing well, the size of the particles in the abrasive and the force provided from the polishing head. The load of the polishing head is changed by adjusting a spring, usually these runs where done with full load, which is 1.8 kg (the weight of the polishing head).

The stop criteria for the copper wire was to stop the grinding 50 μm after the first appearance of the wire through the epoxy. This was done by monitoring the micrometer on the polishing head and by using an optical micro scope to measure the width of the wire. It was realized that it was not possible to place the wires uniformly into the epoxy as the width altered along the length of the wire. When approximately 75 % of the wire had the desired width the grinding was stopped. The copper wire was etched away from the sample with the copper etch mentioned above. After removal of the copper wire, PDMS replicas were made to verify the geometry of the fabricated structures. The structure is circular in shape, but as it is seen in figure 39(A) the grinding process was not stopped exactly half way through the copper wire. The surface structure of the copper wire was transferred to the epoxy surface, see figure 39(B), resulting in a dominating speckle pattern when illuminating the structure with a laser.

Before placing the capillary on the glass substrate a thin layer of glue was applied to the surface. Then the capillary was firmly placed on the surface and fixated until the glue hardened. Thereby the capillaries should not be repositioned when the epoxy was applied afterwards. The largest thickness of the sample was measured to be 420 μm. So 325 μm of material needed to be removed to be half way through the capillary. The sample dimensions has been sketched in figure 40(A). The sample was ground thinner with Al_2O_3–abrasive (9 μm) the first

112 μm at full polishing head load at 40 rpm. This resulted in a grinding speed of 8 μm/h. The abrasive was changed to an 1 μm particle size of Al_2O_3. In between the two kinds of abrasives, the sample, the polishing head and the grinding wheel had to be thoroughly washed and cleaned. Any big particles left would result in scratches instead of an even smooth grinding/polishing. The smaller particles size used the better surface smoothness. The next 140 μm was ground down with a speed of 4 μm/h. The grinding process was stopped and the polishing process started. The sample was polished in a diamond-dust slurry. The particle size is less than one micron. The diamond was suspended in glycerol. Again the integrated micrometer could not be used for monitoring the polishing progress. The process was monitored by measuring the width of the capillary in a microscope. In figure 40(B) is a micrograph of the polished sample, showing the opened capillary. The experiment was not stopped perfectly half way through as can be seen in figure 40(C). The surface was still smooth and shinny inside the capillary. The final polishing step unfortunately left diamond residue inside the capillary, figure 40(D). These residue plugs could not be removed from the capillary.

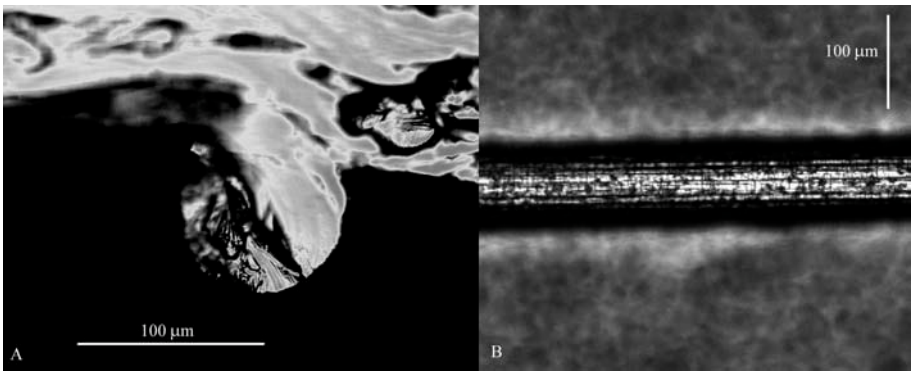

Figure 39. The geometry of the channel is shown in (A) as a cross sectional view of a PDMS replica after the copper wires have been etched away. The geometry of the structure is circular in shape, even though the replication and the cleavage of the PDMS is not perfect, it is seen that the geometry is not perfect. A top view of the structure is seen in (B), the grinding was stopped when the width of the wire was 100 µm, followed by etching. The focus of the confocal microscope image is placed on the bottom of the structure. The surface morphology of the copper wire has been transferred into the epoxy. This surface produced a speckle pattern when impinged by a laser.

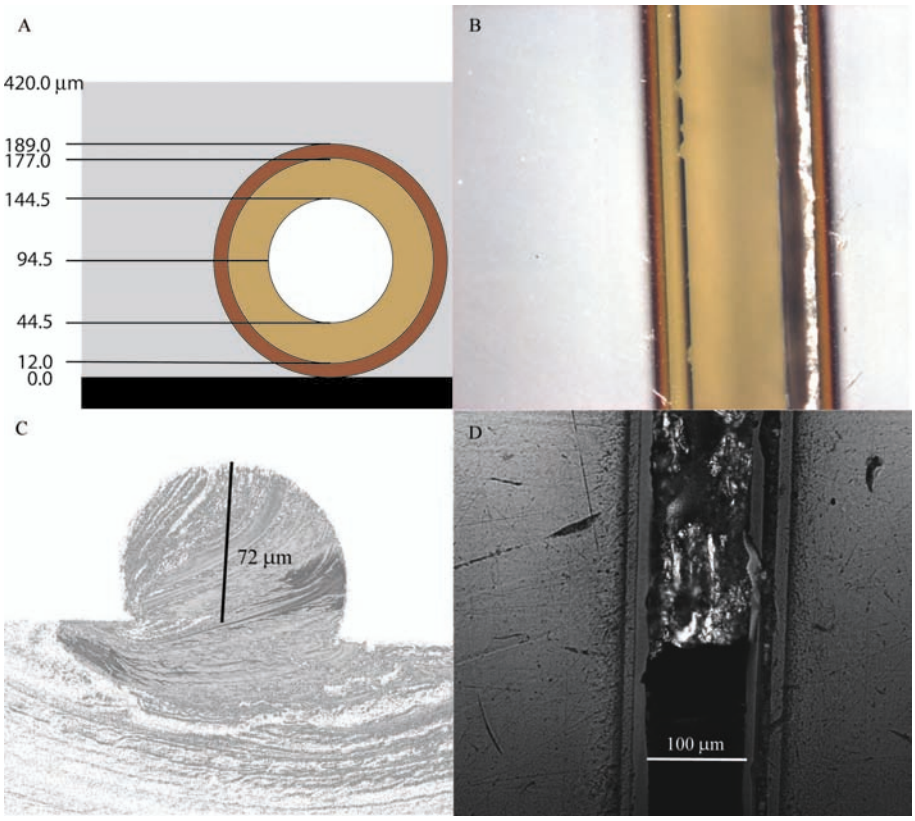

Figure 40. The capillary sample has been drawn in a cross-sectional view in (A). The total thickness of the sample is 420 *µm, which is the epoxy applied (grey) to fixate the capillaries during the process. The capillary used has the polyimide cladding (dark brown) coating the fused silica tube (light brown). The dimensions used are those provided by Polymicro Technologies. In (B) is a micrograph of a capillary after polishing, top view. The color scheme is similar to the one used in (A). The grinding/polishing procedure has damaged parts of the capillary wall, as tiny flakes has been removed. The surface quality of the glass tubes are intact as the slurry only polishes on the touching surface. A PDMS replica of the obtained structure is seen in (C). The geometry of the tube is clearly transferred to the sample. It has not been possible to stop the polishing process with better precision than shown in (C). The online micrometer cannot be used when polishing occurs with the diamond slurry. Another effect of the diamond slurry is shown in (D), as diamond residue is still present in the tube. The diamond residue could not be removed from the sample eventually blocking the micro flow channel.*

The geometry of the ground down capillary was perfect but still the procedure would need some improvement to be acceptable. To overcome the problem of stopping the polishing process at a better place, pillars of SU8 was placed on the sample and the top coated with Gold. As the Gold would be removed by the polishing process, the height would then be well– known. This step did not improve the process significantly. The diamond dust could not be removed from the capillary, eventually blocking the micro flow channel. PDMS replicas was made to see if the hardened silicone could remove the diamond dust as the replica was removed from the sample. A fundamental drawback of this approach is the problem of crossing channels. In micro fluidic flow chips a big advantage compared to capillaries is the ability to introduce one sample flow into another. This approach would need further back processing for this mixing to be achievable.

Photoresist reflow

A growing field in micro optics is the fabrication of micro lenses for integrated optics[73, 74] and the display industry[75]. Although their geometry is often spherical, or curvature in two dimensions, the fabrication techniques used are still of interest for this work, especially photoresist reflow[76, 77]. Usually only the top part of the sphere is used to make up the lens[78], but entire hemispheres has been fabricated by Choi*et al.*[79]. The method is shown in figure 41.

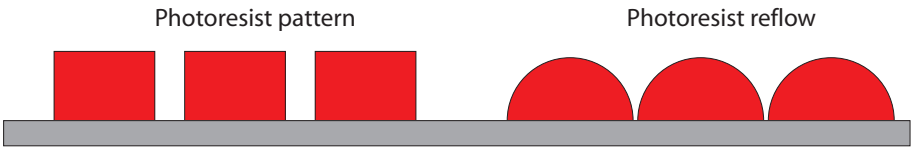

Figure 41. A photoresist pattern is deposited on a substrate by standard photolithography techniques. After development, the sample is heated. As the photoresist melts, gravity and surface tension shapes the soft resist into a curved shape, ideally semicircular.

Preliminary work was done at Risø involving photoresist reflow to fabricate micro lenses. The work was performed by Jørgen Stubager, OPL, Henrik Pedersen, OPL, and Lene Knudsen, OPL/AFM. To summarize their procedures and results: Photoresist, ma-P 100(Microresist, Germany)and S1828 (Shipley, US), were spin coated onto substrates to give the height of the pillars fabricated via UV exposure through a photolithography mask. The results were acceptable up until 8 μm for S1828 and 36 μm for ma-P 100. With thicknesses above 30 μm the heating of the sample resulted in boiling of the photoresist solvent. Several heating attempts were made using laboratory oven, hot plate and IR heating lamp. No reproducible shapes was obtained and the project was stopped attempting to go further up in dimensions. The subject of this thesis would require the photoresist thickness to be at least twice that height to end up with 50 μm radius semicircular shaped features. If these preliminary results had been more successful, I would have been more encouraged to pursue this method of making the micro structures.

3.4 Summary

Several fabrication methods have been tested for their ability to fabricate semicircular structures in a substrate usable for electroplating. Wet etching in the substrate has been most successful. When etching in fused silica the mask has been developed to remove pinholes and withstand the chemical conditions when trying to etch so deep into the substrate as desired (+50μm). The resulting shape became trapezoidal. Etching in silicon provided semicircular channels usable to be further processed to become flow chips used as an optical sensor. The surface roughness is a critical issue as speckle lowers the modulation depth of the signal used in the sensor. With the polishing etch consisting of only HF and HNO_3, used on the laser ablated silicon samples, it has been shown how to make smooth surfaces with surface roughness less than 100 nm. It has been accomplished to develop the tools needed for making semicircular channels with a smooth surface. The further process and usage of the structures made in silicon with the HNA etch is discussed below.

4 Absolute refractive index determination by micro interferometric backscatter detection

Rapid monitoring and detection of ultra small volume samples are in great demand[80]. Two major areas are environmental monitoring [81] and point of care disease detection [82, 83]. This demand covers a huge range of applications, from drinking water quality [84] and food quality [85] to determination of glucose [86] and urea [87]. Several detection techniques have the capability to perform fast measurements on small amounts of analyte. Well-established techniques include electrochemistry [2, 88], mass spectrometry [89, 90, 91] and optical detection [10, 13]. Not all are equally fast since sample preparation often is extensive and requires time-consuming steps such as chemical tagging of molecules [15]. Using structures with varying complexity fabricated to guide the samples to the detector [92, 93] systems can be scaled down so that the required amount of analyte as well as size and cost of the entire system is reduced , thus the miniaturized total analysis system [94, 95].

Simple optical systems are available to perform sensitive measurements on small volumes [96]. One analytical approach, micro interferometric backscatter detection (MIBD), relies on the observation that coherent light impinging on a cylindrically shaped object produces a highly modulated interference pattern. MIBD analyzes reflections from a capillary tube filled with the liquid targeted for the refractive index (RI) measurement. The technique was first used and described by Bornhop et al. [49, 26], and has previously been shown [30] to be capable of measuring changes in refractive index of liquids on the order of 10^{-7}. The MIBD technique is a simple and universal method of detecting refractive index changes in small volumes, having been used to monitor changes in concentrations of solutes [29], flow rates[97] and temperature [28], all conducted in nanoliter volumes. Systems of similar geometrical configurations as the MIBD scheme has previously been modeled by wave theory [35, 36, 37] and ray tracing [38]. The models have been applied to optical fibres, determining the dimensions and absolute refractive index [98]. Thereby considering other phenomena than those observed in the MIBD scheme.

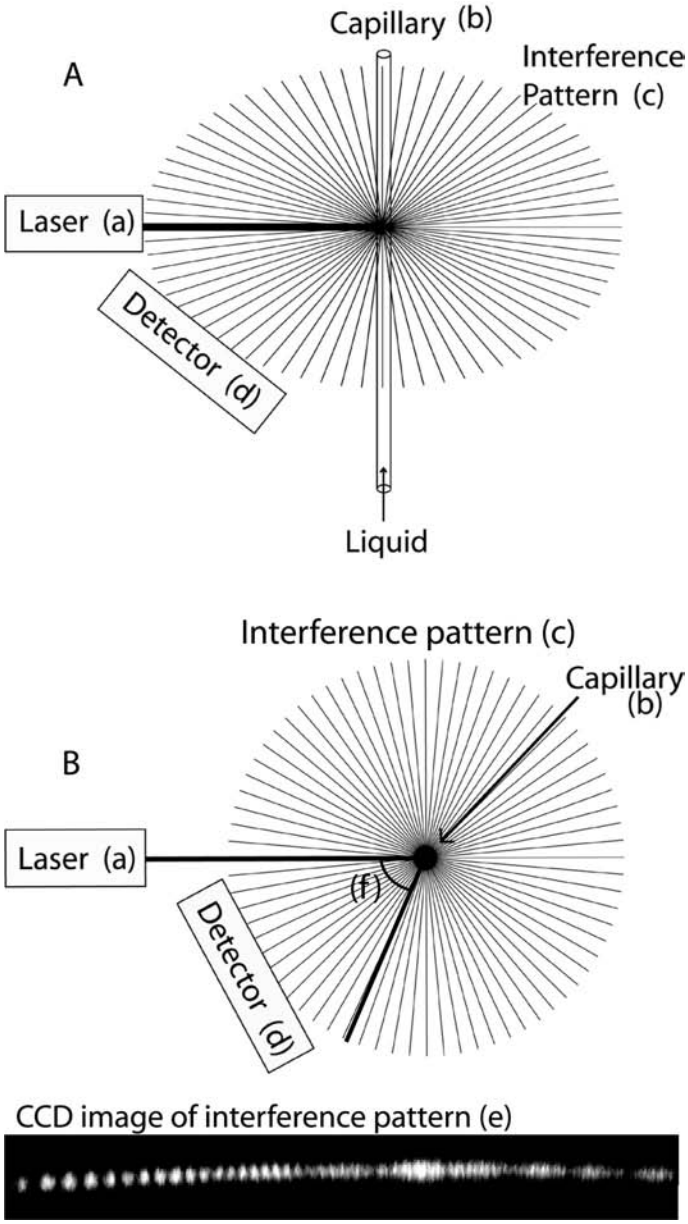

Figure 42. Schematic view of the experimental setup seen isometric (A) and from the top (B). The setup consists of a laser (a) impinging on a capillary (b) tube filled with a liquid, creating an interference pattern (c) in the plane perpendicular to the capillary tube. The backscattered light is then collected using a detector (d). A CCD picture of an interference pattern is seen in (e). The backscatter angle is shown (f).

The MIBD scheme is shown in figure 42. The system consists of a laser (a) that impinges its beam on a capillary tube (b) filled with a liquid of which one wants to measure refractive index, thereby creating an interference pattern (c). This interference pattern, which changes with changes in the liquids RI, is then measured using a detector (d). A typically observed interference pattern in the backscattered direction is seen in (e).

The demonstrated sensitivity of 10^{-7} is reached by following the displacement of the individual light fringes of the interference pattern within 0-3 angular degrees [30] from the directly backscattered direction, as the liquid RI changes. The fringe pattern is periodical in refractive index space with a period of the order of 10^{-3}. This limits the dynamic measurement range to about three decades, which for many purposes requires additional knowledge about the absolute value of the refractive index. As the measurement monitors a displacement of the fringe pattern, it is inherently differential, requiring both calibration for the absolute level of the refractive index as well as for the differential factor. This factor describes the fringe movement corresponding to a given change in the refractive index.

Here, we demonstrate experimentally that the dynamic range of the MIBD system may be increased. Furthermore the absolute refractive index, and thereby the absolute analyte concentration, may be determined. We have tested this observation for two model analytes over a wide concentration range, demonstrating the universal application of our methodology. The observed phenomena may be explained by taking into account variations of the interference pattern with changing refractive index other than those previously considered. The dynamic range is increased without compromising the high differential sensitivity previously reported [30]. The theoretical description of the MIBD scheme has been improved to include an extended ray tracing model that matches the range in angular and refractive index space of the experiments, thus providing novel information about the structure of the backscattered interference pattern. In contrast to the previously proposed model [39], this model is capable of explaining all frequency components that appear in the interference pattern. Furthermore, the model predicts an abrupt change in the intensity of the backscattered light, which depends uniquely on the refractive index of the probed liquid that has been experimentally confirmed. The improved understanding of the MIBD system is used to propose two approaches to an absolute measurement of the refractive index of liquids in the refractive index range between water (1.33) and glass (1.50). One approach is based on the measurement of the depth of modulation of the interference pattern caused by variations in the Fresnel coefficients. The second approach is based on the measurement of the total internal reflection within the capillary. We focus on the latter approach, as it appears most promising experimentally.

4.1 Experimental MIBD setup

The MIBD experiments were done by mounting the capillary on a translation stage and directing a HeNe laser beam so that it impinges perpendicularly onto the capillary. The backscattered light was collected using a screen and a CCD camera (C4742-95, Hamamatsu). The requirements for the laser are a coherence length of at least twice the diameter of the capillary and a wavelength at which the capillary is transparent. The requirements for the detector are one-dimensional high spatial resolution and an adequate intensity resolution, depending on the application, as will be seen later. Passive temperature control consisted of a large thermal reservoir (an aluminum block) thermally connected to the capillary was used to stabilize temperature. Temperature fluctuations affect the refractive index of the liquid substantially. Active temperature control is only needed if the detection of changes in refractive index of less than 10^{-5} is required. In this work passive temperature stabilization is adequate, as the refractive index fluctuations in the system caused by temperature fluctuations in our controlled environment are on the order of 10^{-5}, corresponding to 0.1 $^{\circ}C$ temperature fluctuations for water. The capillaries used in the experiments were purchased from Polymicro Technologies (AZ, US). The dimensions of the two capillaries employed were 100 μm inner diameter (ID), 165 μm outer diameter (OD) with a 12 μm thick polyimid coating (TSP100170) and 542 μm ID, 673 μ OD with a 24 μ thick polyimid coating (TSP530660), respectively. The refractive index was changed, from 1.33 to 1.5, by using aqueous solutions of either sucrose (Sigma Chemicals Company) or NaSCN (Merck). The analytes were chosen to obtain a large refractive index change in our model experiments and at the same time to maintain a low viscosity of the probed liquid. The RI of the solutions was confirmed with a commercial refractometer (RL3, Polskie Zaklady Optyczne, Warsaw) immediately after the sample had been injected into the capillary.

4.2 Interference pattern analysis

A typical pattern is shown in figure 43A, with corresponding line profile of the intensity shown in figure 43C. In figure 43B two of the fringes in 43A is enlarged,

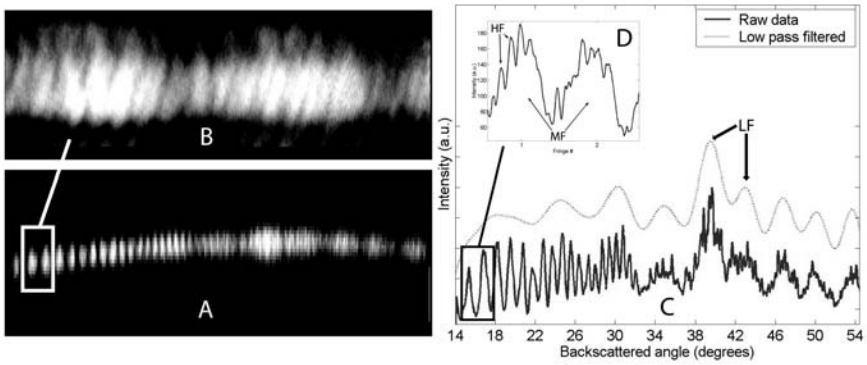

Figure 43. CCD camera images of a typical MIBD interference pattern (A, B) and corresponding line profiles (C, D). A and C shows both low frequency (LF) and medium frequency (MF) variations of the light intensity. The visual appearance is enhanced by low pass (Fourier) filtering of the raw data. The raw data and the low pass filtered data have been offset for clarity. By magnifying the medium frequency variations (B, D) a high frequency (HF) component is seen. This high frequency component does not move as the refractive index of the liquid is changed.

showing a finer structure. A line profile of the intensity from 43B is seen in 43D. It is seen that the intensity pattern contains multiple frequency components. The period of the fringe pattern corresponding to medium frequency (MF) components is shown in figure 43D. Similarly, the period of the fringe pattern corresponding to low frequency (LF) components is shown in figure 43C. In the following, we shall refer to these frequency components as frequencies. Under certain circumstances one is able to observe a faster varying component of the intensity profile, here denoted high frequency (HF) variations, see figure 43B and 43D. As one increases the refractive index of the liquid in the capillary the intensity profile shifts towards lower backscatter angles, see figure 44. However, the high frequency variation component is spatially fixed and does not move as one changes the refractive index in accordance with previous observations[99]. By investigating the experimentally observed frequencies of the fringe pattern, it may be shown by geometrical considerations that the distance between the origin points of the interfering rays (points a through f in figure 3) on the capillary are approximately 5 to 10 times larger in the high frequency case than in the medium frequency case. By using geometrical considerations it is possible to calculate the distance between origins of the interfering rays for all frequency components. We found that the distance required to produce the high frequency variations is on the order of the capillary diameter. This indicates that the rays responsible for this high frequency variation are scattered from the edges of the capillary, thereby not being affected by the liquid within the capillary. This hypothesis fits the observed behavior well, since the high frequency component is not observed to be displaced as one changes the refractive index of the liquid in the capillary. Since this component does not move with changing refractive index, and thus cannot be used in a refractive index determination, it will not be considered further in this work, neither experimentally nor in the modeling of the system.

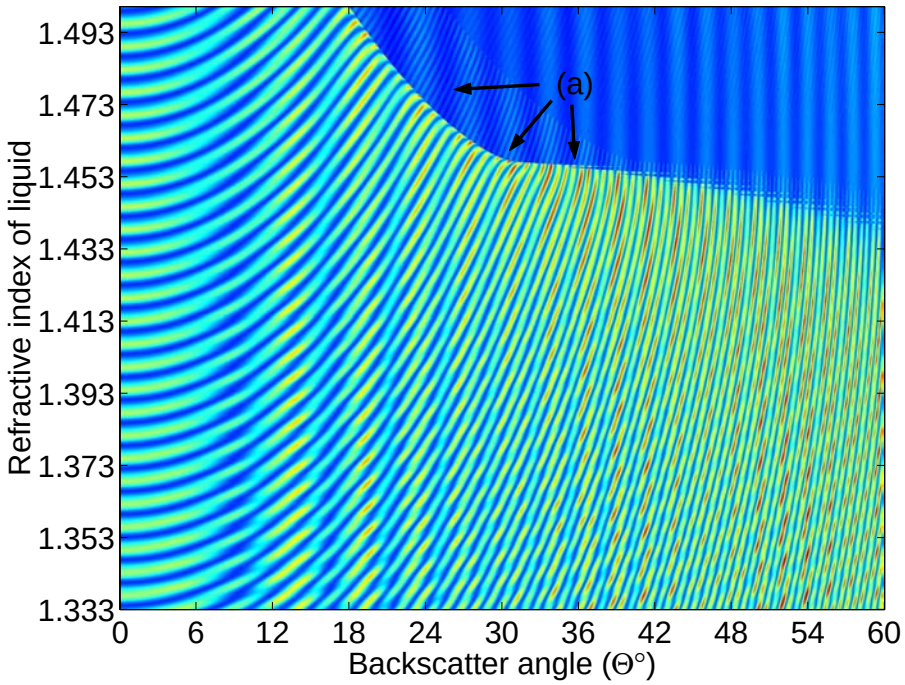

Figure 44. Model predictions of the angle dependent variations in the backscattered light intensity in the plane perpendicular to the capillary tube have been compiled in this plot by stacking line plots for closely spaced liquid refractive indices into a two-dimensional overview of the scattering behavior. This plot corresponds to 1643 liquids with different refractive indices calculated for a 100 *μm ID/*165 *μm OD/* 12 *μm coating capillary. The colormap represents the light intensity in arbitrary units. Bands of light (fringes) move towards larger backscattered angles as the refractive index is increased. Overlaying vertical band structures of higher and lower light intensity are seen. These structures do not move as the refractive index is changed. An abrupt change in the intensity level (a) is seen moving towards lower backscattering angles for refractive indices of the liquid above 1.45.*

The low frequency component is spatially stationary as well, since this component is caused by the common interference between the three rays reflected from the front of the capillary (points a through c in figure 3), as well as the common interference between the three rays reflected from the back of the capillary (points d through f in figure 3). The displacement of this component is zero for the part originating from the front, since these rays do not traverse the liquid and thus experience the same optical path length by different refractive indices of the liquid. For the second part the displacement is small, because all three rays experience almost the same change in optical path length traversed relative to each other.

In contrast to the high and low frequency components, respectively, the medium frequency component originates from the interference between rays reflected at the front (points a to c in figure 3), and at the back of the capillary (points d through f in figure 3). These rays experience a large relative change in optical path length traversed, as the rays from the front do not experience a change in optical path length whereas the rays reflected from the back do. It is this relative change in the optical path length between different paths that causes the movement of the medium frequency component of the interference pattern, yielding the ultra-high sensitivity to fluid RI.

4.3 Comparison of experiments and model

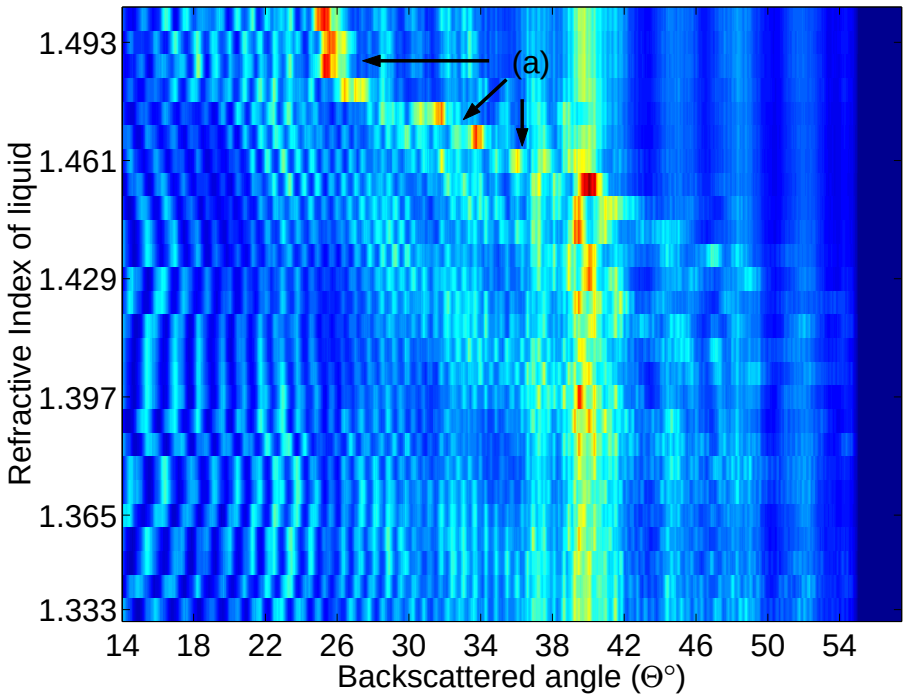

Figure 45. Experimentally obtained data from a 100 μm *ID/*165 μm *OD/* 12 μm *coating capillary showing the low frequency variations of the interference pattern as the refractive index is changed. The analyte is NaSCN. 25 measurements of the interference pattern have been made, each at different refractive index. At each refractive index level a line profile of the interference pattern has been obtained. These fringes do not appear to form continuous bands in the vertical refractive index dependent direction due to the large change in refractive index between measurements. An abrupt change in the intensity (a) is seen for high refractive indices (above 1.43), which moves towards lower backscattering angles for increasing refractive index.*

The results from the model are plotted in figures 44 as function of backscatter angle and refractive index of the liquid for a 100 μm ID/165 μm OD/ 12 μm coating capillary. Both model and experiment, see figure 45 shows an abrupt change in intensity at large backscattering angles. This abrupt change in intensity is somewhat displaced in the modeled results compared to the experimental results, but it is within experimental error. Experimentally, movement of this abrupt change in intensity qualitatively agrees with our modeling of the MIBD system, while the model does not fit experiment quantitatively. The predictions of the model have been used to select the proper capillary dimensions for our applications of the MIBD technique.

4.4 Absolute measurement of refractive index based on *Fresnel coefficients*

Even though the low frequency variations remain stationary in terms of backscattered detection angles, their intensity changes as the refractive index of the liquid changes. Since the intensity of the rays are in part determined by the Fresnel coefficients of the surface of reflection, it is possible to configure the system in such a way that the intensity of the low frequency component can be used as a measure for the refractive index on a coarser scale. This may be done by either index matching the coating and the glass tubing, thereby eliminating the reflection from the surface at the interface of the coating and glass (points b and e in figure 3) or by stripping the coating off the capillary. The low frequency component is then caused by interference between two rays; the ray reflected by the air-coating (points a and f in figure 3) or air-glass interface (points b and e if the coating is removed) and the ray reflected from the glass-liquid interface (points c and d in figure 3). Since the intensity of this last ray is determined by the Fresnel coefficients of this surface consisting of glass with constant refractive index and the liquid to be probed, the absolute value of the refractive index of the liquid may be calculated from the relative intensity of the two rays, which is given by the depth of modulation of the low frequency component. This is only possible if the refractive index of the air, glass and coating is known. This approach has only been theoretically examined due to lack of intensity resolution (8-bit) of the CCD camera. If one wants to measure depth of modulation to a certain degree, one needs at least this degree of intensity resolution in the detection system. Since our CCD camera only has 255 intensity levels we would not be able to acquire more refractive index resolution than the difference in refractive index between air and glass divided by the number of detectable intensity levels, which corresponds to $5 \cdot 10^{-3}$.

4.5 Absolute measurement of refractive index based on *total internal reflection*

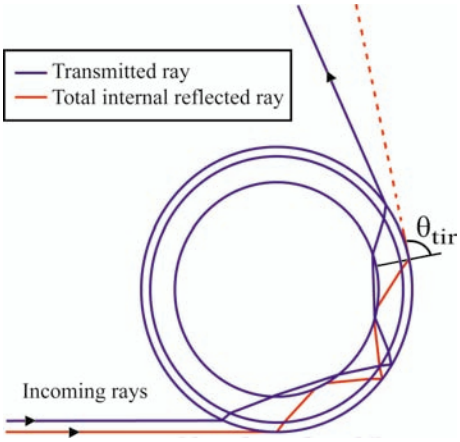

Figure 46. Schematic Cross-sectional view of the capillary. When the angle Θ_{tir} *approaches* $90°$*, the intensity of the transmitted light decreases sharply due to total internal reflection. Blue line shows a ray being transmitted through the system, whereas the red line shows the path of the ray being total internally reflected at the glass-air interface (*$\Theta_{tir} = 90°$*). The outgoing dotted line marks the highest angle at which single reflected rays may be backscattered.*

The model predicts an abrupt change in intensity moving towards lower backscatter angles as the refractive index of the liquid approaches the one of the glass tubing, see line marked by (a) in figure 44. This feature of the interference pattern is also observed experimentally, see (a) in figure 45, and agrees with the predicted feature in position- refractive index space within experimental error. A feature similar to this has been reported for optical glass fibers[38]. However optical fibers have a different optical configuration, therefore the scattering mechanisms responsible for the production of the fringe pattern are different. In the case of optical glass fibers the mechanism responsible is grazing of a certain ray on the core of the fiber being dependent of the inner radius of the glass fiber. In MIBD the mechanism is total internal reflection in the wall of the capillary, which is dependent on the refractive index of the liquid in the capillary. The main source of error in the modeling of the MIBD system is the dimensions of the capillary, which has an uncertainty of 6 μm for the 100 μm ID/165 μm OD/ 12 μm coating capillary according to the manufacturer. The way of determining the absolute value of refractive index on a coarser scale is to look at the abrupt change in intensity of the pattern. Both the model and the experiment show an abrupt change in light intensity at higher backscatter angles, and the position of this change varies with refractive index. Using a 100 μm ID/165 μm OD capillary this change takes place at refractive indices 1.40 to 1.50, which is useful for measurements using organic solvents. Most dilute aqueous solutions of biological relevance have refractive indices in the range from 1.33 to 1.40, in general using our model, one is able to calculate the dimensions of the capillary required to make the abrupt intensity change occur in position/refractive index space at refractive indices above 1.33 and at backscattering angles inside our measurement range.

The model shows that the abrupt change in intensity occurs at lower angles and at lower refractive indices for capillaries with a higher ratio between inner and outer diameter, i.e. thinner walls, specifically the model predicts that a capillary with 542 μm ID/ 673 μm OD/ 24 μm coating will be applicable in this region. The mechanism responsible for this abrupt change in intensity is, according to the model, total internal reflection at the coating-air interface of the rays reflected from the back of the capillary. This total internal reflection prevents these rays from being scattered to larger backscattering angles, thereby causing a sudden decrease in the intensity of the light at a given limiting angle, see figure 46. This angle varies uniformly with the refractive index and may therefore be used as a measure for the refractive index of the liquid.

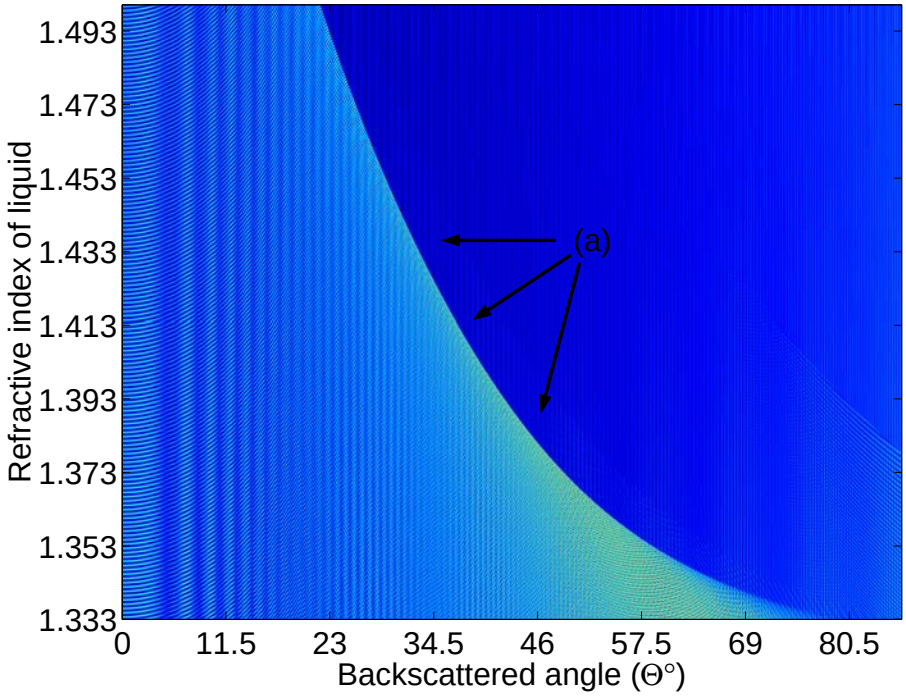

Figure 47. Calculated pattern for a 542 μm *ID/* 673 μm *OD/* 24 μm *coating capillary as function of backscatter angle and refractive index of the liquid. Both low and medium frequency variations as well as the abrupt change in intensity level at high backscatter angles are seen. The abrupt change in intensity for this capillary occurs in a more relevant interval for dilute aqueous solutions, than it does for the* 100 μm *ID/* 165 μm *OD/* 12 μm *coating capillary, as indicated by (a).*

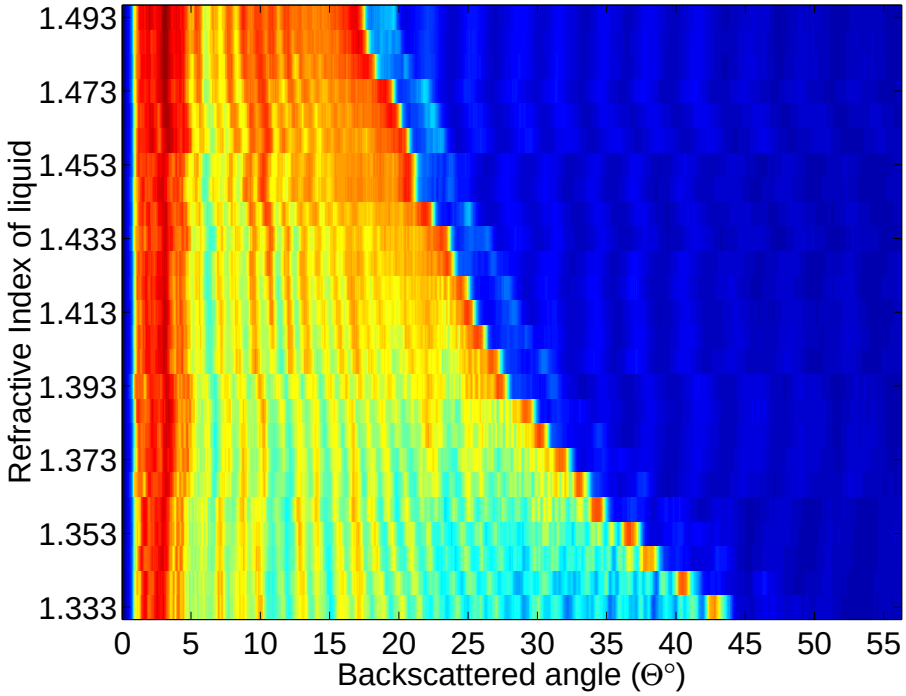

Figure 48. Experimentally obtained pattern for a 542 μm *ID/* 673 μm *OD/* 24 μm *coating capillary. It is seen by comparison to figure 47 that the position of the abrupt change in intensity differs from the model, although the behavior is quantitatively the same. Analyte used is aqueous solutions of NaSCN.*

The modeled interference pattern as function of refractive index for a 542 μm ID/ 673 μm OD/ 24 μm coating capillary is shown in figure 47.Figure 48 shows the experimental results from using a 542 μm ID/ 673 μm OD/ 24 μm coating capillary. The experimental and the modeled results show good agreement. The abrupt change in interference pattern is already detectable at the refractive index of water and is experimentally accessible well beyond refractive indices normally considered for aqueous solutions, see point (a) in figure 47. The discrepancy between the predicted and the measured angles of the abrupt intensity change may be attributed to material parameter tolerances of the experimental setup as follows: The uncertainty of the dimensions of this capillary is 12 μm and 25 μm for the inner and outer diameter, respectively giving an uncertainty of 6.9° in the angle predicted by the model. The uncertainty in refractive index of the polyimid coating (n=1.5-1.8) is causing a further uncertainty in the predicted angle of 3.3°.

From the experiments resulting in figure 49 the precision is found to be $2.5{\cdot}10^{-4}$. The position of the abrupt change in intensity is determined at each refractive index. The refractive index of the injected solutions increases linearly. The positions' deviation from a line is the measure of the precision. Hence we are able to perform an absolute refractive index measurement with accuracy on this level on a 180 nL volume. The main limitations for accuracy such as temperature control and de-

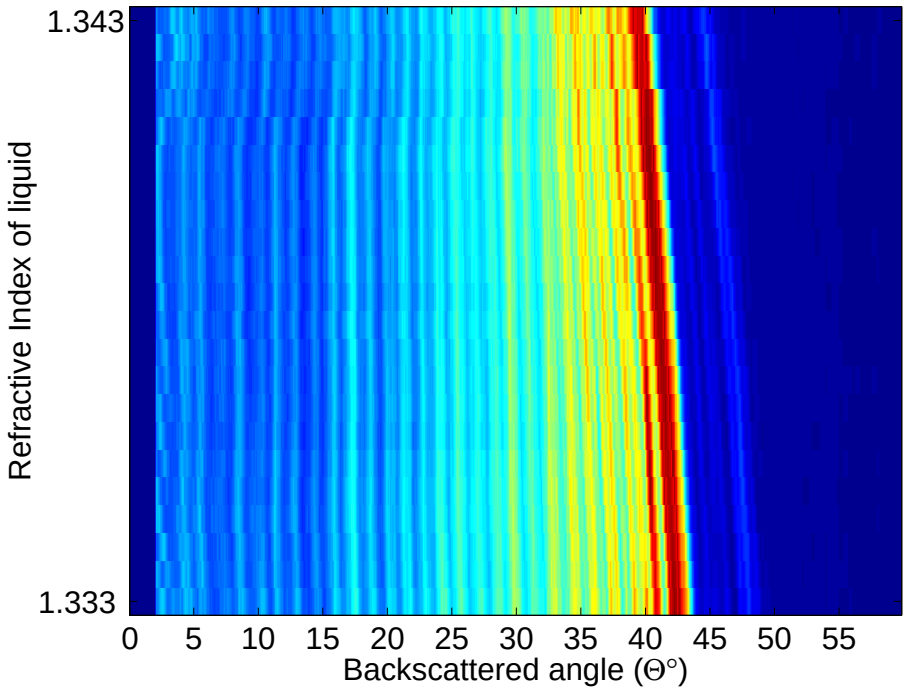

Figure 49. Experimentally obtained data from a 542 μm *ID/* 673 μm *OD/* 24 μm *coating capillary using sucrose as analyte. The position of the abrupt change in intensity is monitored as function of the refractive index of the sucrose solutions. The detection limit for refractive index changes achieved by following the position of this change in position is* $2.5 \cdot 10^{-4}$ *corresponding to 321 ng in a 180 nL probe volume.*

tector resolution are the same as conventional MIBD. The theoretical limit using this approach is therefore similar to the limit achievable by conventional MIBD and it is possible to perform a conventional MIBD measurement simultaneously to our newly proposed method. In principle if the dimensions and refractive index of the capillary tube are known, then there is a one to one relationship between the backscatter angle and the refractive index of the liquid. Thus enabling the determination of the absolute refractive index. Normally, however one needs to calibrate the system by running a set of RI standards.

4.6 Summary on absolute measurements

Our new concept of investigating a larger range of interference fringes offers fundamentally new applications of the micro interferometric backscatter detection scheme. We have shown two possible ways of making absolute measurements of the refractive index of liquid in nanoliter probe volumes with a simple optical setup. The model based on ray tracing has been used to reveal and explain novel features of the interference pattern: An abrupt change in intensity at large backscattered angle is clearly present in the modeled system and in the experimental results. It is shown that this approach enables an absolute determination of the refractive index in the range from 1.33 to 1.5 by using capillary tubes of appropriate dimensions. It has been proven that the model based on ray tracing may be used for describing the MIBD phenomenon. The improved ray tracing model is capable of explaining all the significant features of the MIBD pattern except the stationary high frequency fringes. However, these fringes have been shown to originate from reflections from the edges of the capillary and thereby not being relevant for measuring the refractive index of the liquid within. Our model may be used to select the capillary, with the appropriate dimensions, that optimizes the sensitivity at a given refractive index interval, suited for a specific application. We believe that the reported improvements for the MIBD scheme will significantly enhance the future applicability of the methodology for analysis of minute volumes of aqueous solutions.

5 Surface bound bio sensing in capillary tubes

As the wave–based model has shown, even small changes in the refractive index of a sample can be seen. To be able to detect a small change on the glass surface of the capillary may be used for monitoring biologically relevant events. Proteins and enzymes have dimensions of some nanometers. By having those react and bind to the surface and thereby perturb the interference pattern in MIBD is off great interest. Thereby biological interactions can be monitored label–free and in small volumes. As these protein samples can be expensive a small sample volume is a high priority.

5.1 Validation of surface chemistry at planar surfaces

In order to verify the capillary experiment, the same chemical process has been done on a planar surface in order to obtain the information necessary to understand and explain the events taking place. The thicknesses used for the modeling has been obtained by actual surface chemistry experiments performed on fused silica glass and silicon. A sandwich structure has been fabricated on the surface and the change in thickness has been determined via ellipsometry. The surface has been cleaned before placement in piranha (1:4 H_2O_2:H_2SO_4) for 1 hour. After oxidizing the surface the sample is placed in a solution of N-(6-Aminohexy) aminopropyltrimethoxysilane (1 mL silane, 1ml H_2O, 40 mL 2-propanol) for 3 hours. The surface was passivated with HSA (Human Serum Albumin). A solution of (0.5 mg/mL in PBS) photobiotin was allowed to sit on the surface for 3 hours and then be illuminated by UV-light for 2 hours. The photobiotin then reacted with ExtrAvidin from Sigma (0,5 mg/mL in PBS), which again was reacted with biotinylated Protein A (Pierce Biotechnology). Two different fragments of the Human IgG protein was introduced to the surface bound Protein A. Protein A has a strong binding affinity for the F_c-fragment (Calbiochem) of IgG. The Fab-fragment (Rockland) is then used as a control for the system as it does not bind to Protein A.

Ellipsometry has been used to obtain the optical thickness for each step in the process. Ellipsometry is a very versatile optical technique that has applications in many different fields, from the microelectronics and semiconductor industries (for characterizing oxides or photoresists on silicon wafers, for example) to biology. This very sensitive measurement technique provides capabilities for thin film metrology. As an optical technique, ellipsometry is non-destructive and uses polarized light to probe the dielectric properties of a sample. Through the analysis of the state of polarization of the light that is reflected from the sample, ellipsometry can yield information about layers that are thinner than the wavelength of the light itself, down to a single atomic layer or less. Depending on what is already known about the sample, the technique can probe a range of properties including the layer thickness, morphology, or chemical composition. It is commonly used to characterize, with an excellent accuracy, film thickness for single layer or complex multilayered stacks ranging from a few angstroms to several micrometers. An ellipsometer functions by reflecting a beam of light of known polarization off of a sample, and measuring the polarization change upon reflection. The exact nature

of the polarization change is determined by the sample's properties (thickness and refractive index). Ellipsometry is a specular optical technique (the angle of incidence equals the angle of reflection). In its modern incarnation, ellipsometry uses a laser as the illumination source, usually a HeNe laser which has a wavelength of 632.8 nm. The ellipsometer used for these measurements is a Picometer ellipsometer from Beaglehole Instruments. The ellipsometry data is shown in Figure 50.

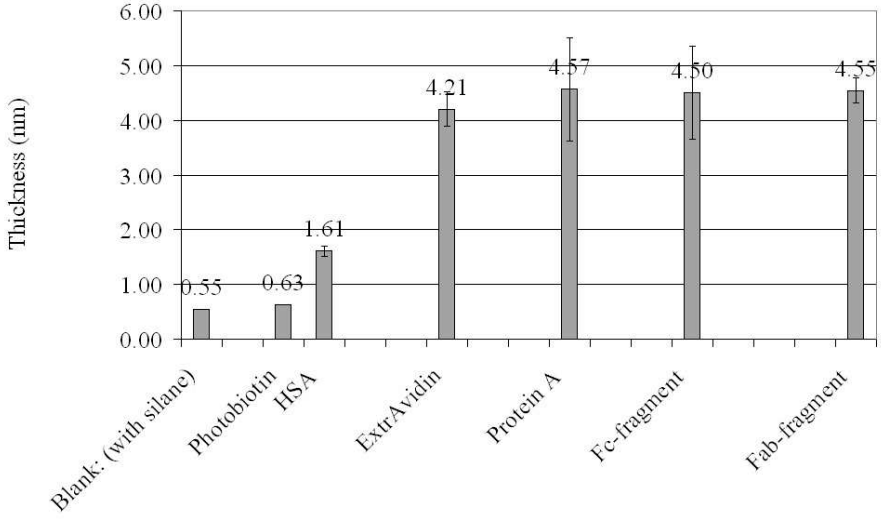

Figure 50. Ellipsometry data from the bio–molecule sandwich fabricated on the silicon wafer. A clear indication of the addition of the ExtrAvidin is seen as the thickness increases. The binding of the later molecules Protein A and the IgG fragments does not give any rise to thickness change.

The most consistent data was achieved when using a silicon wafer as substrate. The fused silica sample had multiple reflections returning to the detector in the ellipsometer, thereby interrupting the measurement. The different substrate material is not believed to have a large influence on the binding events, as the silane attaches to either an oxidized silicon surface or a glass surface appearing the same for the later binding events. In order to obtain the thickness of the layers the refractive index of the bio–molecules has to be known. All have been considered to have a refractive index of 1.42 and the thickness is found with this refractive index of 1.42 used in the iterative process of matching a thickness with the measured reflectance in the ellipsometer.

5.2 Bio-sensing at capillary surfaces

Figure 51. The micro interferometric backscatter detection setup used to monitor the binding events inside the capillary. The beamsplitter makes it possible to detect the centroid and the first fringes.

The procedure for constructing the surface evaluated by the ellipsometry has been repeated in a capillary. The capillary has been impinged by a laser and the occurring interference pattern has been recorded in the setup sketched in Figure 51. In Figure 52 is shown the interference pattern of the experiment when ExtrAvidin, Protein A and Human IgG has been in the capillary. The number of fringes shown is 13 including the centroid, which is shown ranging from pixel 0 to 500. At first it seems like a huge shift from the different reactions, but the large shift is caused by the difference in refractive index of the bulk buffer solution. This sensor is greatly influenced by difference in refractive index, so it is close to impossible to make sample solutions that should have the exact same refractive index. Instead of detecting these fringes before and after reaction has occurred, a real–time monitoring of the fringes and their movement is necessary.

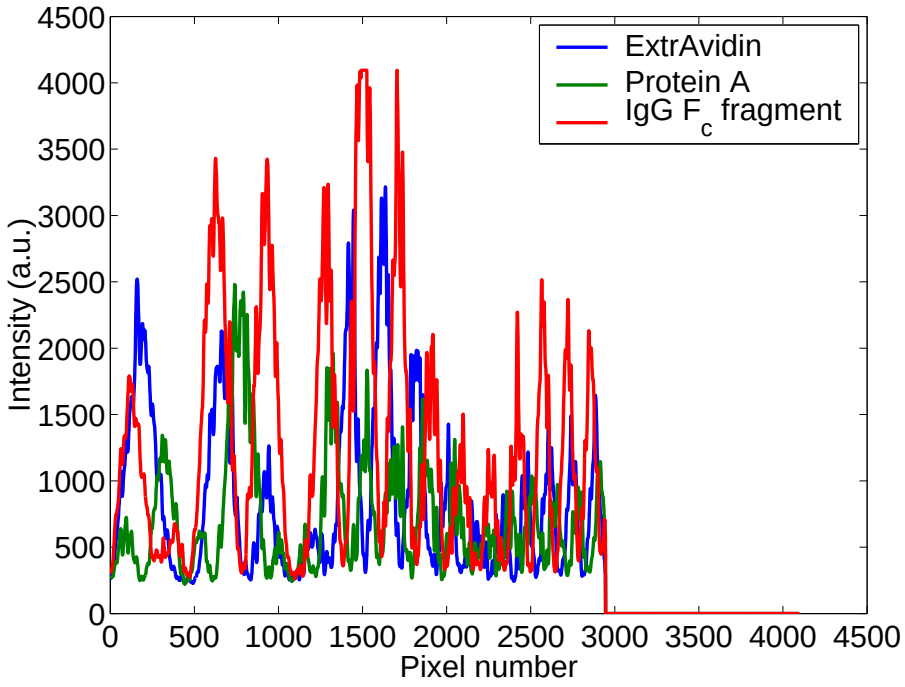

Figure 52. The recorded fringe patterns from ExtrAvidin – Protein A – Human IgG F_c, when injected into the capillary. A large shift in fringe position is seen. At pixels 0 to 500 is the centroid.

As the interference pattern is recorded by the linear CCD–array, the signal is zero–padded from 3000 pixels to 4096. Then the frequency spectrum of the signal is found from a FFT–rutine and the dominant frequency is found. By monitoring the change in phase of the chosen frequency the change in refractive index can be monitored real–time with high precision [41]. In Figure 53 is shown how the refractive index changed (shown as phase change, which is equivalent) along the time span of the these binding experiments. For each run the molecules had 30 minutes to react. The reaction was thought gone to completeness at a much earlier time, so here is just shown the first 200 seconds for each run. The huge shift in fringe pattern, seen in Figure 52 is also seen here, in Figure 53, but it is only the small steps within each run, which is of interest.

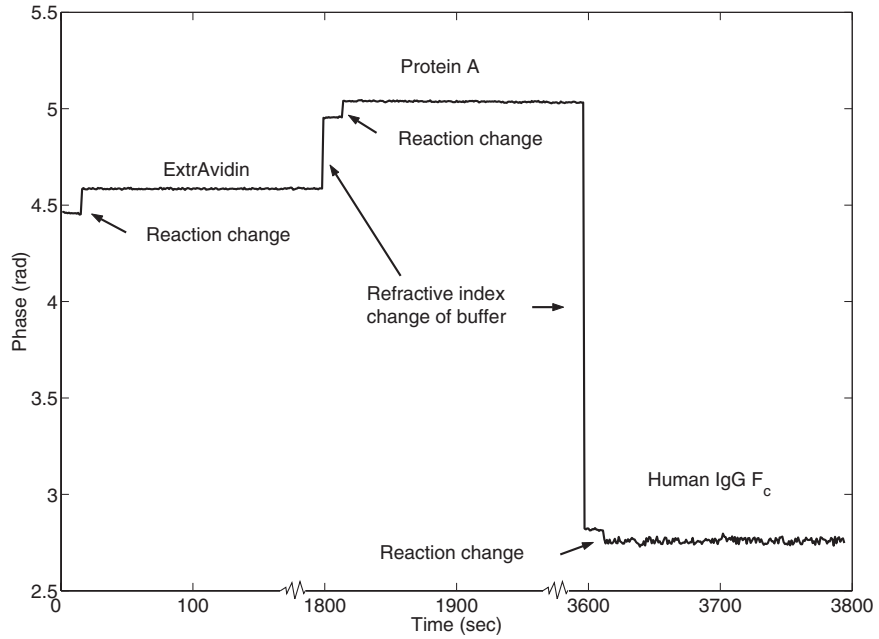

Figure 53. Binding events for ExtrAvidin – Protein A – Human IgG F_c – uncorrected binding. The large shift in phase is caused by the different refractive index of the buffer solution. The change of interest is the change within each run. Each run is 30 minutes long, here is only shown the first 200 seconds for each run.

The step is a direct shift in refractive index caused by the binding reaction occurring inside the capillary. In Figure 54 is shown the refractive index corrected binding events. The buffer refractive index have been subtracted from the signal, so only the steps from the binding events is present. The standard deviation of the phase signal within the runs are $2.8 \cdot 10^{-3}$,$3.4 \cdot 10^{-3}$ and $13 \cdot 10^{-3}$ for ExtrAvidin, Protein A and Human IgG F_c, respectively. The change caused by the reaction is 2.8%, 1.6% and 2.1% for the reaction series, clearly above the noise level.

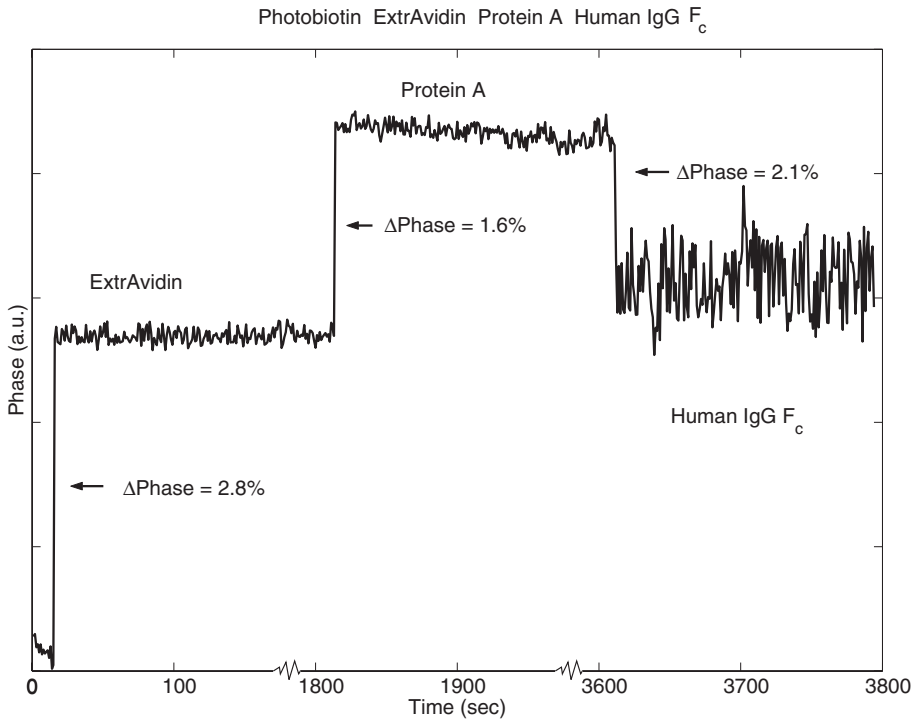

Figure 54. Binding events for ExtrAvidin – Protein A – Human IgG F_c. The signal has been corrected for the different refractive index between the buffer solutions. The change in signal is now a direct change in refractive index caused by the binding events.

The thickness change found from the ellipsometry measurements has been used as input to the wave–based model with 4 material interfaces. The layer thickness has been changed from 0 to 5 nm. The refractive index of the liquid is assumed constant [100] as 1.33. The refractive index of the bio–molecule layer has been set to 1.42, which also has been assumed for the ellipsometry measurements [101]. In Figure 55 is shown the modeled signal from such conditions mimicking the actual experiment. The modeled signal has been treated as the actual signal and run through the FFT–routine, also zero–padded and the phase change has been found. The change in phase from the modeled experiment is 2.8% when changing the layer on the glass surface. It is in excellent agreement with the actual experiment, even though the modeled shift is done with a larger change in thickness. The thickness provided by the ellipsometer shows nearly no change in thickness from ExtrAvidin to IgG, but there is a clear signal with the MIBD sensor.

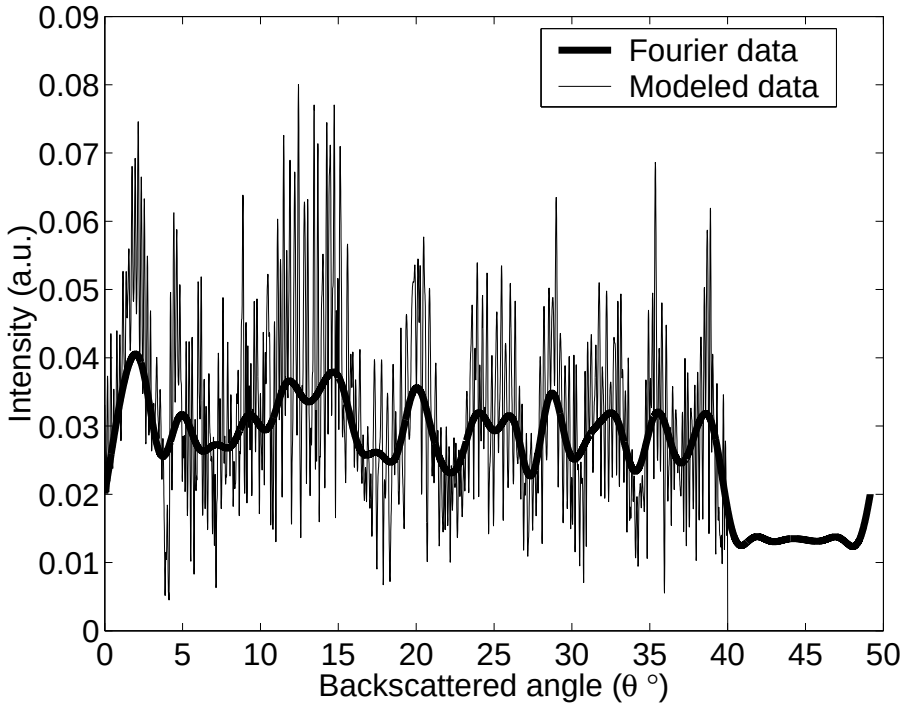

Figure 55. Modeled fringe pattern with surface binding. The system modeled is a capillary with a 250μm inner diameter and outer diameter of 360μm with 12.5μm polyimid cladding. The bio–molecule layer has been changed 5nm and fringe shift found accordingly.

6 Chip scale interferometry

Previously prepared micro structures is further process. The completion of the fabrication process is described in this chapter. Here is presented the interferometric experiments performed using those fabricated rigid polymer flow chips.

6.1 Chip fabrication

From the micro fabrication procedure for etching in silicon, the fabricated structures has been further processed. The silicon wafer is clued to a 4" glass wafer. The glue is cured in UV–light by exposing the glue for short pulses (10 seconds), just to harden it enough so that the Si–wafer does not slide. Then the glue is further exposed for complete curing (30 second pulses). Longer pulsing will introduce boiling of the glue. The sample is then covered by a conducting thin metal layer by sputtering. It is important that the conductance is uniform over the entire surface. Else the electroplating step will not be successful. A non–conducting spot will have a high current resistance and will result in a hole burned through the sample. The electroplating step has been performed by Dandisc, Sakskøbing, DK. The Ni-plate fabricated by the electroplating step is pealed off the sample thereby resulting in a negative relief of the fabricated structure in silicon. The nickel–plate is 400μm thick and is cut into 44 by 40 mm Ni-shims. In Figure 56 is sketched how the shims afterwards then is ground down to become 275μm. The grinding step has been described above, when discussing the grinding down of capillaries. Again the procedure takes several days. It is necessary though. If the nickel shims are only made 275μm (the tool thickness in the injection molding machine) the structure is copied to the backside of the nickel shim. Where the channel begins to rise from the planer surface the plate thickness will be rather thin. During the injection of the polymer a pressure builds up (approximately 300 bar) and flattens anything, ruining the nickel shim, unless its back is completely flat.

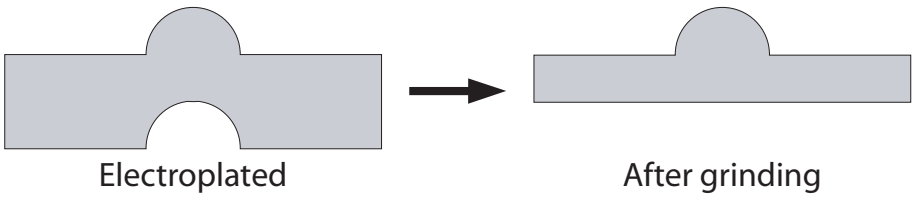

Figure 56. Principle drawing of the nickel shim before and after grinding. As shown the structure is transferred to the backside as well. The structure is present on the back even after electroplating more than 400 microns. The shim has to be flat on the back or it will be crushed during the injection molding at high pressure.

Nickel shim analysis

The parallel flow channels has been transferred to the nickel shims. A 2X2 mm area is depicted in Figure 57 to show the overall features on the nickel shim. The image has been created with the Dektak profilometer sampling 300 lines in the y–direction, where each line is 18000 measurement points in the x-direction.

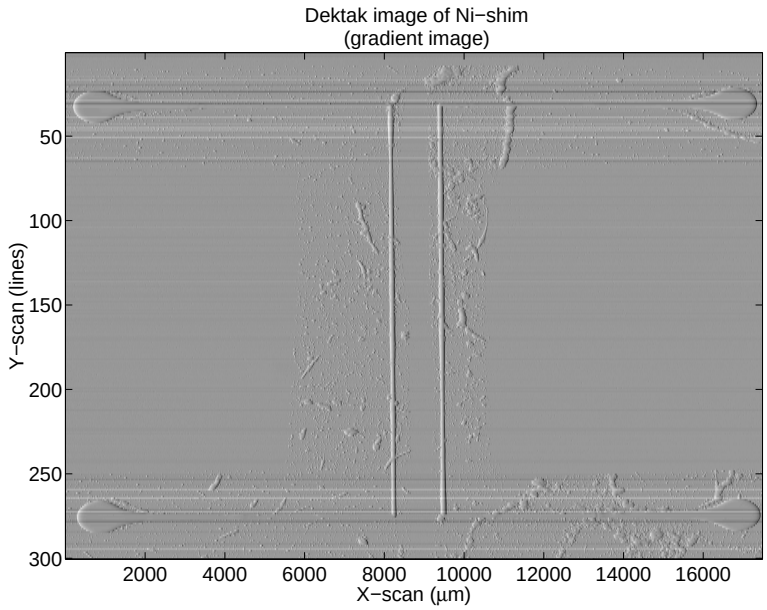

Figure 57. Two channels running parallel is depicted with four reservoirs with droplet shape. Mask penetration is seen as the rough surface surrounding the channels. This is eliminated on the larger part of the wafer by using clean room tape as extra surface protection. The channel on the left is channel 1 mentioned in the statistics below.

Table 12. Shim statistics obtained from the Dektak line profiles. Number of maxima points is 135 for both channels. The number of radii points is 4X62. The channels are wider than they are deep, hence not a perfect semicircular shape. As the mask started to fail the channel sidewalls are broadened. The height is found to be 59.9 µm and the width is 80.6 µm. The needle in the profilometer did not have a symmetric shape as the left radius is always found to be larger than the right radius.

	Channel 1		Channel 2	
Mean radius left	81.2 µm	± 10.5 µm	88.6 µm	± 14.4 µm
Mean radius right	76.4 µm	± 14.7 µm	76.0 µm	± 14.5 µm
Radius	78.8 µm	± 12.6 µm	82.3 µm	± 14.4 µm
Height left	59.9 µm	± 9.0 µm	59.7 µm	± 10.3 µm
Height right	59.7 µm	± 8.3 µm	60.5 µm	± 11.3 µm
Height	59.8 µm	± 8.6 µm	60.1 µm	± 12.0 µm

The desired pattern is clearly visible, but mask failure is also present as unwanted structures is seen. The profilometer data has been analyzed to describe the dimensions of the fabricated structures such as channel width and height. The exact shape of the structure would be desired as to see how semicircular the etching result has been over the entire pattern. The actual shape of the needle in the profilometer is unknown, therefor it has not been possible to subtract the structure shape from the line profiles. The analysis is summarized in Table 12. The height of the channel is found to be 59.9 μm and the width is 80.6 μm. As the mask has not protected the silicon in a perfect manner, the channels has been broadened.

The surface of the nickel–shim is further analyzed. The surface has been investigated by SEM images, see Figure 58. The overall shape is showing some curvature as is expected by the nature of the fabrication method. Again the shape does not appear perfectly uniform on a large scale, but at higher magnifications (2000X) the surface appears uniform. The surface has structure/ roughness features between 1 and 3 μm in size. The surface was expected to be much smoother from the HNA–etching mixture used [68].

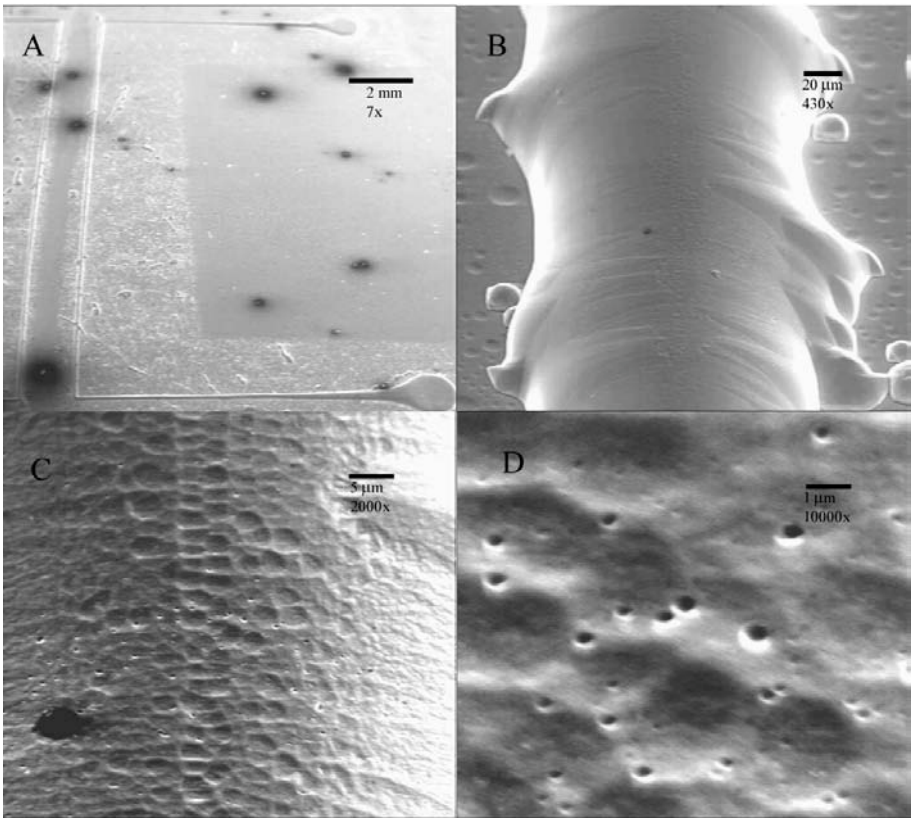

Figure 58. Scanning electron microscope images of nickel shim at different magnifications. In A is the overall view of the shim, the rough structures next to the channels is seen. The dark sports are local build up of a charged field, this is mainly caused by non–conducting dust particles. In B the curvature of the channels is seen. The channel has not been etched uniformly over large (+40μm) areas. The dark spot in the middle is also present in C. The surface is at the magnification in C uniform. In D is seen that the surface is not perfectly smooth and the features are 1 to 3 μm in size.

Injection molding and assembly of polymer flow chips

The nickel shim has been used for micro injection molding of the copolymer Topas 8007 and 5013 from Ticona (Ticona AS, DK). Some typical data for Topas, PMMA and polycarbonate is listed in Table 13. Topas cyclic olefin copolymers are random copolymers of ethylene and norbornene.

Table 13. Material properties of Topas, PMMA and polycarbonate (PC), the data is provided by Ticona ,www.ticona-us.com. The large elongation and birefringence of PC is not desired.

	Topas	PMMA	PC
Thermal conductivity W/m·°K	0.16		
Linear thermal expansion °K^{-1}	$70 \cdot 10^{-6}$		
Density $\frac{g}{cm^3}$	1.02	1.2	1.2
Elongation %	3–10	5	80
Water absorption %	.01	.1	.04
Refractive index	1.53	1.491	1.586
Birefringence	low	low	variable
Light transmission	92%		88%

Topas has been chosen for its excellent optical properties and high moisture containment ability. The copolymer is especially designed for injection molding and is well suited for the following steps by having a low glass transition temperature, T_g, of 70°C and 130°C for Topas 8007 and 5013, respectively. The temperatures used for the injection molding is 220, 200, 200, 180°C for the injection nozzle and the forming tool was cooled with 30°C water. The forming tool rises some degrees in temperature when the hot polymer melt is injected. This is relevant to ensure that the polymer is cooled to temperatures below T_g, but not to fast as the inlet then would be blocked by solid polymer resulting in bad replication. The Ni shim was used in a micro–injection molding machine from Engel and several open polymer flow systems were fabricated.

The circularity of the channels produced was investigated by cross–sectional analysis of PDMS replica of the channel areas. The PDMS replica was cut repeatedly perpendicular to the channel direction to form cross–sectional slices spaced by approximately 3mm along the channels. Each slice was imaged by confocal microscopy and the resulting images were analyzed using the Igor Pro (Wavemetrics, Oregon) software package according to the procedure detailed in the following. The contour of the PDMS edge, i.e. the inverse of the channel contour, was traced manually on the screen to form a set of points faithfully outlining the shape. The points were subsequently used for least–squares–fitting a semicircular shape with an added sloping background:

$$Function\ semicirc(x, x_0, r, background_{offset}, background_{slope}) \tag{78}$$

$$if\ (x\ <\ x_0 - r)|(x\ >\ x_0 + r) \tag{79}$$

$$return\ background_{offset} + (x - x_0) \cdot background_{slope} \tag{80}$$

$$else \tag{81}$$

$$return\ \sqrt{r^2\ - (x - x_0)^2} + background_{offset} + (x - x_0) \cdot background_{slope} \tag{82}$$

$$endif \tag{83}$$

$$End \tag{84}$$

The independent parameter is the position, x, and the fitted parameters are the radius, r, and center position, x_0, of the semicircle as well as the slope, background$_{ground}$, and vertical offset, background$_{offset}$, of the sloping background. A data mask was created manually for each data set so that only data points of the lower half of the etched structure and data points on the surrounding planar background were included in the fitting.

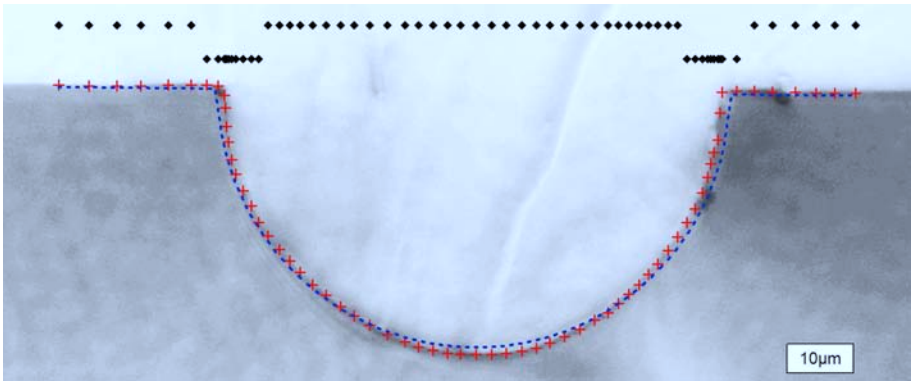

Figure 59. Image analysis of the circularity of an isotropically etched channel after process optimization. The red crosses are a manual trace of the shape by eye. Subsequent fitting to a semicircular shape with a substrate sloping background yields the blue dotted curve. The black dots describes the data mask used for the fitting procedure: data at elevated dots are included in the fitting while data at lowered dots are excluded for the reasons described in the body text.

These areas were selected from previous experience showing that the major deviations from the targeted semi–circular shape occur at the channel corners. The semicircle arising from fitting to the lower half of the channel structure may then be used as a good reference for quantifying this deviation under varying preparation conditions. Figure 59 shows the analysis procedure applied to one of the most recently prepared microchannels. There is clearly very good correspondence between the fitted semicircle and the actual channel shape throughout. The small

deviations from perfect circularity is mainly observed at the corners of the channel. The deviation was found to be quantified in a useful manner by a normalized Chi-value: the total area between the measured shape and the fitted curve normalized to the radius of the fitted semicircle. The results for the nearly perfect channel shown in Figure 59 are a fitted radius r of 37.9μm with a normalized Chi–value NChi of 2.8.

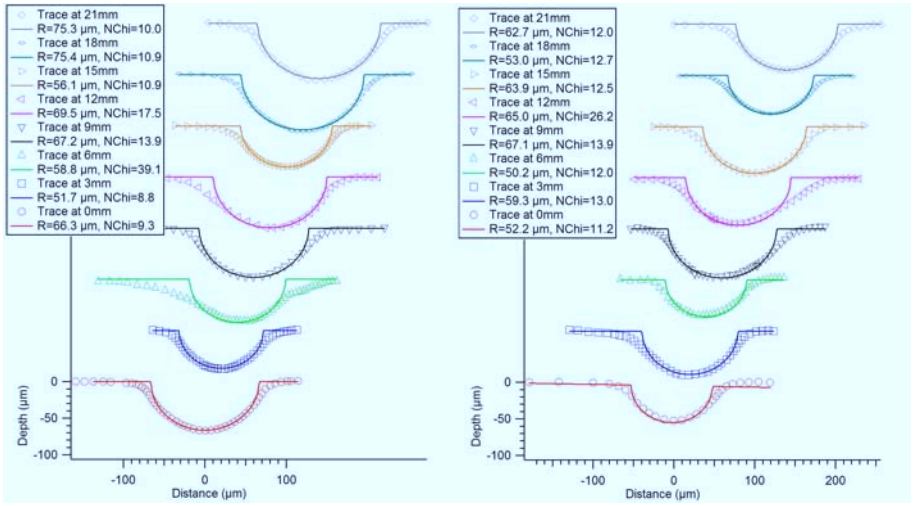

Figure 60. Cross-sectional profiles and fitted semicircles for the left and right channel. Left is the left channel. Each profile has been offset vertically by 70μm and horizontally by 20μm for clarity to emphasize that the actually separation between the sample slices is 3mm. The legend presents the fitting parameters for each trace as a semicircle radius and a deviation from the fitted semicircle normalized to its radius.

Corresponding analysis of the series of images described above, along the two parallel channels of the injection molded channel systems produced within the project period, are presented in Figure 60. The quality and homogeneity of these channels are clearly inferior to the later production methodology but still this quantitative evaluation of fabrication quality is found to be highly useful as a development tool.

The surface of the polymer chips is not hydrophilic and in order to have water based samples flowing in the assembled chips the surface chemistry needed to be altered. A standard procedure from working with PDMS was adopted with these Topas chips. The surface was exposed to an oxygen plasma, after access holes had been drilled into the chips. The plasma conditions were 40 watts for 30 seconds in air at 10^{-5} Pa on an Eni Power System setup. The same procedure has been done for several years for PDMS micro–fluidic systems [31], although the hydrophilic surface of the polymer is stabile for a longer period of time (weeks).

Two injection molded parts were aligned and assembled. The alignment were done by hand. It seamed like the two parts self–aligned it they were close to being aligned. My hypothesis is that there were introduced an electric potential into the surface material during the plasma oxidation step. The potential would then be minimized if the channels were aligned. The self–alignment ability was

not present if the samples had been heated to above T_g and then cooled down to room temperature again. This also changed the hydrophilicity, although the heating time needed to be much longer, than for removing the self–alignment ability. The open system was sealed by aligning two samples facing each other, resulting in a circular channel, and then heated to 100 °C in vacuum oven. The two halves were kept together by a weight resulting in a pressure of 9 kPa for 2 hours. After assembly the completed flow chip was tested firstly for its ability to contain water. In Figure 61 is shown images of such a test, where one channel is

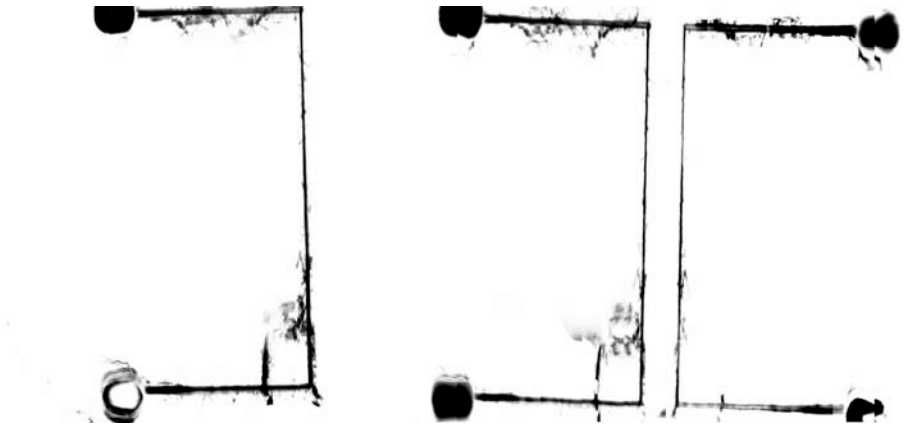

Figure 61. Fluorescent images of assembled chip containing water with rhodamine dye. Left is one channel filled. No liquid is transferred to the other channel when vacuum has been applied to that other channel. Right is both channels filled, no exchange of fluid is seen.

filled with rhodamine dye, then vacuum is applied to the second channel and no liquid is transferred to this channel. When assembled no liquid cross–talk has been seen in the end product. Although present the defects are expected to have little or no effect on the sensing experiment as they are mostly dead–ends. Thereby the defect would be filled and then no liquid is exchanged as the experiment continues.

6.2 Chip Scale Interferometric experiments

The sealed chips has been used in a Chip Scale Interferometric (CSI) detection system as shown in Figure 62. The light source is a fiber coupled (Oz Optics)

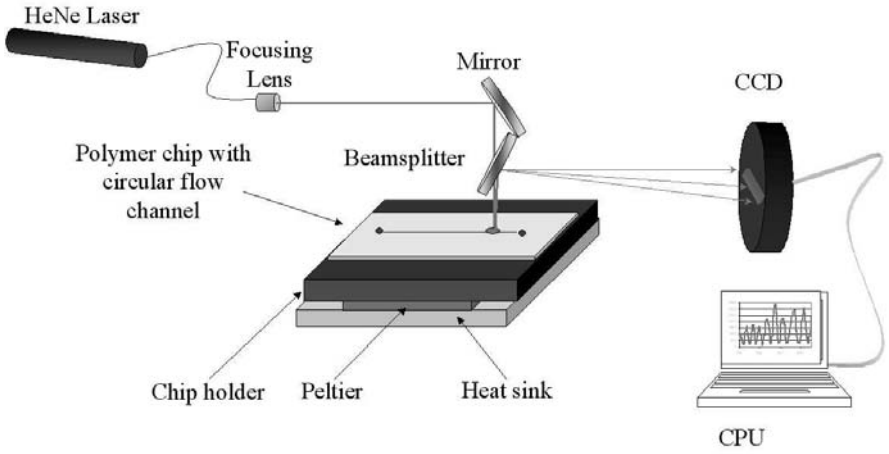

Figure 62. Diagram of experimental setup of the CSI system when performed on injection molded flow chips. The HeNe laser impinges on the circular flow channel via the mirror and through the beamsplitter. The fringe pattern generated from the chip is guided via the beamsplitter to the detecting CCD linear array. The experiments can be monitored in real time on the connected PC. The beamsplitter folds the optical train so that the directly backscattered light can be observed.

HeNe laser (Melles Griot) with a beam diameter of 100 μm, that impinges upon a mirror through a beamsplitter and onto the flow channel. The interference pattern is reflected via the beamsplitter onto the detecting CCD linear array (Ames Photonics) which is connected to a PC to show real time measurements. The optical laboratory is equiped with individual air–conditioning for each optical bench to keep a stabile temperature within 1°C. The flow chip is even further placed in good contact with the x-y stage, which again is temperature controlled within 0.1°C.

In Figure 63 is shown the recorded interference pattern of the nickel–shim, a water filled channel and a channel filled with an optical active aquarius solution of annalin.

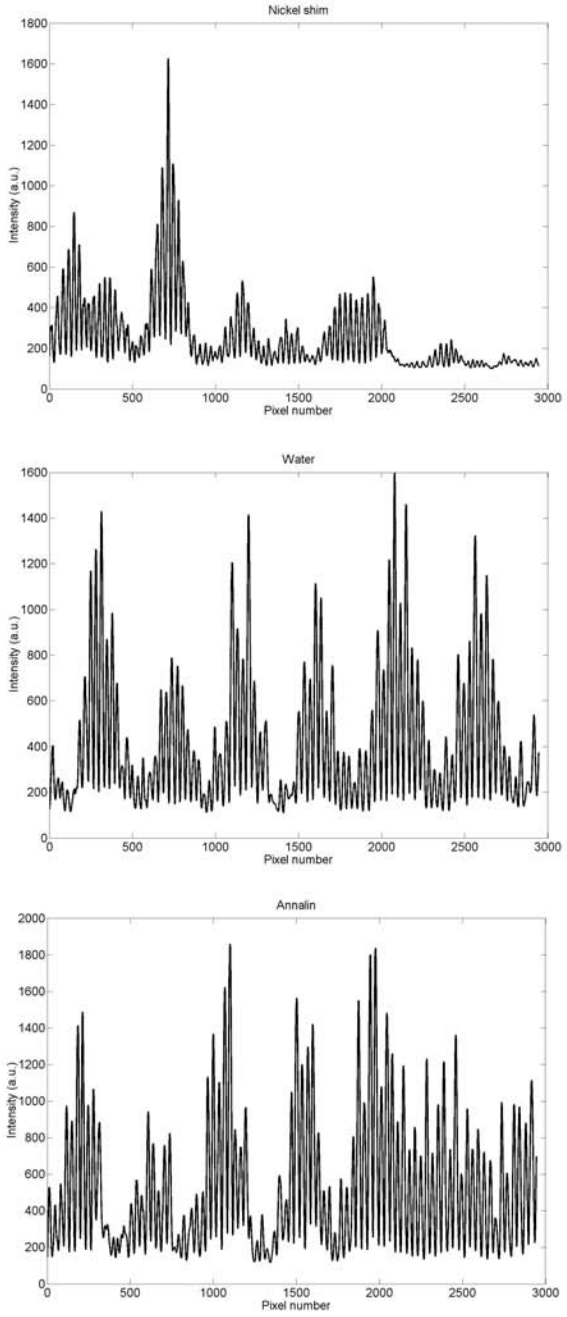

Figure 63. Top: Backscattered pattern from the Ni–shim. Two sets of fringes are present. The low frequency dies out as the angle on incidence gets large. Middle: Backscattered fringe pattern from a water filled flow channel. 6 normally considered fringes is shown. Bottom: Fringe pattern arising from an annalin solution filled channel. Annalin is an optical active material and should influence the high frequency signal seen if this signal is polarization dependent. Changing the polarization did not influence the signal.

Common for all patterns is the normally considered fringes (6 for the case of water) and a high frequency signal. If these high frequency fringes are the ones known to be present with capillary experiments they should be polarization dependent, hence change appearance when changing the polarization of the incoming light. This is not the case neither with water or with the optical active annalin present in the channel. Thereby the high frequency fringes is believed to arise from the surface as changing the liquid has not changed their appearance, plus they are present on the nickel shim as well. When the SEM images also are taken into account it must be concluded that the high frequency fringes arises from the surface morphology effects and as such is not useable in this sensing principle. The high frequency fringes do though play a role in the sensing capability of the sensor as they are contributing considerably to the noise level. The FFT–rutine used in these experiments tries to track the fringe minima and even though the correct frequency is found through the power spectrum, it is troublesome with this high frequency signal overlaying the signal used for sensing.

Temperature experiments

Temperature calibration curves has been run on the system. We have previously had experiences working with flow chips made in PDMS. These chips performed differently as change to the liquid (pressure) is much more present in the interference signal. The PDMS is an elastomer and can thereby absorb some of these effects. To reduce these noisy effects the filled channel had time to reach equilibrium b emptying the reservoirs and then filling with them again with same liquid volume (5μl). The reservoirs were then sealed with a slap of PDMS to reduce liquid evaporation. The temperature of the channel was changed by changing the temperature of the translation stage, thereby changing the temperature of the entire system. In Figure 64 is shown the result of changing the temperature from 25 to 27.5°C. The liquid used is water.

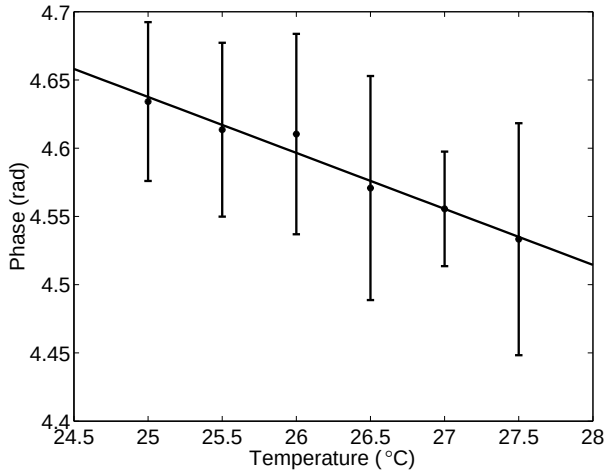

Figure 64. Temperature calibration curve. A water filled channel has experienced a temperature shift from 25 to 27.5° C in 0.5° C steps. The system was allowed to equilibrate for 20 minutes before changing the temperature. The errorbars relates to the noisy signal recorded. The standard deviation is found for each temperature level for a 15 minute time period. The change is shown as the phase change of the dominant frequency in the fringe pattern via the FFT-routine.

The noise level, σ, is found to be 0.0674 and is the average of the standard deviation for each temperature level. The slope, α, of the best fitted line ($R^2 = 0.968$) is -0,0410, which with 3σ statistics gives a detection limit found from equation 85 [102].

$$D.L. = \frac{3 \cdot \sigma}{|\alpha|} \cdot \frac{dn}{dT}_{water} = \frac{3 \cdot 0.0674}{0.0410} \cdot 1.05 \cdot 10^{-4} = 5.2 \cdot 10^{-4} \Delta n \qquad (85)$$

This is not an excellent temperature detection limit. The result is a combination of two things. The first thing is that the sensor is very sensitive towards changing the optical pathlength of the system. This is the reason why the fringe pattern moves. It is caused by the expansion of the materials involved. Water has a dn/dT dependents of $1.05 \cdot 10^{-4} {}^{\circ}C^{-1}$ [103] mainly caused be the expansion and the expansion coefficient for water at 20°C is $207 \cdot 10^{-6} K^{-1}$ and $303 \cdot 10^{-6} K^{-1}$ at 30°C [104, 105]. For comparison Topas has the linear expansion coefficient, α, of $70 \cdot 10^{-6} K^{-1}$, which in a volume is almost similar to that of water. Glass has for comparison a one or two orders of magnitude smaller temperature dependents. As seen by the chip modeling the change of the channel dimension has a dramatic effect on the interference pattern. In this experiment the channel has changed some microns. This leads to the second point on the noise analysis. The change in channel dimension is on the same length scale as the surface roughness thereby changing the surface considerably. This experiment has shown how temperature dependent this sensor is, meant as the temperature changes during an experiment should be kept to a minimum as the noise caused by those fluctuations effects the signal in a significant way.

Concentration experiments

A series of glycerol solutions with changing concentrations has been run through the flow channel. This series of glycerol solutions is the model analyte used before and gives rice for comparison with earlier micro interferometric backscatter detection experiments. Before the liquid is introduced to flow chip the liquid is degassed for 30 minutes and is kept at room temperature. The liquid is pulled through the micro fluidic channel via an external pump. 7 μl of sample is introduced to channel reservoir and when approximately half is at the waste reservoir the liquid is allowed to stabilize for 30 seconds to equilibrate both pressure and temperature, so the only measured effect is the change in concentration. The liquid has been changed to be a concentration series of aqueous glycerol solutions ranging from 20 mM to 100 mM. The solutions has been degassed after mixing to reduce the number of bubbles formed when loading the flow chip. The flow chip is kept at a constant temperature just above room temperature. By keeping the temperature above room temperature the temperature controller will have to send a constant flow to the system, not removing energy also. In Figure 65 is seen the result of a concentration series run.

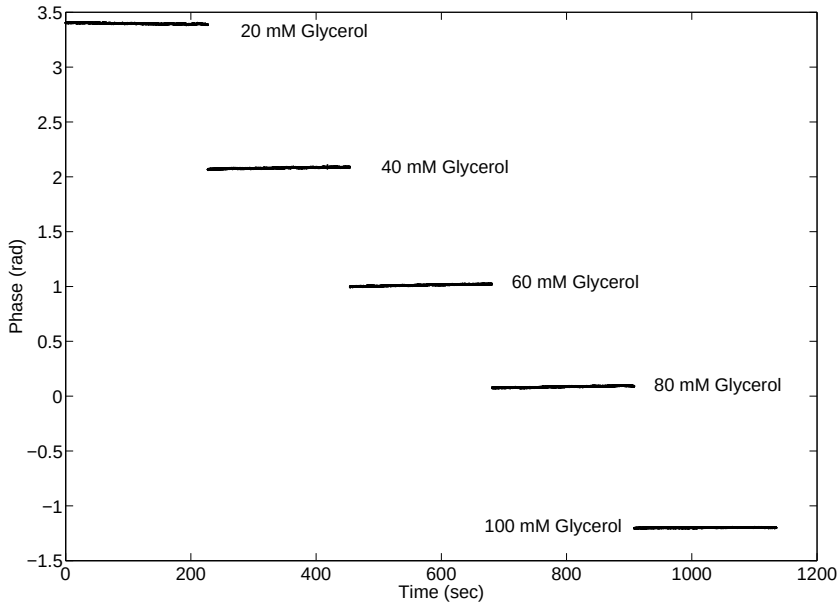

Figure 65. Concentration calibration run. The refractive index has been increased by raising the glycerol concentration in the aqueous sample solutions. The concentration has changed from 20mM to 100 mM in 20mM steps.

The average signal and standard deviation is found for each concentration level and plotted in Figure 66. The slope of the best fitted line ($R^2 = 0.996_7$) is found.

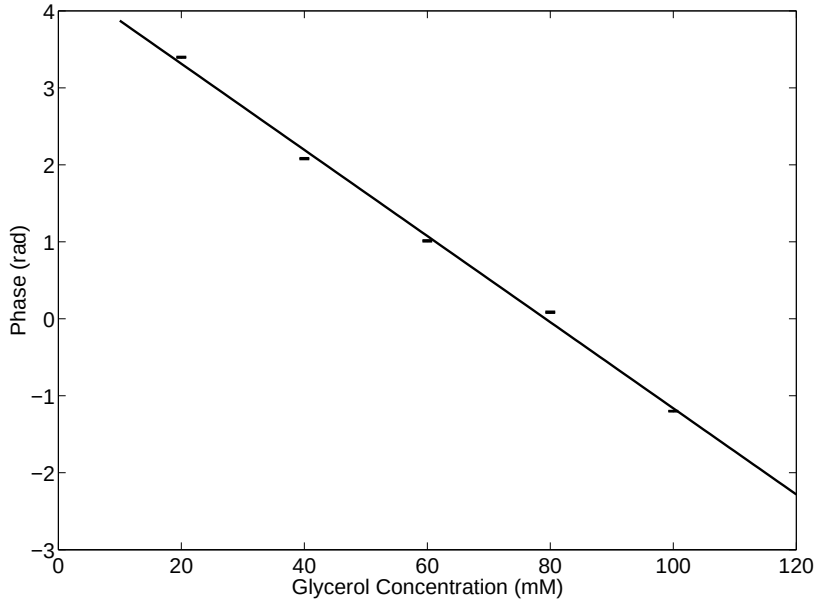

Figure 66. From glycerol concentration series a calibration curve is shown. The slope of the fitted line is directly linked to the sensitivity of the sensor. The errorbars shown reveals the high signal to noise level.

Thereby the detection limit can be derived, se Equation 86.

$$D.L. = \frac{3 \cdot \sigma}{|\alpha|} \cdot \frac{dn}{dC}_{glycerol} = \frac{3 \cdot 0.005549}{0.0559} \cdot 1.32 \cdot 10^{-5} = 3.93 \cdot 10^{-6} \Delta n (86)$$

As these experiments has been repeated the procedure is to find the best fringe pattern before a run. Thereby the spot on the channel has been moved. So for some millimeters the channel has shown an average sensitivity of $1.8 \cdot 10^{-5} \Delta n$ showing the robustness of this sensor. This sensitivity is comparable to what has been obtained before with other flow chips, other materials and geometry [25, 30, 106]. The best detection limits is believed to arise when the structure is the most specular.

6.3 Summary

A complete procedure for making a highly sensitive device comprising completely of polymer has been described by the master fabrication procedure in combination with the procedures from this section. Multiple chips has been injection molded and assembled into flow chips. The procedure can still be optimized, but for the first time it has been shown how Chip Scale Interferometry can be performed in a homogenous polymer platform, fabricated in a mass production like manor with competitive detection limits compared to fare more expensive flow chips. By developing two wet chemical etching procedures for silica glass and silicon, semicircular flow channels with sizes from 50 to 100 μm in radius has been fabricated. Using these fabricated structures as master tools, Ni–shims has been made from electroplating, making it possible to produce multiple flow chips in a cheap and high capacity fashion. The alignment of two semicircular flow channels and followed by sealing has made it possible to perform refractive index measurements on minute samples in micro–fluidic system with close to capillary geometry. This has shown great potential for the CSI scheme here proven to work in the intermediate material of transparent thermoplastic between hard and expensive fused silica and soft PDMS designs.

Multiple thermoplastic flow chips have been fabricated and assembled for chip scale interferometry. The CSI–sensor has shown detection limits of Δn = $2 \cdot 10^{-5}$, well in the range of monitoring biological relevant samples.

7 Label–free interferometric detection of biochemical interactions

When taking advantage of the laminar flow regime in micro fluidic, it has been possible to monitor bio molecular interactions as they occur. If quantitative data is to be obtained from these chemical reactions special care has to be taken for mixing the analytes. In micro fluidics making a useable mixer is not trivial. Here is presented work done with micro fluidics in order to obtain thermodynamic constants from the above mentioned interactions. Surface bound and reactions in free solution is described. DNA–hybridization and protein–protein interactions has been the subject of these studies.The setup is similar to the previously presented MIBD scheme except for the micro fluidic device and a beam splitter has not been used. In this case easy to fabricate PDMS flow chips have been utilized.

In this chapter experiments are presented that has been performed at Texas Tech University, Lubbock, Texas and Vanderbilt University, Nashville, Tennessee both in the US. The work has been performed in close collaboration with fellow students Joey Latham and Dmitry Markov from the Bornhop group.

7.1 Micro fluidics

Micro fluidics are handling and control of small volumes (10^{-15} –10^{-6} L). The liquid is contained in microscopic channels with dimensions in the range from 1 to 1000 μm. From everyday life micro fluidics is used in ink jet printers, when the nozzle delivers the tiny droplets to the paper. A relevant comparison is listed in table 14. Two important factors are listed as well as the measurement volume, number of molecules in the measurement volume and typical diffusion times for a oxygen and a protein molecule. Notable is the fast decreasing number of molecules

Table 14. Typical dimensions used in micro fluidics and their influence on important issues for sensing in these regimes. Diffusion coefficients used are $2 \cdot 10^{-9}$ $m^2 s^{-1}$ *and* $2 \cdot 10^{-11}$ $m^2 s^{-1}$ *for* O_2 *and protein, respectively, from [107].*

Volume	1 μL (10^{-6})	1 nL (10^{-9})	1 pL (10^{-12})	1 fL (10^{-15})
Characteristic length (d)	1 mm	100 μm	10 μm	1 μm
Number of molecules (1 nM concentration)	$6 \cdot 10^8$	$6 \cdot 10^5$	600	0.6
O_2 Diffusion-time across d	250 s	2.5 s	25 ms	250 μs
Protein diffusion–time across d	∼7 h	250 s	2.5 s	25 ms

present in a measurement volume. In this work we have been working in the regime given by the 1nL column.

In micro fluidics the flow of the liquid is laminar. Laminar flow can be described by adjacent layers of flow at different speeds with well–defined streamlines. At the fluid–solid interface the speed of the flow is zero. The fluid flows in parallel layers, with no disruption between the layers. The flow profile is said to be parabolic (in pressure driven flow, which is the case for this work). The dimensionless Reynold's number is usually used to describe if the flow is laminar or not. The Reynold's number is given by Equation 87 [108]:

$$Re = \frac{\rho \cdot v_s \cdot L}{\mu} \tag{87}$$

v_s is mean velocity, ρ is fluid density, μ is dynamic fluid viscosity and L is the characteristic length like the diameter of a tube. For circular tubes a Reynold's number under 2300 means a laminar flow. In micro fluidics the characteristic length is some hundreds of microns at the most usually resulting in Reynold's numbers around 50 and below. In this laminar flow regime the only exchange of material between adjacent layer is by diffusion. This means that by introducing one fully miscible liquid into another, the two liquids flows will stay separated [92] for a considerable time period. Diffusion across these adjacent flows takes time. Diffusion has been described by Fick. The distance traveled over time by diffusion is described by the Einstein-Smoluchowski equation [63], derived from Fick's first law of diffusion, see Equation 88.

$$d_{diff} = \sqrt{2 \cdot D \cdot t} \tag{88}$$

D being the diffusion coefficient and t is time. One big advantage of micro fluidics is the high degree of control of the liquid and flow systems can be designed like integrated circuits with full control of the liquid handling [109]. This means that multiple liquid samples can be introduced into each other with very little consumption of sample. But a challenge is often to mix the analyte samples. As stated above the only possibility of exchange is by diffusion.

Basically "the art of micro mixing" is to efficiently maximize the interfacial surface area and concentration gradient. Mixing can be split into two characters, active and passive mixing. Active mixing is when energy from outside the flow system is introduced to the liquid to enhance mixing. Examples are listed in table 15, [44]. Usually all these active mixing schemes will be complicated to implement into a flow system. Passive mixing uses the flow energy to maximize mixing, examples are also listed in table 15. With passive mixing it is still diffusion based, but as with creation of eddies the surface area of the liquid plug is increased, thereby decreasing the length needed to diffuse before mixing has occurred.

A fast, efficient, in–line mixer is needed to mix the proteins together as rapidly and as uniformly as possible if free-solution protein binding studies are to be possible. Guided by our collaborator Dr. Stremler (Vanderbilt Mechanical Engineering) several micro fluidic mixing techniques were designed and the applicability to our system was investigated. One straightforward way to accomplish mixing is through "hydrodynamic focusing"–reducing the channel width drastically, so the channel appears to be squeezed. Yet, other methods can work more efficiently and less stressful to biological molecules. There are two important considerations related to fluid transport of the proteins:(1) how completely the complementary proteins interact (i.e. what percentage of sample ends up binding – ideally 100% is desired for different molar ratios of the pair), and (2) how much time elapses between the

Table 15. Examples on active and passive mixing techniques.

	Active mixing
Integrated micro valves/pumps	[110]
Magneto-hydrodynamic action	[111]
Ultrasound	[112]
Electrokinetic instabilities	[113]
Acoustically induced vibrations	[114]
Periodic change in flow rate	[115]
Electro wetting induced joint of droplets	[116]
Piezoelectric vibrating membranes	[117]
	Passive mixing
Nozzle injections in flow	[118]
Interdigital multi–lamellae	[119]
Split–and–Recombine	[120]
Chaotic mixing be eddy formation and folding	[121, 122, 43]

initiation of binding and the initiation of observation (Ideally this time is negligible with the need to measure at the time of mixing). It is also desirable that all binding events start at approximately the same time. Despite the small length scales involved (less than 100 μm), relying solely on molecular diffusion to produce the necessary protein-protein interactions could take too long. Our objective is to augment diffusion by using different (fixed) channel geometries to produce flows that, in effect, stir the proteins together. The effectiveness of using channel geometry to enhance mixing in microscale flows is well documented [123, 124], and the importance of applying these techniques to biological and chemical analysis is well understood [125] –[130].

Our preliminary model is a two–dimensional representation of a channel that mixes two different solutions with 'hydrodynamic focusing' , see Figure 67 A. The actual modeling has been done in Dr. Stremler's lab, with input and discussions by the Bornhop group. In this paragraph is shown the results and the discussion thereof. This channel mixes by constricting the flow (in the case from 70 μm down to 16 μm), which stretches the interface between the two solutions and enables diffusion to more rapidly homogenize the flow [131, 132]. In the results shown, the two solutions enter the mixing channel at the left and flow is from left to right. The initial 70 μm–wide channel is 375 μm long, the 16 μm–wide center section is 200 μm long, and the final 70 μm–wide section is 300 μm long. In order to illustrate the mixing, the top incoming stream is assumed to contain a uniform concentration of 'black/dark' molecule with $D = 0.5\mu m^2/ms$. Figure 67 (A) shows the distribution of 'black' molecule when the flow rate through the channel is $Q = 0.2\mu L/min$, typical or at least the same order of magnitude for our experiment– (giving 4mm/s in the constriction). Diffusive mixing in a straight channel is shown for comparison. It is clear that hydrodynamic focusing enhances protein transport across the channel. Ultimately the proteins should be transported into the observation region as quickly as possible. However, as the flow rate through a hydrodynamic system is increased, diffusion has less time to mix the streams and the concentration will be less uniform. This dependence is

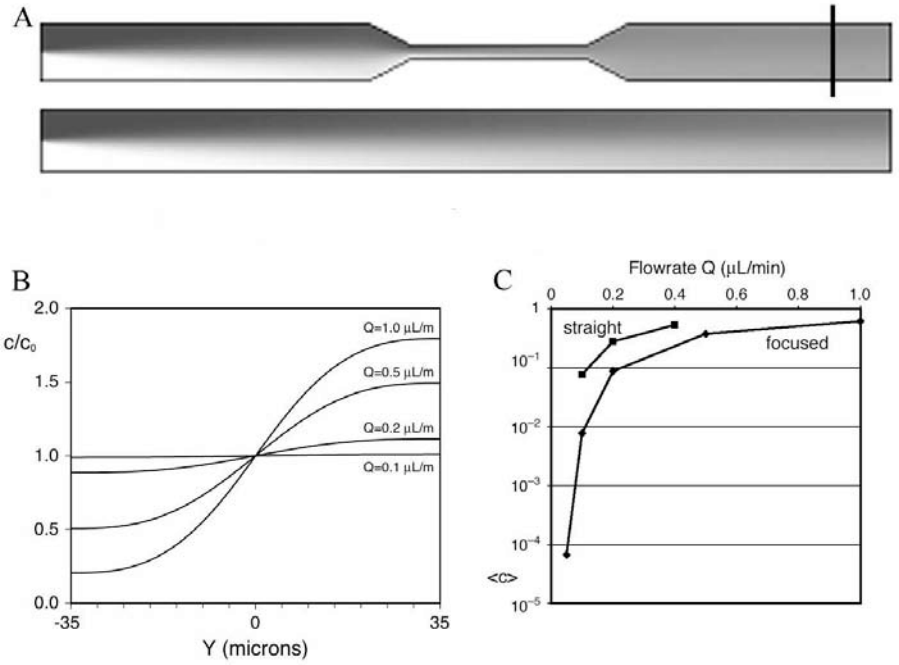

Figure 67. A: Gray scale comparison of modeled diffusion mixing. A hydrodynamic focus will mix better than a straight line. Gray scale is dark mixed with light, at complete mix the channel is uniformly gray. B: Concentration gradient at the position, indicated by vertical line in A, and at various flow rates. C: Mixing performance as a function of flow rate.

shown in Figure 67 (B) by monitoring the variation in concentration across the channel at a cross–section 900 μm downstream from the inlet.

Local concentration values are normalized by the average concentration, c_0, obtained when the two streams are perfectly mixed. The uniformity of the concentration can be quantified by a normalized mean square variation about the average concentration c_0, namely,

$$< c > = \sqrt{\frac{\sum (1 - \frac{c}{c_0})^2}{N}} \tag{89}$$

The variation of $< c >$ with flow rate is shown in Figure 67 (C) for the 'hydrodynamic focusing' channel and a straight channel, with values of $< c >$ less than 10^{-1} giving reasonable uniformity across the channel cross section. The figure shows good mixing is achieved in the focused channel for the target flow rates (Q around 0.1–0.2 μL/min or average velocity of ca. 2–4mm/s in the narrow region). It is noteworthy that for $Q = 0.2\mu L/min$, proteins traveling at the average fluid velocity will take approximately 0.75 s to travel through the focusing channel, while proteins traveling at the maximum velocity will travel through in ca. 0.5 s. In order to achieve an equivalent level of mixing in the straight channel we would need to use half as rapid ($Q = 0.1\mu L/min$). In this case, the average protein travel time is 1.8s, with the minimum travel time 1.2s. Note that in both of these cases the velocity profile is parabolic, so there is a uniform distribution of exit times, with those proteins starting out near the channel wall taking significantly longer to travel through system and taking longer to see a complementary molecule from

the other stream. Therefore it is likely each bound pair will be at a different stage in their evolution when reaching the imaging window.

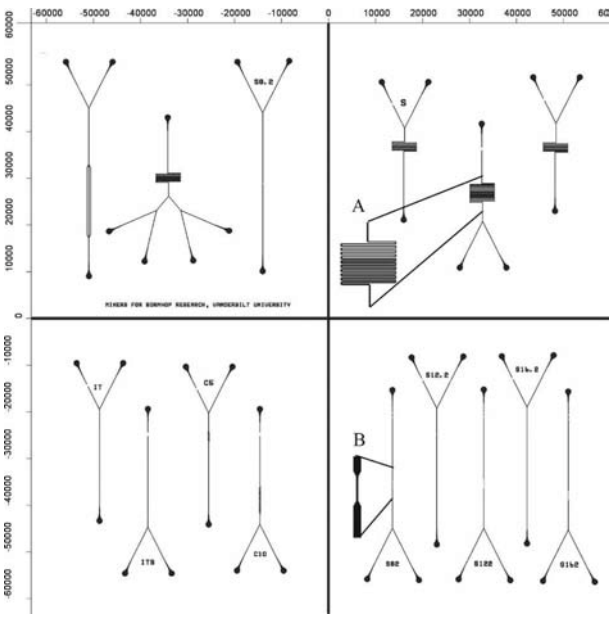

Figure 68. Schematic of photolithographic Cr mask for PDMS chip fabrication. (A) is a magnification of a serpentine mixer. (B) is a magnification of squeezed channel.

Figure 68 shows the layout of our photolithographic chromium mask, fabricated by DeltaMask (Netherlands), used to fabricate chips with mixers. This mask has 'hydrodynamic', serpentine and combined 'hydrodynamic'– serpentine mixers. Included on the mask 10 and 20 u–turn serpentines (Figure 68 A) where mixing is occurring primarily due to the race track effect encountered at the bend leading to a distortion of the laminar flow profile.

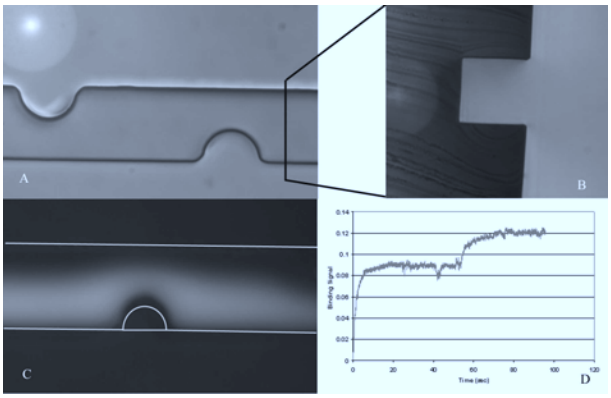

Figure 69. A: Top view of internal bump mixer made in PDMS. B: is the side view of the channel showing its sharp corner geometry. C: Top view of the internal bump mixer with a fluorescent dye flowing through, channel walls is overlayed. The dye is not mixed well in this mixer. D: Incomplete mixing result in binding curves with more than one binding event appearing. This is Calmodulin (16.7kDa) reacting with M13 peptide (2kDa).

Also included on the mask are mixers named 'internal bumps'. The idea is that the race track effect should mix the samples in straight channel. This would have a smaller foot print on the wafer. This is only relevant for a high density packed micro fluidic chip. The mixer is depicted in Figure 69 A. The mixer was tested using fluorescent dye in water. The mixing of the two liquids was incomplete as seen in Figure 69 C. As a result of incomplete mixing binding appears to be a two step process, Figure 69 D. Binding curves has to have a single exponential rise in order to make any sense with the system used in this work.

PDMS chip fabrication

The fabrication of these elastomer chips is done using SU8 as the negative photoresist in a normal photolithography process. Whitesides et al [92, 94, 133, 134] has described how this process can be used for fast prototyping. Some are more suited for single use and production of more than one, than others. PDMS has grown to be a much used material for micro fluidics by others as well [135, 136]. The process flow is shown in Figure 70 and each step is described from 1 to 10.

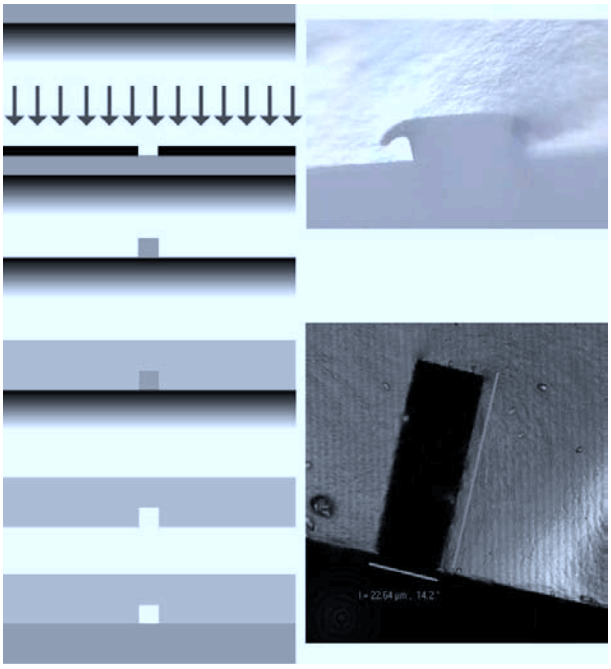

Figure 70. Left: PDMS process flow. It is a standard process in making PDMS micro fluidic systems. Upper right: Microscope image of PDMS channel made without SU8–filter. The upper part of the PDMS has a gutter–like feature, which is unwanted. Lower right: PDMS channel fabricated with SU8–filter, se text for details. The channel is 20µm wide and 70µm tall.

1. Spin coat photoresist. The spin–speed is to give 70μm thick SU8 photoresist.
2. Pre–exposure bake. 3 minute at 60°C on hot plate followed by 10 minutes at 90°C on hot plate.
3. UV exposure. In between the UV–light source on the Karl Süss maskaligner and the lithography mask is placed a glass plate with 30 micron thick SU8 resist. This resist has already been exposed and developed and is now absorbing the light below 350nm. Vertical sidewalls is then accomplished since the transmission through the entire thickness of the resist (both filter and unexposed) is very high. The exposure time is bulb dependent and needs to be verified for each bulb, where the intensity drops over time.
4. Post–exposure bake. 30 minutes in a oven at 90°C .
5. Photoresist development. Developed for 3 minutes in Microchem SU8 developer. Then rinsed in isopropanol. If the liquid turns white there is still undeveloped SU8 on the wafer. Drying is done by cleaned air or nitrogen.
6. Hard bake. After development the SU8 is hardened for 2 hours in a oven at 150°C.
7. Silanize the surface. The microstructure is covered with HMDS for 30 minutes to insert a slip layer in between the structure and the PDMS.
8. Molding/curing of PDMS. PDMS is prepared as described in the PDMS procedure.
9. Plasma oxidation. The PDMS surface is plasma oxidized to insert hydroxy–groups into the surface making the inside of the channel hydrophilic and better seal to the glass surface.
10. Seal micro channel on glass slide. The slap of PDMS is placed on a glass slide sealing the flow channel. Access to the channels are done by punching holes through the PDMS into the droplet shaped reservoirs.

7.2 Surface bound experiments

In order to accurately characterize molecular interactions, determinations should be done in a label–free manner [137, 138]. Furthermore, in order to have the capability to fully evaluate the molecular diversity that exists in nature, it would be most advantageous to make these determinations with micro–total– analysis systems (μ–TAS) [139, 140] configured for high throughput [141, 142]. Yet, conventional detection methods are difficult to implement in μ –TAS and are often volume– or sensitivity– limited, both impediments to performing systems biology analyses.

Investigators have developed various detection methods for use with microfluidic devices that have promise for label–free nanoscale detection. These include the nanoelectrode [143], the porous Si (p–Si)sensor [144, 145], the surface plasmon resonance (SPR) detector [146]–[149], and backscattering interferometry [24, 51, 99]. However, nanoelectrodes foul easily in real–world applications and require multistep manufacturing procedures for the integration into microfluidic chips. The SPR and p–Si methods are sensitive (detection limits of $\approx$ 10-50 nM for protein interactions [144, 145, 150]) and capable of sensing label–free biochemical interactions, yet neither technique is inherently compatible with μ–TAS. Integration or immobilization of p–Si into the fluidic network and long solute–diffusion times hinder the use of this method in μ–TAS. Since SPR relies on the excitation of plasmons - collective oscillations of free electrons that occur predominantly in metals - SPR surfaces are coated with a thin metal layer (for example, gold). This makes integration of SPR sensors into plastics challenging and relatively expensive due to the deposition process. Additionally, the elaborate surface chemistry used to immobilize targets on SPR surfaces has been shown to lose as much as 20 % of binding capacity over a 24–hour period [146]. Backscattering interferometry in rectangular channels (BIRC) [51] was recently shown to be applicable to label–free assays, can be used to study reversible molecular interactions in poly(dimethylsiloxane)(PDMS) chips, and is compatible with μ–TAS. Although promising, BIRC has been limited by tedious immobilization chemistry and, due to less than optimum transduction–scheme concentration detection limits, has bordered on relevance to biological systems.

Here we address many of these problems through the use of simple and robust surface immobilization chemistry on polymer chips and an improved BIRC instrument based on charge–coupled–device (CCD) transduction and fringe pattern Fourier analysis. For the first time, it is shown that simple photoactivatable surface chemistry [151, 152] can be used for the immobilization of substrates onto PDMS–facilitated, label– free, reversible–binding assays. This simplified approach to surface immobilization is a significant alteration to our earlier binding studies and those methods commonly used for surface activation/immobilization chemistry [148, 153].

A two–step biotin/avidin reaction, see Figure 71, with a carbene–generating form of photobiotin consisting of a biotin moiety, spacer arm, and photoactivatable group was used to immobilize target molecules of interest. A solution (7 μL)of

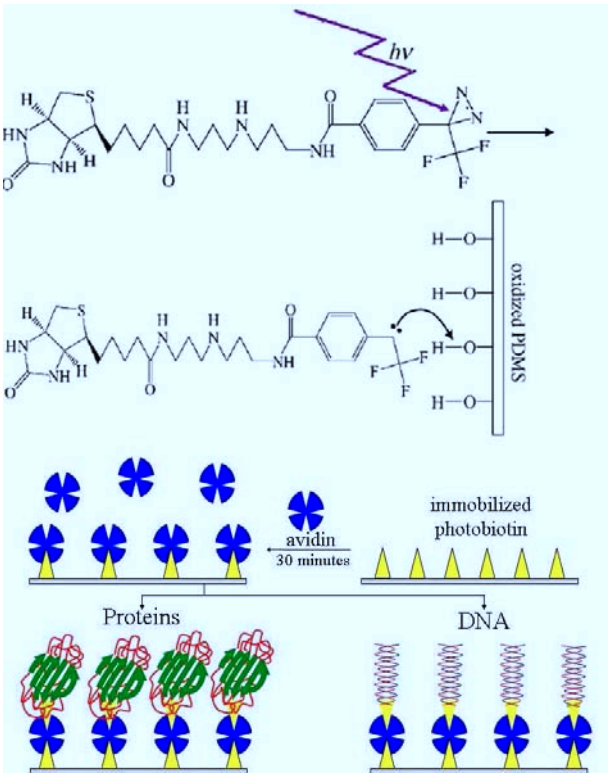

Figure 71. Top: Photobiotin is activated upon exposure to UV light and this promotes insertion into the oxidized PDMS substrate. Center: Avidin binds strongly to the immobilized layer of biotin. The tetrameric nature of avidin signifies that it can simultaneously bind the surfacebound biotin as well as any biotinylated target molecule that passes through the channel (bottom).

carbene–generating photobiotin ($0.5mg/mL^{-1}$) containing 0.02 % Tween 20 and 50 %(v/v) acetone was introduced into the PDMS channels and allowed to dry. Irradiation of the photobiotin molecule caused photolysis of the diazirine group, thereby producing an electronically excited np* state. Formation of an excited–state diradical was followed by internal conversion and production of a carbene. The highly reactive carbene was then inserted into the oxidized substrate. As a result, a homogeneous layer of biotin molecules was strongly bound to the channel surface. A solution of extravidin ($0.5mg/mL^{-1}$) was injected into the same channels and allowed to incubate for 30 min. Extravidin recognizes the imidazole ring that is cis fused to a tetrahydrothiophene ring, and binds to biotin with high affinity (association constant, $K_a = 2.5 \cdot 10^{11} M^{-1}$) [154]. The resulting biotin/avidin complex is very stable to changes in temperature, pH value, and denaturingagents, unlike the lysine/glutaraldehyde/streptavidin/ethanolamine sandwich described in earlier binding experiments performed in the group [51]. Fluorescence images (not shown) of fluorescein isothiocyanate (FITC) labeled avidin were used to confirm that the surface chemistry used for immobilization was successful. Thus, biotinylated targets can be immobilized onto the PDMS–molded channel surface to result in a cost–effective, disposable chip that is applicable to the analysis of a variety of reversible biochemical interactions. As described in detail above

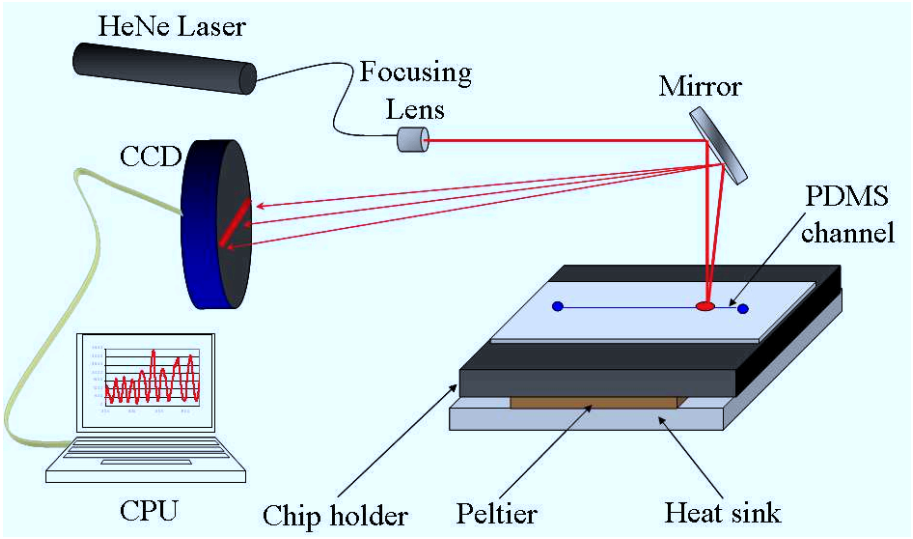

Figure 72. Top: Schematic diagram of BIRC showing the simple optical train consisting of a connected light source, a microfluidic channel, and a phototransducer.

and elsewhere, [30, 51, 50, 99] BIRC , see Figure 72, employs a connected light source that illuminates a microfluidic channel, thereby creating a series of high–contrast interference fringes in the backscattered direction that shift with the optical pathlength. Herein we show that the overall performance of BIRC can be improved 100–fold through proper design and implementation of the photo–transduction method. Use of a CCD combined with spatial Fourier analysis [99] for signal transduction, rather than an avalanche photodiode detector, facilitates improved sensitivity and reproducibility, while greatly simplifying alignment. Direction of multiple fringes onto the CCD array promotes signal averaging and enhanced signal–to–noise (S/N) results. A fringe–pattern Fourier transformation (FFT) algorithm is inherently insensitive to laser–intensity fluctuations [99] and allows spatial phase determination. Since the CCD is a large–area device, three to upwards of eight fringes from the interference pattern can be used, thereby eliminating the need to align the slit–photo–detector with respect to $1/e^2$ intensity on a particular fringe.

Protein A – IgG interactions

To evaluate the new immobilization chemistry and transduction method, two reversibly binding pairs were studied, protein A linked to immunoglobulin G (IgG) and a 30–mer DNA-DNA pair. Protein A, containing four high–affinity ($K_a = 2 \cdot 10^8 - 4.54 \cdot 10^8 M^{-1}$) bindingsites capable of interacting with the F_c region of IgG from several species, including human and rabbit, was immobilized onto a PDMS chip by using the chemistry shown in Figure 71. The reversible–binding assay of Protein A with IgG was repeated five times , see Figure 73. The non–complementary fragment, Fab ,served as the control and showed no signal (change in refractive index/phase; data not shown) when introduced into the Protein A–coated channel. As seen in Figure 73, reversible–binding events can be monitored with an excellent S/N ratio. If it is assumed that complete reaction

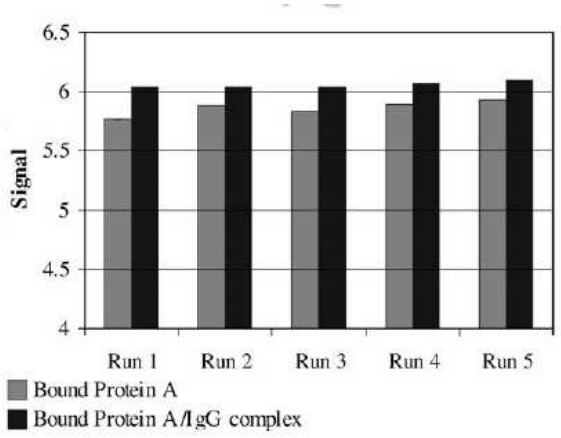

Figure 73. Biotinylated Protein A was immobilized on the channel surface. Unreacted Protein A was washed out with phosphate–buffered saline (PBS)/ Tween 20. A human IgG F_c solution ($0.5 mg mL^{-1}$)in PBS was introduced into the microfluidic channel and allowed to bind to the Protein A for 5 min. The channel was then rinsed with PBS/Tween 20 to remove any unbound IgG. Removal of the bound IgG from Protein A was performed by using an acetic acid wash.

between the bindingpair took place, and based on the target–surface coverage, the 3σ detection limit is $4 \cdot 10^{-17}$ mol (40 attomol) in a 500–pL probe volume. These results represent an increase in sensitivity of two orders of magnitude when they are compared to the Protein A /IgG experiments performed previously[51].

DNA–DNA interactions

The use of microfluidic chips to perform nucleic acid analysis has allowed the detection and discrimination of multiple DNA sequences [155, 156] and can eventually facilitate high–throughput screening techniques [157].

As further demonstration of the utility of BIRC, a label–free reversible DNA assay was performed, see Figure 74. Immobilization of a biotinylated 30–mer of mActin (5ACTCATCGTACTCCTGCTTGCTGATCCACA–3) $M_W = 9622.5$; melting temperature, $T_M = 68.7\ ^\circ C$ onto the PDMS channel was possible with the biotin/avidin surface chemistry described above.

Non–labeled complementary DNA strands were successively hybridized to the immobilized mActin 30–mer and then removed with an NaOH wash. Bindingevents of complementary DNA followed exponential growth for BIRC over concentrations ranging from 5 nM up to roughly 500 mM with excellent convergence ($R^2 = 0.988$). A noncomplementary probe strand, according to the Watson-Crick model, served as the control and showed no appreciable signal. If it is assumed that hybridization went to completion and 100 % channel–surface coverage was attained, at 3σ , 36 attomol DNA were quantifiable in a 500–pL detection volume. Ultimately, it would be desirable to screen for an array of different sequences in a label–free manner to avoid perturbations due to the signaling fluorophore or derivation chemistry. An example of such perturbations is shown in Figure 74, where a FITC–labeled probe has been used. The change in phase over time follows classic Michaelis behavior, thus enabling us to determine G_{bind} through a well established relationship $G_{bind} = -RT \cdot ln\ K_A$, where K_A is determined from line fitting techniques. The

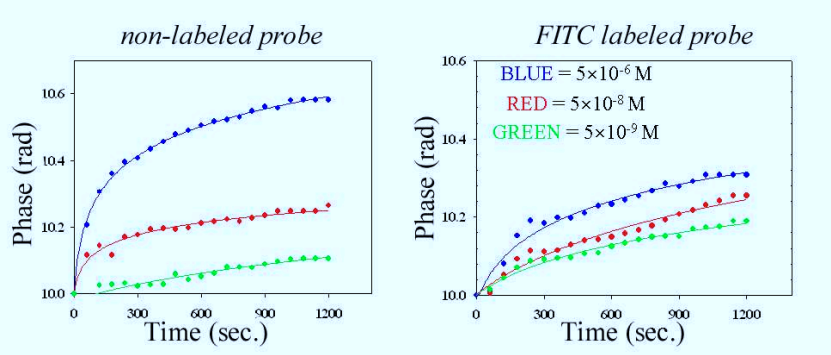

Figure 74. Left: The complementary probe strand was introduced into the channel after target immobilization and allowed to hybridize for 20 minutes. The channel was rinsed with PBS/Tween 20 to flush out any probe DNA that had not bound the immobilized target. Right: The FITC–labeled complementary probe strand was introduced into channel and examined in a similar fashion as the non–labeled probe strand. The change in signal is smaller due to the lower binding energy.

binding energy of DNA hybridization with the FITC labeled probe was found to be $-23.3kJ/mol$ (see Table 16). This result is similar to the $-22.2kJ/mol$ and $-23.9kJ/mol$ reported by Riccelli [158] for fluorescently labeled linear probes of 32 and 16 base strands respectively. Remarkably, the binding energy of DNA hybridization with a non–labeled probe was found to be $-30.9kJ/mol$, an improvement of approximately 7.6 kJ/mol over the binding energy of the FITC labeled probe. Assuming our observations are valid, a perturbation in the binding process caused by the FITC label can generate $> 24\%$ change in G compared to the native ligand. This dramatic alteration in binding affinity due to the FITC tag was also confirmed by a secondary method, ITC.

Table 16. Thermodynamical data extracted from two different methods, BIRC and ITC. The probes are complementary strands to the target DNA for both the non–labeled and the FITC–labeled case. The difference in binding energy between the two probes show excellent agreement between the methods used. The absolute value differs, which is mainly the difference between target being surface bound and in solution.

	ΔG (kJ/mol)		
Method	Non–labeled	FITC–labeled	Difference
BIRC	−30.9	−23.3	−7.6
ITC	−44.6	−37.5	−7.1

Calorimetry is a powerful, simple, and reliable technique, and generally is not used to its full potential. Free energies expressed as equilibrium constants, reaction rates and redox potentials are familiar and valuable to chemists since they refer directly to the chemical driving force for converting a given compound into another species or state. Unfortunately, there are relatively few processes where both rates and equilibrium constants are available. Generally, reactions that provide convenient kinetics proceed to completion and are far from equilibrium. As a result, calorimetry has been employed to determine enthalpy changes in situations where equilibrium constants were impossible to measure. A typical ITC experiment in-

volves titrating small, successive amounts of a ligand (protein, nucleic acid, etc.) into a sample cell containing protein or nucleic acid substrate (or vice versa) and measuring the heat evolved. As the binding sites on the macromolecule are filled, less heat is evolved in the titration. Once the macromolecule is saturated, the only heat evolved is a result of a heat of dilution. The heat peaks produced on the thermogram are integrated, and plotted vs. the mole fraction of macromolecule/ligand to produce a binding isotherm. In table 16 is summarized binding energies for labeled and non–labeled DNA probes. Although the ITC data shows higher absolute values of G compared to those determined by BIRC, it has been reported previously [159] that as much as a 25 kJ/mol difference was observed when comparing Gibbs' energies calculated with ITC and those determined by UV melting studies (UVM). I postulate that part of the difference is due to differences between liquid and surface bound hybridization. Furthermore, the kinetics and rates of reaction for surface bound reactions are less than ideal and can become quite complicated. Flavell [160] demonstrated that approximately 20%–30% of the probe molecules in the liquid phase will interact with themselves before being able to react with the surface bound target. In spite of the differences between ITC and BIRC absolute values (Table 16), both techniques show a nearly identical relative change due to the presence of FITC marker ($-7.1kJ/mol$ and $-7.6kJ/mol$).

A step toward avoiding these perturbations requires the determination of the discrimination that is possible with BIRC. We used an oligomer consisting of a three–base–pair mismatch (at positions 5, 15, and 25) from that of the complementary mActin strand as an initial test of specificity. The experiment consisted of immobilizing the mActin 30–mer as noted above and a subsequent repetitive hybridization test with a 5–μM solution of the mismatch strand. Figure 74 shows the typical output from one of the binding evaluations. Three trials of these experiments produced an average signal corresponding to $> 140\%$ of that for the control and approximately 7% of the signal for the complementary strand.

Table 17. Analytical Figures of Merit for the surfaces bound biomolecular interactions.

DNA Binding Study		
	Probe surface area	$2.9 \cdot 10^{-8} m^2$
	3σ detection limits	35.8 attomoles cDNA
	Corresponding mass detection limits	356 pg cDNA
Protein Binding Study		
	Detection Volume	495 pL
	3σ detection limits	40 attomoles IgG
	Corresponding mass detection limits	2 pg IgG

To summarize, the biotin/avidin surface chemistry significantly simplified substrate preparation, was compatible with PDMS, and facilitated free–solution assays with BIRC. Combination of this new surface chemistry with the CCD FFT transduction has allowed improved detection for Protein A /IgG binding by two orders of magnitude [51]. BIRC was also used to monitor DNA hybridization over a wide range of concentrations and allowed discrimination in binding of a three–base–pair mismatch. The addition of a FITC-label to the cDNA probe perturbed the thermodynamic data, again emphasizing the need for label–free detection.

Use of PDMS microfluidic chips and the exceedingly simple optical train of BIRC represents a cost–effective platform for label–free molecular–interaction determinations as well as for the investigation of reversible biological interactions within subnanoliter volumes and at the attomole level. The methodology and technology are compatible with large–scale integration and should facilitate high–throughput assays.

7.3 Free solution experiments

Miniaturization of instrumentation has recently led μ–TAS technology have gained considerable attention and applications [161]. μ–TAS simplifies multiple analysis on an integrated device providing benefits including reduction in analyte and reagent consumption, shortened analysis times, system portability and inexpensive fabrication. Proteomics could be a major beneficiary of μ–TAS technology [162]–[167], allowing vast numbers of proteins to be identified while having their interactions, functions and pharmaceutical potential studied and understood. To be fully effective, protein binding and structure determinations should be performed in high–throughput without chemical labeling or derivation, so that the proteins and their ligands can be studied in their native state emulating the biological environment [145, 162, 163, 168]. The motivation for assays avoiding labels (i.e. label–free) is to eliminate the possibility that such labels may alter either the structure of a protein, its function, or its binding with another protein or other molecule. Protein binding assays should be done with a detection scheme that meets these requirements, label–free (fluorescent or radioactive) in a non–invasive fashion, and is compatible with microfluidic devices. Yet, presently used label-free detection technologies are inherently incompatible with high throughput schemes and microfluidics. Here is described a label–free method for free solution molecular interaction assays.

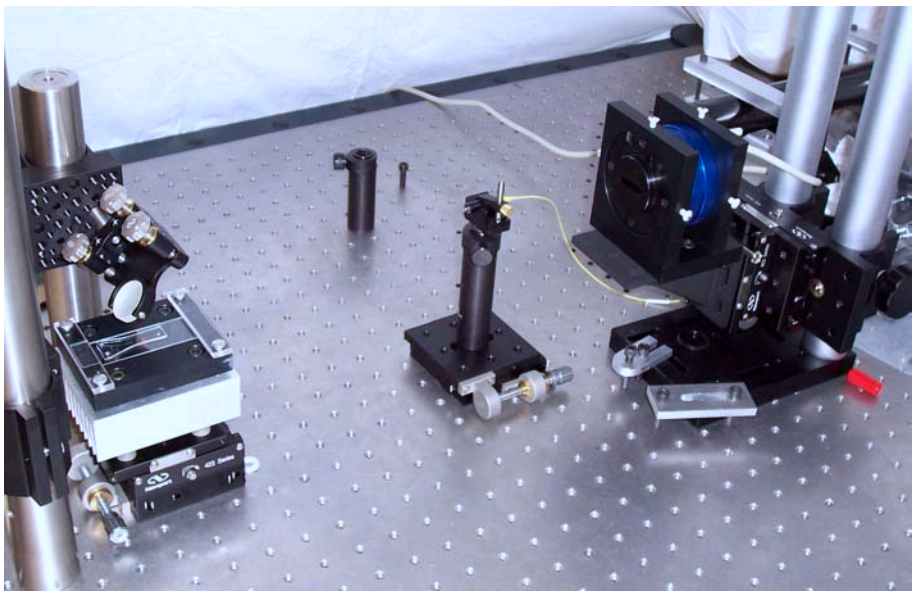

Figure 75. The laboratory setup shown with a PDMS flow chip as the micro channel system used. The light is guided in am optical fiber (yellow line), is reflected off the mirror and impinges the micro channel. The fringe pattern arising from the light–channel interaction is reflected from the mirror onto the CCD–linear array (blue tube), which is connected to the PC, doing the data analysis.

Protein A contains four high affinity ($K_a = 10^8 mole^{-1}$) binding sites capable of interacting with the F_c region of human or rabbit IgG. This protein-protein interaction is reasonably well studied and serves as a reference system for these experiments performed in the setup depicted in Figure 75. To demonstrate the potential of BIRC preliminary experiments were preformed with Protein A and IgG. Protein A (Pierce, Rockford, IL) was reconstituted in PBS buffer (pH = 7.4) at a concentration of $0.5 mg/mL$ and various solutions, ranging from 5 M to 100nM, of IgG F_c (Calbiochem, San Diego, CA) were made in PBS. The microfluidic chip used for the first experiments contained a channel with dimensions of 100 μm X 110 μm and a serpentine for in–line mixing of the ligand/receptor pair. Each sample

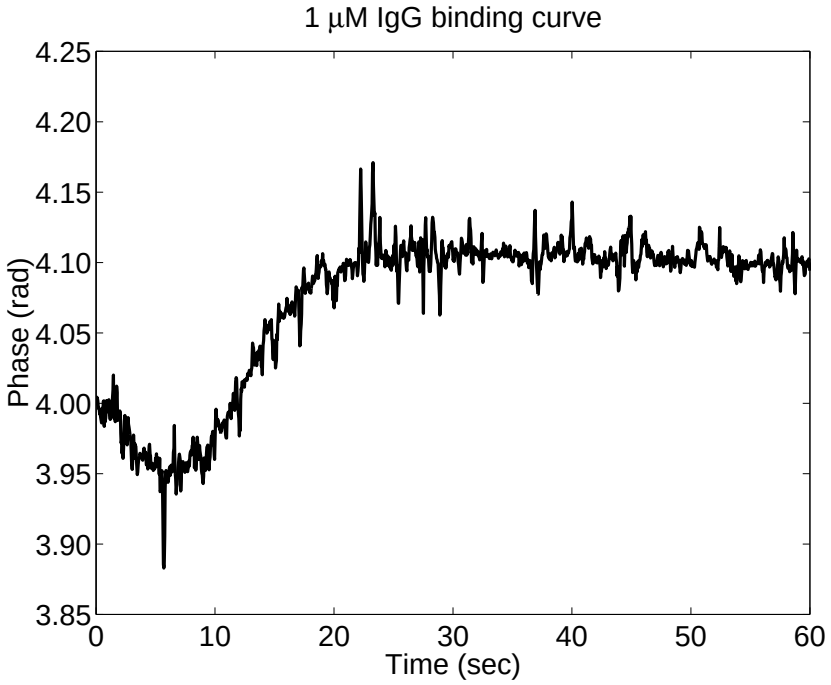

Figure 76. Free solution binding of IgG with Protein A by BIRC. The solution used for IgG and Protein A are 1 μM and 0.5mg/mL, respectively. The change in phase shows the change in the refractive index as interactions are taking place.

reservoir was filled with approximately 4–5 μL of either Protein A or IgG and a vacuum was applied to the outlet reservoir to draw the Protein A and IgG solutions through the mixer at a flow rate of approximately 100 μL/min. Once the liquids had passed through the mixer and into the detection zone, flow was stopped and the protein binding was monitored in real–time using BIRC at a sampling rate of 30Hz. Binding data for this initial free–solution, label–free Protein A – IgG binding experiment, see Figure 76, are analogous to enzyme kinetics following the Michaelis–Menten equation [169]. Shown in Figure 76 are studies using a 1 μM concentration of the IgG F_c fragment with Protein A at a constant concentration of 0.5mg/mL.

While preliminary, this initial set of experiments indicates, that protein binding interactions can be monitored in free solution and in real-time using BIRC.

By fitting a curve with a least square method as described in Equation 90 to the binding data, the concentration dependent value, K_{obs}, is determined. These observed K-values is then plotted according to their concentration as seen in Figure 77. The diagram is drawn for illustration purpose only with realistic values. A linear fit is made to the K_{obs}–data, Equation 91, and the dissociation constant, K_D, is found from the relation in Equation 92.

$$Curve\ fit\ :\ signal = a(1\ -\ e^{-k_{obs}\cdot t}) \tag{90}$$

$$y\ =\ m\cdot x\ +\ b \tag{91}$$

$$K_D\ =\ \frac{b}{m} \tag{92}$$

signal is the phase provided by the FFT rutine. a is the preexponential coefficient. k_{obs} is the fitting parameter and t is time. K_D is the dissociation constant extracted from the binding data.

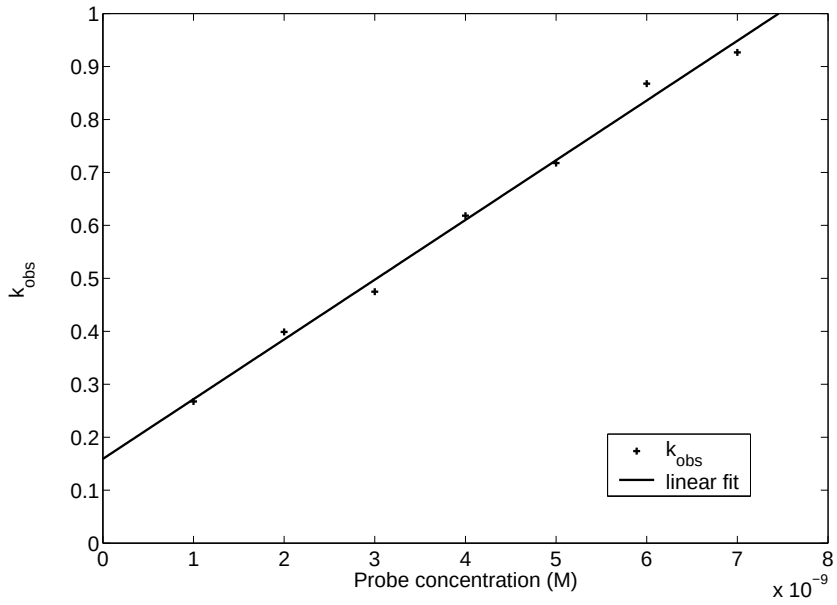

Figure 77. k_{obs} is shown as function of concentration. From the linear fit the dissociation constant is derived.

Traditionally a Scatchard–plot or Linewear–Burke–plot has been used, but that technique has some drawbacks such as basing the fit on the least changing binding curves, the worst S/N-ratio, and the need for complete reactions at maximum concentrations.

A complete set if binding curves is seen in Figure 78. The concentration of Human IgG F_c fragment was in the range from 10 nM to 100 nM. The data was filtered with 0.5 sec window. Also shown in Figure 78 is the control run, which was a PBS solution containing the Human IgG F_{AB} fragment. There is no appreciable change in signal for the control and blank (only PBS solution with Protein A) suggesting, for this system, protein adsorption to the substrate and nonspecific binding exhibit little influence on the technique. A new chip design was used with serpentine mixer plus a 20 μm wide squeezing part of the channel, with the laser imping shortly after the squeeze. From these binding–curves, Figure 78, the

binding energy, ΔG_{bind}, is found to be 3.48 nM. Literature values suggest energies ranging from $2.2 \cdot 10^{-8}$ to $5 \cdot 10^{-9}$M [170, 171].

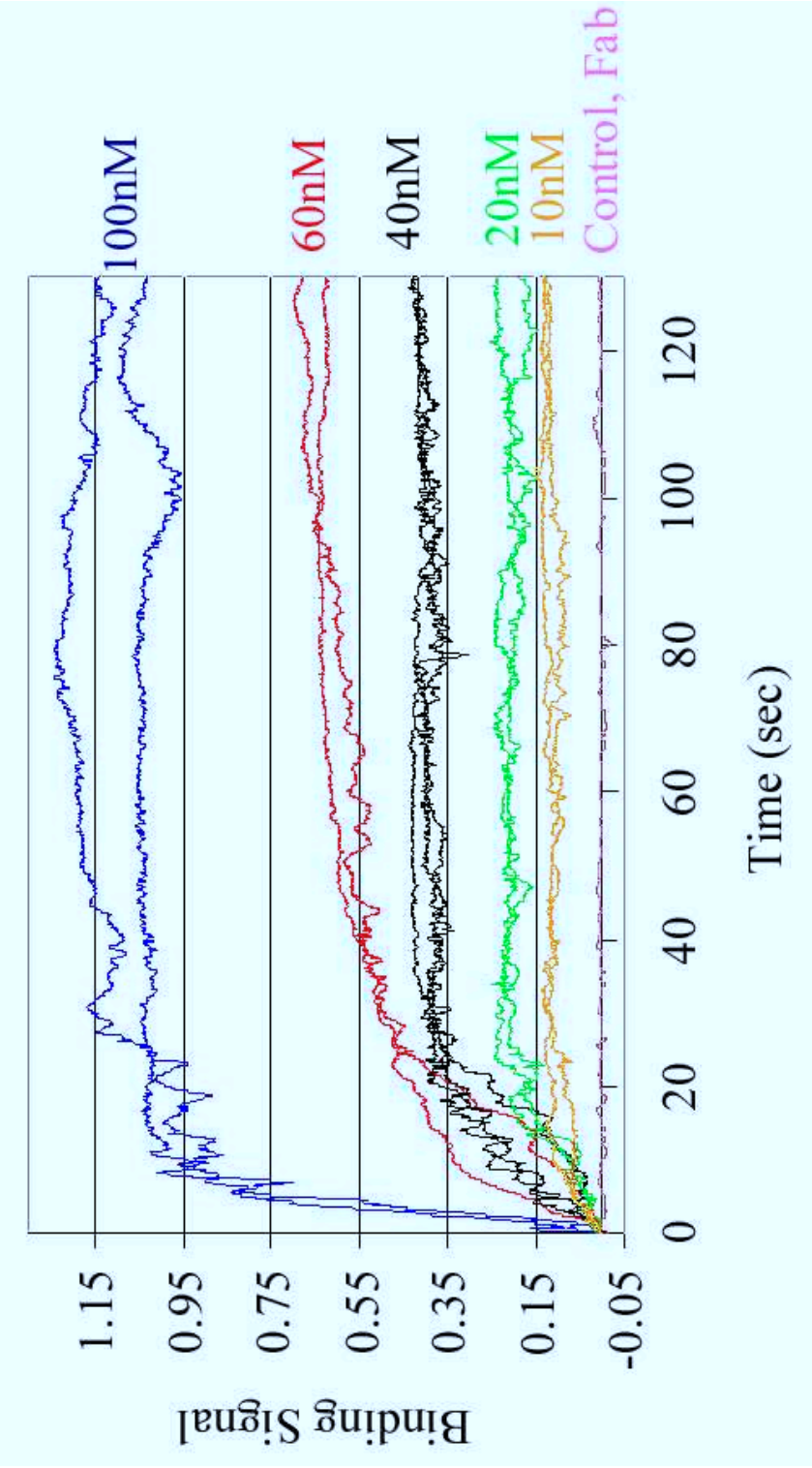

Figure 78. Complete set of binding curves. The concentration of Human IgG F_c is changed from 10 nM to 100 nM and the Protein A concentration is kept constant at 1 μM.

Table 18. Important numbers relevant to the free solution studies and Analytical Figures of Merit (A.F.M.) for the free solution biomolecular interactions.

Important numbers		
	Channel Dimensions	$70X70\mu$m with a 20μm squeeze
	Probe volume	495 pL
	Protein A	MW = 42 kDa
	conc. of Protein A	1μM
	Human IgG F_c	MW = 50 kDa
	conc. of Human IgG F_c	10nM – 100 nM + 1 μM
A.F.M.		
	3σ detection limits	9 attomoles IgG
	Corresponding mass detection limits	450 fg IgG
	K_D (dissociation)	$3.48 \cdot 10^{-9}M$
	k_f (forward)	$1 \cdot 10^6(M \cdot s)^{-1}$
	k_r (reverse)	$0.0025s^{-1}$

In summary, fairly easy to make PDMS flow chips has via the BIRC setup been used to obtained label–free binding data from protein–protein interactions while both reactants was in solution. Thereby eliminating the need for time–consuming surface preparation steps and perturbations of the thermodynamic results do the fact that one probe is bound to the surface limiting the freedom to move. The concentration needed for detection is smaller than the surface bound results (4 times). This might be caused by the fact that the change in refractive index occurs in the entire channel volume and not in the first nm of the PDMS surface. The thermodynamic data is comparable with ITC but in far smaller volumes of samples showing BIRC as the potentially better suited method to do these binding studies on relatively expensive analytes. To the best of my knowledge no other system can compete on the combination of sample volume, time, sensitivity and system simplicity for doing these label–free, in solution protein–protein interaction studies.

7.4 Summary

Different mixers has been tested in PDMS flow chips. The best suited mixer for the molecular system used is the serpentine or serpentine in combination with a squeeze. BIRC has been used for detecting bio molecular interactions both surface bound and in solution. Thermodynamic data has been extracted from binding curves monitored with BIRC. A single fluorophor attached to a 30'mer DNA string perturbed the binding energy considerably. The absolute energy found was different from that found with ITC, but the perturbation difference showed excellent agreement. The free solution protein binding experiments and results places BIRC in a unique position with comparable thermodynamic capabilities with the golden standard ITC, but orders of magnitude faster and less analyte sample consuming. All performed in a relative simple and price competitive manner.

8 Discussion

8.1 Comparisons and improvements

Modeling

In the modeling chapter several models have been described and how they compare. For the capillary models two different methods have been used to describe the system, the electromagnetic wave based and the ray tracing based. The wave based model is only valid for a cylindrical geometry. For this geometry the Bessel and Hankel functions can be used to find the solutions for the differential equations derived from Maxwell's equations. By using the wave based model an exact solution is found and the solutions are valid in all size–regimes. But as discussed earlier a larger feature will require a longer summation in order to keep precision high. This will lead to longer computation times. The computation times are independent of size in the ray tracing model. Here the angles and the propagation length of the ray is calculated. Accordingly the computation times for the ray tracing based model is much shorter, with proper programming in Matlab, as these calculations can be treated as vector elements, which is handled extremely fast by Matlab. Extremely small changes in dimensions have changed the fringe pattern for the ray tracing based model. A surface change of 10nm resulting in a shift does not give any physical meaning, though. The ray tracing model is based on geometrical optics. In this optical regime the dimensions has to be much larger than the wavelength in order for the model to be valid. This is one reason the more complex wave based model was developed as it is valid for changes smaller than the wavelength.

The accuracy of the two models is compared in Figure 79 for the first part of the fringe pattern.

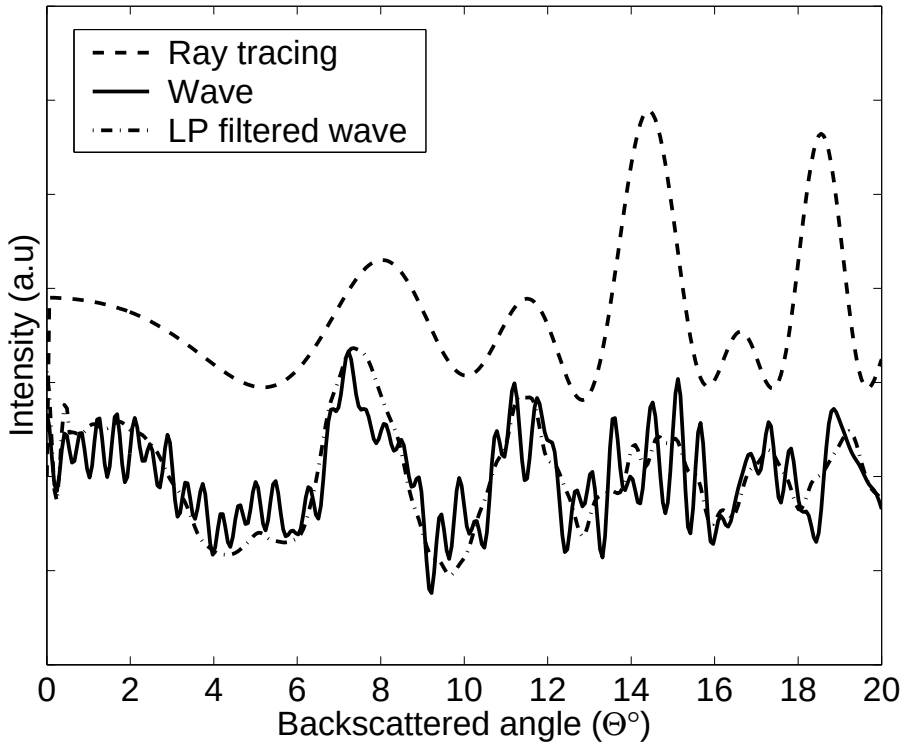

Figure 79. The ray tracing based fringe pattern and the wave based fringe pattern is shown. The ray tracing pattern is offset for clarity. The low pass filter (LP) is a moving average. The two models do show good agreement when describing the fringe pattern. The ray tracing model has a too large centroid and has the fringe positions further out than the wave based model.

A drawback of the wave based model is that it does not provide any information on what has occurred during the light propagations through the system. The ray tracing model has shown that at larger angles total internal reflection occurs and that can be used for determining the absolute refractive index. The wave based model only shows the pattern changing or some frequencies loosing intensity. In Table 19 is shown the comparison between models and experiment where the position of the total internal reflection occurs in angular space. The accuracy of

Table 19. Comparison between the experiment and the models on the prediction on total internal reflection from a 542 μm I.D. 673 μm O.D./24 μm cladding capillary. The uncertainty of the models due to production tolerances of the capillary corresponds to $\pm 6.9°$.

Refractive index	Experiment	Ray based	Wave based
1.333 (water)	$44° \pm 2.2°$	79°	43°
1.359 (ethanol)	$35° \pm 2.2°$	53°	42°
1.429 (ethylene glycol)	$25° \pm 2.2°$	36°	29°

the wave based model is higher than the ray based, seen as better agreement with

experiments. The ray tracing based model still is a good choice for describing the MIBD system. All features of the fringe of the fringe pattern has been shown by the relative fast ray tracing model, although only qualitatively. The total internal reflection method requires that the geometry is curved, so the MIBD method to determining the absolute refractive index cannot be used with the rectangular flow channels in PDMS chips.

Applying the affinity layer to the capillary would require two extra rays, but as mentioned above would not have any physical meaning. The wave based model has been used for describing the changes in the affinity layer. When the change in intensity is calculated for certain changes in the system variables, $\Delta I/I = 2 \cdot 10^{-4}$ for a change in refractive index from 1.42 to 1.44 and $\Delta I/I = 1 \cdot 10^{-4}$ for a thickness change of 1 nm. The $\Delta I/I$ between the Bohren–Huffmann model and this model is many orders of magnitude smaller, showing that the Protein A – Human IgG experiment can be described by this model. The model do also show a comparable change in the fringe pattern as the experiment does. The wave based model may be used to quantitatively describe the changes in the fringe pattern as the refractive index and dimensions is altered.

For more complex systems, e.g. entire chip systems with multiple channels or unusual geometries, ASAP can be used for setting up the model. It has shown to work for different geometries for the MIBD system and is readily prepared to handle more than one channel, without cross–talking though. The danger is though, that much information is "hidden" in the software and therefore is not a good solution for discovering the fundamental nature of the system. In the latest version of the ASAP software (ASAP 2005 version 1, release 3) a hybrid model is possible. A FDTD simulation can be incorporated and used as the basis for the light source. This would be a powerful tool for describing the sharp edged geometries as computing time should be reduced as the input of the FDTD model provides the precise wavefronts and the analysis and further propagation is handled by ASAP.

Fabrication

The uniformity of the HNA–etch used to make a nickel master hsa not been perfect. The fabrication has been severely depending on the quality of the etching mask used. The destruction of the mask has broadened the channel profile. The etching reproducibility is very low when the entire wafer is considered. The replication of the structures has though been able to show that with a better microstructure the patterned features will be copied into the polymer components with high reproducibility. As shown both experimentally and by theoretical work, the channel dimension has not had a large impact on the end results.

During the development of a useable fabrication procedure for making semicircular micro structures many partial results were found, that if implemented could provide even better sensing results. The stress introduced to the nitride mask may be reduced with different procedures. Preliminary results has been obtained by opening the nitride mask with laser ablation, in collaboration with Henrik Pranov, Danish Technological Institute, DK. In combination with the polishing etch used to smooth out the surface after laser ablation on silicon wafers (HF and HNO_3 only) very deep etches has been accomplished ($\sim 100\mu$m in radius), see Figure 80.

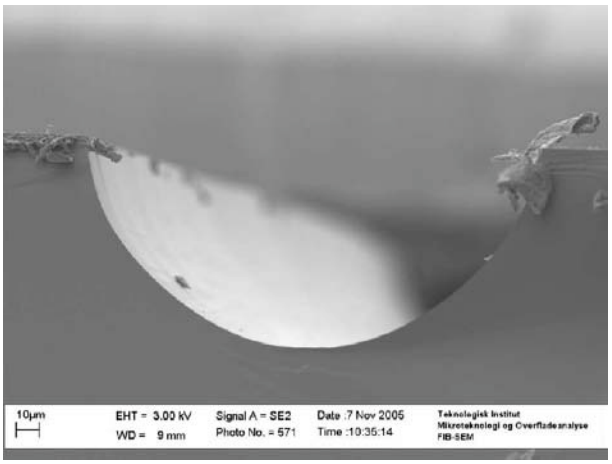

Figure 80. SEM image of isotropic etch in silicon with a HF and HNO_3 mixture. The silicon is protected by a silicon nitride, which is opened by a laser ablating the wafer.

The quality of the mask used is far better at the etching step than those previously used. For future applications the nitride–covered wafers should be purchased and not fabricated by a non–standardized lab. These newer wafers could be in the etching solution in degassing mode (on the sonication bath) for more than twice the amount of time the old ones could withstand and still with very few pinholes. By using the polishing etch, based only on HF and HNO_3 in the ratio (1:4) the surface roughness is found to be less than 100 nm.

The assembly of the injection molded chips has been done by heating and under a press in vacuum, see Figure 81, for some hours. In order to speed up production

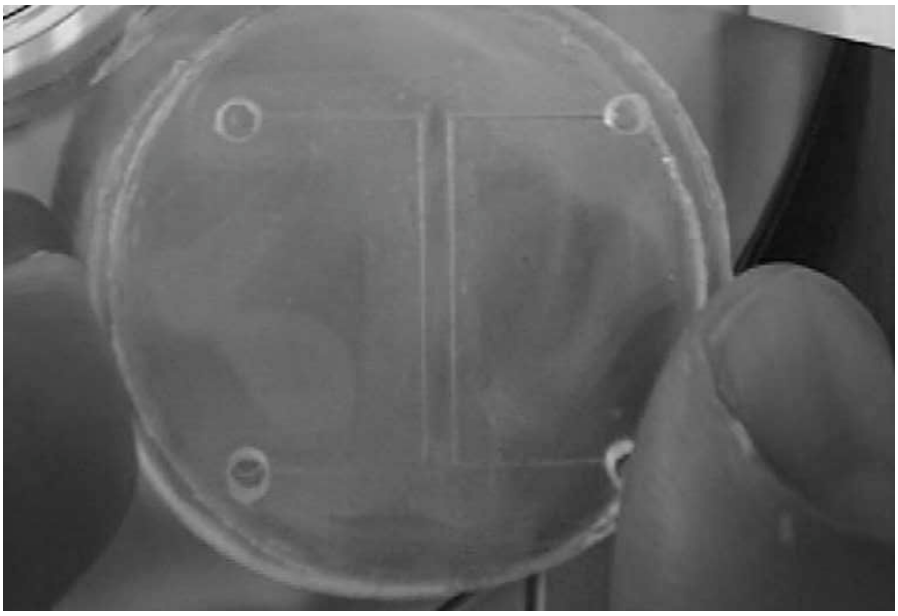

Figure 81. Image of a completed micro flow device. Two opposing injection molded parts has been aligned and assembled. These chips has been used for interferometric sensing performed on flow systems completely fabricated in Topas 8007 copolymer.

of such chips different methods for assembly is suggested. To help alignment when assembling the two parts self–guiding structures should be placed on the chip surface. To faster assemble the parts laser welding, gluing and sonication welding could be an option. The laser welding though requires an absorbing media on the surface, which could effect the performance of an affinity layer already on the surface. The same issue applies for gluing the pieces together although the temperature does not necessarily has to be increased, whereas both laser and sonication welding melts the polymer surface. The sonication welding is in this sense the cleanest as no extra media is applied to the surface.

Experiments

Low detection limits has been accomplished with the MIBD setup. As the concentration of e.g. glycerol increases in the water solutions used to construct calibration curves, the density changes giving rise to a shift in the fringe pattern. But when measuring the binding events the density in the measuring volume does not change. The change in refractive index must arise from at least two things. In all reactions heat is released or consumed during the reaction. This effect is seen to only provide small changes as there usually is much more water than reactants. A conformational change of proteins could also lead to a change in refractive index. As the overall dipole moment shifts between two protein states, the light – matter interaction changes shifting the position of the interference fringes. When Calmodulin reacts with just four Na-ions the protein molecule undergoes major changes going from an open to a closed state. Such a change should be detectable with the refractive index sensor, the shape change of the protein is huge.

In the chip based interferometry setup two geometries has been used, a curved channel and a rectangular shaped channel. From the ASAP modeling the circular channel should be more sensitive than the rectangular. It has not been possible for a direct comparison as different materials and dimensions have been used. The detection limits for the setups is found to be $7{\cdot}10^{-5}$ and $4{\cdot}10^{-6}$ for the rectangular and the curved channel, respectively. As both systems can be improved these limits will be pushed further down in the future, they cannot be used for direct comparison. But the slope found in the calibration curve is directly linked to the sensitivity. The rectangular geometry slope is 0.0038 and for the curved channel the slope is 0.041, showing a 10 times difference in sensitivity.

Data interrogation

For many applications it is not the mass detection limit, which is of interest but the concentrations involved. For the free solution binding our detection limit is found to be 9 atto moles Human IgG and the measurement volume is 495 pico liter, this corresponds to a concentration detection limit of 18nM. Other optical based techniques has lower limits, e.g. in the detection of bio–makers for Alzheimer's disease the detection limit is below 1 pM of the cleaved Tau protein [172]. The low limits is based on the sample preparation, which takes more than 24 hours and it is not performed label–free. The protein is bound to a Gold nano particle increasing the sample mass and refractive index considerately. A close competitive sensor is based on the surface plasmon resonance occurring when the evanescence wave excites a plasmon on the surface of a thin metal layer. At the moment their limits are at the beginning of the $\Delta n = 10^{-6}$ regime [173, 174]. Just recently the MIBD scheme has been published to reach the $\Delta n = 10^{-9}$ regime [27]. These low detection limits has been achieved by reducing the noise arising from temperature fluctuations. Two capillaries has been placed in close proximity of each other and impinged by the same laser. The two arising fringe patterns have been recorded simultaneously. The noise levels are reduced by subtracting one signal from the other. From [27] is found the different detection schemes used for the MIBD system and they are listed in Table 20.

Table 20. Comparison of detection limits produced by different interrogation methods for MIBD fringes. LBA is laser beam analyzer. DCDB is dual capillary dual bicell.

Method of interrogation	detection limits, $\Delta n =$	Ref.
slit–photodetector	$1.5 \cdot 10^{-7}$	[49]
CCD/LBA	$5 \cdot 10^{-5}$	[29]
CCD array w. FFT–routine	$7 \cdot 10^{-8}$	[41]
Bicell	$2.5 \cdot 10^{-6}$	[27]
DCDB	$6.9 \cdot 10^{-9}$	[27]

It is seen that introducing the reference capillary has improved the signal to noise ratio 360-fold compared to the single bicell. An further improvement would be to use the sample–reference setup with the CCD-array as the use of the FFT–routine also has an improving effect on the performance on the MIBD system. The FFT–routine is based on a sinusoidal signal and performs best with a regular fringe pattern (more than the 2nd fringe). An improvement of the system would be

if the fringe tracking algorithm takes into account that the centroid and the first part of the fringe pattern is better described by Bessel functions than a sinusoidal signal.

A self–calibration system based on the MIBD system would be a powerful tool in many analytical situations. The MIBD system can be self–calibrated by different designs. By knowing the absolute refractive index one is able to tell where you are positioned in refractive index space, which is not possible by the relative measurement as the fringe pattern repeats itself for every change in refractive index by 10^{-3}. Incorporated on a chip the channels could be designed so an autogenerated dilution series could be constructed thereby making a self–calibrated system. By using the sample and reference channel, a temperature calibration is made as changes only appears in the sample channel.

8.2 Applications

Cardiac Marker Detection

Using backscattering interferometry it is possible to perform entire K_D determinations with nanoliters total volume of solution and attomole amounts of protein. Here by studying molecular interactions (e.g. protein – protein, protein – DNA, etc) label-free, either in free solution or with surface–immobilized substrates it is possible to determine equilibrium constants, reaction rates, and monitor reaction kinetics in real–time on a single device in picoliter probe volumes. Entire k_{obs} plots can be obtained with nanoliters of the binding pair under investigation. The technology employs an interferometric backscatter detector, which serves as a non–invasive label–free optical detector that is fully compatible with micro fluidic networks and allows molecules to be studied in their native state. While several techniques have been developed to study molecular interactions and to measure these parameters (binding constants, reaction rates, etc) there is still a critical need to for a high throughput scheme that would facilitate these determinations in a label–free and non–invasive fashion and that is compatible with micro fluidics for reducing analyte consumption.

There are two different approaches commonly used for study binding equilibria, those performed in free solution and those where one of the binding pair is immobilized onto a surface. The first approach involves direct measurement of the free and bound ligand. An example of this approach is equilibrium dialysis [175]. There are a number of potential problems with this technique since it is not always convenient or easy to measure low concentrations. The second class of approaches, which includes: calorimetry, surface plasmon resonance (SPR), and On–Chip Interferometric Backcatter Detection (OCIBD), involve measurement of a physically observable parameter that is proportional to the extent of binding saturation of a ligand, protein, DNA fragment, etc. There are three distinct advantages to using calorimetry in order to gain a complete understanding of any binding interaction:

1. Heat is a universal signal, whenever two or more compounds are mixed together in solution, heat is evolved or absorbed by the system;

2. calorimetry is the only analytical technique where one can obtain a complete thermodynamic description of the binding process ($\Delta H, K_a, \Delta G, T\Delta S$) in one experiment;

3. optical transparency is not important as with some spectroscopic experiments.

In isothermal titration calorimetry (ITC), the degree of saturation of a binding site in a protein is defined in terms of the heat associated with the interaction between the ligand and the macromolecule. Yet, ITC is limited to large sample volumes (1.4 mL for VP–ITC instrument by MicroCal), has low throughput and is time consuming due to titration and equilibration time requirements, and is inherently difficult to multiplex. Currently MicroCal is attempting to develop an autosampling ITC instrument. SPR can be also employed for a label–free study of parameters of large bio–molecules such as reaction rates and equilibrium constants [146, 155, 176]. SPR is an optical technique based on total internal reflection. If the interface between two media (e.g. glass and a fluid) is illuminated from the side with higher refractive index, no refraction is observed past a certain angle (all of the light gets reflected). However, if a thin metal film, most commonly gold, is placed at the media interface a sharp intensity minimum will be observed in the reflected beam at a specific angle, because the energy is transferred to the surface film due to resonance coupling of light with the surface plasmons. The position of this intensity minimum is dependent on the refractive index of the media in close proximity of the gold surface. Therefore SPR responds to the mass of the biological molecules immobilized on the sensor surface. Since the signal is dependent on this interfacial refractive index change, this device can be used to obtain the reaction rates, association/dissociation rate constants, and equilibrium constants for ligand to a target immobilized on the gold surface. Detection limits of 10 pM for certain proteins are achievable with current commercial instruments (http://www.biacore.com). Recently published work by Corn and co-workers attests to the value of SPR for studying ligand–substrate binding [149][147]. While extremely powerful and becoming somewhat widely practiced, SPR has limitations that include: high instrumentation cost, the need for expensive gold slides and optics, and the requirement for surface immobilization chemistries, which can adversely affect the results of the measurements.

An alternative technique to ITC and SPR is On–Chip Interferometric Backscatter Detector OCIBD [24, 25, 30, 51, 177]. Unlike ITC, the unique optical train employed in OCIBD allows near real-time quantification of solutes at attomole levels and within detection volumes of tens of picoliters. The micro fluidic channel can be fabricated in a variety of materials such as glass, quartz, fused silica, or some polymers and it can be circular, semi-circular, or rectangular in cross-section. OCIBD is uniquely well suited for the label–free study of protein–ligand interactions and can be easily multiplexed. By simply incorporating multiple micro fluidic channels on a single chip in close proximity of each other and by scanning the laser beam across those channels, multiple analyses can be carried out rapidly, thereby making high–throughput molecular interaction system. Numerous determinations are possible using the OCIBD as a non–invasive optical detector for micro fluidic based investigations. We therefor believe OCIBD can be used as the core component in an integrated device that may overcome the limitations of existing binding assays. This is a fully integrated micro fluidics–based device for monitoring molecular interactions in real–time, permitting the determination of equilibrium constants, reaction rates and monitoring reaction kinetics in real–time with nanoliter to picoliter volumes of solution. It employs OCIBD with a micro fluidic titrator / mixer allowing molecules to be studied non–invasively and

label–free, in their native state. An additional advantage of the technology is that all determinations are performed on single chip within the same physical environment, reducing errors associated with changing experimental and environmental conditions.

Myocardial infarction constitutes a global health problem. Out of 52.2 million deaths worldwide in 2001, cardiovascular disease accounts for 25 to 45 % of deaths depending on the country [178] A myocardial infarction occurs when one of the coronary arteries becomes severely or totally blocked. When the heart muscle does not receive oxygenated blood, it will die in the affected areas. As the heart muscle deteriates proteins is introduced into the blood stream, some known as the cardiac markers. Currently cardiac markers are analyzed individually during the first critical hours when a myocardial infarction has occurred. There are several critical factors involved in determining the best suitable treatment of a patient, one important way is by investigating the concentration level and activity of the cardiac markers, which includes Troponin I, Troponin T, Creatine Kinase, Myoglobin and Creatine Kinase–Myoglobin. These are all present in the blood stream at increased levels after myocardial infarction and is measured at 30 to 700 ng/ml for Myoglobin (Cardiac Reader from Roche Diagnostics). As this molecule has a molecular weight of 18 kDa, the detection limit can be directly correlated to the previously obtained data with other proteins on the OCIBD system. At conservative limits the today available sensitivity can be enhanced by 5 orders of magnitude. By using model systems the final goal is to do a complete decisive analysis on whole blood at near–to real–time speed with unprecedented sensitivity at a bedside–like environment.

9 Conclusion

When illuminating a micro fluidic channel with a laser, a highly modulated fringe pattern occurs perpendicular to the channel. The bright and dark spots shift their angular position when changing the refractive index of the sampled liquid inside the channel. Monitoring this shift is the basis of this sensor. Performed in fused silica capillary tubes has been able to detect changes in the refractive index at 10^{-9} level.

The interferometric sensor has been under constant development in the last 10 years. One major step is to change from capillary tubes and into the micro fluidic network scenario. Normal photolithography processes and following casting of the micro structures usually results in rectangular shaped micro flow system. Those flow chips has been fabricated in elastomer material (PDMS). The reproducibility of these measurements depends critically on the flow channel dimensions. Hence, improvements in performance and system integration are predicted by transferring the well–defined capillary geometry to a rigid polymer chip–based system with a high degree of accuracy and reproducibility. Our channel systems are based on isotropic etching through narrow entry lines defined by photolithographic procedures. Photolithography has traditionally been employed for the generation of rectangular or triangular shaped channels. However, in this study we demonstrate its unconventional combination with isotropic wet etching in fused quartz and in silicon to form well–defined semicircular channels of cross–sectional dimensions of 50 to 100 μm. A number of optimizations of the etching mask have been performed for achieving a satisfactory geometry of the flow system. For the etching in fused quartz a metal mask has been used comprising a thin Cr layer for adhesion and a thick layer of Au for mechanical stability, using buffered HF as etchant. Etch channels in silicon were defined by a patterned Si_3N_4 layer, using a mixture of HF, nitric acid, and acetic acid as etchant. The etched channels have been characterized by microscopy performed on PDMS replicas and by 3D profilometric measurements. The structure, a half circle, is electroplated into a nickel replica that is subsequently used as mold for injection molding. Using these fabricated structures as master tools, Ni-shims has been made from electroplating, making it possible to produce multiple flow chips in a cheap and high capacity fashion. Multiple thermoplastic flow chips have been fabricated and assembled for chip scale interferometry. The chip scale interferometry–sensor has shown detection limits of $\Delta n = 4 \cdot 10^{-6}$, well in the range of monitoring biological relevant samples. This has shown great potential for the micro interferometric backscatter detection scheme here proven to work in the intermediate material of transparent thermoplastic between hard and expensive fused silica and soft PDMS designs.

Our new concept of investigating a larger range of interference fringes offers fundamentally new applications of the micro interferometric backscatter detection scheme. We have shown two possible ways of making absolute measurements of the refractive index of liquid in nanoliter probe volumes with a simple optical setup. The model based on ray tracing has been used to reveal and explain novel features of the interference pattern: An abrupt change in intensity at large backscattered angle is clearly present in the modeled system and in the experimental results. It is shown that this approach enables an absolute determination of the refractive index in the range from 1.33 to 1.5 by using capillary tubes of appropriate

dimensions. It has been proven that the model based on ray tracing may be used for qualitatively describing the MIBD phenomenon used for making absolute and relative measurements based on the fringe shift. The improved ray tracing model is capable of explaining all the significant features of the MIBD pattern except the stationary high frequency fringes. However, these fringes have been shown to originate from reflections from the edges of the capillary and thereby not being relevant for measuring the refractive index of the liquid within. Our model may be used to select the capillary, with the appropriate dimensions, that optimizes the sensitivity at a given refractive index interval, suited for a specific application. This has been done by changing from a 100μm ID/165μm OD/12μm cladding to a 542μm ID/673μm OD/24μm cladding capillary. We believe that the reported improvements for the MIBD scheme will significantly enhance the future applicability of the methodology for analysis of minute volumes of aqueous solutions. For the approach based on total internal reflection has been shown theoretically and demonstrated experimentally. The abrupt change in intensity corresponds to a precision in refractive index space of $2.5 \cdot 10^{-4}$.

The sensitivity of the chip with circular channels has been modeled for different diameters. It has been shown by the wave-based model, that the sensitivity in the range from 50 to 100 μm is almost constant, but is more dependent of the measuring point. The sensitivity is highest with the lowest angles and directly backscattered light. The detection of the centroid and the first fringes has been made possible by inserting a beam splitter into the optical setup, thereby folding the optical train forward. In all the wave based model has out performed the ray based model in agreement with experiments. The ray based model is though still accurate but much faster in computation times.

The electromagnetic wave based model has shown that the capillary can be used as a bio–sensor when an affinity layer is applied. Experiments has been performed by applying a biotin– ExtrAvidin– Protein A sandwich layer on the capillary surface and had it bind to Human IgG flowing in the solution above the surface. The modeled results is in excellent agreement with the actual experiment, even though the modeled shift is done with a larger change in thickness.

Different mixers has been tested in PDMS flow chips. The best suited mixer for the molecular system used is the serpentine or serpentine in combination with a squeeze. Micro interferometric backscatter detection has been used for detecting bio molecular interactions both surface bound and in solution. The biotin/avidin surface chemistry significantly simplified substrate preparation, was compatible with PDMS, and facilitated free–solution assays with micro interferometric backscatter detection. Combination of this new surface chemistry with the CCD FFT transduction has allowed improved detection for Protein A /IgG binding by two orders of magnitude compared to earlier experiments. Micro interferometric backscatter detection was also used to monitor DNA hybridization over a wide range of concentrations and allowed discrimination in binding of a three–base–pair mismatch. Thermodynamic data has been extracted from binding curves monitored with micro interferometric backscatter detection. The addition of a FITC-label to the cDNA probe perturbed the thermodynamic data, again emphasizing the need for label–free detection. Use of PDMS micro fluidic chips and the exceedingly simple optical train of micro interferometric backscatter detection represents a

cost–effective platform for label–free molecular–interaction determinations as well as for the investigation of reversible biological interactions within subnanoliter volumes and at the attomole level. The methodology and technology are compatible with large–scale integration and should facilitate high–throughput assays.

Fairly easy to make PDMS flow chips has via the micro interferometric backscatter detection setup been used to obtained label–free binding data from protein–protein interactions while both reactants was in solution. Thereby eliminating the need for time–consuming surface preparation steps and perturbations of the thermodynamic results. The perturbations is do the fact that one probe is bound to the surface limiting the freedom to move. The concentration needed for detection is smaller than the surface bound results (4 times). The thermodynamic data is comparable with ITC but in far smaller volumes of samples showing micro interferometric backscatter detection as the potentially better suited method to do these binding studies on relatively expensive analytes. A system has been shown, which no other system can compete on the combination of sample volume, time, sensitivity and system simplicity for doing these label–free, in solution protein–protein interaction studies. The free solution protein binding experiments and results places micro interferometric backscatter detection in a unique position with comparable thermodynamic capabilities with the golden standard ITC, but orders of magnitude faster and less analyte sample consuming. All performed in a relative simple and price competitive manner.

9.1 Outlook

Tools has been found to improve the chip scale interferometry sensor, this includes self–calibrating features and better fabrication methods. As preliminary results indicates the surface of the polymer chip may be improved in future iterations of the sensor.

The completion of a Lab–on–a–chip device making a complete blood analysis will be a paradigm shift moving the analysis from the laboratories closer to the bedside. Being able to measure on whole blood will give rise to numerous applications within the medical research area. This technique is universal and may be applied to other small liquid sample areas as drug discovery and environment monitoring as well. It is my hope that this sensor can help saving lives in the future.

References

[1] P. T. Charles and A. W. Kusterbeck. Trace level detection of hexahydro–1,3,5–trinitro–1,3,5–triazine (rdx) by microimmunosensor. *Biosensors & Bioelectronics*, 14(4):387–396, Apr 1999.

[2] F. M. Zhou, J. T. Aronson, and M. W. Ruegnitz. High–throughput fast–scan anodic stripping voltammetry in a microflow system. *Analytical Chemistry*, 69(4):728–733, Feb 1997.

[3] B. Danielsson, I. Surugiu, A. Dzgoev, M. Mecklenburg, and K. Ramanathan. Optical detection of pesticides and drugs based on chemiluminescence–fluorescence assays. *Analytica Chimica Acta*, 426(2):227–234, Jan 2001.

[4] A. van den Berg. Lab–on–a–chip detects ammonia. *Trac–Trends In Analytical Chemistry*, 23(6):VII–VIII, Jun 2004.

[5] M. J. Davies. Proteomics set for billion dollar growth. *Trends in Biotechnology*, 19(11):436–437, Nov 2001.

[6] C. Zander, K. H. Drexhage, K. T. Han, Wolfrum J., and Sauer M. Single–molecule counting and identification in a microcapillary. *Chemical Physics Letters*, 286(5–6):457–465, Apr 1998.

[7] L. C. Waters, S. C. Jacobson, N. Kroutchinina, J. Khandurina, R. S. Foote, and M. J. Ramsey. Microchip device for cell lysis, multiplex pcr amplification, and electrophoretic sizing. *Analytical Chemistry*, 70(1):158–162, January 1998.

[8] C. M. Gregory, J. V. Hatfield, S. Higgins, H. Iacovides, and P. J.Vadgama. A novel open flow microflow sensor for reduced fouling of chemical sensors in physiological sampling environments. *Sensors and Actuators B*, 65:305–309, 2000.

[9] G. P. Rigby, Ahmed S., Horseman G., and Vadgama P. In vivo glucose monitoring with open microflow - influences of fluid composition and preliminary evaluation in man. *Analytica Chimica Acta*, 385(1–3):23–32, Apr 1999.

[10] I. S. Lurie, D. S. Anex, Y. Fintschenko, and W. Y. Choi. Profiling of impurities in heroin by capillary electrochromatography and laser-induced fluorescence detection. *Journal of Chromatography A*, 924:421–427, 2001.

[11] G. B. Lee, S. H. Chen, G. R. Huang, W. C. Sung, and Y. H. Lin. Microfabricated plastic chips by hot embossing methods and their applications for dna separation and detection. *Sensors And Actuators B-Chemical*, 75(1–2):142–148, Apr 2001.

[12] T. Nakanishi, A. Shimizu, N. Okamoto, A. Ingendoh, and M. Kanai. Analysis of serum–protein precipitated with antiserum by matrix–assisted laser–desorption ionization time–of–flight and electrospray–ionization mass–spectrometry as a clinical laboratory test. *Journal Of The American Society For Mass Spectrometry*, 6(9):854–859, Sep 1995.

[13] K. Senior. Fingerprinting disease with protein chip arrays. *Molecular Medicine Today*, 5:326–327, August 1999.

[14] C. S. Effenhauser, A. Manz, and H. M. Widmer. Glass chips for high-speed capillary electrophoresis separations with submicrometer plate heights. *Analytical Chemistry*, 65(19):2637–2642, 1993.

[15] N. J. Hack, B. Billups, P. B. Guthrie, J. H. Rogers, T. M. Muir, E.and N. Parks, and S. B. Kater. Green fluorescent protein as a quantitative tool. *Journal of Neuroscience Methods*, 95:177–184, 2000.

[16] R. Horvath, H. C. Pedersen, N. Skivesen, D. Selmeczi, and N. B. Larsen. Monitoring of living cell attachment and spreading using reverse symmetry waveguide sensing. *Applied Physics Letters*, 86:071101.1–071101.3, February 2005.

[17] H. Kurt and D. S. Citrin. Photonic crystals for biochemical sensing in the terahertz region. *Applied Physics Letters*, 87:041108.1–041108.3, Jul 2005.

[18] A. Otto. Excitation of nonradiative surface plasma waves in silver by method of frustrated total reflection. *Zeitschrift Fur Physik*, 216(4):398–, 1968.

[19] B. Liedberg, C. Nylander, and I. Lundstrom. Surface–plasmon resonance for gas–detection and biosensing. *Sensors And Actuators*, 4(2):299–304, 1983.

[20] A. N. Phayre, N. K. Hartley, and M. A. Hayes. Microdevices for biological analyses recent advances and directions for the future. *Journal of the Association for Laboratory Automation*, 5(4):78–82, Sep 2000.

[21] D. Figeys and D. Pinto. Lab–on–a–chip: A revolution in biological and medical sciences. *Analytical Chemistry*, 72(9), 2000.

[22] A. Y. Fu, Spence C., Scherer A., F. H. Arnold, and S. R. Quake. A microfabricated fluorescence–activated cell sorter. *Nature Biotechnology*, 17(11), 1999.

[23] M. P. Marco, Gee S., and B. D. Hammock. Immunochemical techniques for environmental–analysis .1. immunosensors. *Trac–Trends In Analytical Chemistry*, 14(7), 1995.

[24] K. Swinney, D. Markov, and D. J. Bornhop. Chip-scale universal detection based on backscatter interferometry. *Analytical Chemistry*, 72(13):2690–2695, July 2000.

[25] K. Swinney and D. J. Bornhop. A chip-scale universal detector for electrophoresis based on backscattering interferometry. *Analyst*, 125:1713–1717, 2000.

[26] D. J.Bornhop. Laser-based refractive index detector using backscatter. *US Patent*, (5,325,170):—, June 1994.

[27] Z. Wang and D. J. Bornhop. Dual–capillary backscatter interferometry for high–sensitivity nanoliter–volume refractive index detection with density gradient compensation. *Analytical Chemistry*, 77(24):7872–7877, 2005.

[28] K. Swinney and D. J. Bornhop. Noninvasive picoliter volume thermomerty based on backscatter interferometry. *Electrophoresis*, 22:2032–2036, 2001.

[29] K. Swinney, D. Markov, J. Hankins, and D. J. Bornhop. Micro–interferometric backscatter detection using a diode laser. *Analytica Chimica Acta*, 400:265–280, July 1999.

[30] K. Swinney, D. Markov, and D. J. Bornhop. Ultrasmall volume refractive index detection using microinterferometry. *Review of Scientific instruments*, 71(7):2684–2692, March 2000.

[31] D. C. Duffy, J. C. McDonald, O. J. A. Schueller, and G. M. Whitesides. Rapid prototyping of microfluidic systems ion poly(dimethylsiloxane). *Analytical Chemistry*, 70(23):4974–4984, December 1998.

[32] E. Zubritsky. Faster prototyping for esi-ms chips. *Analytical Chemistry News & Features*, November 1999.

[33] S. A. Soper, S. M. Ford, S. Qi, R. L. McCarley, K. Kelly, and M. C. Murphy. Polymeric microelctromechanical systems. *Analytical Chemistry*, pages 643–651, October 2000.

[34] F. L. Pedrotti and L. S. Pedrotti. *Introduction to Optics*, volume 2. Prentice Hall International, Inc., 1996.

[35] M.Kerker and E.Matijevic. Scattering of electromagnetic waves from concentric infinite cylinders. *Journal of the optical society of America*, 51(5):506–508, 1961.

[36] L.S.Watkins. Scattering from side-illuminated clad glass fibers for determination of fiber parameters. *Journal of the optical society of America*, 64(6):767–772, 1974.

[37] D.Marcuse and H.M.Presby. Light scattering from optical fibers with arbitrary refractive-index distributions. *Journal of the optical society of America*, 65(4):367–375, 1975.

[38] R. Horton and W. J. Williamson. Interference patterns of a plane–polarized wave from a hollow glass fiber. *Journal of the optical society of America*, 63(10):1204–1210, 1973.

[39] H. J. Tarigan, P. Neill, C. K. Kenmore, and D. J. Bornhop. Capillary–scale refractive index detection by interferometric backscatter. *Analytical Chemistry*, 68(10):1762–1770, May 1996.

[40] C.F. Bohren and D.R. Huffman. *Absorption and Scattering of Light by Small Particles*. Wiley, 1983.

[41] D. Markov, D. Begari, and D. J.Bornhop. Breaking the 10^{-7} barrier for ri measurements in nanoliter volumes. *Analytical Chemistry*, 74(20):5438–5441, October 2002.

[42] A. Homsy, S. Koster, J.C.T. Eijkel, A. van den Berg, F. Lucklum, E. Verpoorte, and N.F. de Rooij. A high current density dc magnetohydrodynamic (mhd) micropump. *Lab on A Chip*, 5(4):466–471, 2005.

[43] A.D. Stroock, S.K.W. Dertinger, A. Ajdari, I. Mezic, H.A. Stone, and G.M. Whitesides. Chaotic mixer for microchannels. *Science*, 295(5555):647–651, 2002.

[44] V. Hessel, H. Löwe, and F. Schönfeld. Micromixers–a review on passive and active mixing principles. *Chemical Engineering Science*, 60:2479–2501, 2005.

[45] A. Groisman and S.R. QUAKE. A microfluidic rectifier: Anisotropic flow resistance at low reynolds numbers. *Physical Review Letters*, 92(9):–, 2004.

[46] W. U. Wang, C. Chen, K. H. Lin, Y. Fang, and C. M.Lieber. Label–free detection of small–molecule–protein interactions by using nanowire nanosensors. *Proceedings of the National Academy of Sciences of the United States of America*, 102(9):3208–3212, 2005.

[47] T.T. Goodrich, H.J. Lee, and R.M. Corn. Direct detection of genomic dna by enzymatically amplified spr imaging measurements of rna microarrays. *Journal of the American Chemical Society*, 126(13):4086–4087, 2004.

[48] P. Domachuk, C. Grillet, V. Ta'eed, E. Magi, J. Bolger, B.J. Eggleton, L.E. Rodd, and J. Cooper-White. Microfluidic interferometer. *Applied Physics Letters*, 86(2):–, 2005.

[49] D. J. Bornhop. Microvolume index of refraction determinations by interferometric backscatter. *Applied Optics*, 34(18):3234–3239, June 1995.

[50] H.S. Sorensen, H. Pranov, N.B. Larsen, D.J. Bornhop, and P.E. Andersen. Absolute refractive index determination by microinterferometric backscatter detection. *Analytical Chemistry*, 75(8):1946–1953, 2003.

[51] D. A. Markov, K. Swinney, and D. J. Bornhop. Label-free molecular interaction determinations with nanoscale interferometry. *Journal of the American Chemical Society*, 126(50):16659–16664, 2004.

[52] L.B. Koutny, D. Schmalzing, T.A. Taylor, and M. Fuchs. Microchip electrophoretic immunoassay for serum cortisol. *Analytical Chemistry*, 68(1):18–22, 1996.

[53] S.C. Jacobson, R. Hergenroder, A. W. Moore, and J. M. Ramsey. Precolumn reactions with electrophoretic analysis integrated on a microchip. *Analytical Chemistry*, 66(23):4127–4132, 1994.

[54] S.C. Jacobson, R. HERGENRODER, L.B. Koutny, and J.M. Ramsey. Open-channel electrochromatography on a microchip. *Analytical Chemistry*, 66(14):2369–2373, 1994.

[55] P.C.Simpson, A.T.Wooley, and R.A.Mathies. Microfabrication technology for the production of capillary array electrophoresis chips. *Biomedical Microdevices*, 1:7–25, 1998.

[56] S.R. Liu. A microfabricated hybrid device for dna sequencing. *Electrophoresis*, 24(21):3755–3761, 2003.

[57] A. Grosse, M. Grewe, and H. Fouckhardt. Deep wet etching of fused silica glass for hollow capillary optical leaky waveguides in microfluidic devices. *Journal of Micromechanics and Microengineering*, 11(3):257–262, 2001.

[58] A. T. Woolley and R. A. Mathies. Ultra-high-speed dna fragment separations using microfabricated capillary array electrophoresis chips. *Proceedings of the National Academy of Sciences of the United States of America*, 91(24):11348–11352, 1994.

[59] S. C. Jacobson, A. W. Moore, and J. M. Ramsey. Fused quartz substrates for microchip electrophoresis. *Analytical Chemistry*, 67(13):2059–2063, 1995.

[60] K. Fluri, G. Fitzpatrick, N. Chiem, and D.J. Harrison. Integrated capillary electrophoresis devices with an efficient postcolumn reactor in planar quartz and glass chips. *Analytical Chemistry*, 68(23):4285–4290, 1996.

[61] Z. H. Fan and D. J. Harrison. Micromachining of capillary electrophoresis injectors and separators on glass chips and evaluation of flow at capillary intersections. *Analytical Chemistry*, 66(1):177–184, 1994.

[62] Liu S. Hybrid apparatus for high throughput, high resolution electrophoretic separation, useful for dna sequencing, comprises a microfabricated chip injector attached to capillaries. *Patent*, (WO200104613–A), January 2001.

[63] R C. Jaeger. *Introduction to Microelectronic Fabrication, Second edition*, volume V. Prentice–Hall, Inc., 2002.

[64] A. Schmidt, G. Himmelsbach, R. Luttge, D. Adam, F. Hoke, H. Schacke, N. Belic, H. Hartmann, F. Burkhard, and H. Wolf. High precision mask fabrication for deep x-ray lithography using 40-kv shaped electron beam lithography. *Microelectronic Engineering*, 57-8:761–767, 2001.

[65] L. Wang, Y. M. Desta, R. K. Fettig, J. Goettert, H. Hein, P. Jakobs, and J. Schulz. High resolution x-ray mask fabrication by 100 kev electron-beam lithography system. *Journal of Micromechanics and Microengineering*, 14:722–726, 2004.

[66] A. Eckert and K. Mountfield. Electron beam lithography for data storage: Quantifying the proximity effect as a function of cad design and thin metal layers. *Journal of Vacuum Science and Technology B*, 22(6):2936–2942, Nov/Dec 2004.

[67] K. W. Rhee and M. C. Peckerar. Proximity effect reduction using thin insulating layers. *Applied Physics Letters*, 62(5):533–534, February 1993.

[68] B. Schwartz and H. Robbins. Chemical etching of silicon. *Journal of the Electrochemical Society: Solid-state science and technology*, 123(12):1903–1909, 1976.

[69] C.H. Han and E.S. Kim. Study of self-limiting etching behavior in wet isotropic etching of silicon. *Japanese Journal of Applied Physics Part 1-Regular Papers Short Notes & Review Papers*, 37(12B):6939–6941, 1998.

[70] R. Ulrich, H. P. Weber, E A. Chandross, W. J. Tomlinson, and E. A. Franke. Embossed optical waveguides. *Applied Physics Letters*, 20(6):213–215, March 1972.

[71] L. Martynova, L. E.Locascio, M. Gaitan, G. W.Kramer, R. G Christensen, and W. A MacCrehan. Fabrication of plastic microfluid channels by imprinting methods. *Analytical Chemistry*, 69(23):4783–4789, December 1997.

[72] H. Klank, J. P. Kutter, and O. Geschke. Co_2–laser micromachining and back–end processing for rapid production pf pmma–based microfluidic systems. *Lab On A Chip*, 2:242–246, 2002.

[73] E. Gu, H. W. Choi, C. Liu, C. Griffin, J. M. Girkin, I. M. Watson, M. D. Dawson, G. McConnell, and A. M. Gurney. Reflection/transmission confocal microscopy characterization of single-crystal diamond microlens arrays. *Applied Physics Letters*, 84(15):2754–2756, April 2004.

[74] H. W. Choi, E. Gu, C. Liu, C. Griffin, J. M. Girkin, I. M. Watson, and M. D. Dawson. Fabrication of natural diamond microlenses by plasma etching. *Journal of Vacuum science and Technology B*, 23(1):130–132, Jan/Feb 2005.

[75] H. Urey and K. D. Powell. Microlens-array-based exit-pupil expander for full-color displays. *Applied Optics*, 44(23):4930–4936, August 2005.

[76] A. Schilling, R. Merz, C. Ossmann, and H. P. Herzig. Surface profiles of reflow microlenses under the influence of surface tension and gravity. *Optical Engineering*, 39(8):2171–2176, August 2000.

[77] F. T. O'Neill and J. T. Sheridan. Photoresist reflow method of microlens production part i: Background and experiments. *Optik*, 113(9):391–404, 2002.

[78] T. N. Oder, J. Shakya, J. Y. Lin, and H. X. Jiang. Nitride microlens arrays for blue and ultraviolet wavelength applications. *Applied Physics Letters*, 82(21):3692–3694, May 2003.

[79] W. Choi, J. Lee, W.-B. Kim, B.-W. Min, S. Kang, and S.-J. Lee. Design and fabrication of tungsten carbide mould with micro patterns imprinted by micro lithography. *Journal of Micromechanics and Microengineering*, 14:1519–1525, August 2004.

[80] M.Valcárcel and S.Cárdenas. We need reliable ways to bypass preliminary operations in (bio)chemical measurement. *trends in analytical chemistry*, 21(4):211–212, April 2002.

[81] G. Hanrahan, S. Ussher, M. Gledhill, E. P. Achterberg, and P. J. Worsfold. High temporal and spatial resolution environmental monitoring using flow injection with spectroscopic detection. *trends in analytical chemistry*, 21(4):233–239, April 2002.

[82] K. Schult, A. Katerkamp, D. Trau, F. Grawe, K. Cammann, and M. Meusel. Dispoasble optical sensor chip for medical diagnostics: New ways in bioanalysis. *Analytical Chemistry*, 71(23):5430–5435, December 1999.

[83] M.Valcárcel, S.Cárdenas, and M.Gallego. Continuos flow systems for rapid sample screening. *trends in analytical chemistry*, 21(4):251–258, April 2002.

[84] Yu.A.Zolotov, V.M.Ivanov, and V.G.Amelin. Test methods for extralaboratory analysis. *trends in analytical chemistry*, 21(4):302–319, April 2002.

[85] P.D.Patel. (bio)sensors for measurement of analytes implicated in food safety: a review. *trends in analytical chemistry*, 21(2):96–115, February 2002.

[86] J. Wang. Portable electrochemical systems. *trends in analytical chemistry*, 21(4):226–232, April 2002.

[87] P. S. Francis, S. W. Lewis, and K. F. Lim. Analytical methodology for the determination of urea: current practice and future trends. *trends in analytical chemistry*, 21(5):389–400, May 2002.

[88] G.P.Rigby, S.Ahmed, G.Horseman, and P.Vadgama. In vivo glucose monitoring with open microflow - influences of fluid composition and preliminary evaluation in man. *Analytica Chimica Acta*, 385:23–32, 1999.

[89] M. Aiello and R. McLaren. A sensitive small–volume uv/vis flow cell and total absorbance detection system for micro–hplc. *Analytical Chemistry*, 73(6):1387–1392, March 2001.

[90] R. D. Oleschuk and D. J. Harrison. Analytical microdevices for mass spectrometry. *trends in analytical chemistry*, 19(6):379–388, 2000.

[91] F. M. Lagerwerf, W. D.van Dongen, R. J. J. M. Steenvoorden, M. Honing, and J. H. G. Jonkman. Exploring the boundaries of bioanalytical quantitative lc–ms–ms. *trends in analytical chemistry*, 19(7):418–427, 2000.

[92] Y. Xia and G. M.Whitesides. Soft lithography. *Angewandte Chemie*, 37:550–575, 1998.

[93] J. P. Kutter. Current developments in electrophoretic and chromatograhic separation methods on microfabricated devices. *trends in analytical chemistry*, 19(6):352–363, 2000.

[94] J. C. McDonald, D. C.Duffy, J. R.Anderson, D. T. Chiu, H. Wu, O. J. A. Schueller, and G. M. Whitesides. Fabrication of microfluidic systems in poly(dimethylsiloxane). *Electrophoresis*, 21:27–40, 2000.

[95] S.C.Terry, J.H.Jerma, and J.B.Angell. Gas-chromatographic air analyzer fabricated on a silicon-wafer. *IEEE Transactions on Electron Devices*, 26(12):1880–1886, 1979.

[96] R.G.Heideman and P.V.Lambeck. Remote opto-chemical sensing with extreme sensitivity: design, fabrication and performance of a pigtailed integrated optical phase-modulated mach-zehnder interferometer system. *Sensors and Actuators B*, 61:100–127, 1999.

[97] D. Markov and D. J. Bornhop. Nanoliter–scale non–invasive flow–rate quantification using micro–interferometric backscatter and phase detection. *Fresenius' Journal of Analytical Chemistry*, 371(2):234–237, July 2001.

[98] M. B.van der Mark and L. Bosselaar. Noncontact calibration of optical fiber cladding diameter using exact scattering theory. *Journal of Lightwave Technology*, 12(1):1–5, January 1994.

[99] D. Markov, K. Swinney, K. Norville, D. Lu, and D. J. Bornhop. A fourier analysis approach for capillary polarimetry. *Electrophoresis*, 23(5):809–812, March 2002.

[100] F. Giess, M. G. Friedrich, J. Heberle, R. L. Naumann, and W. Knoll. The protein–tethered lipid bilayer: A novel mimic of the biological membrane. *Biophysical Journal*, 87:3213–3220, November 2004.

[101] J. Vörös. The density and refractive index of adsorbing protein layers. *Biophysical Journal*, 87:553–561, July 2004.

[102] J. V. Gilfrich and L. S. Birks. Estimation of detection limits in x–ray fluorescence spectrometry. *Analytical Chemistry*, 56(1):77–79, 1984.

[103] Weast. *Handbook of chemistry and physics, 64th edition.* CRC Press, 1983–1984.

[104] *www.hypertextbook.com*, Dec 2005.

[105] M. Menaché and Girard G. Concerning the different tables of the thermal expansion of water between 0 and 40° C. *Metrologia*, 12:62–68, 1973.

[106] K. Swinney and D. J. Bornhop. Quantification and evaluation of joule heating in on–chip capillary electrophoresis. *Electrophoresis*, 23:613–620, 2002.

[107] H. Becker and L. E.Locascio. Polymer microfluidic devices. *Talanta*, 56:267–287, Jun 2002.

[108] *Unit operations of chemical engineering, Fifth edition., publisher = McGraw–Hill, year = 1993, author = L. Mccabe, W. and C. Smith, J. and Harriot, P., isbn = 0–07–044844-2,.*

[109] T. Thorsen, S. J. Maerkl, and S. R. Quake. Microfluidic large–scale integration. *Science*, 298:580–584, Oct 2002.

[110] J. Voldman, M.L. Gray, and M.A. Schmidt. *Micro Total Analysis Systems*, chapter Liquid mixing studies with an integrated mixer/valve., pages 181–184. Kluwer Academic Publishers, 1998.

[111] J. West, B. Karamata, B. Lillis, J.P. Gleeson, J. Alderman, J.K. Collins, W. Lane, A. Mathewson, and H. Berney. Application of magnetohydrodynamic actuation to continuous flow chemistry. *Lab on A Chip*, 2(4):224–230, 2002.

[112] Z. Yang, S. Matsumoto, H. Goto, M. Matsumoto, and R. Maeda. Ultrasonic micromixer for microfluidic systems. *Sensors and Actuators A-Physical*, 93(3):266–272, 2001.

[113] M.H. Oddy, J.G. Santiago, and J.C. Mikkelsen. Electrokinetic instability micromixing. *Analytical Chemistry*, 73(24):5822–5832, 2001.

[114] R.H. Liu, R. Lenigk, R.L. Druyor-Sanchez, J.N. Yang, and P. Grodzinski. Hybridization enhancement using cavitation microstreaming. *Analytical Chemistry*, 75(8):1911–1917, 2003.

[115] S.Z. Qian, H.H. Bau, and Analytical iscipline: Chemistry. A chaotic electroosmotic stirrer. *Analytical Chemistry*, 74(15):3616–3625, 2002.

[116] P. Paik, V.K. Pamula, and R.B. Fair. Rapid droplet mixers for digital microfluidic systems. *Lab on A Chip*, 3(4):253–259, 2003.

[117] P. Woias, K. Hauser, and E. Yacoub-George. *Micro Total Analysis Systems*, chapter An active silicon micromixer for μTAS applications, pages 277–282. Kluwer Academic Publishers, 2000.

[118] R. Miyake and et al. Micromixer with fast diffusion. In *IEEE–MEMS'93*, pages 248–253, Fort Lauderdale, USA, 1993.

[119] J. Branebjerg, U.D. Larsen, and G. Blankestein. Fast mising by parallel multilayer lamination. In *Proceedings of the Second International Symposium on Miniturized Total Analysis Systems; Analytical Methods & Instrumentation, Special Issue μTAS'96*, pages 228–230, Basel, 1996.

[120] N. Schwesinger, T. Frank, and H. Wurmus. A modulator microfluid system with an integrated micromixer. *Journal of Micromechanics and Microengineering*, 6(1):99–102, 1996.

[121] G. B. Lee, S. H. Chen, G. R Huang, W. C. Sung, and Y. H. Lin. Microfabricated plastic chips by hot embossing methods and their applications for dna separation and detection. *Sensors and Actuators B*, 75:142–148, 2001.

[122] R. H. Liu and et al. Plastic on–line chaotic icomixer for biological applications. In *Micro Total Analysis Systems, Ramsey, J.M. and van den Berg, A.*, pages 163–164, Kluwer Academic Publishers, 2001.

[123] R.H. Liu, M.A. Stremler, K.V. Sharp, M.G. Olsen, J.G. Santiago, R.J. Adrian, H. Aref, and D.J. Beebe. Passive mixing in a three-dimensional serpentine microchannel. *Journal of Microelectromechanical Systems*, 9(2):190–197, 2000.

[124] G. M. Whitesides and A. D. Stroock. Flexible methods for microfluidics. *Physics Today*, 54(6):42–48, 2001.

[125] D.D. Cunningham. Fluidics and sample handling in clinical chemical analysis. *Analytica Chimica Acta*, 429(1):1–18, 2001.

[126] D.J. Beebe, G.A. Mensing, and G.M. Walker. Physics and applications of microfluidics in biology. *Annual Review of Biomedical Engineering*, 4:261–286, 2002.

[127] T. Chovan and A. Guttman. Microfabricated devices in biotechnology and biochemical processing. *Trends in Biotechnology*, 20(3):116–122, 2002.

[128] D.R. Meldrum and M.R. Holl. Microscale bioanalytical systems. *Science*, 297(5584):1197–1198, 2002.

[129] T.H. Schulte, R.L. Bardell, and B.H. Weigl. Microfluidic technologies in clinical diagnostics. *Clinica Chimica Acta*, 321(1-2):1–10, 2002.

[130] B.H. Weigl, R.L. Bardell, and C.R. Cabrera. Lab-on-a-chip for drug development. *Advanced Drug Delivery Reviews*, 55(3):349–377, 2003.

[131] E. Kauffmann, N. C. Darnton, R. H. Austin, C. Batt, and K. Gerwert. Lifetimes of intermediates in the β–sheet to α–helix transition of β–lactoglobuling by using a diffusional ir mixer. *Proceedings of the National Academy of Sciences of the United States of America*, 98(12):6646–6649, Jun 2001.

[132] E. A. Lipman, B. Schuler, O. Bakajin, and W. A. Eaton. Single–molecule measurement of protein folding kinetics. *Science*, 301:1233–1235, Aug 2003.

[133] J. R. Anderson, D. T. Chiu, R. J. Jackman, O. Cherniavskaya, J. C. McDonald, H. Wu, S. H. Whitesides, and G. M. Whitesides. Fabrication of topologically complex three–dimensional microfluidic systems in pdms by rapid prototyping. *Analytical Chemistry*, 72(14):3158–3164, July 2000.

[134] H.K. Wu, T.W. Odom, D.T. Chiu, and G.M. Whitesides. Fabrication of complex three-dimensional microchannel systems in pdms. *Journal of the American Chemical Society*, 125(2):554–559, 2003.

[135] T. McCreedy. Fabrication techniques and materials commonly used for the production of microreactors and micro total analytical systems. *trends in analytical chemistry*, 19(6):396–401, 2000.

[136] A. Papra, A. Bernard, D. Juncker, N. B.Larsen, B. Michel, and E. Delamarche. Microfludic networks made of poly(dimethylsiloxane), si, and au coated with polyethylene glycol for patterning proteins onto surfaces. *Langmuir*, 17(13):4090–4095, 2001.

[137] M.A. Cooper. Label-free screening of bio-molecular interactions. *Analytical and Bioanalytical Chemistry*, 377(5):834–842, 2003.

[138] F.E. Torres, P. Kuhnt, D. De Bruyker, A.G. Bell, M.V. Wolkin, E. Peeters, J.R. Williamson, G.B. Anderson, G.P. Schmitz, M.I. Recht, S. Schweizer, L.G. Scott, J.H. Ho, S.A. Elrod, P.G. Schultz, R.A. Lerner, and R.H. Bruce. Enthalpy arrays. *Proceedings of the National Academy of Sciences of the United States of America*, 101(26):9517–9522, 2004.

[139] C. Hansen and S.R. Quake. Microfluidics in structural biology: smaller, faster... better. *Current Opinion in Structural Biology*, 13(5):538–544, 2003.

[140] S.K. Sia and G.M. Whitesides. Microfluidic devices fabricated in poly(dimethylsiloxane) for biological studies. *Electrophoresis*, 24(21):3563–3576, 2003.

[141] J.R. Heath, M.E. Phelps, and L. Hood. Nanosystems biology. *Molecular Imaging and Biology*, 5:312–325, 2003.

[142] M. Ferrari. Cancer nanotechnology: Opportunities and challenges. *Nature Reviews Cancer*, 5(3):161–171, 2005.

[143] J. Hahm and C.M. Lieber. Direct ultrasensitive electrical detection of dna and dna sequence variations using nanowire nanosensors. *Nano Letters*, 4(1):51–54, 2004.

[144] V.S.Y. Lin, K. Motesharei, K.P.S. Dancil, M.J. Sailor, and M.R. Ghadiri. A porous silicon-based optical interferometric biosensor. *Science*, 278(5339):840–843, 1997.

[145] K.P.S. Dancil, D.P. Greiner, and M.J. Sailor. A porous silicon optical biosensor: Detection of reversible binding of igg to a protein a-modified surface. *Journal of the American Chemical Society*, 121(34):7925–7930, 1999.

[146] R.L. Rich, Y.S.N. Day, T.A. Morton, and D.G. Myszka. High-resolution and high-throughput protocols for measuring drug/human serum albumin interactions using biacore. *Analytical Biochemistry*, 296(2):197–207, 2001.

[147] E. A. Smith, W. D. Thomas, L. L. Kiessling, and R. M. Corn. Surface plasmon resonance imaging studies of protein–carbohydrate interactions. *Journal of the American Chemical Society*, 125(20):6140–6148, 2003.

[148] J.M. Brockman, A.G. Frutos, and R.M. Corn. A multistep chemical modification procedure to create dna arrays on gold surfaces for the study of protein-dna interactions with surface plasmon resonance imaging. *Journal of the American Chemical Society*, 121(35):8044–8051, 1999.

[149] G. J. Wegner, N. J. Lee, G. Marriott, and R. M. Corn. Fabrication of histidine–tagged fusion protein arrays for surface plasmon resonance imaging studies of protein–protein and protein–dna interactions. *Analytical Chemistry*, 75(18):4740–4746, 2003.

[150] T. Sakai, K. Shinahara, A. Torimaru, H. Tanaka, Y. Shoyama, and K. Matsumoto. Sensitive detection of glycyrrhizin and evaluation of the affinity constants by a surface plasmon resonance-based immunosensor. *Analytical Sciences*, 20(2):279–283, 2004.

[151] S.A. Brooks, W.P. Ambrose, and W.G. Kuhr. Micrometer dimension derivatization of biosensor surfaces using confocal dynamic patterning. *Analytical Chemistry*, 71(13):2558–2563, 1999.

[152] S.A. Brooks, N. Dontha, C.B. Davis, J.K. Stuart, G. O'Neill, and W.G. Kuhr. Segregation of micrometer-dimension biosensor elements on a variety of substrate surfaces. *Analytical Chemistry*, 72(14):3253–3259, 2000.

[153] G.M. Whitesides, E. Ostuni, S. Takayama, X.Y. Jiang, and D.E. Ingber. Soft lithography in biology and biochemistry. *Annual Review of Biomedical Engineering*, 3:335–373, 2001.

[154] A. Chilkoti and P.S. Stayton. Molecular-origins of the slow streptavidin-biotin dissociation kinetics. *Journal of the American Chemical Society*, 117(43):10622–10628, 1995.

[155] A. J. Thiel, A. G. Frutos, C. E. Jordan, R. M. Corn, and L. M. Smith. In situ surface plasmon resonance imaging detection of dna hybridization to oligonucleotide arrays on gold surfaces. *Analytical Chemistry*, 69(24):4948–4956, 1997.

[156] Y.W.C. Cao, R.C. Jin, and C.A. Mirkin. Nanoparticles with raman spectroscopic fingerprints for dna and rna detection. *Science*, 297(5586):1536–1540, 2002.

[157] F. Vinet, P. Chaton, and Y. Fouillet. Microarrays and microfluidic devices: miniaturized systems for biological analysis. *Microelectronic Engineering*, 61-2:41–47, 2002.

[158] P. V. Riccelli, F. Merante, K. T. Leung, R.; Janeczko R. Bortolin, S.and L. Zastawny, and A. S. Benight. Hybridization of single–stranded dna targets to immobilized complementary dna probes: comparison of hairpin versus linear capture probes218. *Nucleic Acids Research*, 29(4):996–1004, 2001.

[159] S.; Butler J.M. Schwarz, F.P.; Robinson. Thermodynamic comparison of pna/dna and dna/dna hybridization reactions at ambient temperature. *Nucleic Acids Research*, 27(24):4792–4800, 1999.

[160] R. A. Flavell, E. J. Birfelde, J. P. M. Sanders, and P. Borst. Dna–dna hybridization on nitrocellulose filters .1. general considerations and non–ideal kinetics220. *European Journal of Biochemistry*, 47(3):535–543, 1974.

[161] A. Manz, N. Graber, and H. M. Widmer. Miniaturized total chemical–analysis systems – a novel concept for chemical sensing. *Sensors and Actuators B–Chemical*, 1(1-6):244–248, 1990.

[162] S. Fields. Proteomics - proteomics in genomeland. *Science*, 291(5507):1221–+, 2001.

[163] M. Rothmund, A. Schutz, A. Brecht, G. Gauglitz, G. Berthel, and D. Grafe. Label free binding assay with spectroscopic detection for pharmaceutical screening. *Fresenius Journal of Analytical Chemistry*, 359(1):15–22, 1997.

[164] S. Hu and N.J. Dovichi. Capillary electrophoresis for the analysis of biopolymers. *Analytical Chemistry*, 74(12):2833–2850, 2002.

[165] N. Lion, T.C. Rohner, L. Dayon, I.L. Arnaud, E. Damoc, N. Youhnovski, Z.Y. Wu, C. Roussel, J. Josserand, H. Jensen, J.S. Rossier, M. Przybylski, and H.H. Girault. Microfluidic systems in proteomics. *Electrophoresis*, 24(21):3533–3562, 2003.

[166] G. Marko-Varga, J. Nilsson, and T. Laurell. New directions of miniaturization within the proteomics research area. *Electrophoresis*, 24(21):3521–3532, 2003.

[167] S. Mocellin, C.R. Rossi, P. Traldi, D. Nitti, and M. Lise. Molecular oncology in the post-genomic era: the challenge of proteomics. *Trends in Molecular Medicine*, 10(1):24–32, 2004.

[168] J.R. Broach and J. Thorner. High-throughput screening for drug discovery. *Nature*, 384(6604):14–16, 1996.

[169] P. W. Atkins. *Physical Chemistry, Fifth edition.* Oxforn University Press, 1994.

[170] J.J. Langone. Protein-a of staphylococcus-aureus and related immunoglobulin receptors produced by streptococci and pneumococci. *Advances in Immunology*, 32:157–252, 1982.

[171] K. Saha, F. Bender, and E. Gizeli. Comparative study of igg binding to proteins g and a: Nonequilibrium kinetic and binding constant determination with the acoustic waveguide device. *Analytical Chemistry*, 75(4):835–842, 2003.

[172] D. G. Georganopoulou, L. Chang, J. M. Nam, C. S. Thaxton, E. J. Mufson, W. L. Klein, and C. A. Mirkin. Nanoparticle–based detection in cerebral spinal fluid of a soluble pathogenic biomarker for alzheimer 's disease. *Proceedings of the National Academy of Sciences of the United States of America*, 102(7):2273–2276, Feb 2005.

[173] Liu X., D. Q. Song, Q. L. Zhang, Tian Y., Ding L., and H. Q. Zhang. Wavelength-modulation surface plasmon resonance sensor. *Trends In Analytical Chemistry*, 24(10):887–893, Nov 2005.

[174] W. W. Lam, L. H. Chu, C. L. Wong, and Y. T. Zhang. A surface plasmon resonance system for the measurement of glucose in aqueous solution. *Sensors and Actuators B*, 105:138–143, 2005.

[175] S. J. Zargar and A. Rabbani. Interaction of daunomycin antibiotic with histone h–1: ultraviolet spectroscopy and equilibrium dialysis studies. *International Journal of Biological Macromolecules*, 30:113–117, 2002.

[176] E. C. de Macario, U. H. Rudofsky, and A. J. L. Macario. Surface plasmon resonance for measuring tbp–promoter interaction. *Biochemical and Biophysical Research Communications*, 298:625–631, 2002.

[177] Z. L. Wang, K. Swinney, and D. J. Bornhop. Attomole sensitivity for unlabeled proteins and polypeptides with on–chip capillary electrophoresis and universal detection by interferometric backscatter. *Electrophoresis*, 24:865–873, 2003.

[178] J. Mackay and G. Mensah. *Atlas of Hearth Disease and stroke*. WHO, Sep 2004.

10 Appendix

Anal. Chem. **2003,** *75,* 1946−1953

Absolute Refractive Index Determination by Microinterferometric Backscatter Detection

Henrik Schiøtt Sørensen,[†,‡] Henrik Pranov,[‡,§] Niels B. Larsen,[§] Darryl J. Bornhop,*[,∥] and Peter E. Andersen*[,†]

Department of Optics and Fluid Dynamics, Risø National Laboratory, P.O. Box 49, 4000 Roskilde, Denmark, Department of Manufacturing Engineering and Management, Technical University of Denmark, Bygning 424, 2800 Kgs. Lyngby, Denmark, Danish Polymer Centre, Risø National Laboratory, P.O. Box 49, 4000 Roskilde, Denmark, and Department of Chemistry and Biochemistry, Texas Tech University, Lubbock, Texas 79409-1061

Microinterferometric backscatter detection (MIBD) has previously been shown capable of measuring changes in the refractive index of liquids on the order of 10^{-7}. The MIBD technique is based on interference of laser light after it is reflected from different regions in a capillary. These reflections generate an interference pattern that moves upon changing refractive index of the liquid in the capillary. The small-angle interference pattern traditionally considered has a repetition frequency in the refractive index space that limits the ability to measure refractive index-to-refractive index changes causing such a repetition. Such refractive index changes are typically on the order of three decades. Recent modeling and experiments with the MIBD technique have shown that other intensity variations in the pattern are present for larger backscattered angles. By considering these variations, we have shown two methods by which it is possible to extend the dynamic measurement range to make an absolute refractive index measurement. One method utilizes variations in the Fresnel coefficients while the second approach is based on the refractive index-dependent onset of total internal reflection angles. With the second approach, we have been able to measure the absolute refractive index of a liquid with a precision of 2.5×10^{-4}.

Rapid monitoring and detection of ultra-small-volume samples are in great demand.[1] Two major areas are environmental monitoring[2] and point-of-care disease detection.[3,4] This demand covers a huge range of applications, from drinking water quality[5] and food quality[6] to determination of glucose[7] and urea.[8] Several detection techniques have the capability to perform fast measurements on small amounts of analyte. Well-established techniques include electrochemistry,[9,10] mass spectrometry[11−13] and optical detection.[14,15] Not all are equally fast since sample preparation often is extensive and requires time-consuming steps such as chemical tagging of molecules.[16] Using structures with varying complexity fabricated to guide the samples to the detector,[17,18] systems can be scaled down so that the required amount of analyte as well as size and cost of the entire system is reduced, thus the miniaturized total analysis system.[19,20]

Simple optical systems are available to perform sensitive measurements on small volumes.[21] One analytical approach, microinterferometric backscatter detection (MIBD), relies on the observation that coherent light impinging on a cylindrically shaped object produces a highly modulated interference pattern. MIBD analyzes reflections from a capillary tube filled with the liquid targeted for refractive index (RI) measurement. The technique was first used and described by Bornhop et al.,[22,23] and has previously been shown[24] to be capable of measuring changes in refractive index of liquids on the order of 10^{-7}. The MIBD

* Corresponding authors. E-mail: darryl.bornhop@ttu.edu and peter.andersen@risoe.dk.

† Department of Optics and Fluid Dynamics, Risø National Laboratory.

‡ Technical University of Denmark.

§ Danish Polymer Centre, Risø National Laboratory.

∥ Texas Tech University.

(1) Valcárcel, M.; Cárdenas, S. *Trends Anal. Chem.* **2002**, *21*, 211−212.
(2) Hanrahan, G.; Ussher, S.; Gledhill, M.; Achterberg, E. P.; Worsfold, P. J. *Trends Anal. Chem.* **2002**, *21*, 233−239.
(3) Schult, K.; Katerkamp, A.; Trau, D.; Grawe, F.; Cammann, K.; Meusel, M. *Anal. Chem.* **1999**, *71*, 5430−5435.
(4) Valcárcel, M.; Cárdenas, S.; Gallego, M. *Trends Anal. Chem.* **2002**, *21*, 251−258.
(5) Zolotov, Y. A.; Ivanov, V. M.; Amelin, V. G. *Trends Anal. Chem.* **2002**, *21*, 302−319.
(6) Patel, P. D. *Trends Anal. Chem.* **2002**, *21*, 96−115.
(7) Wang, J. *Trends Anal. Chem.* **2002**, *21*, 226−232.
(8) Francis, P. S.; Lewis, S. W.; Lim, K. F. *Trends Anal. Chem.* **2002**, *21*, 389−400.
(9) Zhou, F.; Aronson, J. T.; Ruegnitz, M. W. *Anal. Chem.* **1997**, *69*, 728−733.
(10) Rigby, G. P.; Ahmed, S.; Horseman, G.; Vadgama, P. *Anal. Chim. Acta* **1999**, *385*, 23−32.
(11) Aiello, M.; McLaren, R. *Anal. Chem.* **2001**, *73*, 1387−1392.
(12) Oleschuk, R. D.; Harrison, D. J. *Trends Anal. Chem.* **2000**, *19*, 379−388.
(13) Lagerwerf, F. M.; van Dongen, W. D.; Steenvoorden, R. J. J. M.; Honing, M.; Jonkman, J. H. G. *Trends Anal. Chem.* **2000**, *19*, 418−427.
(14) Lurie, I. S.; Anex, D. S.; Fintschenko, Y.; Choi, W.-Y. J. *Chromatogr., A* **2001**, *924*, 421−427.
(15) Senior, K. *Mol. Med. Today* **1999**, *5*, 326−327.
(16) Hack, N. J.; Billups, B.; Guthrie, P. B.; Rogers, J. H.; Muir, E. M.; Parks, T. N.; Kater, S. B. J. *Neurosci. Methods* **2000**, *95*, 177−184.
(17) Xia, Y.; Whitesides, G. M. *Angew. Chem., Int. Engl. Ed.* **1998**, *37*, 550−575.
(18) Kutter, J. P. *Trends Anal. Chem.* **2000**, *19*, 352−363.
(19) McDonald, J. C.; Duffy, D. C.; Anderson, J. R.; Chiu, D. T.; Wu, H.; Schueller, O. J. A.; Whitesides, G. M. *Electrophoresis* **2000**, *21*, 27−40.
(20) Terry, S. C.; Jerma, J. H.; Angell, J. B. *IEEE Trans. Electron Dev*ices **1979**, *26*, 1880−1886.
(21) Heideman, R. G.; Lambeck, P. V. *Sens. Actuators, B* **1999**, *61*, 100−127.
(22) Bornhop, D. J. *Appl. Opt.* **1995**, *34*, 3234−3239.
(23) Bornhop, D. J. U.S. Patent 5,325,170, 1994.

10.1021/ac0206162 CCC: $25.00
Published on Web 03/06/2003

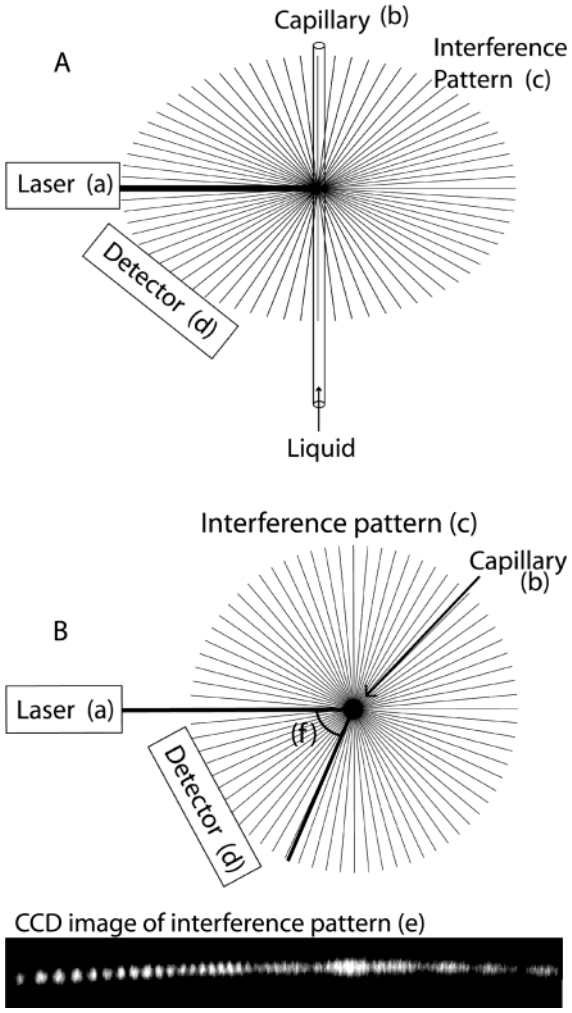

Figure 1. Schematic view of the experimental setup seen isometric (A) and from the top (B). The setup consists of a laser (a) impinging on a capillary (b) tube filled with a liquid, creating an interference pattern (c) in the plane perpendicular to the capillary tube. The backscattered light is then collected using a detector (d). A CCD picture of an interference pattern is seen in (e). The backscatter angle is shown (f).

technique is a simple and universal method of detecting refractive index changes in small volumes, having been used to monitor changes in concentrations of solutes,[25] flow rates,[26] and temperature,[27] all conducted in nanoliter volumes. Systems of geometrical configurations similar to that of the MIBD scheme have previously been modeled by wave theory[28−30] and ray tracing.[31] The models have been applied to optical fibers, determining the dimensions and absolute refractive index,[32] thereby considering phenomena other than those observed in the MIBD scheme.

The MIBD scheme is shown in Figure 1. The system consists of a laser (a) that impinges its beam on a capillary tube (b) filled with a liquid for which one wants to measure refractive index, thereby creating an interference pattern (c). This interference pattern, which changes with changes in the liquid's RI, is then measured using a detector (d). A typically observed interference pattern in the backscattered direction is seen in (e).

The demonstrated sensitivity of 10^{-7} is reached by following the displacement of the individual light fringes of the interference pattern within 0−3 angular degrees[24] from the directly backscattered direction, as the liquid RI changes. The fringe pattern is periodical in refractive index space with a period of the order of 10^{-3}. This limits the dynamic measurement range to about three decades, which for many purposes requires additional knowledge about the absolute value of the refractive index. As the measurement monitors a displacement of the fringe pattern, it is inherently differential, requiring both calibration for the absolute level of the refractive index and for the differential factor. This factor describes the fringe movement corresponding to a given change in the refractive index.

In this paper, we demonstrate experimentally that the dynamic range of the MIBD system may be increased. Furthermore, the absolute refractive index, and thereby the absolute analyte concentration, may be determined. We have tested this observation for two model analytes over a wide concentration range, demonstrating the universal application of our methodology. The observed phenomena may be explained by taking into account variations of the interference pattern with changing refractive index other than those previously considered. The dynamic range is increased without compromising the high differential sensitivity previously reported.[24] The theoretical description of the MIBD scheme has been improved to include an extended ray tracing model that matches the range in angular and refractive index space of the experiments, thus providing novel information about the structure of the backscattered interference pattern. In contrast to the previously proposed model,[33] this model is capable of explaining all frequency components that appear in the interference pattern. Furthermore, the model predicts an abrupt change in the intensity of the backscattered light, which depends uniquely on the refractive index of the probed liquid that has been experimentally confirmed. The improved understanding of the MIBD system is used to propose two approaches to an absolute measurement of the refractive index of liquids in the refractive index range between water (1.33) and glass (1.50). One approach is based on the measurement of the depth of modulation of the interference pattern caused by variations in the Fresnel coefficients. The second approach is based on the measurement of the total internal reflection within the capillary. We focus on the latter approach, as it appears most promising experimentally.

EXPERIMENTAL SECTION

Experimental MIBD Setup. The MIBD experiments were done by mounting the capillary on a translation stage and directing a HeNe laser beam so that it impinges perpendicularly onto the capillary. The backscattered light was collected using a screen and a CCD camera (C4742-95, Hamamatsu). The requirements for the laser are a coherence length of at least twice the diameter

(24) Swinney, K.; Markov, D.; Bornhop, D. J. *Rev. Sci. Instrum.* **2000**, *71*, 2684−2692.
(25) Swinney, K.; Markov, D.; Hankins, J.; Bornhop, D. J. *Anal. Chim. Acta* **1999**, *400*, 265−280.
(26) Markov, D.; Bornhop, D. J. *Fresenius J. Anal. Chem.* **2001**, *371*, 234−237.
(27) Swinney K.; Bornhop, D. J. *Electrophoresis* **2001**, *22*, 2032−2036.
(28) Kerker, M.; Matijevic, E. *J. Opt. Soc. Am.* **1961**, *51*, 506−508.
(29) Watkins, L. S. *J. Opt. Soc. Am.* **1974**, *64*, 767−772.
(30) Marcuse, D.; Presby, H. M. *J. Opt. Soc. Am.* **1975**, *65*, 367−375.
(31) Horton, R.; Williamson, W. J. *J. Opt. Soc. Am.* **1973**, *63*, 1204−1210.
(32) van der Mark, M. B.; Bosselaar, L. *J. Lightwave Technol.* **1994**, *12*, 1−5.
(33) Tarigan, H. J.; Neill, P.; Kenmore, C. K.; Bornhop, D. J. *Anal. Chem.* **1996**, *68*, 1762−1770.

of the capillary and a wavelength at which the capillary is transparent. The requirements for the detector are one-dimensional high spatial resolution and an adequate intensity resolution, depending on the application, as will be seen later. Passive temperature control consisted of a large thermal reservoir (an aluminum block) thermally connected to the capillary was used to stabilize temperature. Temperature fluctuations affect the refractive index of the liquid substantially. Active temperature control is only needed if the detection of changes in refractive index of less than 10^{-5} is required. In this work, passive temperature stabilization is adequate, as the refractive index fluctuations in the system caused by temperature fluctuations in our controlled environment are on the order of 10^{-5}, corresponding to 0.1 °C temperature fluctuations for water.

The capillaries used in the experiments were purchased from Polymicro Technologies. The dimensions of the two capillaries employed were 100-μm i.d., 165-μm o.d. with a 12-μm-thick polyimid coating (TSP100170) and 542-μm i.d., 673-μm o.d. with a 24-μm-thick polyimid coating (TSP530660), respectively. The refractive index was changed, from 1.33 to 1.5, by using aqueous solutions of either sucrose (Sigma Chemical Co.) or NaSCN (Merck). The analytes were chosen to obtain a large refractive index change in our model experiments and at the same time to maintain a low viscosity of the probed liquid. The RI of the solutions was confirmed with a commercial refractometer (RL3, Polskie Zakłdy Optyczne, Warsaw) immediately after the sample had been injected into the capillary.

Extended Ray Tracing Model of the MIBD Scheme. Previously, systems of a geometry similar to the MIBD scheme have been modeled by obtaining solutions to Maxwell's equations governing light propagation[34] or by optical ray tracing. Kerker and Matijevic[28] made the first complete model based on solutions to Maxwell's equations describing two concentric cylinders. Watkins confirmed these results experimentally.[29] However, Watkins considered optical glass fibers with thick claddings and did therefore obtain results significantly different from those observed in MIBD, as the interference pattern is claimed not to be dependent on the refractive index of the core in the backscatter angle regime. Marcuse and Presby[30] extended this model to also take into account the case of a thin cladding of the fibers. From their results, an abrupt change in the backscattered light intensity pattern is observed. However, it was not realized that this abrupt change could be utilized to obtain the absolute refractive index with high precision, since they were attempting to determine the outer radius of the glass fiber, and they were not concerned with the core index. Note that the position of the abrupt change depends on the core index; see below. Horton and Williamson[31] made a ray tracing model of an optical fiber, obtaining information about the ratio between inner and outer radii of the fiber. The approach they used is a back calculation assuming a planar wave front of the output. The rays considered in their model are not the same as in our model, as they consider fibers with a thick cladding and make use of multiple reflections inside the cladding. This is because they use refractive indices of the core significantly different from those considered in MIBD. The MIBD system has been modeled using a ray-tracing model by Tarigan et al.[33]

(34) Pedrotti, F. L.; Pedrotti, L. S. *Introduction to Optics*, 2nd ed.; Prentice Hall: Upper Saddle River, NJ, 1996; Chapter 27.

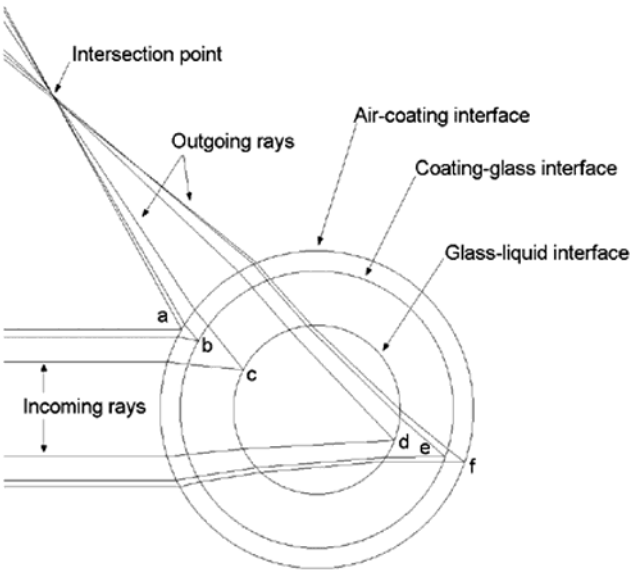

Figure 2. View of the cross section of the capillary showing the ray paths through the capillary system. Six types of parallel incoming beams are considered corresponding to their interface of reflection (a−f). For each type of beam, a number of rays (typically 1000) are traced yielding information about phase and intensity as function of position in a given detection plane for each type of beam. The interference between these six different types of beams is then calculated for multiple intersection points in the detection plane.

However, their model is limited by considering only small-angle backscattered light (0−3°).

We have extended the model to include backscattering angles up to 90° (side scattered). This is done in the geometric optics regime by using Snell's law,

$$n_i \sin(\theta_i) = n_j \sin(\theta_j) \tag{1}$$

where n_i and n_j are the refractive indices of the media and θ_i and θ_j are the angles of light propagation in the respective media. Furthermore, the law of reflection, $|\theta_{in}| = |\theta_{out}|$, is used. For angles beyond a few degrees, it is not possible to use the assumption ($\sin\theta \approx \theta$) of Tarigan et al. This implies that a simple analytical equation cannot be obtained. Our model traces six beams (see Figure 2) through the system and calculates their interference in a detection plane placed in the far-field region. For each type of beam, a number of rays (typically 1000) are traced. The information carried along with each ray is its position, angle, intensity, and phase. At the detection plane, the interference is calculated based on the information packages of all rays. The six beams considered in the model interfere by

$$I_{ij} = 2\sqrt{I_i I_j}\cos(\rho_i - \rho_j) \tag{2}$$

where i is the intensity and ρ is the phase of each individual ray and i and j are indices for each ray, respectively. The model is developed to also take into account the polymer coating on the capillary, thus requiring six beams. The model assumes that the capillary has circular geometry and that the laser can be described by plane waves.

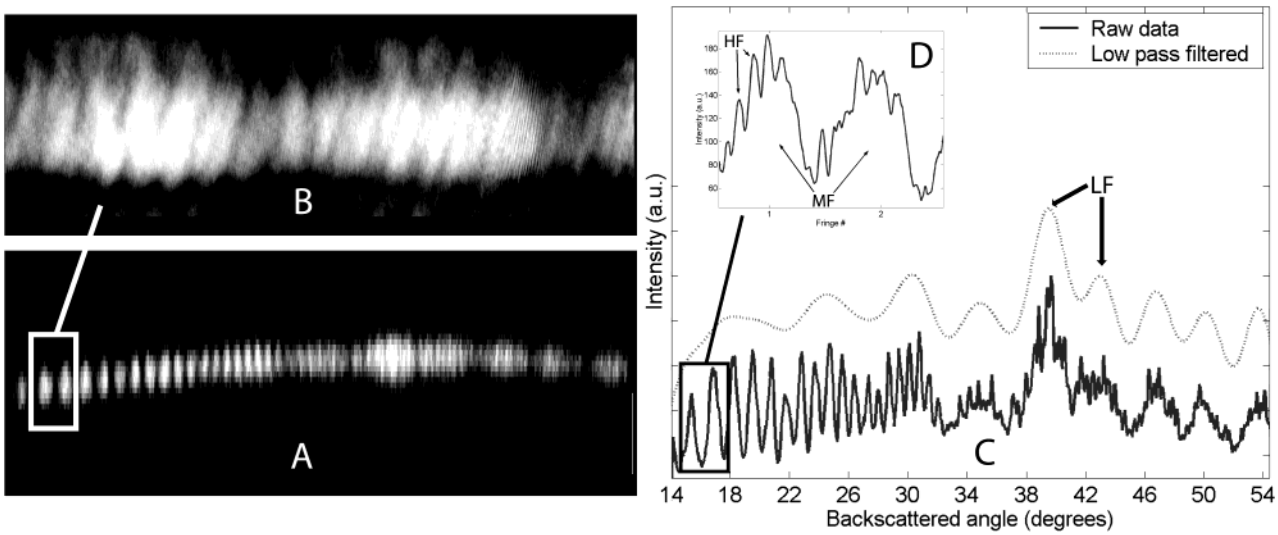

Figure 3. CCD camera images of a typical MIBD interference pattern (A, B) and corresponding line profiles (C, D). (A) and (C) show both LF and MF variations of the light intensity. The visual appearance is enhanced by low-pass (Fourier) filtering of the raw data. The raw data and the low-pass-filtered data have been offset for clarity. By magnifying the MF variations (B, D), a HF component is seen. This HF component does not move as the refractive index of the liquid is changed.

Justification of Assumptions. The model assumption of capillary circular geometry is justified by the observation that no significant change in the pattern was observed during rotation of the capillary (TSP100170, Polymicro Technologies) around the capillary central axis. The tilt of the wave front from the laser (05-LHR-HeNe, Melles Griot) was analyzed using a beam analyzer (CLAS-2D, Wave Front Sciences) and was observed to be less than 0.01 μrad, thus justifying the assumption of a planar wave front. The smallest spacing of refractive index changes is the thickness of the coating of 12 μm. The assumption of geometrical optics being adequate is justified since the wavelength used (632.8 nm) is much smaller than the distances otherwise present in the system.

RESULTS AND DISCUSSION

Interference Pattern Analysis. A typical pattern is shown in Figure 3A, with corresponding line profile of the intensity shown in Figure 3C. In Figure 3B, two of the fringes in (A) are enlarged, showing a finer structure. A line profile of the intensity from (B) is seen in (D). It is seen that the intensity pattern contains multiple frequency components. The period of the fringe pattern corresponding to medium-frequency (MF) components is shown in Figure 3D. Similarly, the period of the fringe pattern corresponding to low-frequency (LF) components is shown in Figure 3C. In the following, we shall refer to these frequency components as frequencies. Under certain circumstances, one is able to observe a faster varying component of the intensity profile, here denoted high-frequency (HF) variations (see Figure 3B and D). As one increases the refractive index of the liquid in the capillary, the intensity profile shifts toward lower backscatter angles (see Figure 4). However, the high-frequency variation component is spatially fixed and does not move as one changes the refractive index in accordance with previous observations.[35]

By investigating the experimentally observed frequencies of the fringe pattern, it may be shown by geometrical considerations that the distance between the origin points of the interfering rays (points a−f in Figure 2) on the capillary are approximately 5−10 times larger in the high-frequency case than in the medium-frequency case. By using geometrical considerations, it is possible to calculate the distance between origins of the interfering rays for all frequency components. We found that the distance required to produce the high-frequency variations is on the order of the capillary diameter. This indicates that the rays responsible for this high-frequency variation are scattered from the edges of the capillary, thereby not being affected by the liquid within the capillary. This hypothesis fits the observed behavior well, since the high-frequency component is not observed to be displaced as one changes the refractive index of the liquid in the capillary. Since this component does not move with changing refractive index, and thus cannot be used in a refractive index determination, it will not be considered further in this paper, neither experimentally nor in the modeling of the system.

The low-frequency component is spatially stationary as well, since this component is caused by the common interference between the three rays reflected from the front of the capillary (points a−c in Figure 2), as well as the common interference between the three rays reflected from the back of the capillary (points d−f in Figure 2). The displacement of this component is zero for the part originating from the front, since these rays do not traverse the liquid and thus experience the same optical path length by different refractive indices of the liquid. For the second part, the displacement is small, because all three rays experience almost the same change in optical path length traversed relative to each other.

In contrast to the high- and low-frequency components, respectively, the medium-frequency component originates from the interference between rays reflected at the front (points a−c in Figure 2), and at the back of the capillary (points d−f in Figure 2). These rays experience a large relative change in optical path length traversed, as the rays from the front do not experience a change in optical path length whereas the rays reflected from the back do. It is this relative change in the optical path length

(35) Markov, D.; Swinney, K.; Norville, K.; Lu, D.; Bornhop, D. J. *Electrophoresis* **2002**, *23*, 809−812.

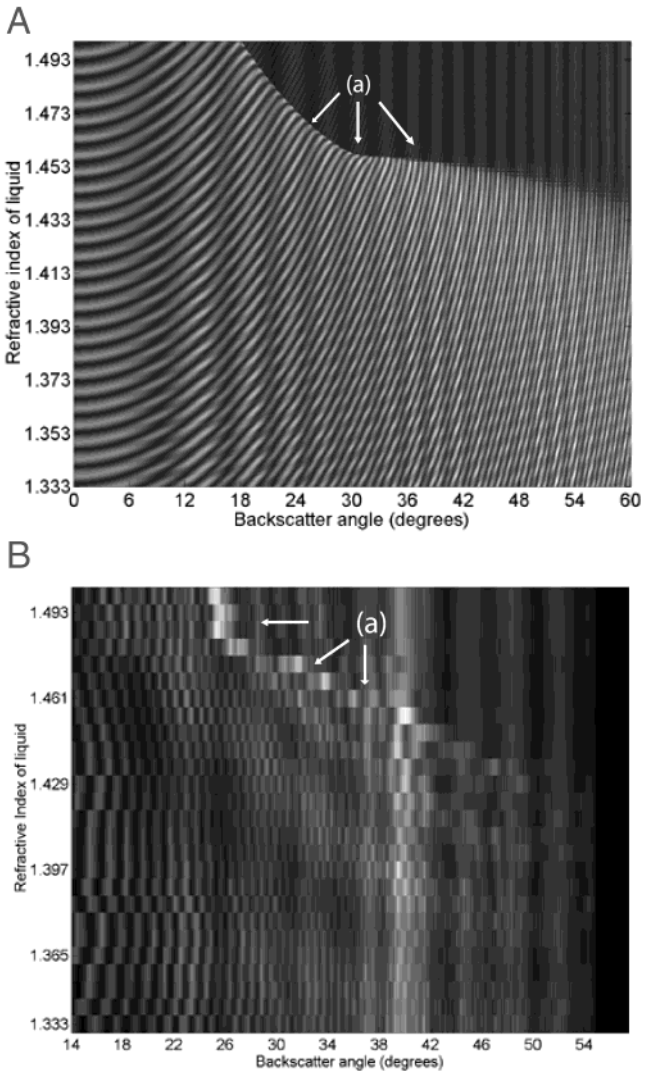

Figure 4. (A) Model predictions of the angle-dependent variations in the backscattered light intensity in the plane perpendicular to the capillary tube compiled by stacking line plots for closely spaced liquid refractive indices into a two-dimensional overview of the scattering behavior. This plot corresponds to 1643 liquids with different refractive indices calculated for a 100-μm-i.d./165-μm-o.d./12-μm coating capillary. The gray scale represents the light intensity in arbitrary units. Bands of light (fringes) move toward larger backscattered angles as the refractive index is increased. Overlaying vertical band structures of higher and lower light intensity are seen. These structures do not move as the refractive index is changed. An abrupt change in the intensity level (a) is seen moving toward lower backscattering angles for refractive indices of the liquid above 1.45. (B) Experimentally obtained data from a 100-μm-i.d./165-μm-o.d./12-μm coating capillary showing the low-frequency variations of the interference pattern as the refractive index is changed. The analyte is NaSCN. A total of 25 measurements of the interference pattern were made, each at a different refractive index. At each refractive index level, a line profile of the interference pattern was obtained. These fringes do not appear to form continuous bands in the vertical refractive index-dependent direction due to the large change in refractive index between measurements. An abrupt change in the intensity (a) is seen for high refractive indices (above 1.43), which moves toward lower backscattering angles for increasing refractive index.

between different paths that causes the movement of the medium-frequency component of the interference pattern, yielding the ultrahigh sensitivity to fluid RI.

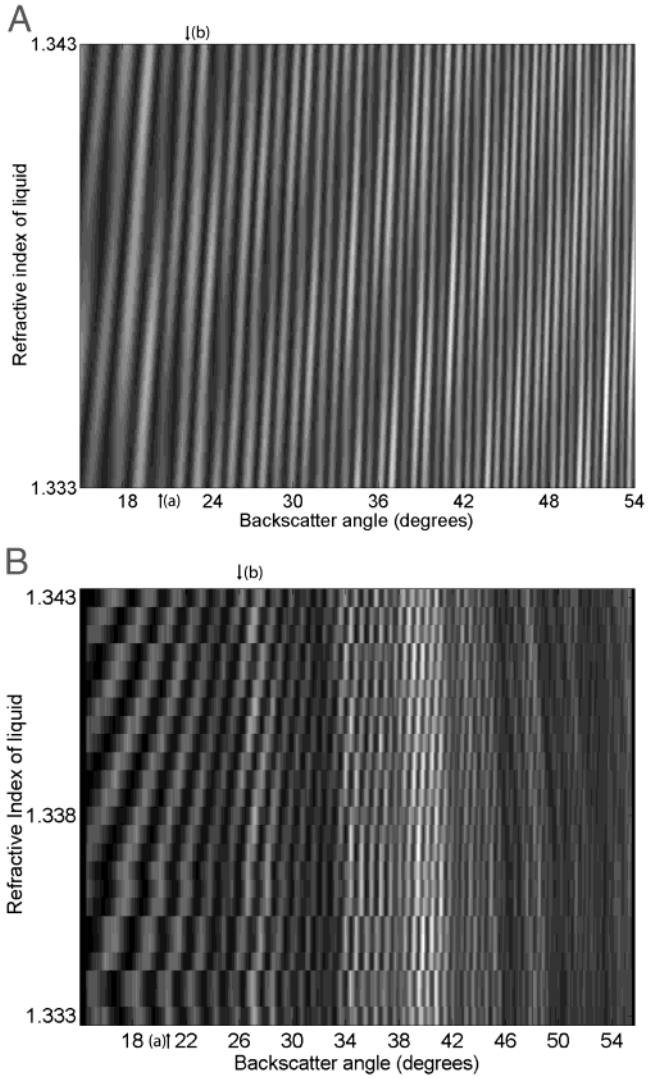

Figure 5. (A) Calculated backscattering pattern for a smaller refractive index range from a 100-μm-i.d./165-μm-o.d./12-μm coating capillary. The movement of the fringes at a backscatter angle of 20° is measured to be ~2.1° per 0.01 refractive index change, measuring from (a) to (b). (B) Experimentally obtained data for dilute sucrose solutions in a 100-μm-i.d./165-μm-o.d./12-μm coating capillary. The refractive index interval between measurements is less than the change required to move a fringe one fringe width, thus allowing one to monitor the medium-frequency fringes as continuous bands. The movement of these fringes varies with backscattering angle. For a backscattering angle of 20°, this movement is measured to be 4.0° per 0.01 refractive index change, measuring from (a) to (b). Low-frequency variations are seen as vertical light bands.

Comparison of Experiment and Model. The results from the model are plotted in Figures 4A and 5A as a function of backscatter angle and refractive index of the liquid for a 100-μm-i.d./165-μm-o.d./12-μm coating capillary. The gray scale represents the intensity of the pattern in the given backscattered angle for the given refractive index of the liquid. Experimentally obtained data are plotted the same way as the model, and the results are shown in Figures 4B and 5B. At each refractive index, a line profile of the intensity of the interference pattern has been made (Figure 3C and D). Each line profile has been extended vertically. The extended line profiles have been stacked into a single plot. These figures are used to directly compare the model and the experi-

ment. In the MIBD experiments, two sets of fringes are always present. The fringes moving outward (medium frequency) with increasing refractive index are measured to move 4.0° when the refractive index is changed by 0.01 at a backscattering angle of 20° (a, b in Figure 5B). The model predicts a movement of 2.1° (a, b in Figure 5A). These are the fringes traditionally used for measuring refractive index using the MIBD technique. This model predicts both low-frequency and medium-frequency variations of the pattern. These frequencies will be discussed below. The low-frequency fringes are not moving significantly with changing refractive index. The model predicts no movement of these fringes. The number of these fringes in the model is 13, and in the experiment, 10 fringes are observed within a range of backscattering angles from 14 to 54°. Both model and experiment show an abrupt change in intensity at large backscattering angles. This abrupt change in intensity is somewhat displaced in the modeled results compared to the experimental results, but it is within experimental error. Experimentally, movement of this abrupt change in intensity qualitatively agrees with our modeling of the MIBD system, while the model does not fit experiment quantitatively. The predictions of the model have been used to select the proper capillary dimensions for our applications of the MIBD technique.

Absolute Measurement of Refractive Index Based on Fresnel Coefficients. Even though the low-frequency variations remain stationary in terms of backscattered detection angles, their intensity changes as the refractive index of the liquid changes. Since the intensity of the rays are in part determined by the Fresnel coefficients of the surface of reflection, it is possible to configure the system in such a way that the intensity of the low-frequency component can be used as a measure for the refractive index on a coarser scale. This may be done by either index matching the coating and the glass tubing, thereby eliminating the reflection from the surface at the interface of the coating and glass (points b and e in Figure 2), or by stripping the coating off the capillary. The low-frequency component is then caused by interference between two rays: the ray reflected by the air-coating (points a and f in Figure 2) or air−glass interface (points b and e if the coating is removed) and the ray reflected from the glass−liquid interface (points c and d in Figure 2). Since the intensity of this last ray is determined by the Fresnel coefficients of this surface consisting of glass with constant refractive index and the liquid to be probed, the absolute value of the refractive index of the liquid may be calculated from the relative intensity of the two rays, which is given by the depth of modulation of the low-frequency component. This is only possible if the refractive index of the air, glass, and coating is known. This approach has only been theoretically examined due to lack of intensity resolution (8-bit) of the CCD camera. If one wants to measure depth of modulation to a certain degree, one needs at least this degree of intensity resolution in the detection system. Since our CCD camera only has 255 intensity levels, we would not be able to acquire more refractive index resolution than the difference in refractive index between air and glass divided by the number of detectable intensity levels, which corresponds to 5×10^{-3}.

Absolute Measurement of Refractive Index Based on Total Internal Reflection. The model predicts an abrupt change in intensity moving toward lower backscatter angles as the refractive index of the liquid approaches the one of the glass tubing (see line marked by (a) in Figure 4A). This feature of the interference pattern is also observed experimentally (see (a) in Figure 4B) and agrees with the predicted feature in position−refractive index space within experimental error. A feature similar to this has been reported for optical glass fibers.[31] However, optical fibers have a different optical configuration; therefore, the scattering mechanisms responsible for the production of the fringe pattern are different. In the case of optical glass fibers, the mechanism responsible is grazing of a certain ray on the core of the fiber being dependent on the inner radius of the glass fiber. In MIBD, the mechanism is total internal reflection in the wall of the capillary, which is dependent on the refractive index of the liquid in the capillary. The main source of error in the modeling of the MIBD system is the dimensions of the capillary, which has an uncertainty of 6 μm for the 100-μm-i.d./165-μm-o.d./12-μm coating capillary according to the manufacturer. The way of determining the absolute value of refractive index on a coarser scale is to look at the abrupt change in intensity of the pattern. Both the model and the experiment show an abrupt change in light intensity at higher backscatter angles, and the position of this change varies with refractive index. Using a 100-μm-i.d./165-μm-o.d. capillary, this change takes place at refractive indices 1.40−1.50, which is useful for measurements using organic solvents. Most dilute aqueous solutions of biological relevance have refractive indices in the range from 1.33 to 1.40; in general using our model, one is able to calculate the dimensions of the capillary required to make the abrupt intensity change occur in position/refractive index space at refractive indices above 1.33 and at backscattering angles inside our measurement range. The model shows that the abrupt change in intensity occurs at lower angles and at lower refractive indices for capillaries with a higher ratio between inner and outer diameter, i.e., thinner walls, and specifically the model predicts that a capillary with 542-μm-i.d./673-μm-o.d./24-μm coating will be applicable in this region. The mechanism responsible for this abrupt change in intensity is, according to the model, total internal reflection at the coating−air interface of the rays reflected from the back of the capillary. This total internal reflection prevents these rays from being scattered to larger backscattering angles, thereby causing a sudden decrease in the intensity of the light at a given limiting angle (see Figure 6A). This angle varies uniformly with the refractive index and may therefore be used as a measure for the refractive index of the liquid.

The modeled interference pattern as function of refractive index for a 542-μm-i.d./ 673-μm-o.d./24-μm coating capillary is shown in Figure 6B. Figure 6C shows the experimental results from using a 542-μm-i.d./ 673-μm-o.d./24-μm coating capillary. The experimental and the modeled results show good agreement. The abrupt change in interference pattern is already detectable at the refractive index of water and is experimentally accessible well beyond refractive indices normally considered for aqueous solutions, see point a in Figure 6B. The discrepancy between the predicted and the measured angles of the abrupt intensity change may be attributed to material parameter tolerances of the experimental setup as follows: The uncertainty of the dimensions of this capillary is 12 and 25 μm for the inner and outer diameters, respectively, giving an uncertainty of 6.9° in the angle predicted by the model. The uncertainty in refractive index of the polyimid

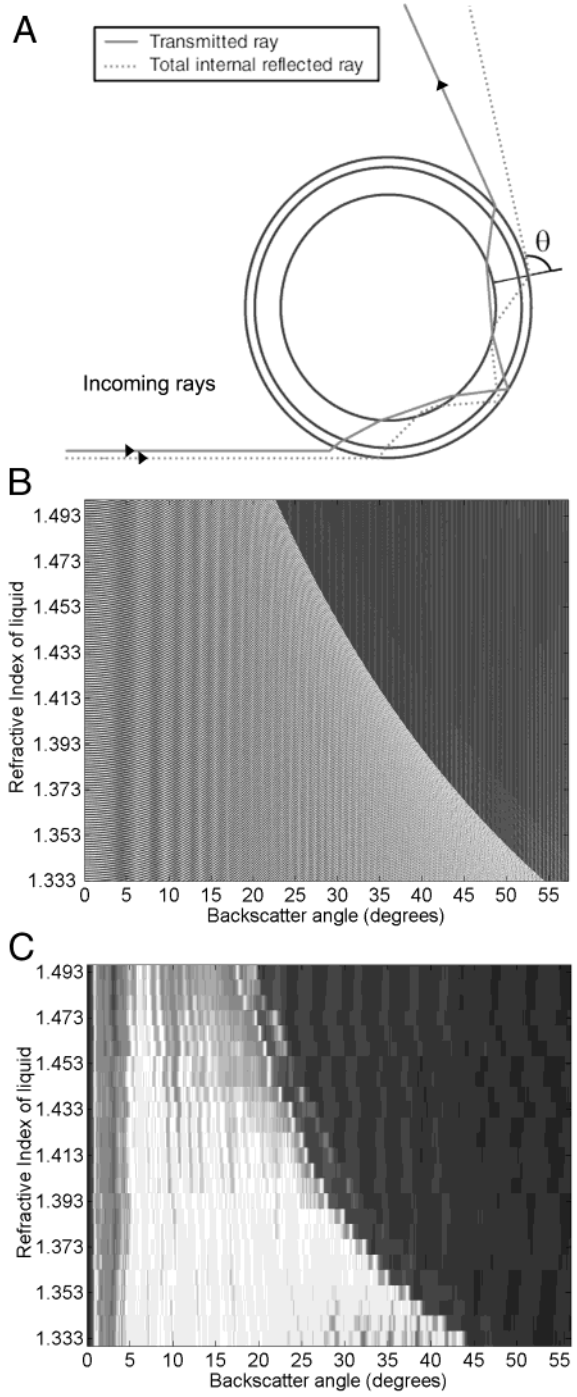

Figure 6. (A) Schematic cross-sectional view of the capillary. When the angle θ approaches 90°, the intensity of the transmitted light decreases sharply due to total internal reflection. Solid line shows a ray being transmitted through the system, whereas the dotted line shows the path of the ray being total internally reflected at the glass−air interface ($\theta = 90°$). The outgoing dotted line marks the highest angle at which single reflected rays may be backscattered. (B) Calculated pattern for a 542-μm-i.d./673-μm-o.d./24-μm coating capillary as function of backscatter angle and refractive index of the liquid. Both low- and medium-frequency variations as well as the abrupt change in intensity level at high backscatter angles are seen. The abrupt change in intensity for this capillary occurs in a more relevant interval for dilute aqueous solutions than it does for the 100-μm-i.d./165-μm-o.d./12-μm coating capillary, as indicated by (a). (C) Experimentally obtained pattern for a 542-μm-i.d./673-μm-o.d./24-μm coating capillary. It is seen by comparison to (B) that the position of the abrupt change in intensity differs from the model, although the behavior is quantitatively the same. Analyte used is aqueous solutions of NaSCN.

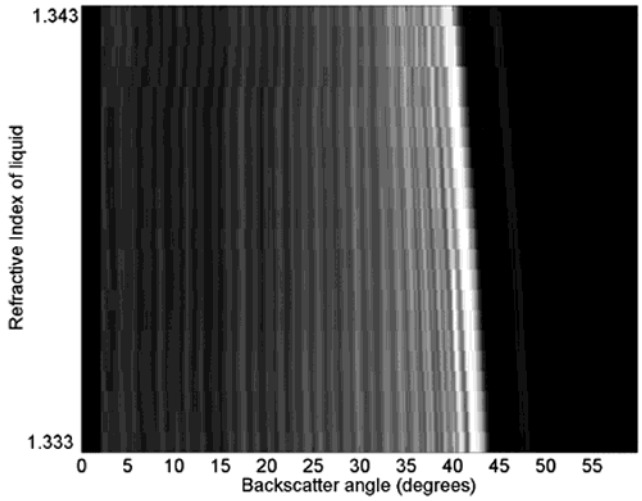

Figure 7. Experimentally obtained data from a 542-μm-i.d./673-μm-o.d./24-μm coating capillary using sucrose as analyte. The position of the abrupt change in intensity is monitored as a function of the refractive index of the sucrose solutions. The detection limit for refractive index changes achieved by following the position of this change in position is 2.5×10^{-4} corresponding to 321 ng in a 180-nL probe volume.

coating ($n = 1.5-1.8$) is causing a further uncertainty in the predicted angle of 3.3°. From the experiments shown in Figure 7 the precision is found to be 2.5×10^{-4}. The position of the abrupt change in intensity is determined at each refractive index. The refractive index of the injected solutions increases linearly. The positions' deviation from a line is the measure of the precision. Hence, we are able to perform an absolute refractive index measurement with accuracy on this level on a 180-nL volume. The main limitations for accuracy such as temperature control and detector resolution are the same as conventional MIBD. The theoretical limit using this approach is therefore similar to the limit achievable by conventional MIBD, and it is possible to perform a conventional MIBD measurement simultaneously with our newly proposed method. In principle, if the dimensions and refractive index of the capillary tube are known, then there is a one-to-one relationship between the backscatter angle and the refractive index of the liquid, thus enabling the determination of the absolute refractive index. Normally, however, one needs to calibrate the system by running a set of RI standards.

CONCLUSION

Our new concept of investigating a larger range of interference fringes offers fundamentally new applications of the microinterferometric backscatter detection scheme. We have shown two possible ways of making absolute measurements of the refractive index of liquid in nanoliter probe volumes with a simple optical setup. The improved model based on ray tracing has been used to reveal and explain novel features of the interference pattern: An abrupt change in intensity at large backscattered angle is clearly present in the modeled system and in the experimental results. It is shown that this approach enables an absolute determination of the refractive index in the range from 1.33 to 1.5 by using capillary tubes of appropriate dimensions. It has been proven that the model based on ray tracing may be used for describing the MIBD phenomenon. The improved ray tracing

model is capable of explaining all the significant features of the MIBD pattern except the stationary high-frequency fringes. However, these fringes have been shown to originate from reflections from the edges of the capillary and are not relevant for measuring the refractive index of the liquid within. Our model may be used to select the capillary, with the appropriate dimensions, that optimizes the sensitivity at a given refractive index interval, suited for a specific application. We believe that the reported improvements for the MIBD scheme will significantly enhance the future applicability of the methodology for analysis of minute volumes of aqueous solutions.

ACKNOWLEDGMENT

The authors acknowledge the financial support from the National Science Foundation and the Royal Society of Chemistry.

Received for review October 8, 2002. Accepted January 16, 2003.

AC0206162

Label-Free Biosensors

DOI: 10.1002/anie.200502418

Photobiotin Surface Chemistry Improves Label-Free Interferometric Sensing of Biochemical Interactions**

*Joey C. Latham, Dmitry A. Markov, Henrik S. Sørensen, and Darryl J. Bornhop**

To accurately characterize molecular interactions, determinations should be done in a label-free manner.[1,2] Furthermore, in order to have the capability to fully evaluate the molecular diversity that exists in nature, it would be most advantageous to make these determinations with micro-total-analysis systems (μ-TAS)[3,4] configured for high throughput.[5,6] Yet, conventional detection methods are difficult to implement in μ-TAS and are often volume- or sensitivity-limited, both impediments to performing systems-biology analyses.

Investigators have developed various detection methods for use with microfluidic devices that have promise for label-free nanoscale detection. These include the nanoelectrode,[7] the porous Si (p-Si) sensor,[8,9] the surface plasmon resonance (SPR) detector,[10–13] and backscattering interferometry.[14–16] However, nanoelectrodes foul easily in real-world applications and require multistep manufacturing procedures for the integration into microfluidic chips. The SPR and p-Si methods are sensitive (detection limits of ≈10–50 nM for protein interactions[8,9,17]) and capable of sensing label-free biochemical interactions, yet neither technique is inherently compatible with μ-TAS. Integration or immobilization of p-Si into the fluidic network and long solute-diffusion times hinder the use of this method in μ-TAS. Since SPR relies on the excitation of plasmons—collective oscillations of free electrons that occur predominantly in metals—SPR surfaces are coated with a thin metal layer (for example, gold). This makes integration of SPR sensors into plastics challenging and relatively expensive as a result of the deposition process. Additionally, the elaborate surface chemistry used to immobilize targets on SPR surfaces has been shown to lose as much as 20% of binding capacity over a 24-hour period.[10] Backscattering interferometry in rectangular channels (BIRC)[15] was recently shown to be applicable to label-free assays, can be used to study reversible molecular interactions in poly(dimethylsiloxane) (PDMS) chips, and is compatible with μ-TAS. Although promising, BIRC has been limited by tedious immobilization chemistry and, owing to less than optimum transduction-scheme concentration detection limits, has bordered on relevance to biological systems.

Herein we address many of these problems through the use of simple and robust surface immobilization chemistry on polymer chips and an improved BIRC instrument based on charge-coupled-device (CCD) transduction and fringe-pattern Fourier analysis. For the first time, it is shown that simple photoactivatable surface chemistry[18,19] can be used for the immobilization of substrates onto PDMS-facilitated, label-free, reversible-binding assays. This simplified approach to surface immobilization is a significant alteration to our earlier binding studies and those methods commonly used for surface activation/immobilization chemistry.[12,20]

A two-step biotin/avidin reaction (Figure 1) with a carbene-generating form of photobiotin consisting of a

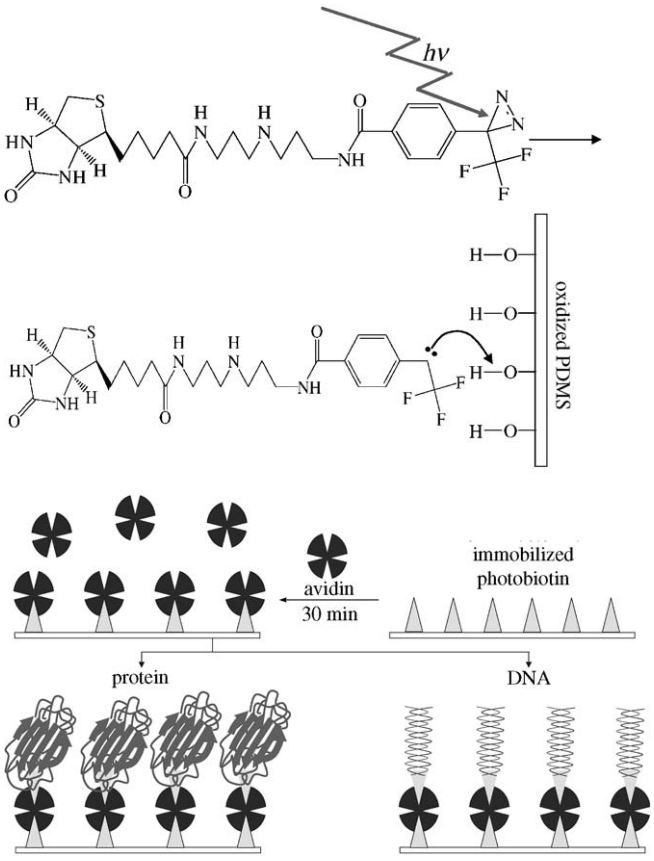

Figure 1. Top: Photobiotin is activated upon exposure to UV light and this promotes insertion into the oxidized PDMS substrate. Center: Avidin binds strongly to the immobilized layer of biotin. The tetrameric nature of avidin signifies that it can simultaneously bind the surface-bound biotin as well as any biotinylated target molecule that passes through the channel (bottom).

[*] J. C. Latham, D. A. Markov, Prof. Dr. D. J. Bornhop
Vanderbilt University
Department of Chemistry
4226 Stevenson Center, Nashville, TN 37235 (USA)
Fax: (+1) 615-343-1234
E-mail: darryl.bornhop@vanderbilt.edu

H. S. Sørensen
RISØ National Laboratory
Department of Optics and Plasma Research
Building 130, Frederiksborgvej 399, 4000 Roskilde (Denmark)

[**] This work was supported by the National Science Foundation, National Eye Institute, BioP graduate school, Applied Biosystems, and NASA. Affiliations include the Vanderbilt Institute of Nanoscience and Engineering, Vanderbilt Institute of Chemical Biology, and Vanderbilt Institute for Integrative Biosystem Research and Education.

Supporting information for this article is available on the WWW under http://www.angewandte.org or from the author.

biotin moiety, spacer arm, and photoactivatable group was used to immobilize target molecules of interest. A solution (7 μL) of carbene-generating photobiotin (0.5 mg mL^{-1}) containing 0.02% Tween 20 and 50% (v/v) acetone was introduced into the PDMS channels and allowed to dry. Irradiation of the photobiotin molecule caused photolysis of the diazirine group, thereby producing an electronically excited np* state. Formation of an excited-state diradical was followed by internal conversion and production of a carbene. The highly reactive carbene was then inserted into the oxidized substrate. As a result, a homogeneous layer of biotin molecules was strongly bound to the channel surface.

A solution of extravidin (0.5 mg mL^{-1}) was injected into the same channels and allowed to incubate for 30 min. Extravidin recognizes the imidazole ring that is *cis* fused to a tetrahydrothiophene ring, and binds to biotin with high affinity (association constant, $K_a = 2.5 \times 10^{11}$ M^{-1}).[21] The resulting biotin/avidin complex is very stable to changes in temperature, pH value, and denaturing agents, unlike the lysine/glutaraldehyde/streptavidin/ethanolamine sandwich described in our earlier binding experiments.[15] Fluorescence images (not shown) of fluorescein isothiocyanate (FITC) labeled avidin were used to confirm that the surface chemistry used for immobilization was successful. Thus, biotinylated targets can be immobilized onto the PDMS-molded channel surface to result in a cost-effective, disposable chip that is applicable to the analysis of a variety of reversible biochemical interactions.

As described in detail elsewhere,[14,15,22,23] BIRC (Figure 2) employs a connected light source that illuminates

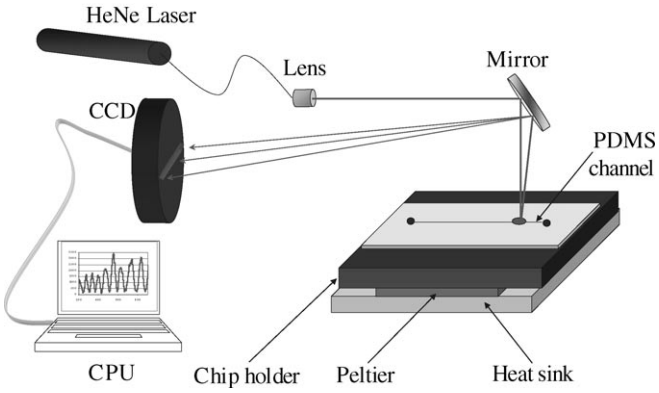

Figure 2. Schematic diagram of BIRC showing the simple optical train consisting of a connected light source, a microfluidic channel, and a phototransducer.

a microfluidic channel, thereby creating a series of high-contrast interference fringes in the backscattered direction that shift with the optical pathlength. Herein we show that the overall performance of BIRC can be improved 100-fold through proper design and implementation of the photo-transduction method.

The use of a CCD combined with spatial Fourier analysis[14] for signal transduction, rather than an avalanche photodiode detector, facilitates improved sensitivity and reproducibility, while greatly simplifying alignment. Direction of multiple fringes onto the CCD array promotes signal averaging and enhanced signal-to-noise (S/N) results. A fringe-pattern Fourier transformation (FFT) algorithm is inherently insensitive to laser-intensity fluctuations[14] and allows spatial phase determination. Since the CCD is a large-area device, three to upwards of eight fringes from the interference pattern can be used, thereby eliminating the need to align the slit-photodetector with respect to $1/e^2$ intensity on a particular fringe.

To evaluate the new immobilization chemistry and transduction method, two reversibly binding pairs were studied, protein A (P_A) linked to immunoglobulin G (IgG) and a 30-mer DNA–DNA pair. P_A, containing four high-affinity ($K_a = 2 \times 10^8$–4.54×10^8 M^{-1}) binding sites capable of interacting with the F_c region of IgG from several species, including human and rabbit, was immobilized onto a PDMS chip by using the chemistry shown in Figure 1. The reversible-binding assay of P_A with IgG was repeated five times (Figure 3). The non-

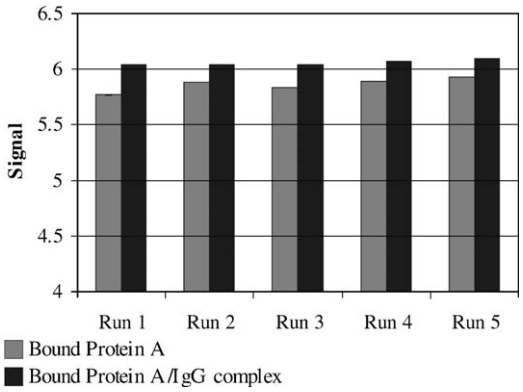

Figure 3. Biotinylated P_A was immobilized on the channel surface. Unreacted P_A was washed out with phosphate-buffered saline (PBS)/Tween 20. A human IgG F_c solution (0.5 mg mL^{-1}) in PBS was introduced into the microfluidic channel and allowed to bind to the P_A for 5 min. The channel was then rinsed with PBS/Tween 20 to remove any unbound IgG. Removal of the bound IgG from P_A was performed by using an acetic acid wash.

complementary fragment, F_{ab}, served as the control and showed no signal (change in refractive index/phase; data not shown) when introduced into the P_A-coated channel. As seen in Figure 3, reversible-binding events can be monitored with an excellent S/N ratio (pooled standard deviation = 0.0017). If it is assumed that complete reaction between the binding pair took place, and on the basis of the target-surface coverage, the 3σ detection limit is 4×10^{-17} mol (40 attomol) in a 500-pL probe volume. These results represent an increase in sensitivity of two orders of magnitude when they are compared to the P_A/IgG experiments performed previously.[15]

The use of microfluidic chips to perform nucleic acid analysis has allowed the detection and discrimination of multiple DNA sequences[24,25] and can eventually facilitate high-throughput screening techniques.[26] As further demonstration of the utility of BIRC, a label-free reversible DNA assay was performed (Figure 4). Immobilization of a biotinylated 30-mer of mActin (5′-ACTCATCGTACTCCTGCT-

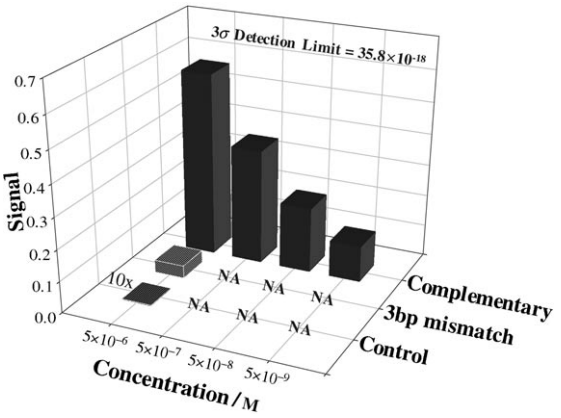

Figure 4. The binding affinity of a complementary DNA strand to an immobilized target over a multiple complementary strand. The complementary strand is also compared to a 3-bp mismatch and control strands at high concentration. All probe strands were allowed 20 min for hybridization. The control signal is shown at ten times its actual signal to allow visualization.

TGCTGATCCACA-3′; $M_W = 9622.5$; melting temperature, $T_M = 68.7\,^{\circ}C$) onto the PDMS channel was possible with the biotin/avidin surface chemistry described above. Nonlabeled complementary DNA strands were successively hybridized to the immobilized mActin 30-mer and then removed with an NaOH wash. Binding events of complementary DNA followed exponential growth for BIRC over concentrations ranging from 5 nM up to roughly 500 mM with excellent convergence ($R^2 = 0.988$). A noncomplementary probe strand, according to the Watson–Crick model, served as the control and showed no appreciable signal. If it is assumed that hybridization went to completion and 100% channel-surface coverage was attained, at 3σ, 36 attomol DNA were quantifiable in a 500-pL detection volume.

Ultimately, it would be desirable to screen for an array of different sequences in a label-free manner to avoid perturbations due to the signaling fluorophore or derivation chemistry. A step toward this requires the determination of the discrimination that is possible with BIRC. We used an oligomer consisting of a three-base-pair mismatch (at positions 5, 15, and 25) from that of the complementary mActin strand as an initial test of specificity. The experiment consisted of immobilizing the mActin 30-mer as noted above and a subsequent repetitive hybridization test with a 5-μM solution of the mismatch strand. Figure 4 shows the typical output from one of the binding evaluations. Three trials of these experiments produced an average signal corresponding to greater than 140% of that for the control and approximately 7% of the signal for the complementary strand.

In conclusion, the biotin/avidin surface chemistry significantly simplified substrate preparation, was compatible with PDMS, and facilitated free-solution assays with BIRC. Combination of this new surface chemistry with the CCD FFT transduction has allowed improved detection for P_A/IgG binding by two orders of magnitude.[15] BIRC was also used to monitor DNA hybridization over a wide range of concentrations and allowed discrimination in binding of a three-base-pair mismatch. The use of PDMS microfluidic chips and the exceedingly simple optical train of BIRC represents a cost-effective platform for label-free molecular-interaction determinations as well as for the investigation of reversible biological interactions within subnanoliter volumes and at the attomole level. The methodology and technology are compatible with large-scale integration and should facilitate high-throughput assays.

Received: July 11, 2005
Published online: ■■ ■■, ■■■■

Keywords: biosensors · interferometry · nucleic acids · proteins · surface chemistry

[1] M. A. Cooper, *Anal. Bioanal. Chem.* **2003**, *377*, 834.
[2] F. E. Torres, P. Kuhnt, D. De Bruyker, A. G. Bell, M. V. Wolkin, E. Peeters, J. R. Williamson, G. B. Anderson, G. P. Schmitz, M. I. Recht, S. Schweizer, L. G. Scott, J. H. Ho, S. A. Elrod, P. G. Schultz, R. A. Lerner, R. H. Bruce, *Proc. Natl. Acad. Sci. USA* **2004**, *101*, 9517.
[3] C. Hansen, S. R. Quake, *Curr. Opin. Struct. Biol.* **2003**, *13*, 538.
[4] S. K. Sia, G. M. Whitesides, *Electrophoresis* **2003**, *24*, 3563.
[5] J. R. Heath, M. E. Phelps, L. Hood, *Mol. Imaging Biol.* **2003**, *5*, 312.
[6] M. Ferrari, *Nat. Rev. Cancer* **2005**, *5*, 161.
[7] J. Hahm, C. M. Lieber, *Nano Lett.* **2004**, *4*, 51.
[8] V. S. Y. Lin, K. Motesharei, K. P. S. Dancil, M. J. Sailor, M. R. Ghadiri, *Science* **1997**, *278*, 840.
[9] K.-P. S. Dancil, D. P. Greiner, M. J. Sailor, *J. Am. Chem. Soc.* **1999**, *121*, 7925.
[10] R. L. Rich, Y. S. N. Day, T. A. Morton, D. G. Myszka, *Anal. Biochem.* **2001**, *296*, 197.
[11] E. A. Smith, W. D. Thomas, L. L. Kiessling, R. M. Corn, *J. Am. Chem. Soc.* **2003**, *125*, 6140.
[12] J. M. Brockman, A. G. Frutos, R. M. Corn, *J. Am. Chem. Soc.* **1999**, *121*, 8044.
[13] G. J. Wegner, N. J. Lee, G. Marriott, R. M. Corn, *Anal. Chem.* **2003**, *75*, 4740.
[14] D. Markov, D. Begari, D. J. Bornhop, *Anal. Chem.* **2002**, *74*, 5438.
[15] D. A. Markov, K. Swinney, D. J. Bornhop, *J. Am. Chem. Soc.* **2004**, *126*, 16659.
[16] K. Swinney, D. Markov, D. J. Bornhop, *Anal. Chem.* **2000**, *72*, 2690.
[17] T. Sakai, K. Shinahara, A. Torimaru, H. Tanaka, Y. Shoyama, K. Matsumoto, *Anal. Sci.* **2004**, *20*, 279.
[18] S. A. Brooks, W. P. Ambrose, W. G. Kuhr, *Anal. Chem.* **1999**, *71*, 2558.
[19] S. A. Brooks, N. Dontha, C. B. Davis, J. K. Stuart, G. O'Neill, W. G. Kuhr, *Anal. Chem.* **2000**, *72*, 3253.
[20] G. M. Whitesides, E. Ostuni, S. Takayama, X. Y. Jiang, D. E. Ingber, *Annu. Rev. Biomed. Eng.* **2001**, *3*, 335.
[21] A. Chilkoti, P. S. Stayton, *J. Am. Chem. Soc.* **1995**, *117*, 10622.
[22] H. S. Sorensen, H. Pranov, N. B. Larsen, D. J. Bornhop, P. E. Andersen, *Anal. Chem.* **2003**, *75*, 1946.
[23] K. Swinney, D. Markov, D. J. Bornhop, *Rev. Sci. Instrum.* **2000**, *71*, 2684.
[24] A. J. Thiel, A. G. Frutos, C. E. Jordan, R. M. Corn, L. M. Smith, *Anal. Chem.* **1997**, *69*, 4948.
[25] Y. W. C. Cao, R. C. Jin, C. A. Mirkin, *Science* **2002**, *297*, 1536.
[26] F. Vinet, P. Chaton, Y. Fouillet, *Microelectron. Eng.* **2002**, *61–62*, 41.

Communications

Label-Free Biosensors

J. C. Latham, D. A. Markov,
H. S. Sørensen,
D. J. Bornhop* ———— ■■■■-■■■■

Photobiotin Surface Chemistry Improves Label-Free Interferometric Sensing of Biochemical Interactions

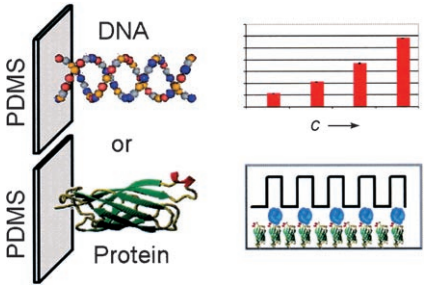

A highly sensitive and cost-effective biosensor: Simple surface chemistry of photobiotin , bound with a layer of avidin, allows convenient immobilization of any biotinylated molecule of interest onto microfluidic channels molded in poly(dimethylsiloxane) (PDMS). The biosensor obtained this way is capable of monitoring biomolecular interactions in label-free situations and in small (picoliter) volumes.

Mission

To promote an innovative and environmentally sustainable technological development within the areas of energy, industrial technology and bioproduction through research, innovation and advisory services.

Vision

Risø's research **shall extend the boundaries** for the understanding of nature's processes and interactions right down to the molecular nanoscale.

The results obtained shall **set new trends** for the development of sustainable technologies within the fields of energy, industrial technology and biotechnology.

The efforts made **shall benefit** Danish society and lead to the development of new multi-billion industries.